Optical Crosspoint Switch Based on a Novel Active Vertical Coupler Structure

Submitted by Riccardo Varrazza for the degree of Ph.D.

Department of Electrical and Electronic Engineering

University of Bristol

2002

Optical Crosspoint Switch Based on a Novel Active Vertical Coupler Structure

Submitted by Riccardo Varrazza for the degree of Ph.D.

Department of Electrical and Electronic Engineering

University of Bristol

2002

Copyright and Author's Declaration

Unless otherwise acknowledged, the content of this thesis is the original and sole work of the author. No portion of the work in this thesis has been submitted by the author in support of an application for any other degree or qualification, at this or any other university or institution of learning

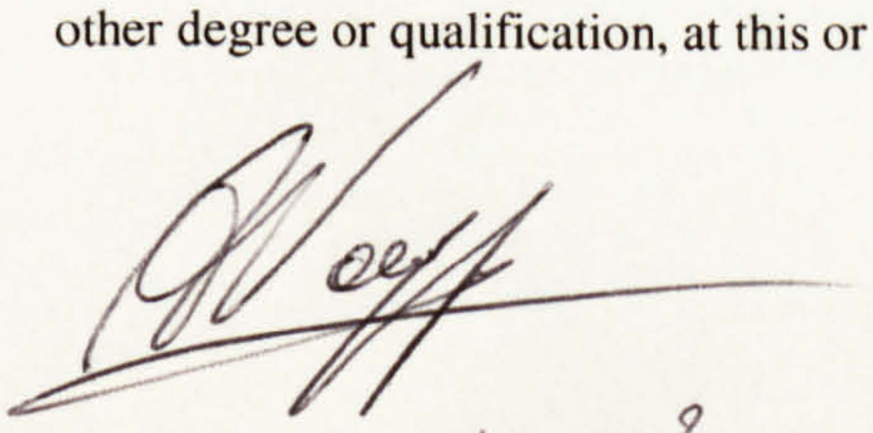

30/04/2003

Abstract

The work of this thesis concerns the theoretical analysis, fabrication and characterisation of a novel optical crosspoint switch that can be employed in future optical packet switching networks.

The switching technique is based in a novel approach, which uses vertical couplers in order to redirect the light to different outputs. The structure, which employs an active and a passive waveguide layers, only requires a single epitaxial growth process on InP substrate. Such process can be precisely controlled and reproduced allowing coupling lengths in the order of 250μm. This allows fabrication of very compact devices, using normal photolitography and etching steps.

When carriers are injected, because of refractive index change and gain change in the active layer, the two waveguide layers becomes optically coupled and the light is transferred between them. Incoming light in the passive waveguide layer will be coupled to the active waveguide layer, reflected by a total internal reflection mirror, and couple back to passive waveguide in other direction. Fast optical switch is therefore achievable with high extinction ratio and low crosstalk.

A theoretical study revealed design guideline for realisation of good device performance. Some vertical coupler structures, designed by Dr. Yu previously, have been analysed showing that ON-OFF contrast and Crosstalk in the order of 60dB and -52dB respectively can be achieved in some structures.

Switch devices have been made at the University of Bristol Clean Room facility with the aim of investigating and optimising each single fabrication step of the 4x4 optical crosspoint switch including a novel passivation process that improves sensibly the electro-optical characteristics of the device.

The characterisation results have shown ON-OFF contrast and Crosstalk in the same order of the theoretical results. Furthermore, the measured 3dB optical bandwidth is greater than 40nm and the measured switching time is as low as 1.5ns.

Packet routing using the device has been demonstrated with data rates up to 10Gbps. In particular simultaneous switching and wavelength conversion of the packets has also been demonstrated confirming the high reconfiguration flexibility of the device and the suitability for the next generation of optical networks.

Acknowledgements

I would first like to thanks Dr. Siyuan Yu for the many opportunities he has given to me so far and on his patience with me. I have gained a lot of work experience and life experience, which would not be without his constant supervision.

Many thanks must also go to BAE SYSTEMS for encouragement and financial support along with the EPSRC under the CROSSPOINT scheme.

I want also thanks Professor I.H. White for his contribution and the life lessons given to me during his staying in Bristol.

Great thanks to Dr. Martin Cryan and Ms. Liz Tyler for help and thesis supervision.

Much of the work realised in clean room is also due thanks to the initially tuition and support of Dr. Bullent Cakmak.

Special thanks to Mr. Mike Redwood for his constant support provided in clean room.

Thanks also to Dr. Mike Bordovsky for his theoretical and psychological support during and also after his stay in Bristol.

Thank to all the Optics Group of the University of Bristol and finally as good Italian tradition I want to thank and dedicate this work and this step of my life to my parents and my brother always beside me in each single minute.

Publications

1. S.Yu, **R.Varrazza**, M. Owen, R.V. Penty and I.H. White (Univ. Of Bristol), D. Rogers, S. Perrin (BT Laboratories), C.C. Button (EPSRC Central III-V Facilities Univ. Of Sheffield); "Ultra-low Crosstalk, Compact Integrated Optical Crosspoint Space Switch Arrays Employing Active InGaAsP/InP Vertical Waveguide Couplers"; Postdeadline Paper – CLEO 99, May 23-28, 1999, Baltimore USA.
2. S.Yu, M.Owen, **R.Varrazza**, R.V. Penty and I.H. White (Univ. Of Bristol), D. Rogers, S. Perrin (BT Laboratories), C.C. Button (EPSRC Central III-V Facilities Univ. Of Sheffield); "Compact Integrated Optical Crosspoint Switches Employing Active InGaAsP/InP Vertical Waveguide Couplers with Ultralow Crosstalk"; ECOC 99- Sep. 1999, Nice France.
3. S.Yu, M.Owen, **R.Varrazza**, R.V. Penty and I.H. White; "High Speed, Ultralow Crosstalk Integrated Optical Crosspoint Switch Array Employing Vertical Waveguide Couplers"; APCC/OECC 99, Oct. 18-22, 1999, Beijing, China.
4. **R.Varrazza**, S.Yu, M. Owen, I. Khrushchev, R.V. Penty and I.H. White (University of Bristol) S.V. Dewar (University of Wales, Cardiff); "All-Optical switching in a vertical coupler space switch employing photocarrier-induced non-linearity"; CLEO 2000, May 7-12, 2000, S. Francisco, USA.
5. S.Yu, M.Owen, **R.Varrazza**, R.V. Penty and I.H. White; "High Speed Optical Packet Routing Demonstration of a Vertical Coupler Crosspoint Space Switch Array"; CLEO 2000, May 7-12, 2000, S. Francisco, USA.
6. S.Yu, M.Owen, **R.Varrazza**, R.V. Penty and I.H. White; "Demonstration of High Speed Optical Packet Routing Using Vertical Coupler Crosspoint Space Switching Array"; Electronics Letters, Vol.36, pp 556-558, 2000.
7. **R.Varrazza**, A. Wonfor, S. Yu, B. Cakmak, R.V. Penty and I.H. White; "Demonstration of Simultaneous Packet Routeing and Wavelength Conversion at 10Gb/s in a Highly Compact, Lossless Vertical Coupler Optical Space Switch"; ECOC 2000, Sep. 3-7, 2000 Munich, Germany.
8. K.Guild, A. Tzanakaki H. Lee, M.J.O'Mahony(Univ. of Essex), M.Chia M. Nizam, I. Andonovic, D. Hunter (Univ. of Strathclide), S.Yu, A.Wonfor, **R.Varrazza** R.V. Penty and I.H. White (Univ. of Bristol); "Cascading and Routing 14 Optical Packet Switches"; ECOC 2000, Sep. 3-7, 2000 Munich, Germany.

Contents

Tables and Figures

Chapter 1

Chapter 2

Chapter 3

Chapter 4

Chapter 5

Chapter 6

Chapter 7

Chapter 1

Introduction to Future Optical Networks

The work presented in this thesis investigates a novel optoelectronics Optical Crosspoint Switch (OXS) designed to be deployed into future optical networks.

This introductory chapter summarises the tendency of optical telecommunications to focus on optical packet switching networks. Hence, the chapter discusses in detail a network node and its components focusing in the importance of the OXS into actual and future networks.

The chapter investigates also optical wavelength conversion with its potentialities as Wavelength Division Multiplexing (WDM) router. It shows the methods used to achieve the conversion using one or more Semiconductor Optical Amplifiers (SOAs).

Glossary of the abbreviations

(OWC)	Optical Wavelength Conversion
(WDM)	Wavelength Division Multiplexing
(SOA)	Semiconductor Optical Amplifier
(EDFA)	Erbium-Doped Fiber Amplifier
(OTDM)	Optical Time Division Multiplexing
(DFB)	Distribute FeedBack
(ITU)	International Telecommunications Union
(OXS)	Optical Crosspoint Switch
(MEMS)	MicroElectroMechanical Systems
(XGM)	Cross-gain modulation
(XPM)	Cross-Phase Modulation Interoferometric
(FWM)	Four Wave Mixing
(CW)	Continuos Wave
(AR)	Anti Reflection
(ER)	Extinction Ratio
(MZI)	Mach-Zehnder Interferometer
(SCU)	Switch Control Unit

1.1. Introduction

Following the tendency of the past years there has been an increase in the demand for telecommunication bandwidth due to the high growth in telephone voice/data traffic also helped by the advent of internet-based services.

Since 70's optical fibres have played an important role in the transmission of huge quantities of information over many kilometres. Early technology made exclusive use of the 800-900 nm low loss window. The reduction of concentration of hydroxyl ions and metallic ion impurities in the fiber material has permitted the use of the 1100-1600 nm region, which is characterised by very low loss in the 1300 nm and 1550 nm windows [1], Figure1.1. Thus, in 1974 a 2 dB/Km attenuation was announced at 850 nm [2] followed two years later by a 0.5 dB/Km attenuation at 1300 nm [3] and 0.2 dB/Km attenuation at 1550 nm in 1979 [4].

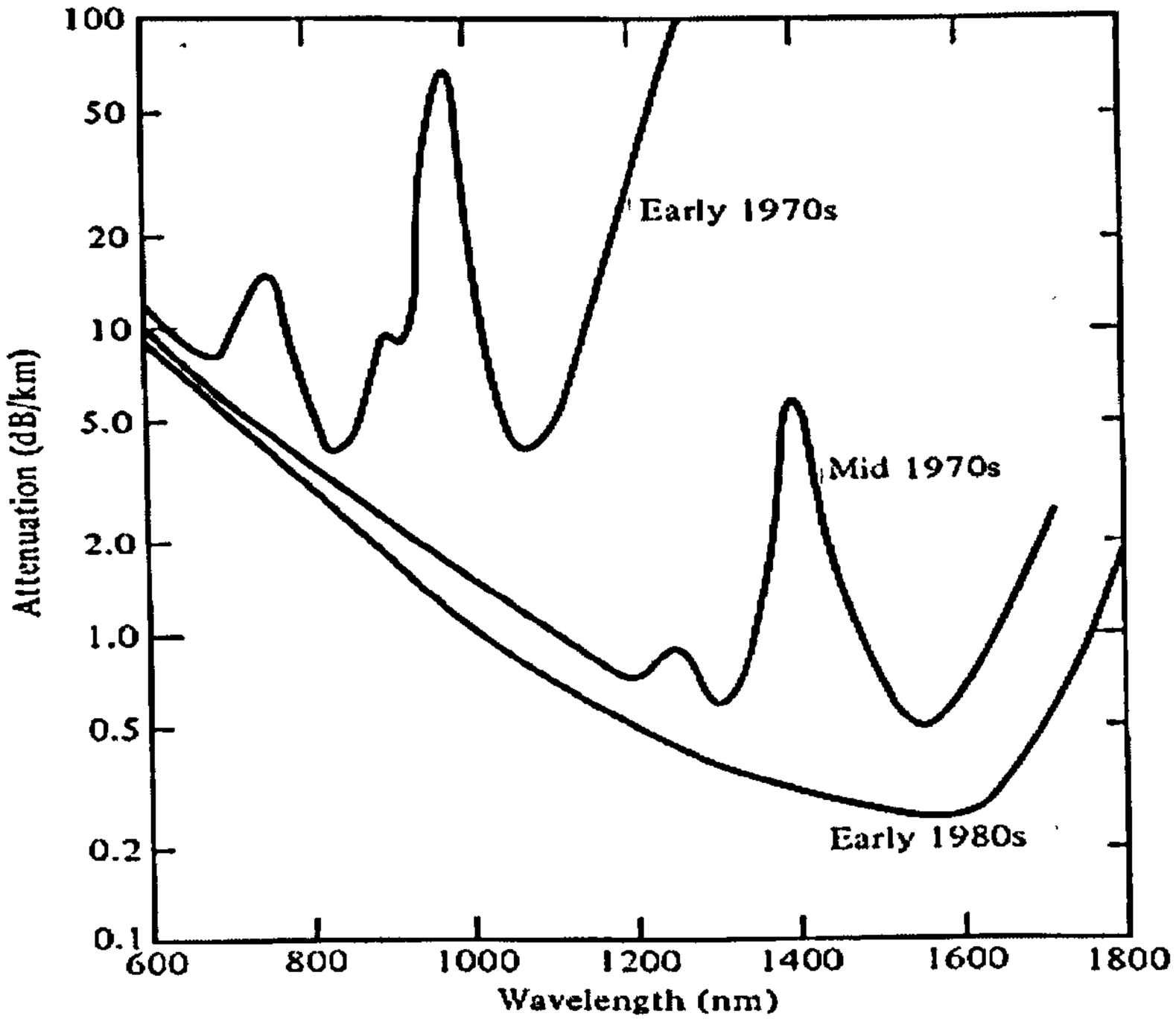

Figure1.1 Optical fiber attenuation as a function of wavelength [1]

An initial application of the fibers was in point-to-point digital telecommunications systems, shown in Figure 1.2, here the signal is converted from electrical into optical and via a transmitter coupled into an optical fiber. At the other end of the fiber the light signal is detected, amplified, restored and finally converted again into an electrical signal. The information is transmitted by encoding it in "ones" and "zeros" of digital data realised respectively with light source "on" and "off".

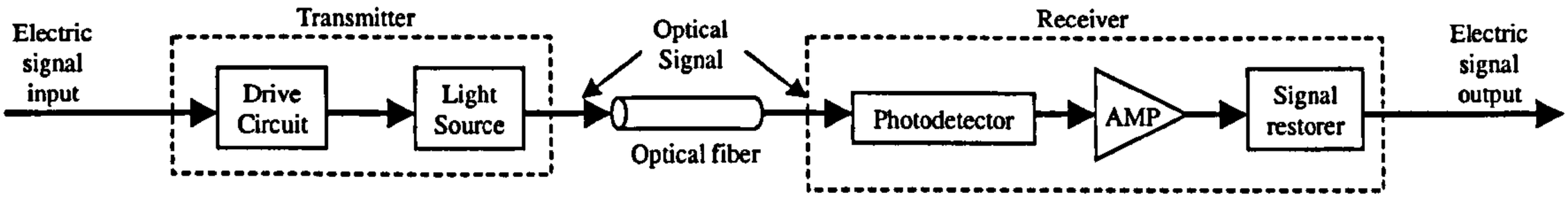

Figure1.2 Basic elements in an optical fiber transmission link

During 1980's there was a rapid growth in the fraction of telecommunication traffic carried on point-to-point single mode fiber links. This resulted in very long non-repeated link e.g. in 1994 the first 280 Km non-repeated link at 10Gbit/s was shown [5].

In the late 1980's, with the advent of Erbium-Doped Fiber Amplifiers (EDFAs) [6] the length of point-to-point distances were increased drammatically. This amplifier has played an important role in the development of 1.5 μm (1530 – 1570 nm) optical telecommunications allowing the regeneration of the optical signal without any electronic conversion. This permits high data rates to be maintained and does not introduce any electronic "bottleneck" into the network. An EDFA is fabricated by doping an optical fiber with erbium and optically pumping it with a laser at 980 nm or 1480 nm. The fiber can be spliced directly on the network and gains up to 60 dB, with very low noise figures (below than 5dB) achievable. Furthermore, the cost of an EDFA is very low when compared with that of an electronic generator.

With the advent of new telecom services the fibers, already installed by public and private operators, did not have sufficient capacity generating a strong interest in the use of the fibres at 100% of their capability. This has driven world wide Research & Development to find new signal processing techniques in order to improve the performances of each single fiber.

The next section of the present introductory chapter treats optical packet switching techniques followed by a description of different multiplexing techniques. Section 1.4 gives a description of a typical network node, highlighting the importance of the crosspoint switch function in it. Furthermore, wavelength conversion will be treated in section 1.5 and finally in section 1.6 a complete presentation of all thesis chapters.

1.2. High Speed Optical Network

Currently installed systems can transmit, with Wavelength Division Multiplexing (WDM) technique, at bit rates of 3.4 Tbit/s over a single fiber for many kilometres; the lightwave transmission capability has been doubling every year and the trend is expected to be the same for the next two decades [8]. This growth trend could make network equipment rapidly obsolete unless upgradable. This is the main reason that optical multiplexing techniques have become so successful. However the more signals travel into a fiber the more they need to be controlled, redirected, restored and so on. This confirms the importance of the optical space switch into optical networks.

Two network schemes have been adopted so far,

- Wavelength Division Multiplexing (WDM)
- Optical Time Division Multiplexing (OTDM).

1.2.1. Wavelength Division Multiplexing (WDM)

Figure1.3 shows that the spectral transmission band of a fiber is far larger than the part used by a single optical source. Thus, ideally a dramatic increase of information capacity can be achieved if it is possible to transmit more than one spectral channel simultaneously in the same fiber [1].

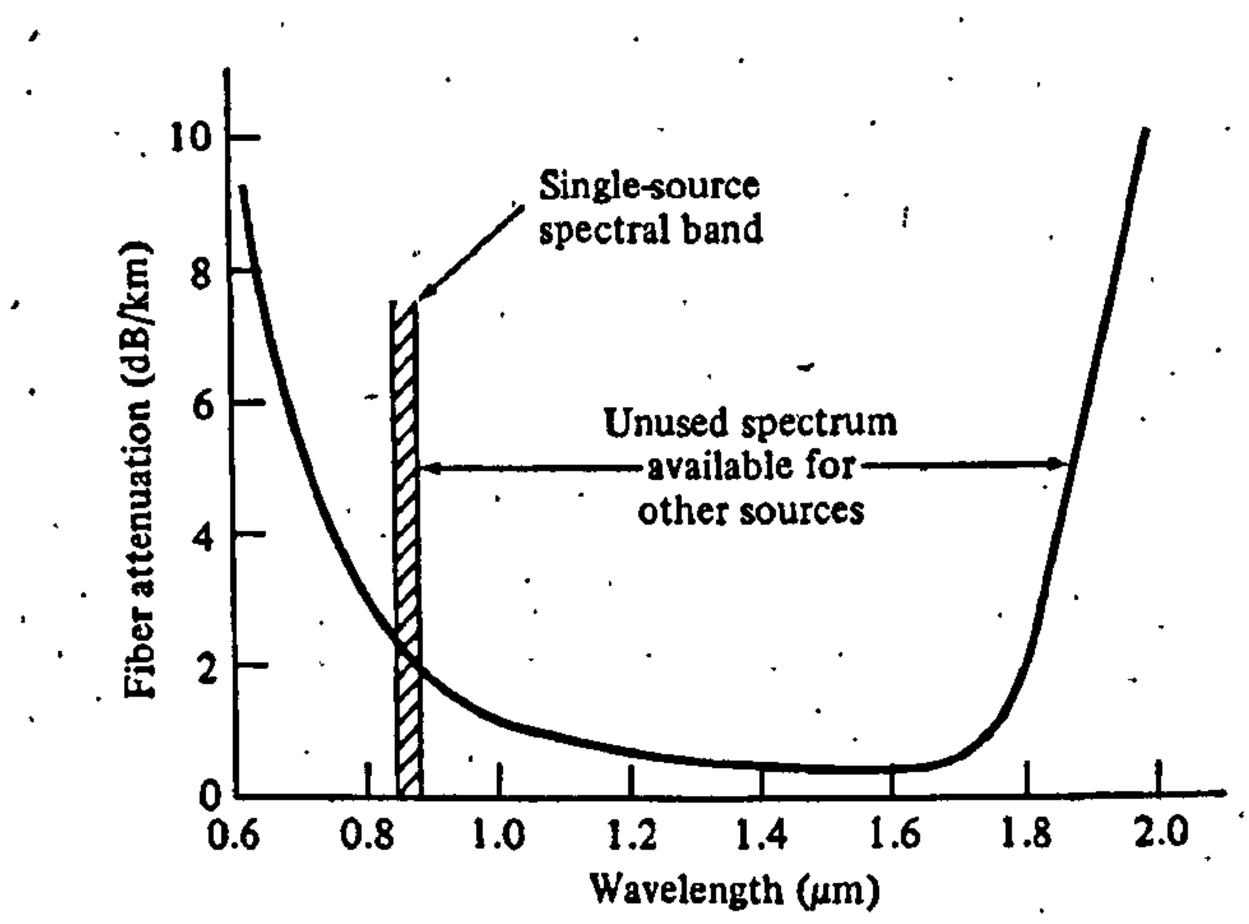

Figure1.3 Spectral Transmission Band of a Single WDM Channel [1]

WDM is a multiplexing technique based on different messages carried, in the same fiber, by different light sources with peak wavelengths far enough apart such that they do not interfere each other.
Such light is generated by a Distribute FeedBack (DFB) laser that can lase in a single longitudinal mode with a linewidth of less than 0.1 nm. These lasers are temperature dependent but it can be controlled with wavelength feedback [7].

As shown in Figure1.4, the sources, after being modulated with data, are multiplexed and transmitted down a single fiber across the link. At the other end of the link each wavelength is easily extracted using a passive demultiplexer. The individual channels are then decoded recovering the original data.
The International Telecommunications Union (ITU) has proposed first a channel spacing of 200 GHz (1.6 nm), but moving into Dense WDM the spacing channel has been reduced to 100 GHz (0.8 nm) with the channels grid centred at 193.1 THz (1552.52 nm) [9]. It is clear that with such narrow channels the system will require very stable wavelength sources in order to prevent any channel drift and hence any increase in inter-channel crosstalk.

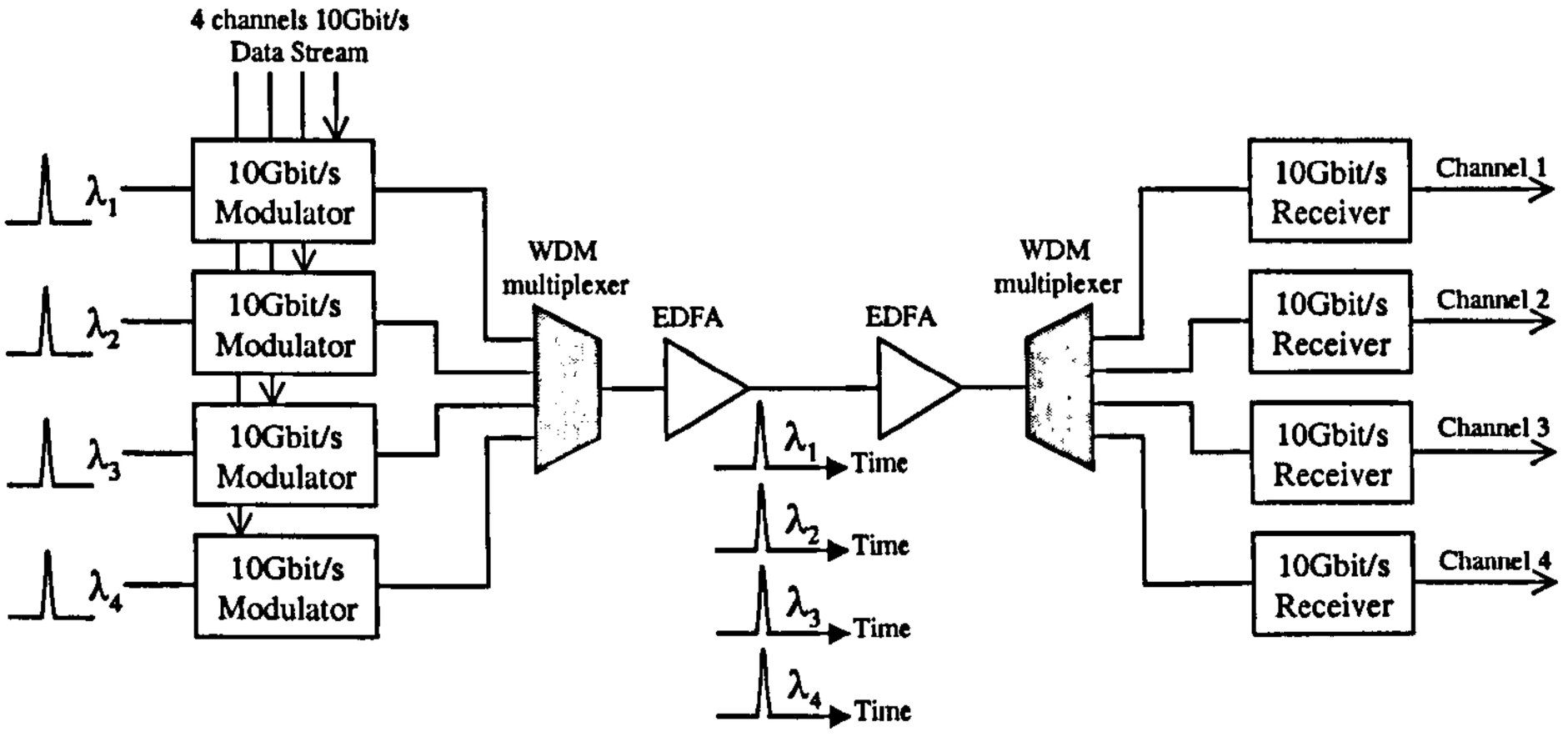

Figure1.4 A four channel point to point WDM network

1.2.2. Optical Time Division Multiplexing (OTDM)

OTDM is another multiplexing algorithm that is used in major optical trunk communication systems, where a large capacity of information needs to be transferred.

A real system example is used here to show the functioning of OTDM networks. Using 10Gbit/s technology the capacity of the fiber can be increased to 40Gbit/s [10] as shown in Figure1.5. In this case a pulse stream made using mode-locked or gain switching lasers, which are able to generate pulses with width as short as 10ps and repetition rates of order of the tens of gigahertz [11, 12], is optically split. Each channel is modulated at 10Gbit/s with an Electroabsorption modulator [13] and delayed using different fiber lengths. Hence, the signal is amplified with an EDFA, the channels are transmitted down into the same optical fiber.

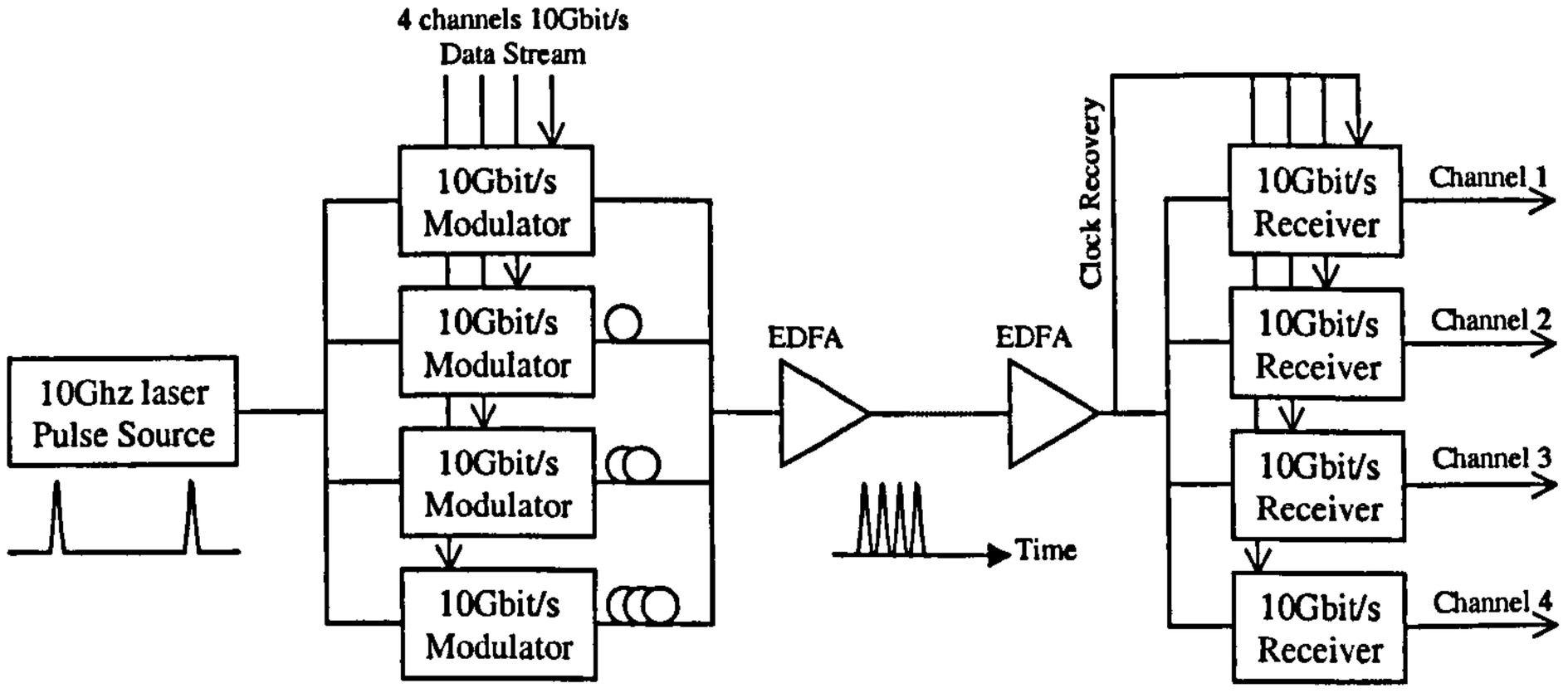

Figure1.5 A 4 channel OTDM System

At the other end of the fiber the signal is regenerated and decoded using an integrated clock recovery and a synchronised receiver.

However, even though the potential increase in the network capacity offered by OTDM is significant, the technology is not completely developed yet. In fact due to the high manufacturing costs, the decoding of the multiplexed data streams [14] and clock recovery [15] are still important research topics.

Comparing OTDM with DWDM the latter is the simpler, needing only passive components, and more flexible technique to increase fiber capacity [16].

Finally, under investigation are Tbit/s communications systems that are the combination of OTDM and WDM multiplexing techniques. A number of transmission tests have carried out so far, by changing number of channels multiplexed [17], link length [18], or architecture used [19].

1.3. Optical network nodes

The utilisation of WDM and OTDM can be extended from point to point links to optical networks with the introduction of components able to process the data of each single channel. Of course optical-electronic-optical conversion must be avoided in order not to penalise the network data rate, thus, all the functions previously carried out in electronics need to move to the optical domain. Figure1.6 shows the key components present in a general optical network node.

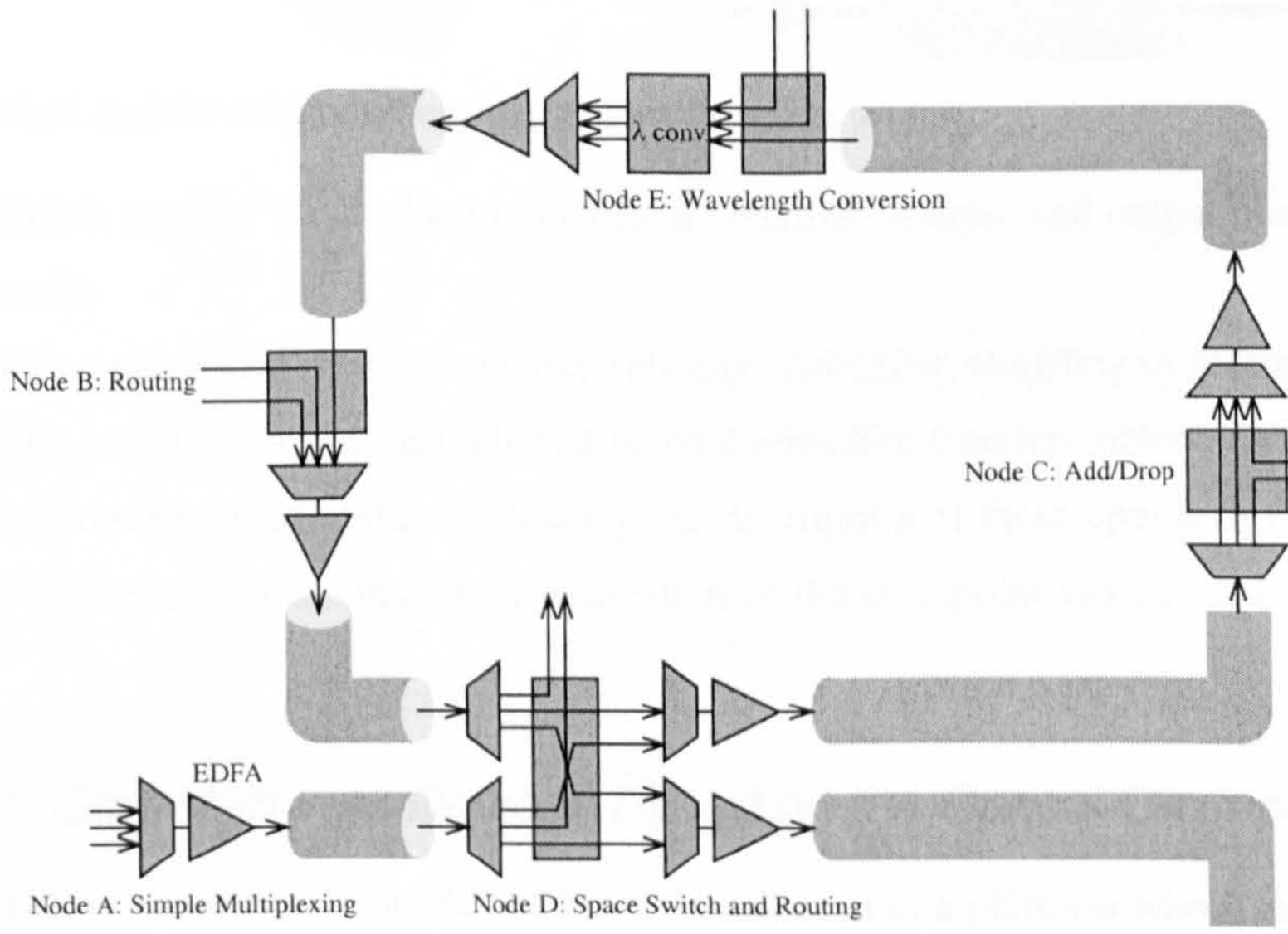

Figure1.6 A schematic optical network with different kind of nodes

It can be seen that the nodes can be as simple as a normal passive multiplexer together with an amplifier or very complex including components that can route, switch, add or drop or wavelength convert. In all these cases the presence of a space switch is vital. Furthermore, in order to make flexible and highly

reliable networks they need to be based on fast switching technology, which enable the development of many applications such us:

- Optical packet routing
- Flexible optical packet add/drop
- Optical crosspoint switching
- Network reconfiguration to allocate bandwidth on demand
- Nodes By-Pass
- Optical wavelength management
- Optical line protection
- Equipment redundancy

1.3.1. Optical Crosspoint Switch

Whenever an optical signal needs to be add, dropped, or routed from one fiber to another a crosspoint switch is necessary. An OXS can be defined as an active system able to switch the incoming signal between two output.

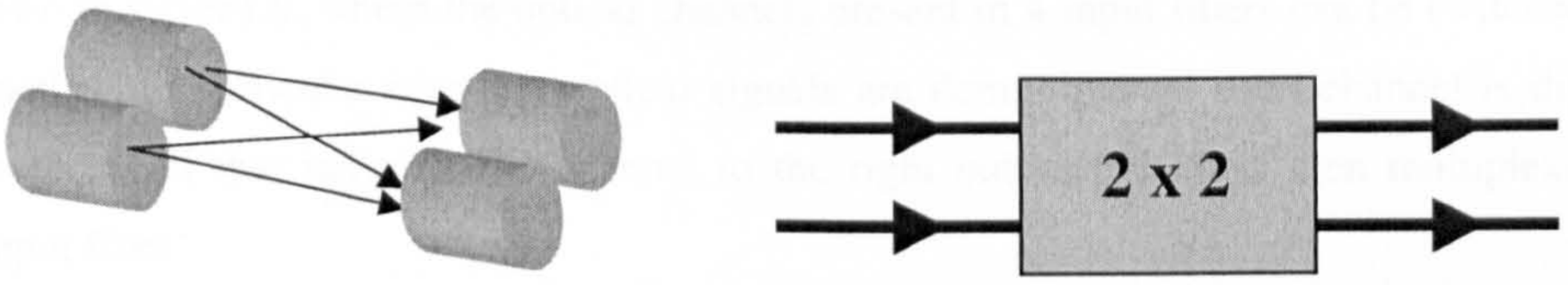

Figure1.7 The ideal and the schematic optical crosspoint space switch

Figure1.7 the OXS is marked 2 x 2 which indicates the number of input and output ports (input x output) involved in the node.

Basically an OXS can be based on functions like splitting, switching, shuffling or redirecting. The routing mechanism can be based on already established technologies like Interferometers, Directional Couplers, SOAs, and Electroabsorption Modulators. A complete description of these optical devices may be found in literature [20-24], while for a complete investigation of the crosspoint switch the reader is referred to chapter 2.

1.3.2. Other Network Devices Based on the Optical Crosspoint Switch

However, the OXS is not just a simple device but it can be seen as a platform whose technology is useful for many other network components. Routing, add/drop, and switching are functions that need the direct presence of the OXS but it can be also present in other strategic nodes like wavelength conversion.

In an Add-Drop network node, shown in Figure1.8, once the channels are decoded from the input signal, the main function is done by the OXS which, if necessary, redirects the channel to the DROP port. On the other hand if a channel needs to be added to the output signal once again the OXS transfers the channel

from the ADD port to the output multiplexer. The devices currently present in literature are based on the monolithic integration of waveguides and a 2x2 OXS, or using MicroElectroMechanical Systems (MEMS). However, the device characteristics are not good enough to satisfy future packet switching networks requirements [25].

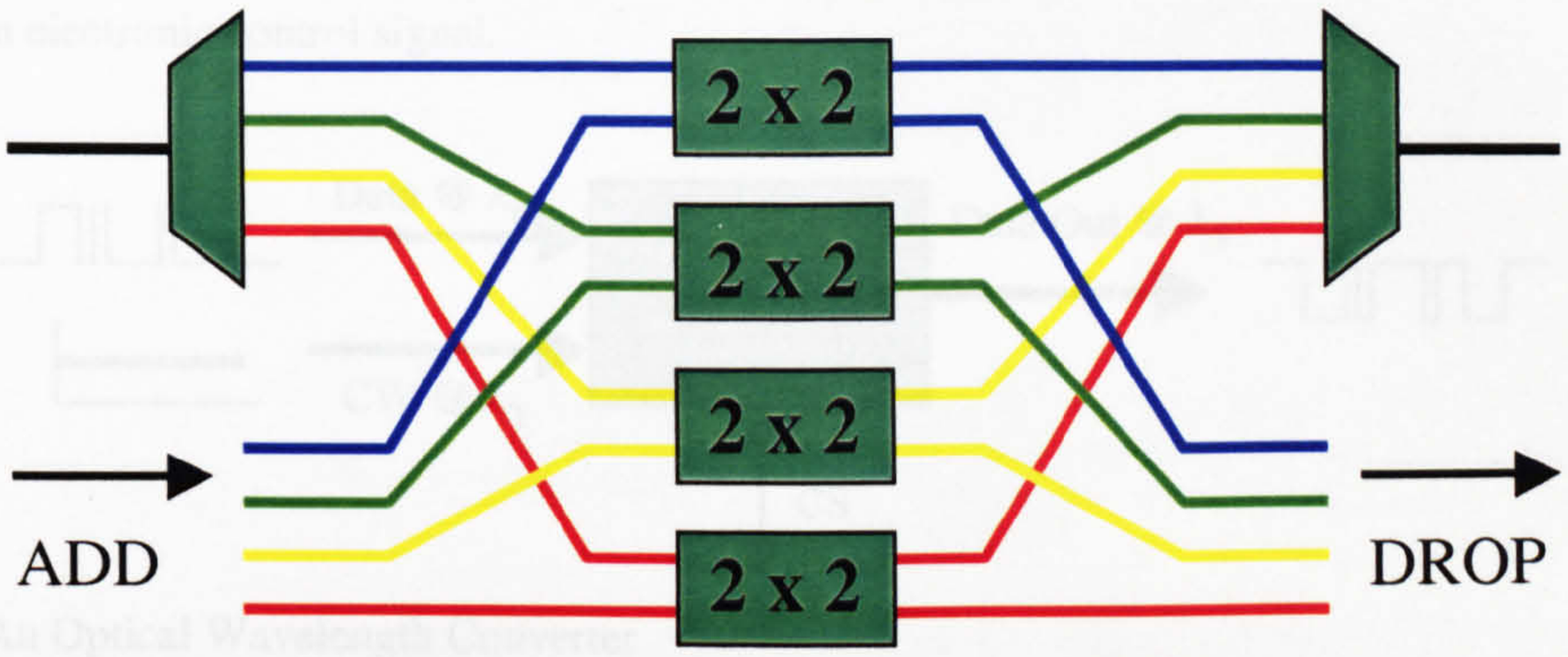

Figure1.8 4 channel Add-Drop WDM node

Optical crosspoint switches are heavily present in DWDM switching matrixes. An example is the switch matrix shown in figure1.9, where the optical channels present in 4 input fibers can be switched from one fiber to another. In particular after the optical signals are demultiplexed each channel is directed in a different switch cell that redirects the channel to the right output, which is then multiplexed into the wanted output fiber.

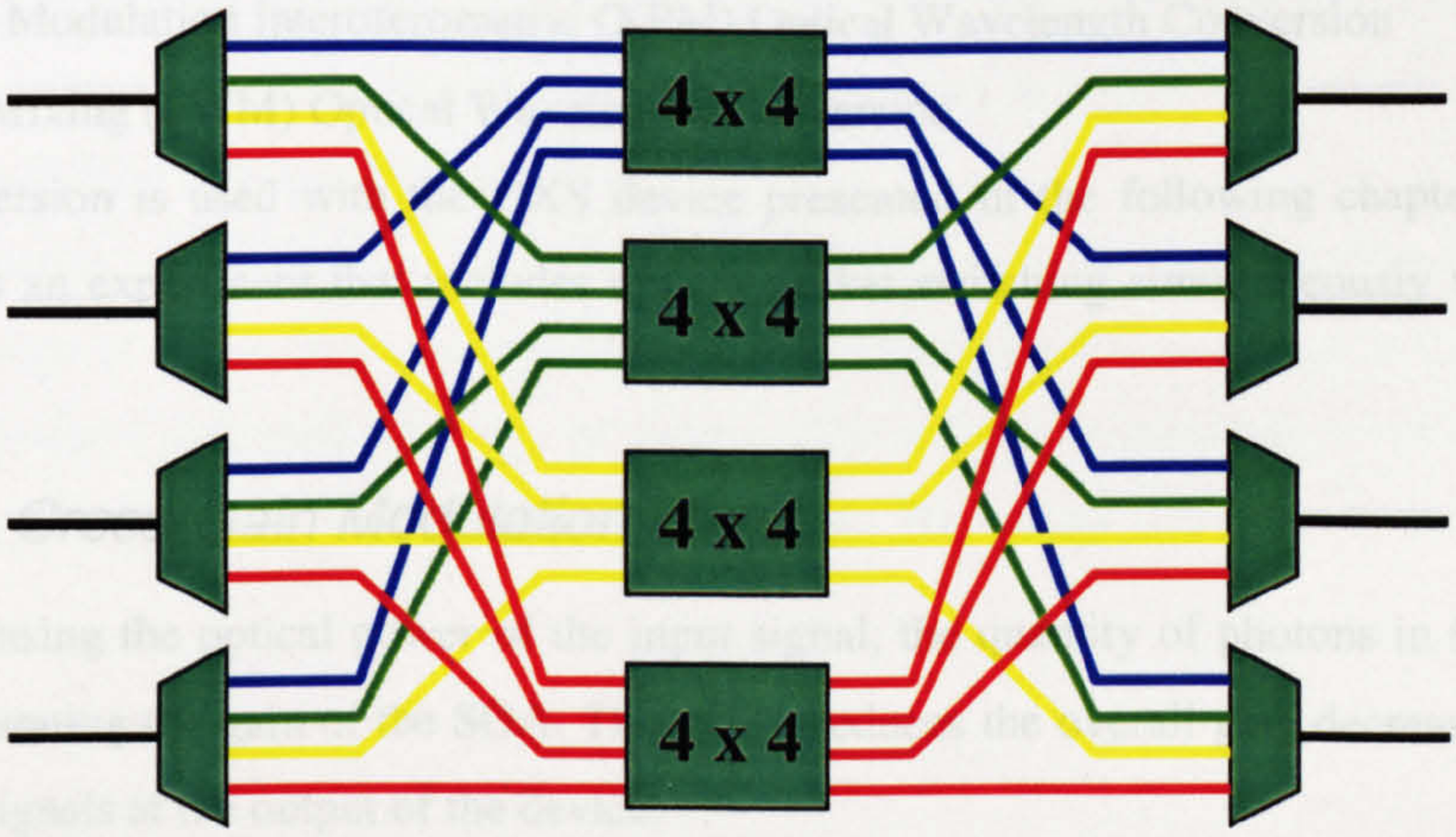

Figure1.9 4 Channel 4x4 WDM network node

1.4. Wavelength Conversion as WDM router

The ability to transfer digital information from one wavelength to another without first having to convert it back into an electrical signal is a critical step for optical WDM networks and in particular for future

optical packet switching. In fact these technologies need to be very flexible with reduced network management complexity and high scalability. Wavelength conversion can provide tremendous advantages in such terms, especially when different networks need to be interfaced and for routing or switching wavelengths, solving network contentions and blockages.

An Optical Wavelength Converter (OWC) can be seen as a 4 terminal device, two inputs, one output, plus eventually an electronic control signal.

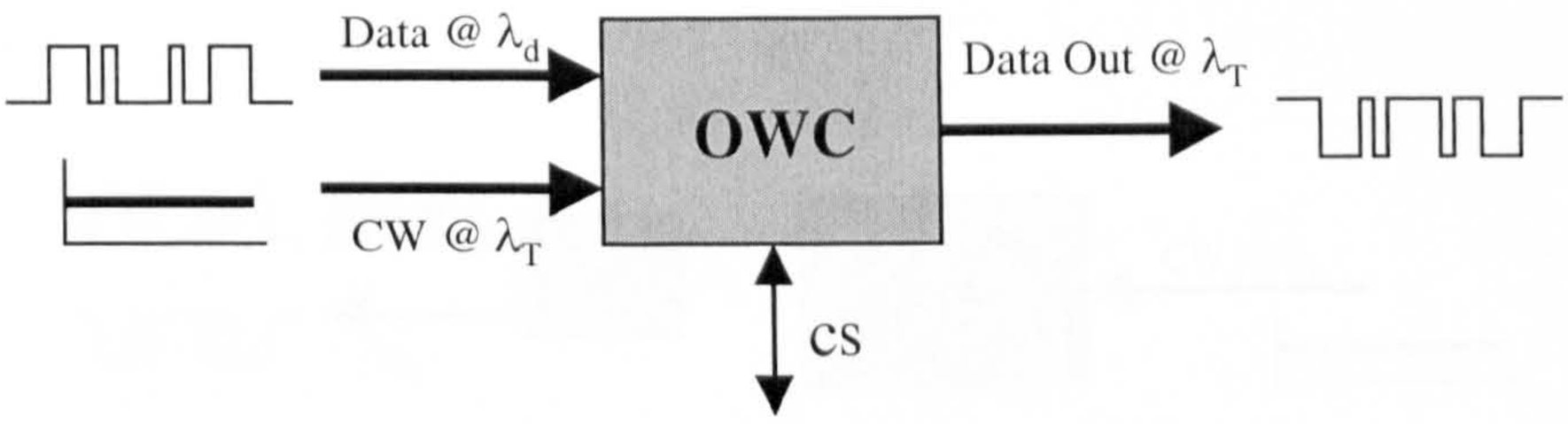

Figure1.10 An Optical Wavelength Converter

When a data signal λ_d and a Continuous Wave (CW) signal at wavelength λ_T are coupled into the input of the OWC the input data signal bit-stream is imprinted at the output wavelength λ_T. Furthermore, the data-stream can be inverted or not depending from the conversion method.

Highly integrated and low power conversion up to 10Gbps can be achieved adopting InGaAsP integrated optics, which employs SOAs. In this case the wavelength conversion can be classified as:

- Cross-gain modulation (XGM) Optical Wavelength Conversion
- Cross-Phase Modulation Interoferometric (XPM) Optical Wavelength Conversion
- Four Wave Mixing (FWM) Optical Wavelength Conversion

Cross-gain conversion is used with the OXS device presented in the following chapters, in particular chapter 6 reports an experiment that includes optical packet switching simultaneously with wavelength conversion.

1.4.1. Cross-Gain Modulation OWC

In an SOA increasing the optical power of the input signal, the quantity of photons in the active region also increase saturating the gain of the SOA. This effect reduces the overall gain decreasing the intensity of other optical signals at the output of the device.

This effect can be extended to an optical source λ_d, which carries a data-stream and saturates the SOA in the "ON" state. Let us introduce a second CW optical signal, at wavelength λ_T, into the SOA cavity. As a consequence of the gain modulation, this signal is less amplified when λ_d data stream is in the on-state. Thus, it is easy to understand that a data sequence of 1 and 0, at wavelength λ_d, can be transformed into an inverted data-stream at wavelength λ_T.

Two different configurations can be made:

- Co-propagation
- Counter-propagation

they are shown in Figure1.11 *a)* and *b)*.

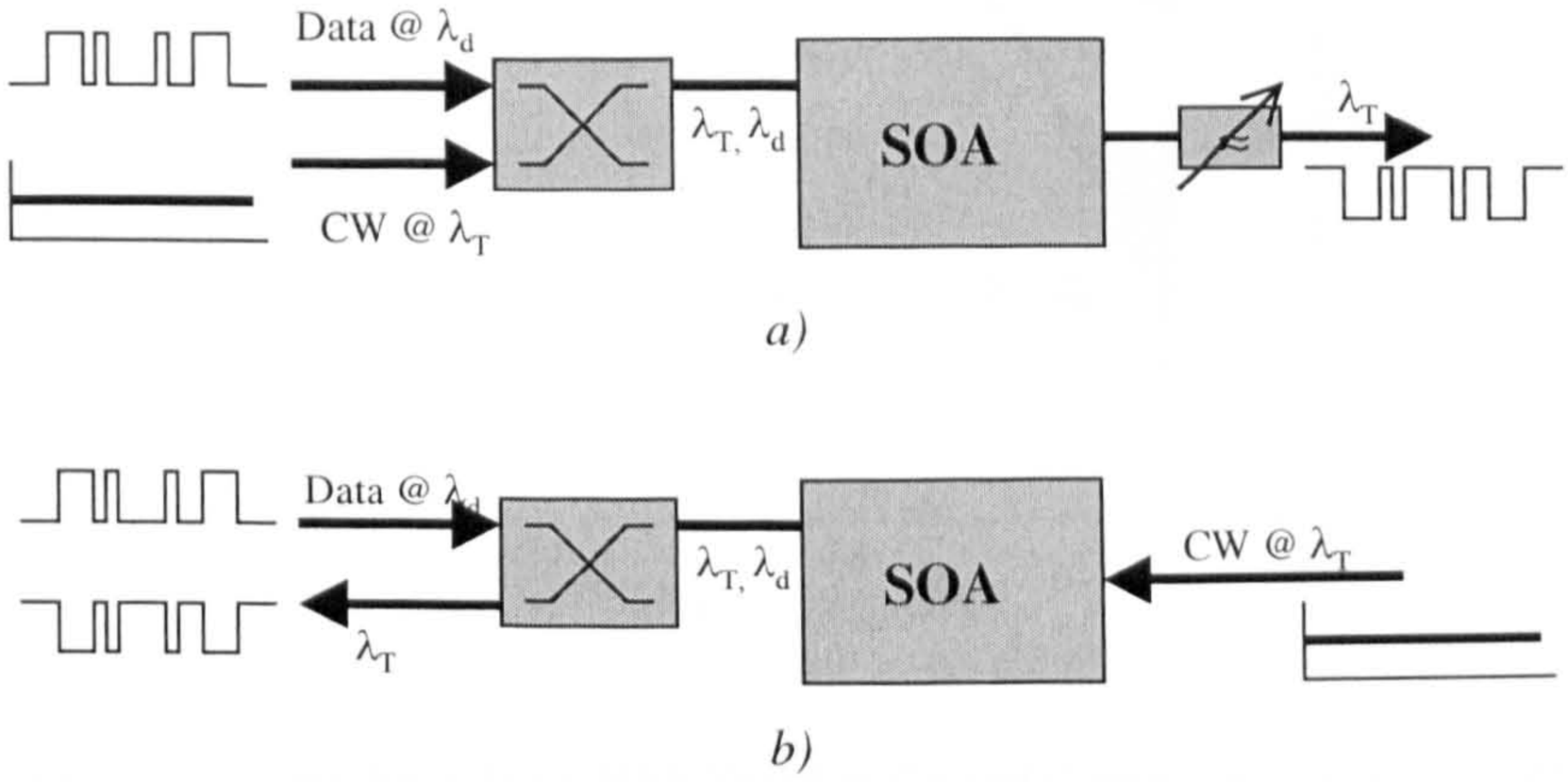

a) Co-propagation Configuration
b) Counter-Propagation Configuration
Figure1.11 Wavelength Conversion Using Cross Gain Modulation in SOA

Co-propagation Wavelength Conversion is defined as the configuration with data-stream and CW signals coupled together into the SOA at the same facet. Counter-Propagation Wavelength Conversion, instead, is defined as coupling the data-stream and the CW signals into the two opposites facets of the SOA. This last set-up has the advantage that it does not require any optical filtering of the output signal when the facets of the SOA are Anti Reflection (AR) coated. On the other hand, it suffers speed limitation thought due to the phase mismatching between the two wave propagating in opposite direction, as the frequency response for a 2mm SOA shows in Figure1.12 .

However, wavelength conversion up to 20Gbps has been realised with such configuration [26]. It is thought that, because of the intrinsic carrier lifetime, the conversion speed is limited at 0.5 ns but recently tests have demonstrated that such limit can be higher. This is because under high optical injection, the stimulated emission rate in the SOA increases reducing the carrier lifetime down to few tens of picoseconds [27].

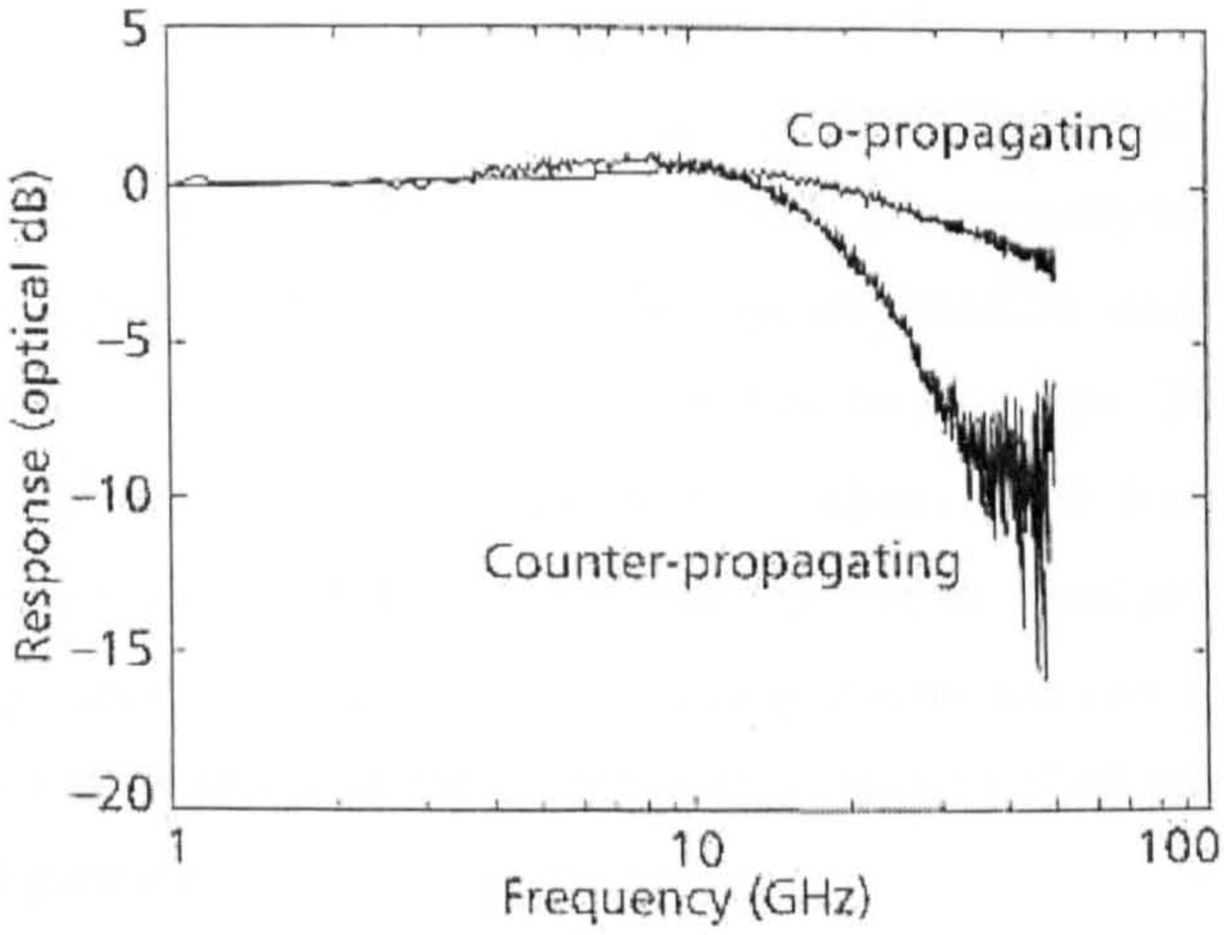

Figure1.12 Frequency response for a 2mm SOA XGM in Co and Counter-propagation configurations [27]

Besides the simplicity with which λ–conversion can be implemented, these devices have a high conversion efficiency and polarisation insensitivity. On the other hand, they suffer from poor Extinction Ratio (ER), which is dependent on variables like: gain peak of the SOA, wavelength λ_d and target wavelength λ_T. Instead the Crosstalk introduced is a function of the injected current, power levels and wavelengths of the two signals. A study on the relationship between all these variables [28] has shown that optimising them for high extinction ratio leads to poor crosstalk and viceversa. Thus, in order to reduce this problem, a lower residual facet reflectivity SOA need to be used.

1.4.2. Cross-Phase Modulation OWC

So far it has been shown that two light signals operating at different wavelengths interact each other when coupled into a SOA cavity. It has also shown that the gain in the active region of the SOA plays a very important role when, without any electro-optic conversion, the information contained in one signal is transferred to a second.

Another method to achieve wavelength conversion uses the XPM effect in an interferometric structure.

In the Mach-Zehnder Interferometer (MZI) configuration, Figure1.13 *a) b)*, the idea is that the input signal depletes the carrier concentration in only one of the SOAs thereby creating a wanted phase difference between the two arms. Two different configuration can be analysed:

- Asymmetric Mach-Zehnder configuration and symmetric data signal input, Figure1.13 *a)*

Data λ_d and CW signal λ_T are coupled into both interferometer arms. Phase difference between the two arms is obtained by employing asymmetric splitters so that the carrier density and hence the phase is modulated differently in the two arms.

It is understandable that in this configuration adjustment and control of the MZI is not easy. Nevertheless, good results have been achieved with this device configuration [29].

- Symmetric Mach-Zehnder configuration and asymmetric data signal input, Figure1.13 *b)*

In this configuration the CW signal λ_T, coupled into the MZI, splits equally between the two arms of the interferometer. On the other splitter the two CW signals interfere each other constructively or destructively depending on the phase difference achieved in the two arms. The incoming data signal at wavelength λ_d, injected in just one arm, saturates the SOA when in state 1 consequently, with a proper choice of the input signal power and MZI phase difference, an output signal at wavelength λ_T is produced. With this device configuration inverting and non-inverting conversion can be realised. Furthermore, a gain variation of only 4-5 dB is necessary for the conversion against a 10dB gain variation for wavelength converter in XGM configuration.

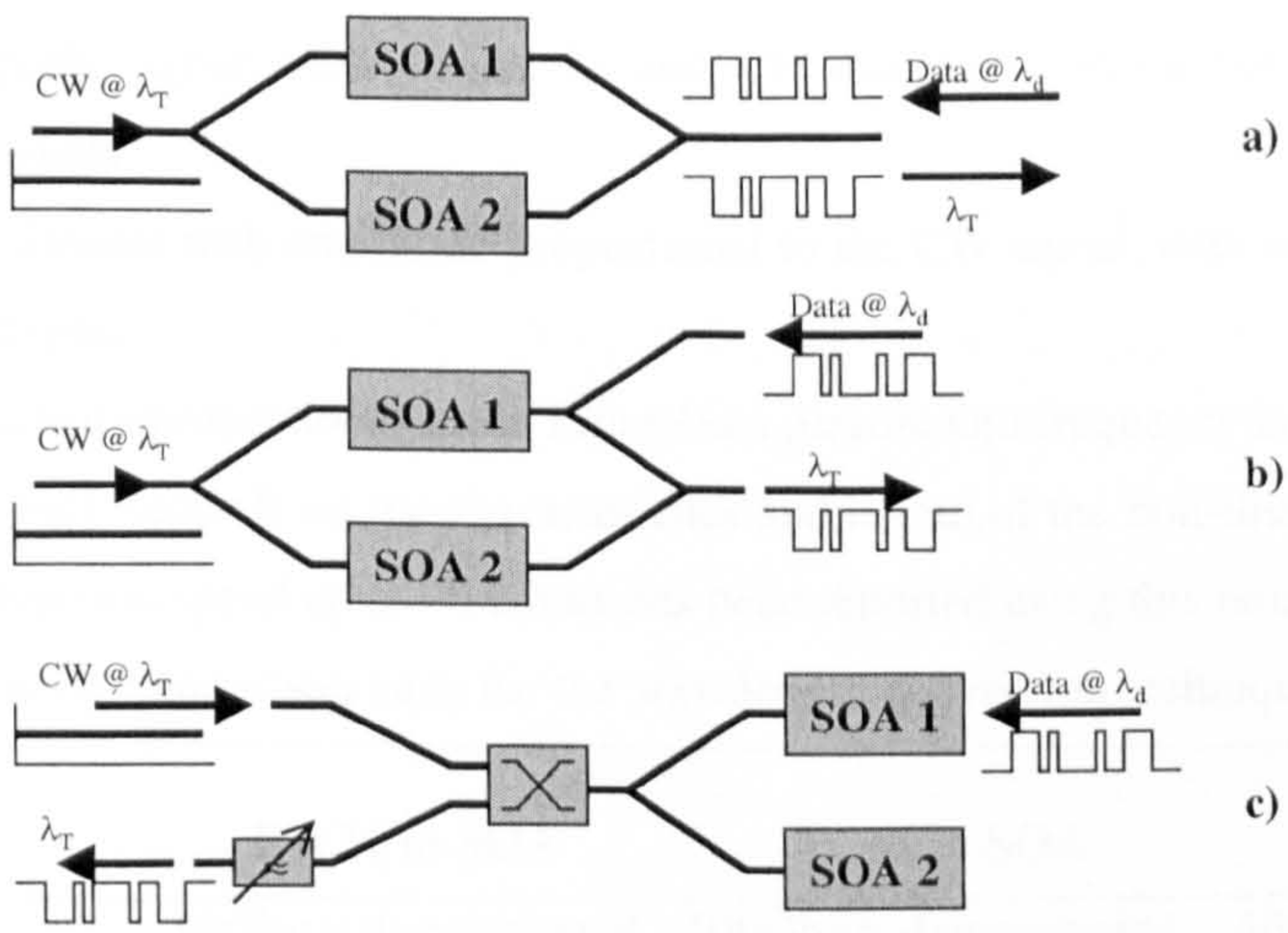

a) asymmetric Mach-Zehnder configuration,

b) symmetric Mach-Zehnder and asymmetric coupling,

c) Michelson interferometer

Figure1.13 Wavelength conversion with cross phase modulation

- Michelson interferometer configuration, Figure1.13 *c)*

Figure1.13 c) shows an OWC adopting a Michelson interferometer configuration. In this case because of the presence of a reflective facet it works very similarly to a MZI converter. However, this configuration allows the data signal to be coupled directly into the SOA reducing the loss.

Finally wavelength conversion up to 40Gbit/s has been demonstrated using this technique [30], with hybrid integration of SOAs and couplers [31].

1.4.3. Four-Wave Mixing OWC

This wavelength conversion is based on the nonlinearity effect occurring in passive waveguides or SOAs when more than one wave interacts. FWM is a third order of nonlinearity.

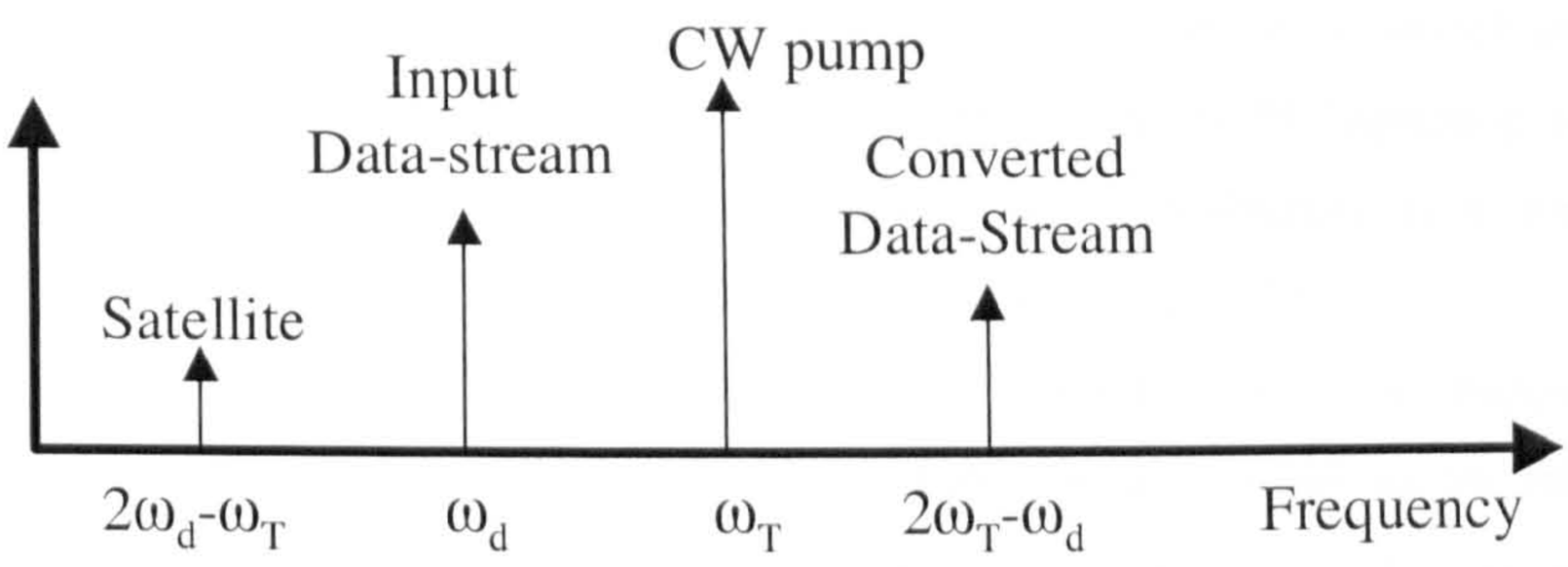

Figure1.14 FWM Wavelength Conversion

The input of two signals, *Input Data Stream* λ_d and *CW Pump* λ_T, into a nonlinear optical element generates two more signals:

- *Converted Data Stream* with amplitude proportional to the CW signal, data stream impressed into it and frequency $2\omega_T-\omega_d$
- *Satellite* with intensity proportional to the *Input Data Stream* and frequency $2\omega_d-\omega_T$

The conversion efficiency depends on the characteristics and length of the non-linear medium, which can be SOA or fiber. Conversion speed up to 40 Gbit/s has been reported using this non-linear effect [32].

Next table1.1 represents a comparison table for the wavelength conversion techniques investigated.

	FWM in SOA	**XGM in SOA**	**XPM in SOA**
Data rate limit	10Gbit/s demonstrated (100Gbit/s possible)	100Gbit/s demonstrated	40Gbit/s demonstrated
Regeneration	None	R	2R
Transparency	Strict	Digital	Digital
Polarization insensitivity	No, insensitive for multiple pumps	Yes (for polarization-indep SOAs)	Yes (for polarization-indep SOAs)
Mapping function	$\omega_{out} = \omega_{pump} - \omega_{in}$	$\omega_{out} = \omega_{probe}$	$\omega_{out} = \omega_{probe}$
Wavelength dependence (within 20 nm span)	Strong	Moderate	Weak
Chirp	Reverse	High	Small/reverse
Preserves signal polarity	Yes	No	Yes
Simultaneous conversion of several WDM channels	Yes	No	No
Optical filtering	Must filter strong pump and satellite wavelength	Not needed for counter-propagation geometry	Must filter strong input signal
Advantages	Transparency	Simple implementation	Regeneration of the converted signal
Disadvantages	λ_{out} depends on λ_{in}, narrow conversion λ span	Signal degradation and chirp	Narrow dynamic range of input power

Table1.1 Comparison of different wavelength conversion techniques [33]

1.5. Optical Packet Routing

With the increasing of the data traffic there is much interest from the carriers to switch from connection-oriented networks to photonic packet-switched networks which adopts Multiplexing techniques such WDM and OTDM. The great advantage is that Photonic Packet Switching is a very fast scheme characterised by transparent data rate/format and by high reconfigurability [34].

When information needs to be sent from one point to another of the network, it is chopped into different pieces, each one forming the payload, which is combined with a header containing the information about the payload. The payload and header make up optical packets that, at this point, are ready to be sent over the network. At the other end of the network all the packets are collected and after reading the header they are joined together forming the original information.

Once again it can be seen that in a node where all the packets are processed the importance of a fast space switch is further stressed confirming that an OXS able to process the incoming data is the challenge of the optical packet switching networks. Following two kind of packet switching networks will be shown. In both cases the crosspoint switch plays a main role, furthermore it will be shown that in order to reduce contention and synchronisation problems it must be very fast.

Packet organisation characterises the kind of networks in two main categories [35]:

- Slotted or Synchronous Network

All the payloads have the same size and they are placed inside of a time slot that, in order to provide guard-time, is larger than the sum of payload and header. At the input of any individual photonic switch node the packets can arrive at different times, thus, they need to be aligned, before being introduced into the switch fabric. This process necessitates synchronisation at bit-level and fast clock recovery for packet header recognition and packet delineation. The packet delay is realised using optical buffers, which are usually made using a fiber loop, or delay lines with delay time of a time slot or multiple of it [36].

- Unslotted or Asynchronous Network

In this case the packets can have different sizes and they don't need to be aligned before entering the switch. This "anarchic management" allows the possibility to have packets arriving at the same time generating contention. However at the same time gives the network advantages of being low cost, easier to build, robust and more flexible than the slotted network.

The following sections give a description of different solutions proposed to synchronise packets and solve packet contention.

1.5.1. Slotted Networks - The Synchronisation of the packets

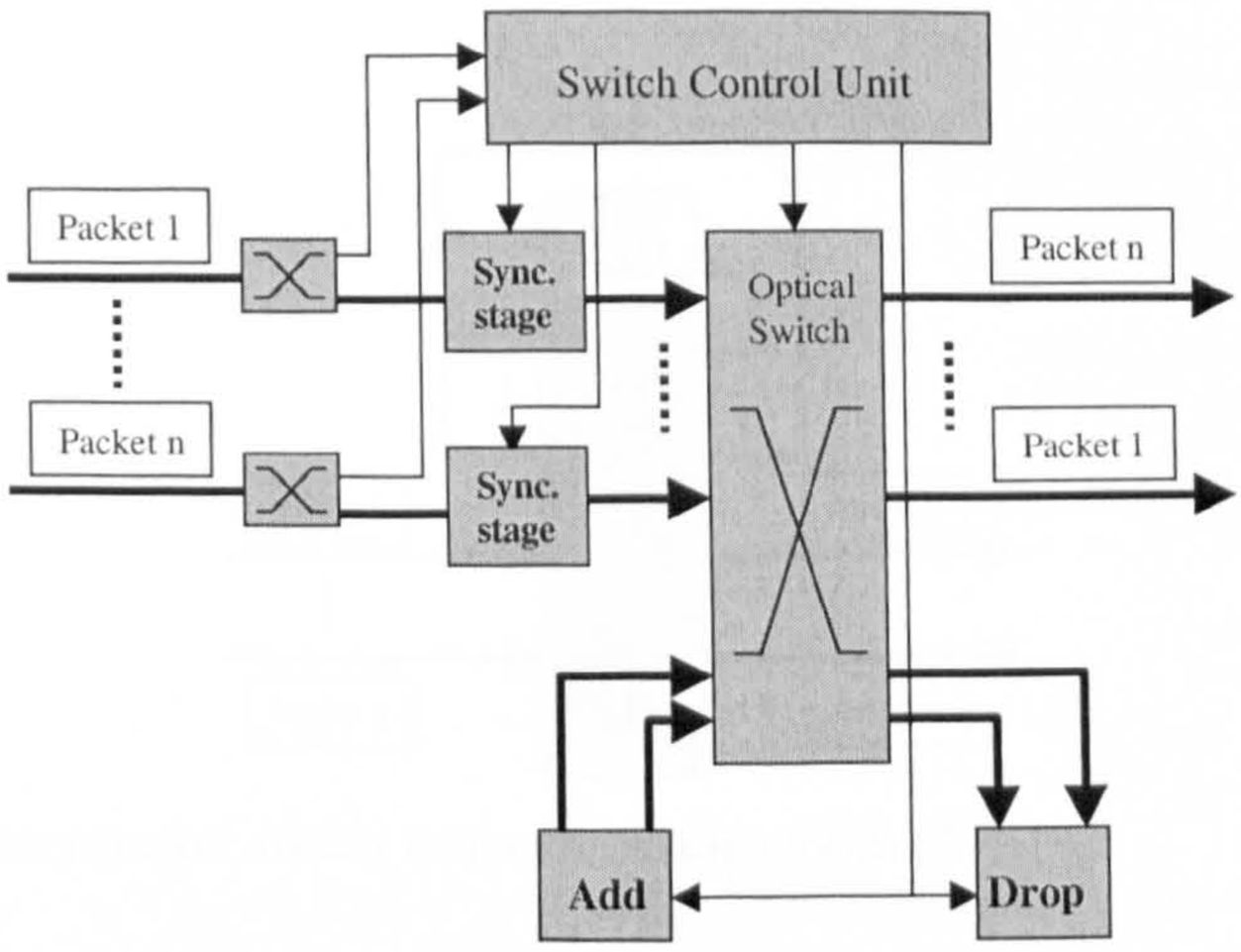

Figure1.15 A Slotted Network Node

All the control of a slotted network node is in the Switch Control Unit (SCU). When the packets arrive to its gates they need to be aligned before entering in the optical fabric switch. In order to do so a splitter sends part of the signal into the SCU, which reads the header and configures the synchronisation stages and the Optical Switch. When the packet also has a guard time between the header and the beginning of the timeslot, the node also necessitates synchronisation stages on the output of the optical switch in order to compensate the fast time jitter generated in the node.

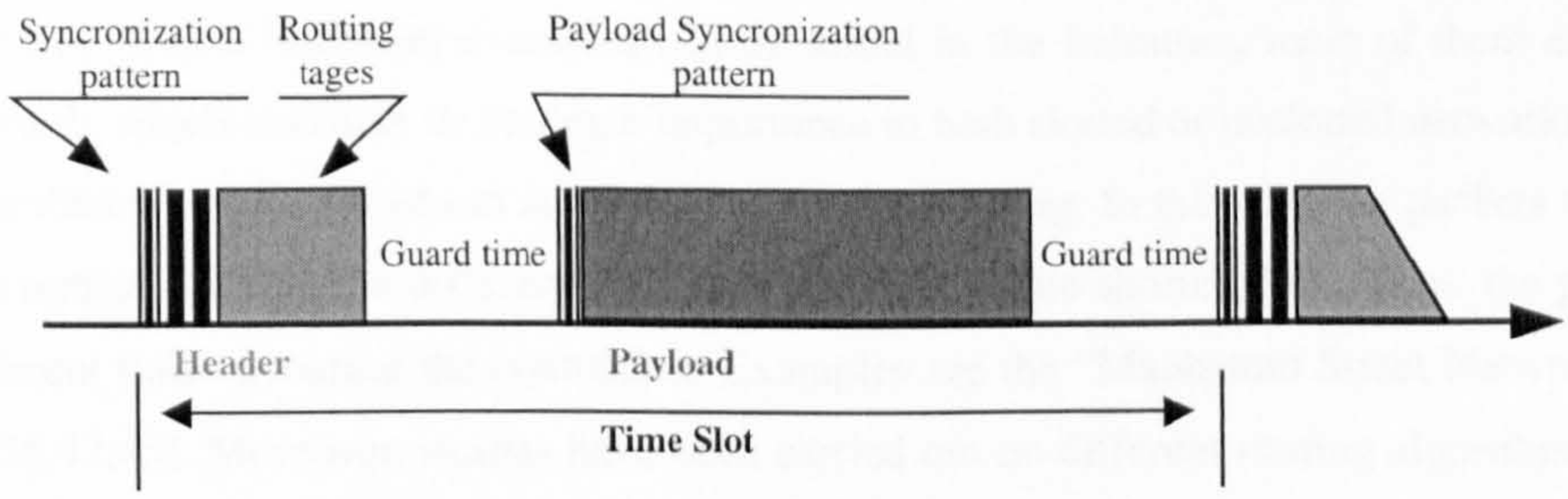

Figure1.16 Example of an optical packet format

When different packets arrive at a node, for different reasons, they can be out of phase relative to each other. Thus the synchronisation of incoming data signals is a key function that permits the reduction of contention problems and increases the switching efficiency. A number of different delay methods have been proposed and most are based on space switches and delay lines.

Figure1.17 shows an example of shared memory. The delay lines are based on a resolution scheme of $1/2^n$ time slot duration, where n is the number of delay lines [35]. This kind of devices suffers from high

insertion loss and crosstalk, mostly due to the presence of a matrix switch and signal to noise ratio degradation due to the necessity to recover the loss with a regeneration of the signal.

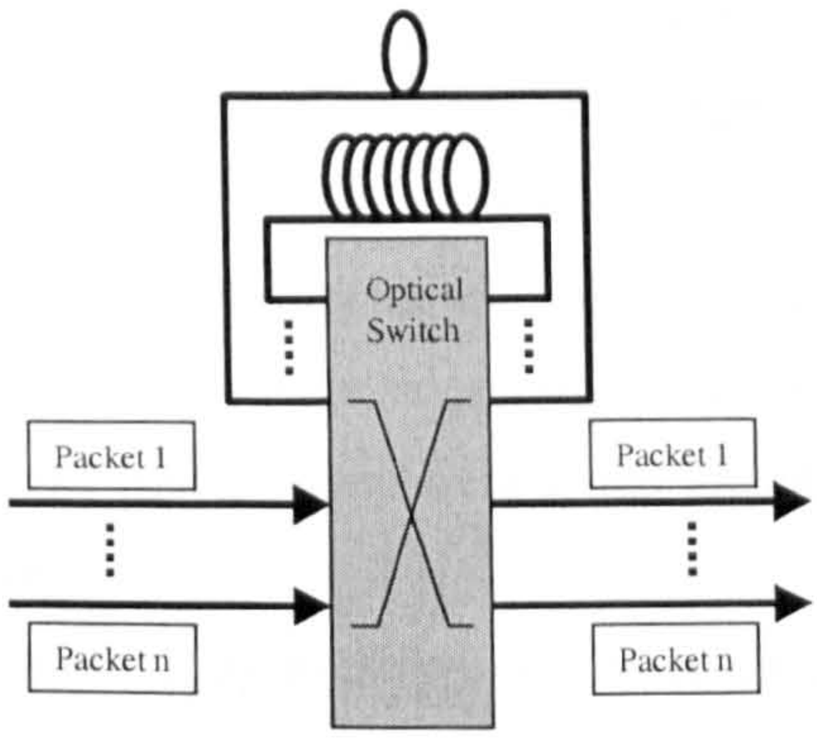

Figure1.17 Shared memory packet switch with recirculating loops [37]

1.5.2. Unslotted Networks – Contention Resolution

The necessity to solve or to reduce contention is one of the main disadvantages of an unslotted network. In fact the unslotted scheme processes the packets directly without any previous alignment stage, which can generate high contention problems. Different resolution methods have been proposed based on buffering, space deflection or wavelength conversion [37-39].

Also in this case the single packets need to be buffered. It is done using very similar buffers for slotted networks but in this case the delay lines are timeslot multiples [37]. However, depending on the delay the packets will suffer different power loss thus optical amplification is also necessary, degrading the signal-noise ratio. Many optical buffering examples can be found in the literature, most of them employing a crosspoint switch, which confirms its strategic importance in both slotted or unslotted networks[40,41].

Contention problems can be sorted out adopting Deflection Routing. In this case the packets that need to use the same output, are sent via different links and just one via the shortest link. Thus, the packets will arrive in different times avoiding the contention. Examples are the "Manhattan Street Network" and the ShuffleNet [38,42,43]. Moreover, studies have been carried out on different routing algorithms, like Hot-Potatoes routing, Store-and-Forward routing or Single-Buffer Deflection routing, with the aim of avoiding network congestion [44,45].

A final method of resolving contention problems adopts wavelength conversion in combination with the previous methods, overcoming or minimising the disadvantages. Thus, Hot-Potato routing with wavelength conversion becomes a very interesting option [46]. Wavelength conversion associated with deflection routing or with buffers offers several combinations. The ultimate aim of these techniques is to achieve low implementation cost, low packet delay, low packet loss ratio and high network throughput. However, it is known that the best combination of such techniques depends on the characteristics of the real network involved.

1.6. Scope of Thesis

After an introduction to future networking with the optical data multiplexing techniques, this chapter has described the most important components in an optical node with a particular focus on the Optical Crosspoint Switch. Finally the techniques in order to make wavelength conversion have been outlined.
Chapter 2 treats the theory of the crosspoint switch followed by an investigation of the devices present in literature and available commercially. The chapter closes with the theoretical analysis of a novel, highly compact, crosspoint architecture, which is the main subject of this thesis.
Chapter 3 presents the design of this new architecture and the theoretical model followed in order to prototype the total crosspoint device.
Chapter 4 hence uses the theoretical model to investigate some vertical coupler structures fabricated at an earlier time.
Chapter 5 is dedicated to the manufacture of the device. It also includes the resolution of some problems related to the photolithography and to the semiconductor etching phases. In particular a novel sidewall passivation process, which might be introduced into the manufacture of the device is presented.
Chapters 6 and 7 introduce the characterisation of the crosspoint switch. The first one presents static and dynamic performance including a section dedicated to the device used in the non-linear domain. Chapter 7, instead, is dedicated to experiments where the device is deployed in optical packets routing. In particular it shows that the novel crosspoint is able to switch optical packets at a bitrate of 10Gbit/s. The chapter also presents simultaneous packet switching and wavelength conversion at 10Gbit/s. Finally a description of the crosspoint in the WASPNET project closes the chapter.
Chapter 8 concludes this work and presents few suggestions that could help in the improvement of the device characteristics.

1.7. References

[1] G. Keiser, "Optical Fiber Communications", 2nd ed., 1991, McGraw-Hill

[2] W.G. French, J.P. MacChesney, P.B. O'Connor and G.W. Tasker, "Optical Waveguides With Very Low Losses", Bell Sys Tech. J., Vol. 53, May 1974, pp. 951-954

[3] M. Horiguchi and H. Osanai, "Spectral Losses of Low-OH Content Optical Fibres" Electronics Lett., Vol. 12, 1976, pp. 310-312

[4] T. Miya, Y. Terubuma, T. Hosaka and T. Niyashita, "Ultimate Low-Loss Single-Mode Fibre at 1.55 um" Electronics Lett., Vol. 15, 1979, pp.106-108

[5] Y. Miyamoto, T. Kataoka, A. Sono, K. Hagimoto, K Tida and Y. Kobayashi, "10 Gbit/s 280 Km Nonrepeatered Transmission with Suppression of Modulation Instability", Electronics Lett., Vol. 30, No. 10, May 1994, pp. 797-798

[6] C.R. Giles, M. Newhouse, J. Wright and K. Hagimoto, (eds), "Special Issue on System and Network Application of Optical Amplifiers" IEEE/OSA J. Lightwave technol., Vol. 13, No.5 , May 1995, pp.701-981

[7] R. Zengerle, O. Leminger, "Phase-Shifted Bragg-Grating Filters with Improved Transmission Characteristics", Journal of Lightwave Technology, Vol. 13, No. 12, 1995, pp. 2354-2358

[8] E. Suhir, "Microelectronics and Photonics – The Future", Microelectronics J., Vol.31, 2000, pp.839-851

[9] C.Gamache, M. Tetu, C. Latrace, N. Cyr, M.A. Duguay, B. Villeneuve, "An Optical Frequency Scale in Exact multiples of 100GHz for Standardization of Multifrequency Communications", IEEE Photon. Tech. Lett., Vol. 8, No. 2, 1996, pp. 290-292.

[10] M. Owen, "Monolithic Integration of Optical Space Switches", 1998, PhD Thesis University of Bristol

[11] C. Wu, N.K. Dutta, "High-Repetition-Rate Optical Pulse Generation Using a Rational Harmonic Mode-Locked Fiber Laser", IEEE J. of Quantum Electronics, Vol. 36, No. 2, 2000, pp. 145-150

[12] S. Nogiwa, Y. Kawagichi, H. Ohta and Y. Endo, "Generation of Gain-Switched Optical Pulses with Very Low Timing Jitter by Using External CW-Light Injection Seeding", Electronics Lett., Vol. 36, No. 3, 2000, pp.235-236.

[13] V. Kaman, Y.-J. Chiu, T. Liljeberg, S.Z. Zhang and J.E. Bowers, "Compact 40 Gbit/s Demultiplexing Receiver Based on Integrated Tandem Electroabsorption Modulators", Electronics Lett., Vol. 36, No. 23, 2000, pp.1943-1944.

[14] I.D. Phillips, A. Gloag, D.G. Moodie, N.J. Doran, I. Bennion, A.D. Ellis, "Simultaneous Demultiplexing and Clock Recovery Using a Single Electroabsorption Modulator in a Novel Bi-directional Configuration" Optics Communications, 150, 1998, pp. 101-105

[15] P. Toliver, I. Glesk, P.R. Prucnal, "All-Optical Clock and Data Separation Technique for Asynchronous Packet- Switched Optical Time Division Multiplexed Networks" Optics Communications, 173, 2000, pp. 101-106

[16] S. Li, C. Huang, T. Wang, G. Zhang, "OTDM Communication System Exploiting a Modelocked Fiber Laser as The Clock Extractor", Optics Communications, 149, 1998, pp.252-254

[17] C.D. Cheng, I Kim, O. Mizuhara, T.V. Nguyen, K. Ogawa, R.E. Tench, L.D. Tzeng, P.D. Yeates, "1.2 Tbit/s (30ch x 40Gbit/s) WDM Transmission Over 85 km Fibre", Electronics Lett., Vol. 34, No.10, 1998, pp. 1002-1004

[18] C.D. Cheng, I Kim, O. Mizuhara, T.V. Nguyen, K. Ogawa, R.E. Tench, L.D. Tzeng, P.D. Yeates, "40 Gbit/sx25ch (1 Tbit/s aggregate capacity) WDM Transmission Over 342 Km of Fibre", Electronics Lett., Vol. 35, No. 8, 1999, pp. 645-646

[19] H.T. Yamada, H. Murai, A. R. Pratt and Y. Ozeki, "Scaleable 80 Gbit/s OTDM Using a Modular Architecture Based on EA Modulators", ECOC 2000 September 3-7, 2000 Munich, Germany

[20] N. Yoshimoto, Y. Shibata, S. Oku, S. Kondo and Y. Noguchi, "Design and Demostration of Polarization Insensitive Mach-Zehnder Switch Using a Lattice-Matched InGaAlAs/InAlAs MQW and Deep-Etched High-Mesa Waveguide Structure", J. of Lightwave Technology, Vol. 17, No. 9, 1999, pp.1662-1669.

[21] M. Kohtoku, K. Kawano, S. Sekine, H. Takeuchi, N. Yoshimoto, M. Wada, T. Ito, M. Yanagibashi, S. Kondo, Y. Noguchi and M. Nadanuma, "High-Speed InGaAlAs/InAlAs MQW Directional Coupler Waveguide Switch Modules Integrated with a Spotsize Converter Having a Lateral Taper, Thin-Film Core, and Ridge", J. of Lightwave Technology, Vol. 18, No. 3, 2000, pp.360-369.

[22] B.C. Qiu, Y.H. Qian, O.P. Kowalsky, A.C. Bryce, J.S. Aitchison, R.M. De La Rue, and J.H. Marsh, M.Owen, I.H. White and R.V.Penty, A. Franzen, D.K. Hunter and I. Andovonic, "Low Cost Fabricationof 2x2 Crosspoint Switches", ECOC 1999 September 26,30, 1999, Nice, France.

[23] S.M. Lee, K.R. Oh,K.H. Kim, J.S. Kim, S.G. Kang, M.K. Song and H.M. Kim, "Fabrication of 1×4 Optical Switch with Gain Using Dual InGaAsP/InP Laser Diode Amplifier", Jpn. J. Appl. Phys. Part 2, Vol.38, No. 3B, 1999, pp. L320-L321.

[24] Owen, M.; Asghari, M.; White, I.H.; Poguntke, K.R.; Robertson, M.J., "Theoretical design of a novel N×N two-dimensional integrated optical crosspoint switch architecture", J. of Lightwave Technology, Vol. 16, No. 3, 1998, pp. 380-387.

[25] Y. Shibata, S. Oku, Y. Kondo, T. Tamamura and M. Naganuma, "Semiconductor Monolithic Add-Drop Multiplexer Using a Grating Switch Integrated with Coupler Structure", Electronics Lett., Vol. 35, No.6, 1999, pp.489-491.

[26] D. Wolfson, and K.E. Stubkjaer, "Bit Error rate assessment of 20Gbit/s all-optical wavelength conversion for co- and counter-directional coupling scheme", Electronics Letters, 1998, Vol. 34, No. 23, pp. 2259-2261.

[27] D. Nesset, T. Kelly, and D. Marcenac, "All-Optical Wavelength Conversion Using SOA Nonlinearities", IEEE Communication Magazine, Vol.36, No.12, 1998, pp.56-61

[28] A. Tzanakaki, and M.J. O'Mahony, "Analysis of Tunable Wavelength Converter based on Cross-Gain Modulation in Semiconductor Optical Amplifier Operating in the Counter-Propagation Mode", IEEE Proceedings – Optoelectronic, Vol. 147, No. 1, 2000, 49-55.

[29] F. Ratovelomanana, N. Vodjdani, A. Enard, G. Glastre, D. Rondi, R. Blondeau, C. Joergensen, T. Durhuus, B. Mikkelsen, K.E. Stubkjaer, A. Jourdan, and G. Soulage, "An All-Optical Wavelength Converter with Semiconductor Optical Amplifiers Monolithically Integrated in a Asymmetric Passive Mach-Zehnder Interferometer", IEEE Photon. Tech. Lett., Vol. 7, No. 9, 1995, pp. 992-994.

[30] D. Wolfson, T. Fjelde, A. Kloch, B. Dagens, C. Janz, F. Poingt, I. Guillemot, F. Gaborit, A. Coquelin, and M. Renaud, "All-Optical Wavelength Conversion Scheme in SOA-Based Interferometric Device", Electronics Letters, Vol. 36, No.21, 2000, pp. 1794-1795.

[31] C. Joergensen, S.L. Danielsen, K.E. Stubkjaer, M. Schilling, K. Daub, P. Doussiere, F. Pommerau, P.B. Hansen, H.N. Poulsen, A. Kloch, M. Vaa, B. Mikkelsen, E. Lach, G. Laube, W. Idler, K. Wunstel, "All-optical wavelength conversion at bit rates above 10 Gb/s using semiconductor optical amplifiers", IEEE J. on Selected Topics in Quantum Electronics, Vol. 3, No. 5, 1997, pp. 1168-1180.

[32] M.F.C. Stephens, D. Nesset, R.V. Penty, I.H. White, "40 Gbit/s via Four Wave Mixing in Semiconductor Optical Amplifier with Integrated Pump Laser", Electronics Letters, Vol. 35, No.3, 1999, pp. 420-421.

[33] D. Campi, C. Coriasso, "Wavelength Coversion Technologies", Photonic Network Communications, Vol. 2, No. 1, 2000, pp. 85-95.

[34] R.D. Rosner, "Packet Switching, Tomorrow's Communications Today", 1982, Van Nostrand Reinhold

[35] S. Yao, B. Mukherjee, S. Dixit, "Advances in Photonic Packet Switching: an Overview", IEEE Communications Magazine, Vol. 38, No. 2, 2000, pp. 84-94.

[36] D.K. Hunter, M.C. Chia, I. Andonovic, " Buffering in Optical Packet Switches", J. of Lightwave Technology, Vol. 16,No. 12, 1998, pp. 2081-2094

[37] M. Karol, "Shared Memory Optical Packet (ATM) Switch", SPIE-Multigigabit Fibre Communication Systems, Vol. 2024, 1993, pp. 212-222

[38] N Mir-Fakhraei, "Evaluation of an ATM LAN constructed with a cyclic deflection-routing network", Computer Communications, Vol. 21, No. 7, 1998, pp. 662-669

[39] P.B. Hansen, S.L. Danielsen, and K.E. Stubkjaer, "Optical Packet Switching without Packet Alignment" ECOC 98, Madrid Spain, 1998

[40] F. Masetti, J. Benoit, F. Brillouet, J.M. Gabriagues, A. Jourdan, M. Renaud, D. Bottle, G. Eilenberger, K. Wunstel, M. Schilling, D. Chiaroni, P. Gavignet, J.B. Jacob, G. Bendelli, P. Cinato, et. al., "High speed, high capacity ATM optical switches for future telecommunication transport networks" IEEE Journal on Selected Areas in Communications, Vol. 14, No. 5, 1996, pp. 979-998

[41] D.K. Hunter, W.D. Cornwell, T.H. Gilfedder, A. Franzen, I. Andonovic, "SLOB: A switch with large optical buffers for packet switching", J. of Lightwave Technology, Vol.16, No.10, 1998, pp. 1725-1736

[42] J. Brassil, R. Cruz, "Nonuniform Traffic, in the Manhattan Street Network", Performance Evaluation, Vol.25, 1996, 233-242

[43] F. Ayadi, J.F. Hayes, M. Kavehrad, "Performance Analysis of the Bilayered ShuffleNet and the SR_Net under Deflection Routing" Computer Communications, Vol.20, No.2, 1997, pp.125-137

[44] A.S. Acampora, and I A. Shah, "Multihop Lightwave Network: a Comparison of Store-and-Forward and Hot-Potato Routing", IEEE Transactions in Communications, Vol.40, No.6, 1992, pp.1082-1090

[45] F. Forghieri, A. Bonomi, and P.R. Prucnal, "Analisys and Comparison of Hot-Potato and Single-Buffer Deflection Routing in Very High Bit Rate Optical Mesh Networks", IEEE Transactions in Communications, Vol.43, No.1, 1995, pp.88-98

[46] A. Bononi, G.A. Castanon, and O.K. Tonguz, "Analisys of Hot-Potato Optical Networks with Wavelength Conversion", J. Ligthwave Technology, Vol. 17, No. 4, 1999, pp. 525-534

Chapter 2

Optical Crosspoint Switch Theory and Real Samples

After an introduction to future optical networks in chapter 1, this chapter explores one of the key components used in these networks: The Optical Crosspoint Switch (OXS).

Initially the chapter discusses the OXS in ideal networks and the features that it has to satisfy in order to be used in new packet switching networks.

It discusses different types of architectures, described in literature, applied to different types of materials.

Afterwards the chapter monitors several commercialised OXSs, pointing out that at present there is no technology satisfying the characteristics required by an optical packet switching network.

The final section 2.3 provides a description of a novel OXS, which is based on an InGaAsP/InGaAs/InP active vertical coupler structure able to route data-packets within few nanoseconds. The chapter finishes with a description of the expected features of this novel architecture.

Glossary of the abbreviations

(OXS)	Optical Crosspoint Switch
(RI)	Refractive Index
(EO)	Electro-Optic
(QWs)	Quantum Wells
(QCSE)	Quantum Confined Stark Effect
(MMI)	MultiMode Interference
(SOAs)	Semiconductor Optical Amplifiers
(DC)	Directional Couplers
(MZI)	Mach-Zehnder Interferometers
(MQWs)	Multi Quantum Wells
(DOS)	Digital Optical Switch
(MEMS)	Micro Electro Mechanical Systems
(TO)	Thermo-Optic
(PLCs)	Planar Lightwave Circuits
(PDL)	Polarization Dependent Loss
(3D)	Three-Dimensional
(VC)	Vertical Couplers
(TIR)	Total Internal Reflection
(LC)	Lower Cladding
(PLW)	Passive Lower Waveguide
(AUW)	Active Upper Waveguide

2.1. Ideal Design

Future telecommunications networks, will be characterised by a very high optical data rate and ability to route optical packets. Different components, such as tuneable lasers, wavelength converters, switching matrix, amplifiers, will be needed for these networks. The current available technology for an OXS cannot support the development of optical devices which are able to satisfy future networks requirements. This is restricting the network data routing to expensive optical-electronic-optical (O/E/O) routing nodes or slow optical (O/O/O) switching, resulting in a network bottleneck. Thus, this future vision is pushing researchers to find out new technologies and new materials able to solve this problem.

2.1.1. Conventional OXS architecture

Optical networks use two kinds of OXS architectures: Broadcast and Point to Point. Both of these network architectures are based on a different switching matrix approach. The broadcast OXS, shown in Figure2.1, splits the input into the same numbers of outputs, i.e. in a 1x4 matrix the input is split into 4 channels. At this point an optical gate turns the signal OFF or ON, routing only one channel to the correct output.

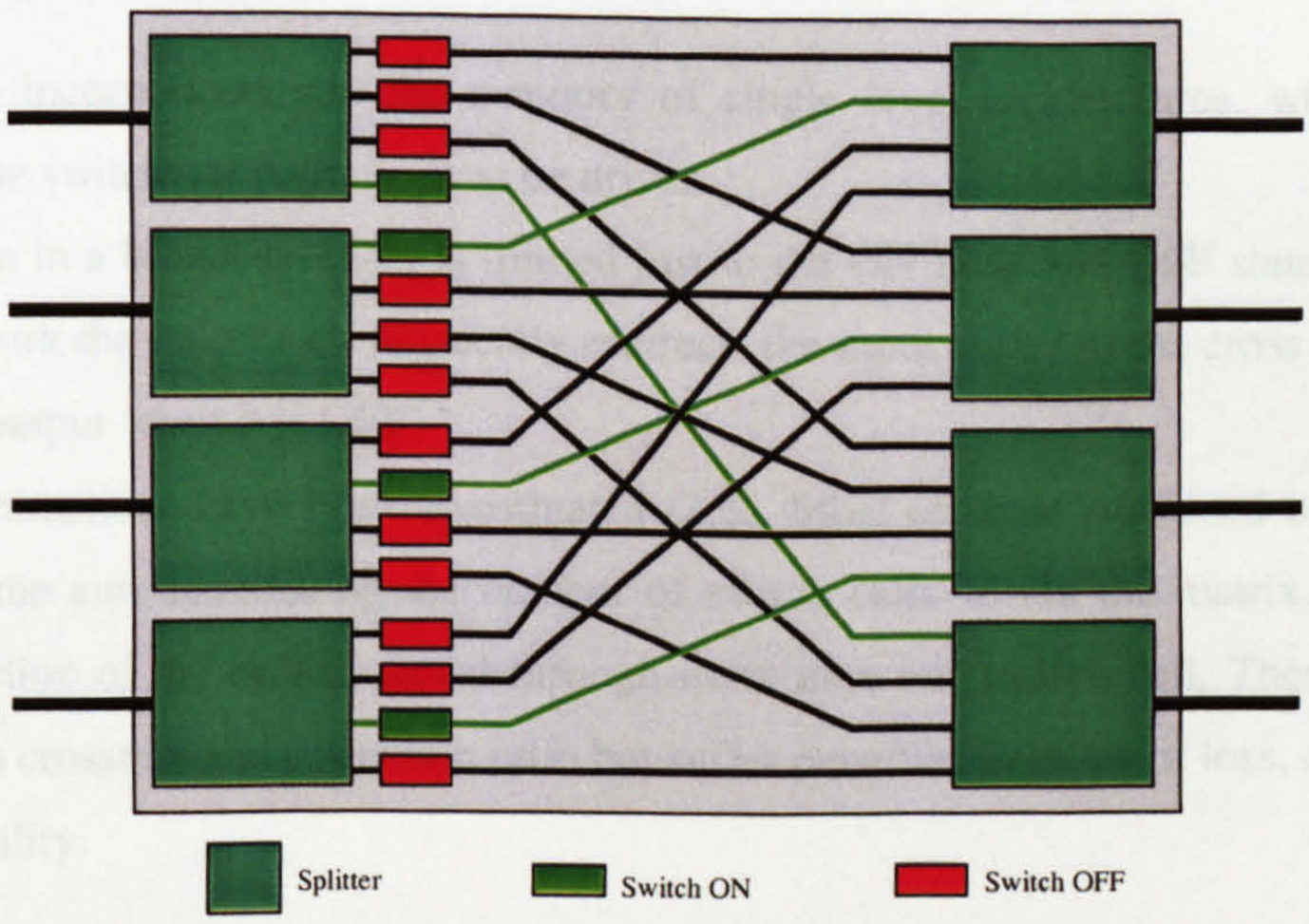

Figure2.1 A 4x4 Broadband OXS

Extending the concept to a generic network with N outputs the input signal suffers a loss of $10\log_{10} N$ dB plus, if the device is single mode, another $10\log_{10} N$ dB loss is caused by the recombining of N incoherent beams at the output [1]. Thus, in a real 4x4 OXS the theoretical losses will be as high as 12 dB. Moreover this architecture suffers a high number of path crossings with a dependence of 2N-1 for orders higher than 4, thus, in a 4x4 sample the number of crossings for the longest path is 7.

A manner to improve the loss to about $10\log_{10} N$ dB is to redirect the signal using a single OXS cell as shown in next Figure2.2. In this case for the point to point architecture the number of optical waveguide crossing is dependent on the switching path adopted.

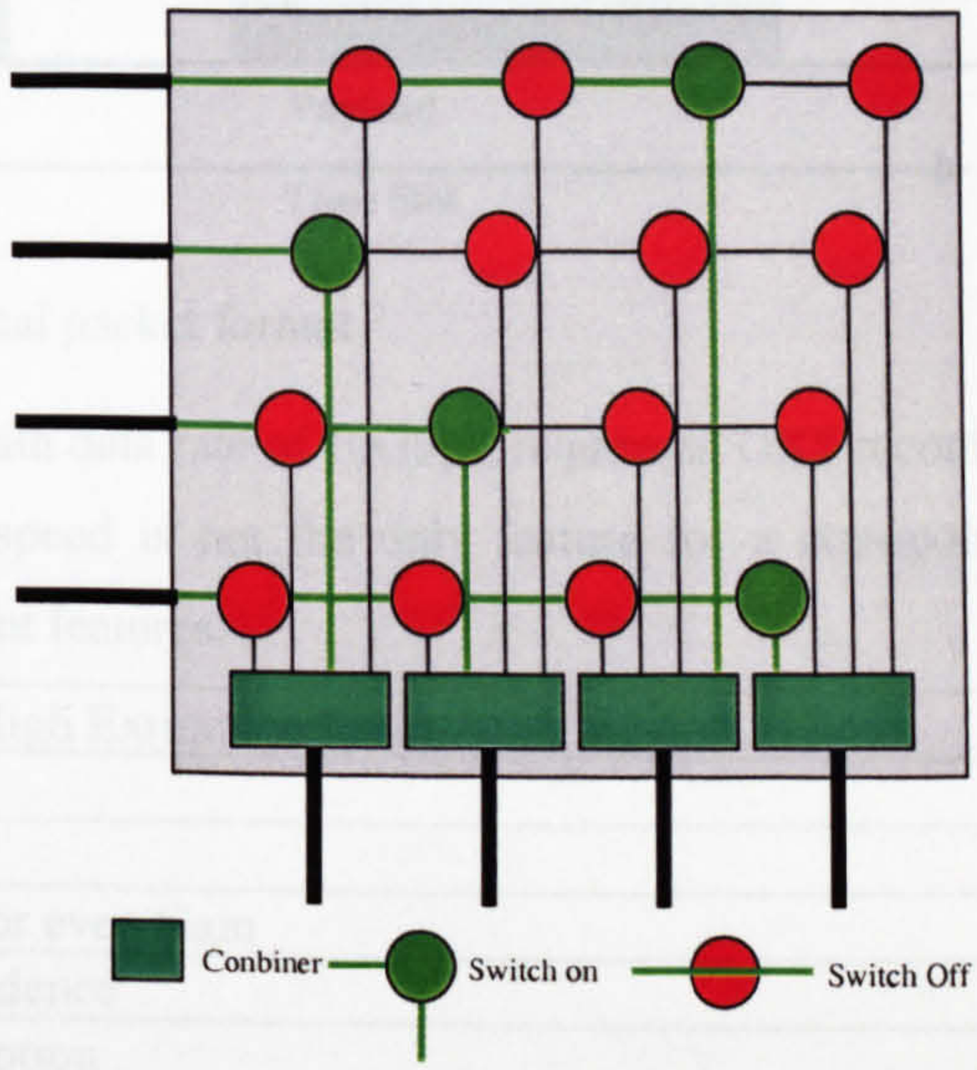

Figure2.2 A 4x4 Point to Point OXS

Both networks are incorporated into the category of single level architectures, which necessitate N^2 switches but just one switch per path needs to be driven.

The switch function in a broadcast OXS is limited just to the ON state and OFF state. Alternatively in a Point to Point network the switch cell physically redirects the input signal to the cross direction when it is ON and to the bar output when it is OFF.

Other kinds of architectures have been investigated [2,3]. Most of them are based on using Multi-level architectures with the aim of reducing the number of switch cells within the matrix. They are complex and use the redirection of the optical signal through more than one switch cell. These architectures can give good results in crosstalk and extinction ratio but suffer penalties in terms of loss, complex fabrication process, and scalability.

2.1.2. Features of a crosspoint switch used in a optical packet routing networks

When optical packets are routed in an optical network the OXS involved needs to be fast enough to keep up with the packet flow.

The switch needs to be reconfigured in a time as short as the guard time between the header, which gives the information about the direction of the packet, and the payload that need to be switched. A typical time slot example is shown in Figure2.3.

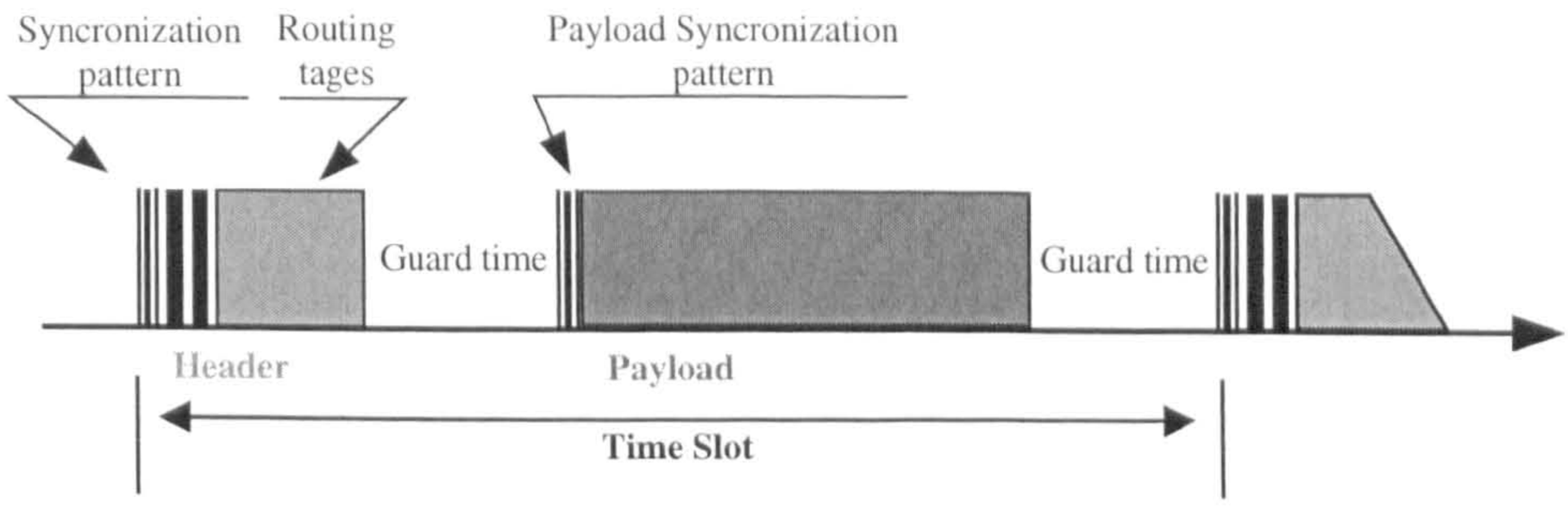

Figure2.3 Example of an optical packet format

Packet switching networks, with data rate of 10Gbps, require an OXS reconfiguration time of the order of nanoseconds [4]. However, speed is not the only feature for a crosspoint switch. Table2.1 shows a summary of the most important features.

• Low Crosstalk and High Extinction Ratio
• Compactness
• Fast Switching
• Low-Insertion Loss or even Gain
• Polarization Independence
• Low Power Consumption
• Temperature Stability
• Reliability
• Loss Uniformity
• Scalability
• Easy fabrication
• Operability within the EDFA wavelength range

Table2.1 requirement for next generation space switch

2.2. Materials for Optical Switches

Three main kinds of materials are used for optical crosspoint switches: III-V Semiconductor, Lithium Niobate ($LiNbO_3$) and Silica-Polymer based. The next subsections illustrate some OXS architectures, which adopt different materials.

2.2.1. The Optical Switch adopting III-V semiconductor materials

The easy integration with other devices like couplers, Semiconductor Optical Amplifiers (SOAs) and wavelength converters, makes semiconductor materials very suitable for the realisation of Optical crosspoint switches [5]. OXS architectures, based on semiconductor material, are related to the change of refractive index (RI) or gain in a particular area of the device. The RI change can be achieved by inducing a variation of the device temperature, defined as Thermo-Optic (TO) effect. Instead when the RI change is caused by the injection of carriers into the p-i-n junction the effect is called Electro-Optic (EO). In

particular this last effect linearly modulates the RI of the active region, changing the absorption coefficient in the active region and in proximity of the bandgap it can procure gain. Linear change of the RI can also be induced with an electric field, but in this case the RI change can be up to 100 times smaller for both polarization TE and TM [6].

Non-linear effects can also induce RI change, by quadratic Kerr effect [6] or, if Quantum Wells (QWs) are included into the structure, by Quantum Confined Stark Effect (QCSE) [7].

The architectures adopted so far for optical switches require functions such as:

- splitting or combining
- switching
- redirection

Different kind of optical couplers, like Y-Branch couplers [8-10], Directional couplers (DC) [11-13], Star couplers [14-16], MultiMode Interference (MMI) couplers [17-19] can be used to split and combine signals. Switching and redirection, instead, is achieved using interferometers, modulators or SOAs.

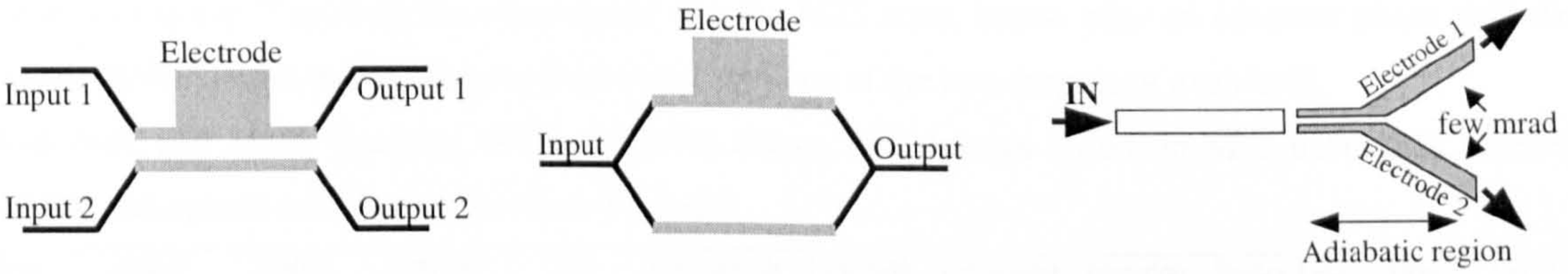

Figure2.4 schematic view of semiconductor optical switches

Once the input signal is split it needs to be switched and routed to the correct output. Optical switching can be realised using DC, Mach-Zehnder Interferometers (MZI) or even Digital Optical Switches (DOSs), as shown in Figure2.4.

2.2.1.1. Directional Couplers

Directional coupling is achieved with two waveguides close enough to each other to produce reciprocal power exchange [20,21]. The coupling can be controlled via RI change. In fact injecting carrier in one branch of the coupler the RI drops matching the two waveguides and hence allowing the coupling. On the other hand, such devices are polarization dependent due to the transmission modes, TE or TM, which have different coupling length. This could create some problems in devices that have to allow both modes. A selection of realised DC switches is summarised in Table2.2

Year	Author	Matrix	Material	Size [mm]	Wavelength [nm]	Crosstalk [dB]	Extinction Ratio [dB]	Insertion Loss [dB]	Device Loss [dB/cm]	Drive	Speed
1993	NTT	4x4	InGaAlAs	9x0.4	1550	-17	-	-	18.5*	5-6V	-
1994	NTT	2x2	InGaAlAs	6	1550	-15	-	16	-	-	100ps**
1995	Fujikura	2x2	InGaAs/InP	<1.2	1550	-12	-	-	-	3V	-
1996	NTT	2x2	InGaAsP	<0.8	1550	-15	10	15	-	25mA	1ns
2000	NTT	4x4	InGaAlAs	16.5	1550	-13	-	18-21	-	9.8V	<70ps

Ref [22-27], * Transmission Loss in dB, ** [86]

Table2.2 Optical directional coupler switches fabricated to date

2.2.1.2. Mach-Zehnder Interferometers

MZI use a Y-junction splitter, which redirects the input signal in two arms, Figure2.4 b), where one of them is able to change the signal phase. The merge of the two signals in a second Y-junction gives the resulting output, which assumes value 0, if the phase shift between the two arms is π and 1 when no phase shift is applied [28].

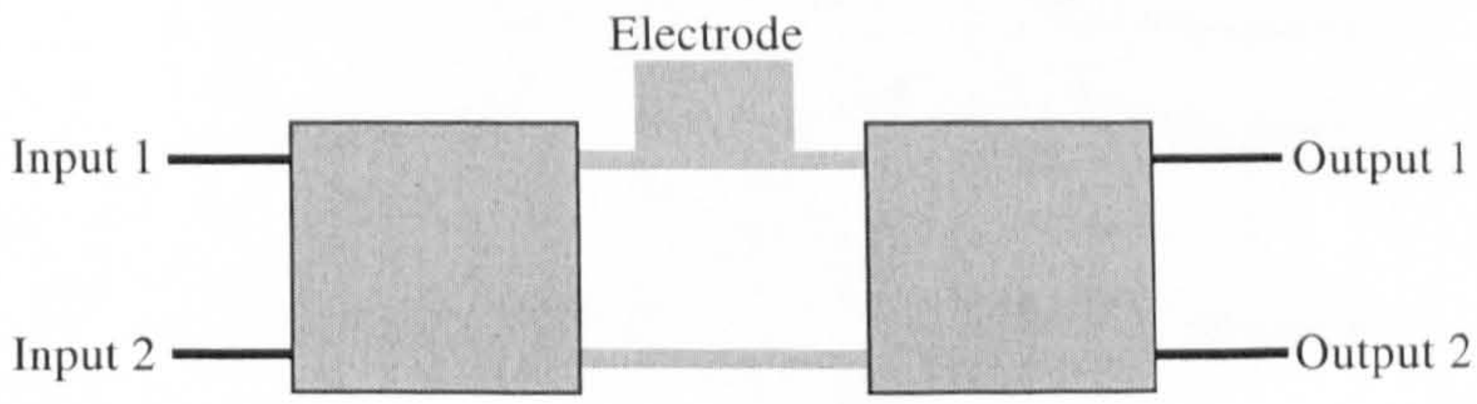

Figure 2.5 2x2 Mach-Zehnder interferometer using MMI 3dB coupler

Multi-Mode Interference couplers can also be used for MZI configuration. They make the y-junction as shown in Figure2.5 splitting the input signal into the MZI arms, hence, after an adequate phase shift the second MMI couples the resulting optical signal into one of the two outputs or even both.

With bulk and Multi Quantum Wells (MQWs) alloys, fast devices based on MZI have been realised [29,30] and optical switches as shown in Table2.3.

Year	Author	Matrix	Material	Size [mm]	Wavelength [nm]	Crosstalk [dB]	Extinction Ratio [dB]	Insertion Loss [dB]	Device Loss [dB/cm]	Drive	Speed
1996	SFIT	4x4	InP/InGaAsP	20x5	1550	-	15	-	5	4.5V	200ps
1997	Col. Univ.	1x2	GaAs/AlGaAs	-	1300- 1550	-	20	1.5	-	19.6V	-
1998	NTT	2x2	InGaAlAs	-	1550	-30	-	13	4.7	4V	-
1999	NTT	2x2	InGaAlAs	4	1550	-20	-	14.1	5	3.5V	-

Ref [31-33], * Very similar to paper [] in 1996 from the same authors

Table2.3 Mach-Zehnder Interferometer optical switches fabricated to date

2.2.1.3. Digital Optical Switch

Based on the adiabatic mode evolution [34] DOS works as a normal 3dB splitter when no bias is applied and when bias is applied, the RI change causes the switching to occur, see Figure2.4. It has been proved that DOS can be polarization independent and have a bandwidth of more than 50 nm for TE and TM modes [35].

Year	Author	Matrix	Material	Size [mm]	Wavelength [nm]	Crosstalk [dB]	Extinction Ratio [dB]	Insertion Loss [dB]	Device Loss [dB/cm]	Drive	Speed
1991	Phil.-Erics.	1x2	InGaAsP	-	1550	-20	-	-	2	30mA	-
1993	Alcatel	1x4	InGaAsP	<5mm	1550	-15	-	15	-	6mA	300ps
1994	GTE	1x2	InGaAsP	3	1300-1550	-	20	-	2	100mA	-
1995	AT&T	1x2	InGaAsP	0.9	1550	-10.5	-	8.25	1.25*	5dBm	-
1997	Lucent	1x2	InGaAsP	3	1550	<-13	-	-	3*	-7V	-
2000**	Col. Univ.	1x4	InGaAsP	20	1550	<-23	-	-	-		2ns

Ref [36-40],* Transmission Loss in dB, ** Theoretic proposal

Table2.4 Digital Optical Switches fabricated to date

Switching architectures also deploy SOAs as switching gates. Figure2.6 shows a schematic diagram of such device. When the gate is unbiased, "OFF state", the input signal is completely absorbed. Instead, a

gain higher than 25 dB can be attained when the SOA is in "ON state". The loss/gain nature of the SOA achieves high extinction ratio switches[41].

The main advantage of an optical crosspoint switch adopting SOAs is that the gain generated can be used to compensate for the device losses. Furthermore, the adoption of strained MQWs structures allows the polarization sensitivity to be reduced or even neglected [46].

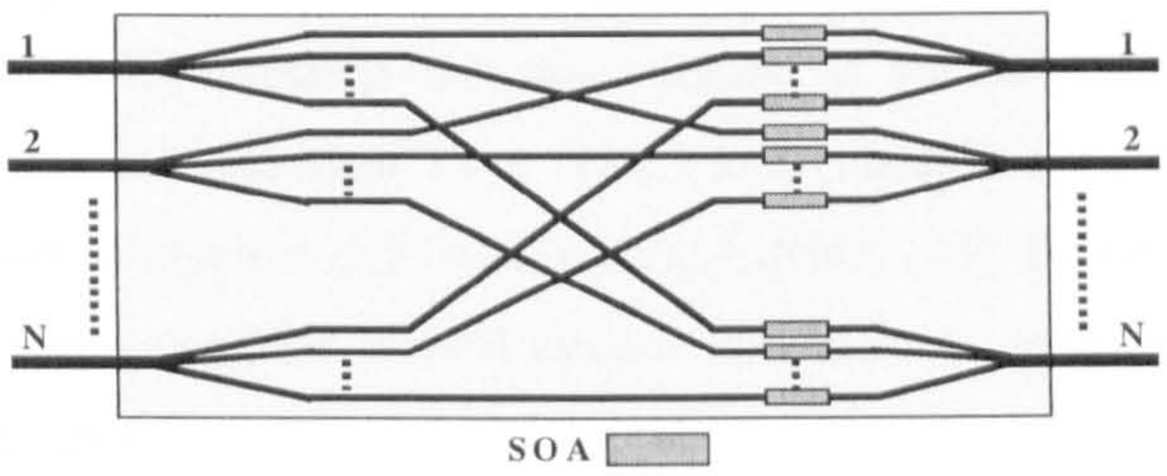

Figure 2.6 NxN Switch using SOAs. Schematic diagram

The adoption of Brewster facets, tilt with an angle between 7° and 10°, reduces the back reflections. Next Table2.5 shows the switches based on SOA's fabricated to date.

Year	Author	Matrix	Material	Size [mm]	Wavelength [nm]	Crosstalk [dB]	Extinction Ratio[dB]	Gain [dB]	Insertion Loss [dB]	Device Loss [dB/cm]	Drive [mA]	Speed
1992	Ericsson	4x4	InGaAs/InP	-	1550	-40	40	6*	-	0dB+	50	-
1993	Philips	2x1	InGaAs/InP	1.8	1550	-13	-	<15	7	1.7	100	-
1997	NEC	4x4	-	-	-	-	40	-	0	-	27	-
1999	NTT	gate	InP	<1.2	1550	-	35	10	2.6	0	28	0.6ns
1999	NEC	gate	InGaAs/InP		1550	-	30	0	3		30	

Ref [41-45], * On Chip, + Fiber to Fiber

Table2.5 SOA-based optical switches and gates fabricated to date

Similar 2x2 space switches but using EA modulators rather than SOAs have been also realised [47]. However, the absence of gain requires the introduction of SOAs before and after the OXS.

2.2.2. *Optical switches with Inorganic Crystals: Lithium Niobate ($LiNbO_3$)*

Lithium Niobate crystals (LiNbO3) are at the same time a ferroelectric, piezoelectric, pyroelectric and have high nonlinear optical and electro-optical coefficients and photorefractive sensitivity. These properties allow it to be used for optical and acoustic devices. These material properties are determined by the crystal structure, which is sensitive to physical and chemical effects [48].

Also with this material OXS based on directional couplers, MZI and DOS have been realised.

Year	Author	Matrix	Architecture	Size [mm]	Wavelength [nm]	Crosstalk [dB]	Extinction Ratio [dB]	Insertion Loss [dB]	Device Loss [dB/cm]	Drive	Speed
1990	NEC	8x8	DC	65	1300	20-30	-	6-12	-	85 V	-
1994	Ericsson	8x8	DOS	15x80	1550	<15.5	-	9-15	-	±105	-
1995	ATT	8x8	DC	-	1300	22-45	-	8-11	-	10	-
1996	NEC	8x8	MZ	-	1300	20-40	-	8-12	-	±48	-
1997	ATT	4x4	DOS	-	1300	<21	-				

Ref [49-53]

Table2.6 Optical switches in $LiNbO_3$ technology fabricated to date

Table2.6 shows reported switch arrays and their performances. Most of the devices present in literature are 8x8 switch arrays mostly working at 1300 nm with reasonable crosstalk but relatively high insertion loss. The main problem of these devices is the large size plus they need high drive voltage. Furthermore, even if it is known that such materials can rapidly switch within few nanoseconds no mention is made about the reconfiguration time that could be high due to the number of driven switches. Finally because they are passive devices, signal restoration is necessary before and after the matrix switch.

Despite these demonstrations the research was discontinued in the early 1990s because of technical limitations such as Polarization Dependent Loss (PDL) and crosstalk almost. These have since been resolved by the introduction of titanium diffusion in z-cut $LiNbO_3$ [48]. However the devices still suffer tight manufacturing tolerances, complex control circuits necessary to drive the switch matrix and low scalability of array architectures.

2.2.3. Switching Using Polymer Materials

As they can be easily combined with different materials, Polymer and Fused Silica produce interesting materials in terms of realising different functions inside integrated optics devices. Most of the research is based on Micro Electro Mechanical Systems (MEMS) or TO and EO effects.

Over the past decade there has been a lot of interest in silicon-based MEMS. The research in this area has produced microscopic versions of many macro machines, widening the potential applications from display technologies to aeronautics, from chemistry to optical telecommunication. So far several optical switch architectures have been investigated. Most of them deploy an electrostatic moveable mirror in order to divert the input light to different outputs. In particular the voltage applied, between actuator-plate and substrate, generates an electrostatic force, which is able to tilt the mirror plate and redirect the light signal. Electrostatic actuation allows low-power consumption devices to be made with a typical switching power value of few microwatts.

Year	Author	Switch	Matrix	Size [mm]	Crosstalk [dB]	Extinction Ratio [dB]	Insertion Loss [dB]	Device Loss [dB/cm]	Drive	Speed
1998	AT&T	FS-MOS	4x4	2.3x2.3	<-60	60	19.9	-	±100V	<700us
1998			2x2	-	-	-	0.81	-	40V	64us
1999	UCLA	SI-MEMS	2x2	-	<-80	-	0.7	-	20V	600us
1999	Bell Lab	Tilt-uMirr.	16x16	-	<-30	-	8	5	20V	20us

Ref. [54-57], * Fiber to Fiber Transmission Losses

FS-MOS – Free Space Micromachined Optical Switch
Tilt-uMirr. – Tilting-MicroMirrors
SI-MEMS – Stress Induced - Micro-Electro-Machined System

Table 2.7 Silicon based MEMS optical switches fabricated to date

Table2.7 shows a summary of the main characteristics of this architecture. These MEMS based switches have very low crosstalk and high extinction ratio. The insertion loss is usually low but increases with the introduction of micro lenses. The switching speed is on average about half millisecond. This value is not fast enough to enable optical packet switching. However, such devices find a very good application in an emergency role for optical restoration mechanism [58]. Finally, for such devices, little mechanical stress investigation has been published so far. In fact in adopting moveable parts devices as these could have a low lifetime.

TO devices have a simple and flexible control of the switch. It is induced by a temperature change to the material, which creates a RI match between two waveguides. The rise in temperature is achieved by current injection and it is proportional to the dissipated electrical power density but inversely proportional to the thermal conductivity of the waveguide material. In particular, it has been demonstrated that "silica on silicon" waveguides require seven times more power than polymer waveguides to induce the same temperature difference [59].

Year	Author	Switch	Matrix	Material	Size [mm]	Crosstalk [dB]	Extinction Ratio [dB]	Insertion Loss [dB]	Device Loss [dB/cm]	Drive [mW]	Speed
1996	H-H-Institut	DC	2x2	Polymer	7	< -40	-	6	0.85	20	1ms
1996	H-H-Institut	DOS	2x2	Polymer	25	< -25	-	6.5	0.9	>45	-
1996	T-U-Berlin	DOS	1x2	Polymer	8	-	>20	4*	-	200	-
1996	T-U-Berlin	DOS	1x2	Polymer	8x70	-28.8	-	12.8	-	<5W	250us
1998	IQE-Zurich	MZI	2x2	Silica	5x0.05	-	21	1	-	110	180us
1998	ETRI-Korea	MZI	2x2	Polymer	23	-20	-	4.5	0.6	10W	2ms
1998	NTT	2 MZI	16x16	Silica	100x107	-43	55	6.6	-	17W	-
1999	NTT	2 MZI	8x8	Silica	68x68	-43.3	60.3	5.1	-	16W	-
2000	H-H-Institut	VDC	1x2	Pol-Sil	-	<-23	-	3.5	<0.8	<80	-
2001	H-H-Institut	VDC	1x8	Pol-Sil	-	<-25	-	<5	<0.8	85	-

Ref [60-69], * In Chip

DC – Directional Coupler
DOS – Digital Optica Switch
MZI, 2 MZI – Single, Double Mach Zehnder Interferometer
VDC – Vertical Directional Coupler

Table2.8 Polymer & Silica on Silicon based optical switches fabricated to date

Also, TO polymer and silica based optical crosspoint switches employ switching architectures like Mach-Zender interferometer, DC and digital optical switch. Table2.8 shows that such devices necessitate large areas, plus the crosstalk and the extinction ratio are never better than –25dB. This is thought to be due to the passive nature of the device. Improvements of crosstalk and extinction ratio can only be made by adopting double-switch architecture. Power consumption is dependent on the material and on the physics principle used, it can be low as 20mW and as high as 5W for a single switch. In particular the switch matrix has the total power consumption always dependent on the total number of switches turned in ON State. Finally the recovery speed is always in the order of milliseconds or hundreds of microseconds, which is too high value to allow optical packet routing.

Another switching mechanism, which can be used with this kind of materials, adopts the EO effect.

Year	Author	Switch	Matrix	Size [mm]	Crosstalk [dB]	Extinction Ratio [dB]	Insertion Loss [dB]	Device Loss [dB/cm]	Drive	Speed
1995	ETRI-Korea	DC	2x2	-	-	<15	-	-	23V	-
1997	ETRI-Korea	MZI	2x2	-	-22	-	9-10	-	15V	-
1997	AIST-Korea	DOS	1x2	-	-16	>16	-	-	35, 110V	-
1999	AIST-Korea	DOS	1x2	-	-15	-	-	-	15V	-

Ref. [72-75], * Fiber to Fiber Transmission Losses

DC – Directional Coupler
MZI – Mach Zender Interferometer
DOS – Digital Optical Switch

Table 2.9 Polymer based EO optical switches fabricated to date

It is a very competitive technology in terms of switching speed because it is related to the phase relaxation time, corresponding to a few tens of femtoseconds [70]. On other hand the manufacture of a switching device is very difficult because EO polymers contain non-linear molecules that have to be arranged in a non-centrosymmetric structure [71] obtained by spin deposition and electric field poling processing. Spin and coating look like simple processes but they need highly controlled operational conditions because a single pinhole can make the sample useless. The poling process, instead, is realised

by applying a strong electric field while the sample is heated and successively cooled. Also in this case operational conditions are very important because a small change of the temperature or a small change of the applied field can modify the process characteristics.

Furthermore, most of the EO polymers need to be RI tuned by photo-bleaching process, in other words, by absorption of UV-light the RI of the material can be reduced to a chosen value. All these fabrication conditions increase the difficulties to make and to repeat successful EO devices. As a confirmation Table2.9 shows that the real results achieved with EO technology, like crosstalk, extinction ratio and insertion loss, are never in agreement with the prediction from theoretic models.

2.3. Examples Of Real Crosspoints

To meet the necessities of the telecommunication service providers and the requirements of the market, so far only few suppliers have a ready to sell commercial product. This section investigates the most important OXSs available, to date, on the market. In particular it focuses on technologies adopted and characteristics achieved.

The first in examination is a 8x8 matrix switch offered by NTT Electronics, which adopts switching units based on a double Mach-Zehnder Interferometer architecture, with TO phase shifters [76].

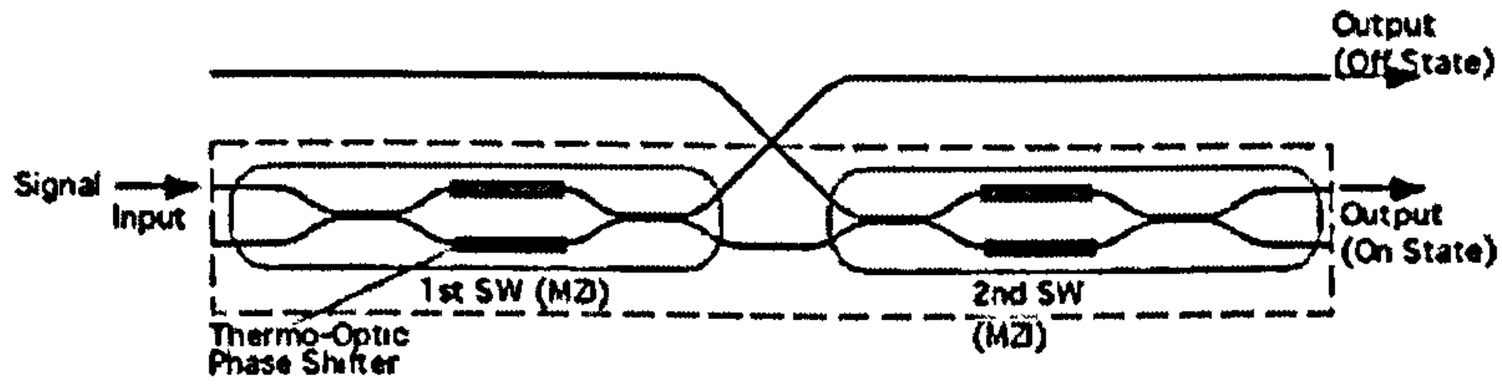

Figure2.7 Switching Unit Configuration

When the switching unit of Figure2.7 has both MZ cells in "OFF state" the light, launched into the input port, is transmitted through the OFF path to the Output (OFF state). In the "ON state" the current injected into a arm of the MZ cell allows a different path redirecting the light to the Output (ON state).

The specifications provided by the manufacturer, which are summarised in Table2.10 show that these switches have a small size, with a good extinction ratio and low polarization sensitivity. On the other hand the switch needs 3ms to recover and requires forced air-cooling.

Item	Specifications
Input/Output Port	8 × 8(non-blocking)
Operating Wavelength	1.55um region
Insertion Loss	<8dB
Loss Uniformity	<2dB
Extinction Ratio	>40dB
PDL	<0.5dB
Return Loss	>40dB
Switching Speed	<3ms
Power Consumption	<8W(PLC Module), 2.8W(drive circuit)

Operating Ambient Temperature	0 to 65
Switching Control	TTL Drive (+5V)
Supply Voltage	+24V±5% / 0.85A (max)
Cooling	Forced Air cooling required (>1.5m/sec. Recommended)
Dimensions(W × D × H)*	145 × 156 × 23 mm

*excluding PCB fixing Parts and fibers

Table2.10 NTT electronics Sample Specifications Switch [77]

Using two well-known technologies, silica Planar Lightwave Circuits (PLCs) and thermal inkjet technology, Agilent has made a basic building block for all-optical switch [78]. The Agilent photonic switch directs the light from an input to an output by using a thermal inkjet element. This creates a bubble, in an index-matching fluid at the intersection between the input and the desired output waveguide, that reflects the light by means of total internal reflection.

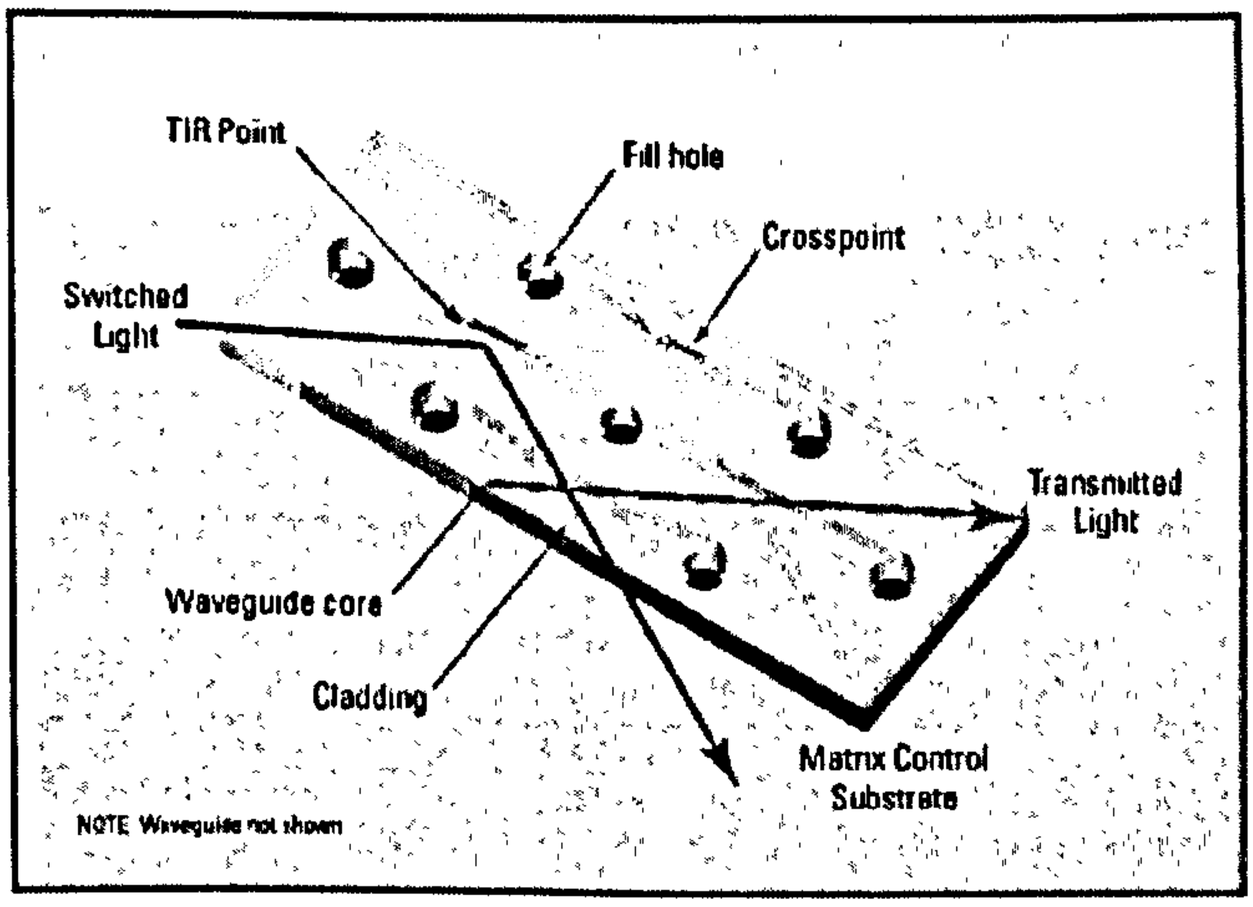

Figure2.8 Agilent Optical Switch Diagram [79]

The company proposes two kind of photonic switches a 32x32port and a dual 16x32. Table2.11 reports the features of the 32x32 port.

Even if the declared characteristics of PDL, loss and crosstalk are appreciable the switching speed is the slowest seen so far.

Item	Features
PDL	<.25 dB
Switching speed	<10 ms
Loss	<15 dB in a 512x512 WIXC matrix <5 dB in a WSXC matrix Uniform 3.5 dB for OADM express channels
Crosstalk	<-50 dB intelligent control sub- system and high-level API
Transparent at	1300 and 1550 nm wavelength bands
Subsystem connection	5V and 15V

Table2.11 32x32 Agilent OXS features [80]

Agere Systems, former Microelectronics Group of Lucent Technologies, proposes a fully integrated Three-Dimensional (3D) MEMS optical switch. It is a 64x64 matrix adopting a 2-axis tilt mirror architecture [81].

The light from the input fiber hits the first tilt mirror, steers to a reflector that rebounds to a second tilt mirror, and finally is steered and coupled into the output fiber. Unfortunately, to date, the characteristics of such a crosspoint switch are not available, however it has previously shown that "tilt mirror" architectures suffer an exhibit a slow switching time in the range of the tens of ms.

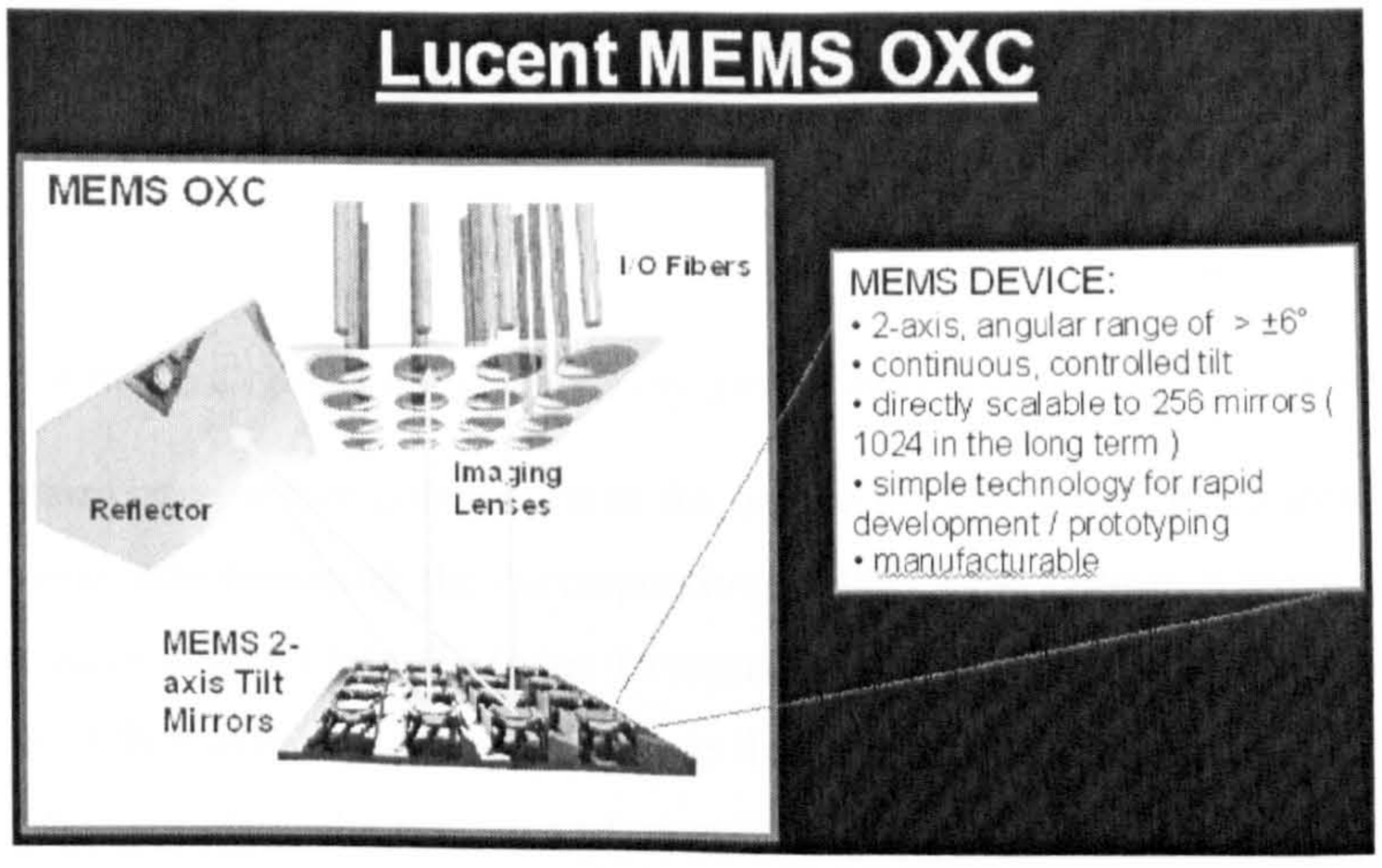

Figure2.9 The Lucent 3D Optical Crossconnect [82]

The three devices available on the market confirm that to date there is not an optical crosspoint switch that can be deployed for fast routing of data packets confirming that the challenge is still open.

After the research of what has been investigated and what technology can supply to the market about OXSs, next section shows a novel OXS device, based on an active vertical coupler architecture, which satisfy the requirements to suit future optical packet routing networks. Its theoretical modelling, the manufacturing phases and the investigation of its characteristics are treated in the next chapters of this thesis.

2.4. A Highly Compact Crosspoint Architecture

This section describes and discusses a novel highly compact crosspoint architecture that is the main subject of investigation of this thesis.

The crosspoint, realised using quaternary (III-V) semiconductors deposited on top of an InP substrate, consists of two perpendicular groups of ridge passive waveguides which represent the inputs and the outputs of the OXS. On top of the waveguide crosses an active layer is deposited that together with the lower passive waveguide forms two Vertical Couplers (VC) as shown in Figure2.10 (b). A Total Internal Reflection (TIR) mirror vertically penetrates the active waveguide with an angle of 45° with respect to the

two couplers directions. This turns the light direction of 90° redirecting the optical signal from the input to the output waveguide.

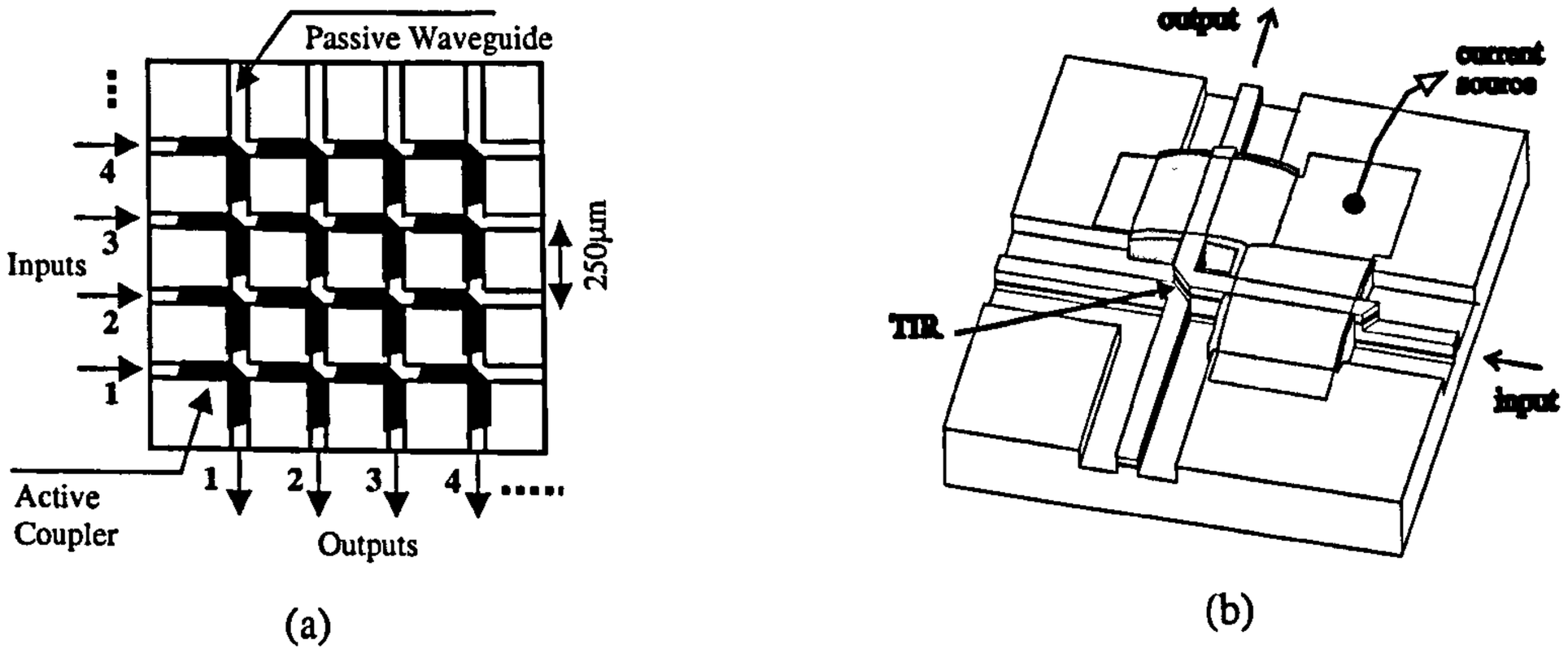

(a) (b)

Figure2.10 Layout of the 4x4 crosspoint switch array and schematic of a switch unit cell

The injection of carries into the two couplers turns the device in "ON state". It reduces the effective RI of the active upper waveguide matching the corresponding value of the bottom passive waveguide. In this situation the input signal injected into the input waveguide couples up to the upper waveguide at the first VC, is steered by the TIR mirror and couples down, at the second VC, to the bottom waveguide and so on to the cross output. Nevertheless, the presence of an active layer provides also optical gain that boosts the signal and consequently increases the ON/OFF contrast.

When in "OFF state" the OXS is not biased, thus, the input optical signal travels along the input passive layer up to the bar output, Figure2.10(b) or to the next crosspoint cell when in 4x4 configuration as in Figure2.10(a). Because of the unmatched waveguides, only a small part of the input signal couples up to the active layer and thanks to the absorptive nature of such layer, the signal at the cross output is drastically reduced giving an ultra-low crosstalk.

2.4.1. The Active Vertical Coupler

In integrated optics applications the directional coupler is a very useful device when a low coupling length is required. In order to reduce the device length to values in the order of 100 µm the coupling architecture needs to be changed from a planar waveguide design to the vertical waveguide design [83]. Technically a planar coupler necessitates a large spacing between the waveguides inducing a longer coupling length. Instead in the VC the growth process can be easily controlled within few nanometers allowing structures with very close layers which can become waveguides of a vertical directional coupler and hence reduces the coupling length to few hundred microns.

Carrier injection in a p-i-n junction induces a RI change due to free-carrier plasma and bandfilling/shrinkage effects. Figure2.11 (a) shows the carrier density dependence from the total current injected in a p-i-n diode structure for four different thickness of the active layer which is 1µm wide, 500

μm long, efficiency η=0.8 and has a p-doping of $10^{18}cm^{-3}$. Figure2.11 (b) indicates how the RI changes at a wavelength of 1550 nm, with the material bandgap at a fixed carrier density value.

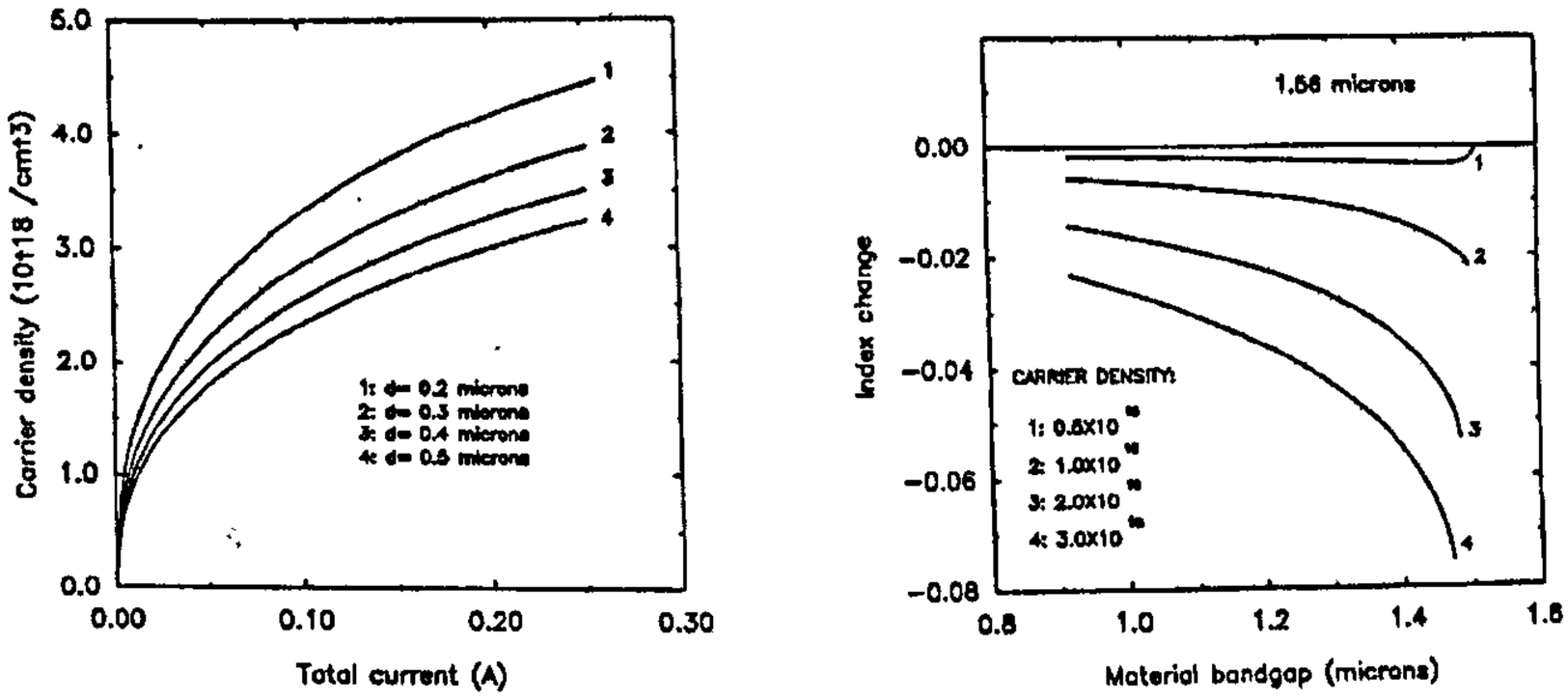

(a) (b)

Figure2.11 Induced index change as a function of the currier density and hence of the total current, after [51]

In particular the curves show a weak index change for wavelength below the bandgap, while becoming stronger closer to the bandgap due to the dominance of the bandfilling/shrinkage effect [51].

These effects are polarization insensitive for bulk materials but not for MQWs that have a TE mode dominance which can be reduced or even cancelled by the introduction lattice strain into the MQW [85, 86].

Nevertheless, the speed is determined by the carrier lifetime, in other words the time it takes to eliminate free carriers from the semiconductor layer. This value is limited to approximately a few nanoseconds for current injection [20].

Vertical couplers have been realised adopting p-i-n structures[87-92] or similar design [93, 94]. However, all of them are based on passive design where both the coupling waveguides are made with passive layers, achieving switching only by RI variation Δn_x.

It will be seen, instead, that the optical crosspoint switch investigated in this thesis is realised using a p-i-n junction but the top layer is an active layer. This permit to add a second key parameter: the variation of the active layer gain Δg. This helps in both ON and OFF states of the crosspoint. In ON state gain is added to the switched signal while in OFF state the high absorption of the unbiased active layer suppress the crosstalk. It will be seen that from the model simulation the device can improve dramatically the switched optical signal and the crosstalk between bar and cross output.

2.4.1.1. The vertical coupler description

Figure2.12 summarised the basic p-i-n structure. Over the substrate a first layer is grown that acts as *Lower Cladding (LC)* for the *Passive Lower Waveguide* (*PLW*) which stands above and represents the input and the bar output of the optical switch. Hence, a n-doped layer called *spacing layer* is in between

the *(PLW)* and the *Active Upper Waveguide (AUW)*. The *(AUW)* is the i layer of the p-i-n junction and act as cross output. The InP *upper cladding* and the final *cap layer* in InGaAs complete the device.

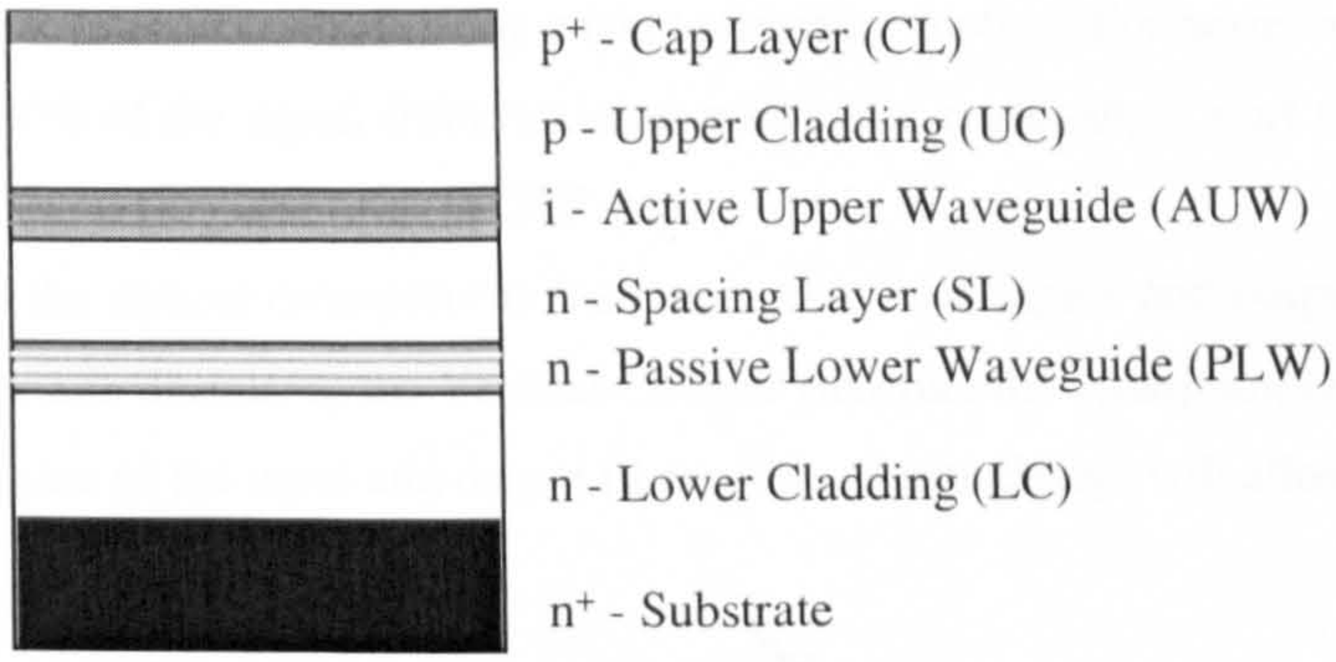

Figure2.12 Wafer layer structure

Injection of carriers, into the active upper waveguide, reduces the RI, which matches with the value of the passive bottom waveguide allowing switching to occur.

2.4.2. Total Internal Reflecting Mirror

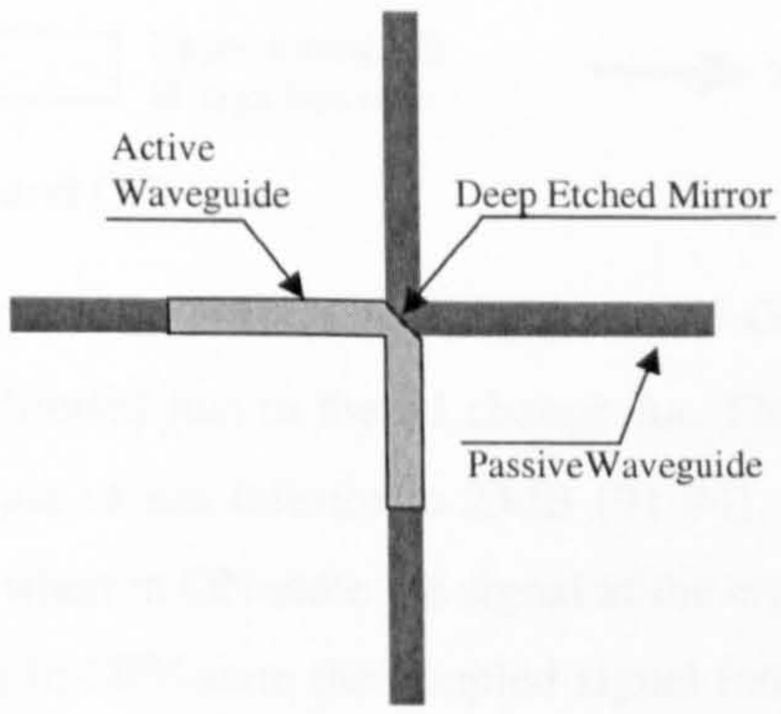

Figure2.13 Total Internal Reflecting Mirror adapted to the OXS structure

The TIR mirror plays a very important role in the structure of such OXS. It enables the device to be very compact compared to adopting S-Bend waveguides. Also, the realisation of an S-Bend in such vertical waveguide architecture is more difficult than a 45° etch.

TIR Mirrors have been already adopted in several crosspoint architectures [97-99] but because of the induced loss, their use inside a switching path is limited in number. However, this is not a problem for the crosspoint proposed which includes just one mirror per path.

Chapters 3 and 5 are dedicated to the design and to the fabrication of the crosspoint and give a complete analysis of TIR mirrors.

2.4.3. Advantages and problems of the Architecture

For the nature of the material and physical principle adopted the optical crosspoint switch transition time is expected to be of few nanoseconds allowing packet switching routing. Furthermore the device has been designed to switch 100% of the signal from the input port to the cross-output port when in ON state and to reduce the crosstalk to a very low level in OFF state.

Another key issue of the optical crosspoint is the connection with inputs and outputs fibers making the device size very important. Thanks to the Vertical Coupler structure the crosspoint result very small and it is limited only by the size of the input and output fibers. The chosen design will allow fibre-ribbon pitch.

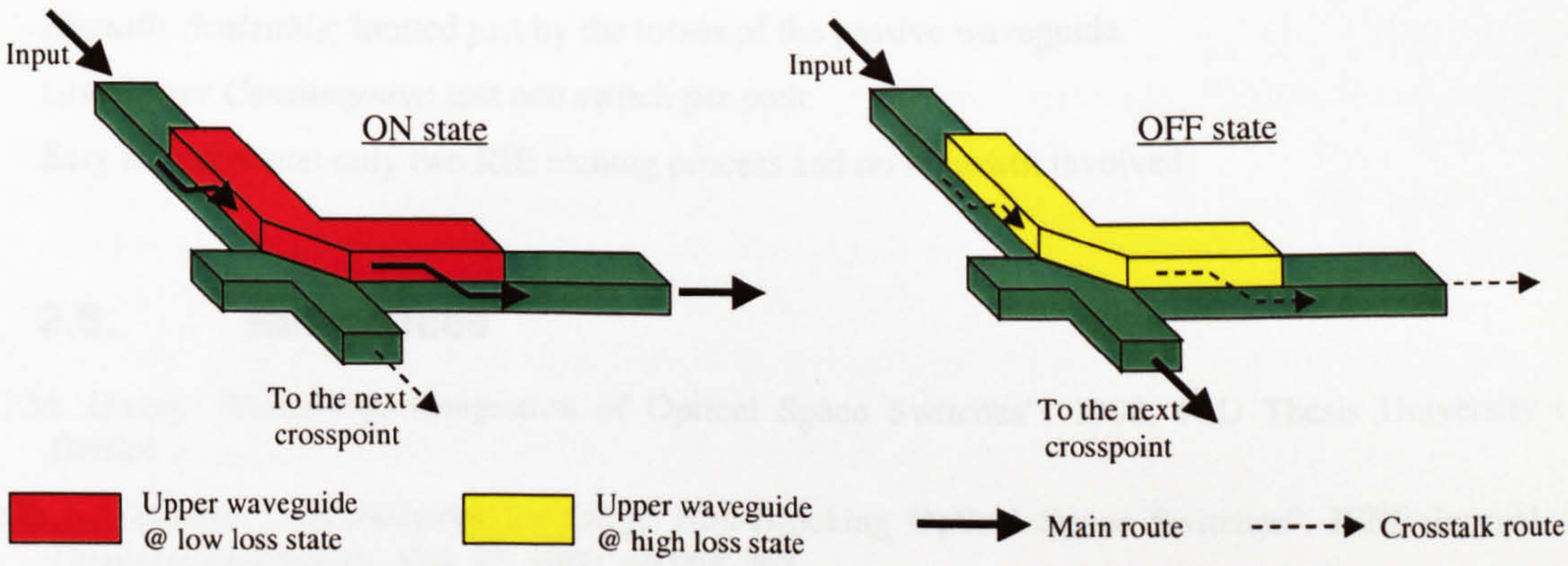

Figure 2.14 Schematic of the ON and OFF state

Optically passive directional-couplers are characterised by poor ON-OFF contrasts and high crosstalk due to the switching principle that is limited just to the RI change Δn. This is confirmed by prior-art devices which had shown ON-OFF contrast values inferior to 25dB [91-94], plus no mention is made about the crosstalk. This is mostly because when in ON-state the signal at the cross-output is penalised by the losses of the passive device while when in OFF-state the coupled signal into the cross-output is high giving as result a low ON-OFF contrast and high crosstalk.

The proposed device instead, approaches the problem differently. An injection of carriers in a III-V semiconductor medium with gain, generates a simultaneous variation of RI Δn and gain $\Delta g(\Delta\alpha)$ is achieved,. Thus, is shown in Figure2.14, when in ON-state the carriers injected into the device reduce the RI Δn allowing the coupling and the switch of the optical signal to the cross output. At the same time, in the active layer, a variation of gain $\Delta g(\Delta\alpha)$ is generated permitting to cover all the losses and possibly giving gain to the switched signal.

On the other hand when the device is in OFF-state no carriers are injected into the crosspoint structure, hence, the optical signal travels along the passive waveguide to the Bar-output. Like for passive crosspoint switches also the proposed device has a leaking of optical signal in the cross output but in this case, because the device is not biased, the active region has an high absorption reducing the crosstalk at very low values. Such effect permits a very low crosstalk and a very high extinction ratio to be achieved.

2.5. Conclusion

The current status of optical crosspoint switches has been investigated. This included analysis of the materials, architectures and physics principles involved. The study of the main crosspoint switches present in literature and in commerce has confirmed that the technology is not yet ready to make a device deployable in packet routing networks. Finally a novel OXS based on a vertical coupler architecture is introduced, which enables very ambitious targets to be achieved, such as:

- *Compactness*: Size only limited by fibre diameter.
- *Speed*: Fast enough to realise packets switching.
- *Low Crosstalk*: thanks to the double variation of RI Δn and gain $\Delta g(\Delta\alpha)$.
- *Spatially Scaleable*: limited just by the losses of the passive waveguide.
- *Low Power Consumption*: just one switch per path.
- *Easy to Fabricate*: only two RIE etching process and no regrowth involved.

2.6. References

[1] M. Owen, "Monolithic Integration of Optical Space Switches", 1998, PhD Thesis University of Bristol

[2] R.A. Spankle, "Architectures for Large Non-Blocking Optical Space Switches", IEEE Journal of Quantum Electronics, Vol. 22, 1986, pp.964-968.

[3] R.A. Spankle, "Architectures for Guided-Wave Optical Space Switching Systems", IEEE Communications Magazines, Vol. 25, No. 5, 1987, pp.42-48.

[4] D. Sadot, and I. Elhanany, "Optical Switching Speed Requirements for Terabit/Second Packet Over WDM Networks", IEEE Photonics Technology Letters, Vol. 12, No. 4, 2000, pp. 440-442.

[5] M. Renaud, M. Bachmann, and M. Erman, "Semiconductor Optical Space Switches" IEEE Journal of Selected Topics in Quantum Electronics, Vol. 2, No. 2, 1996, pp. 277-288

[6] L.R. Friedman, R.A. Soref, J.B. Khurgin, "Linear and quadratic electrooptic effects in symmetric and asymmetric quantum-well structures", IEEE Journal of Quantum Electronics, Vol. 31, No. 2, 1995, pp. 219-227.

[7] T. Aizawa, K.G. Ravikumar, S Suzaki, T. Watanabe, R. Yamauchi, "Polarization-independent quantum-confined Stark effect in an InGaAs/InP tensile-strained quantum well", IEEE Journal of Quantum Electronics, Vol. 30,No. 2, 1994, pp. 585-592.

[8] H.P. Chan, S.Y. Cheng, and P.S. Chung, "Low Loss Wide-Angle Symmetric Y-Branch Waveguide", Electronics Letters, Vol. 32, No. 7, 1996, pp. 652-654.

[9] H.-B. Lin, R-S Cheng, and W.-S. Wang, "Wide-Angle Low-Loss Single-Mode Symmetric Y-Junction", IEEE Photonics Technology Letters, Vol. 6, No. 7, 1994, pp. 825-827.

[10] M. Rangaraj, M. Minakata, S. Kawakami, "Low Loss Integrated Optical Y-Branch", Journal of Lightwave Technology, Vol. 7, No. 5, 1989, pp.753-758.

[11] D.R. Rowland, "Analysis of optical directional couplers composed of asymmetrically curved waveguides", IEE Proceedings Optoelectronics, Vol. 142, No. 6, 1995, pp. 305-312

[12] R.J. Deri, F.G. Pattersbon, and S.P. Dijaili, "Birefringence Compensation for Polarization-Indipendent Directional Coupler Wavelength Filters", IEEE Photonics Technology Letters, Vol. 7, No.4, 1995, pp.376-378.

[13] P.D. Trinh, S. Yegnanarayanan, B. Jalali, "Integrated optical directional couplers in silicon-on-insulator", Electronics Letters, Vol. 31, No. 24, 1995, pp 2097-2098.

[14] C. Dragone, "Efficient NxN Star Couplers Using Fourier Optics", Journal of Lightwave Technology, Vol. 7, No. 3, 1989, pp. 479-489.

[15] M. Zirngibil, C. Dragone, C.H. Joyner, M. Kuznetsov, and U. Koren, "Efficient 1x16 Optical Power Splitter Based on InP", Electronics Letters, Vol. 28, No.13, 1992, pp1212 - 1213.

[16] K. Suzuki, F. Koyama, A. Matsutani, J. Kato, T. Mukaihara, and K.Iga, "Miniature Semiconductor Optical Power Splitters with Submicrometre Wide Aperture", Electronics Letters, Vol. 32, No. 7, 1996, pp. 654 – 655.

[17] L.B. Soldano, and E.C.M. Pennings, "Optical Multi-Mode Interference Devices Based on Self-Imaging: Principles and Applications", Journal of Lightwave Technology, Vol. 13, No. 4, 1995, pp. 615-627.

[18] L.H. Spiekman Y.S. Oei, E.G. Metaal, F.H. Groen, I. Moerman, and M.K. Smit, "Extremely Small Multimode Interference Couplers and Ultrashort Bends on InP by Deep Etching", IEEE Photonics Technology Letters, Vol. 6, No. 8, 1994, pp. 1008-1010.

[19] P.A. Besse, M. Bachmann, H. Melchior, L.B. Soldano, and M.K. Smit, "Optical Bandwitdth and Fabrication Tolerances of Multimode Interference Couplers", Journal of Lightwave Technology, Vol. 12, No. 6, 1994, pp.1004-1009.

[20] L.A. Coldrane, S.W. Corzine, "Diode Lasers and Photonic Integrated Circuits", John Wiley & Sons, 1995.

[21] W.-P. Huang, "Coupled-Mode Theory for Optical Waveguides: an Overview", Journal of Optical Society of America / A, Vol.11, No.3, 1994, pp.963-983.

[22] H. Takeuchi, Y. Hasumi, S. Kondo, and Y. Noguchi, "4x4 Directional Coupler Switch Matrix with an InGaAlAs/InAlAs Multiquantum Well Structure", Electronics Letters, Vol. 29, No. 6, 1993, pp.523-524.

[23] K. Kawano, M. Kohtoku, N. Yoshimoto, S. Sekine and Y. Noguchi, "2x2 InGaAlAs/InAlAs multiquantum well (MQW) directional coupler waveguide switch modules integrated with spotsize convertors", Electronics Letters, Vol. 30, No. 4, 1994, pp.353-355

[24] T. Ito, M. Kohtoku, N. Yoshimoto, K. Kawano, S. Sekine, M. Yanagibashi and S. Kondo, "Dynamic Response of 2x2 InGaAlAs/InAlAs Multiquantum Well (MQW) directional Coupler waveguide switch Modules", Electronics Letters, Vol. 30, No. 11, 1994, pp.1936-1937

[25] T. Aizawa, Y. Nagasawa, K.G. Ravikumar, and T. Watanabe, "Polarization Independent Switching Operation in Directional Coupler Using Tensile-Strained Multi-Quantum Well", IEEE Photonics Technology Letters, Vol. 7, No. 1, 1995, pp.47-49.

[26] Y. Shibata, S. Oku, Y. Kondo, T. Tamamura, and M. Naganuma, "Semiconductor Monolithic Wavelength selective Router Using a Grating Switch Integrated with a Directional Coupler", Journal of Ligthwave Technology, Vol. 14, No. 6, 1996, pp. 1027-1032.

[27] M. Kohtoku, K. Kawano, S. Sekine, H. Takeuchi, N. Yoshimoto, M. Wada, T. Ito, M. Yanagibashi, S. Kondo, Y. Noguchi, and M. Naganuma, "High-Speed InGaAlAs-InAlAs MQW Directional Coupler Waveguide Switch Modules Integrated with a Spotsize Converter Having a Lateral Taper, Thin-Film Core and Ridge", Journal of Ligthwave Technology, Vol. 18, No. 3, 2000, pp. 360-368.

[28] N.S. Lagali, M.R. Paiam, R.I. MacDonald, K. Worhoff, A. Driessen, "Analysis of generalized Mach-Zehnder interferometers for variable-ratio power splitting and optimized switching", Journal of Lightwave Technology, Vol. 17, No. 12, 1999, pp. 2542-2550.

[29] C. Kim, D.A. May-Arrioja, P. LiKamWa, P. Newman, J. Pamulapati, "Ultrafast all-optical multiple quantum well integrated optic switch", Electronics Letters, Vol. 36, No. 23, 2000, pp.1929-1930.

[30] S. Diez, C. Schubert, R. Ludwig, H.-J. Ehrke, U. Feiste, C. Schmidt, H.G. Weber, "160 Gbit/s all-optical demultiplexer using hybrid gain-transparent SOA Mach-Zehnder interferometer", Electronics Letters, Vol. 36, No. 17, 2000, pp.1484-1486

[31] R. Krähenbuhl, R. Kyburz, W. Vogt, M. Bachmann, T. Brenner, E. Gini, and H. Melchior, "Low-Loss Polarization-Insensitive InP-InGaAsP Optical Space Switches for Fiber Optical Communication", IEEE Photonics Technology Letters, Vol. 8, No. 5, 1996, pp.632-634.

[32] N. Yoshimoto, Y. Shibata, S. Oku, S. Kondo, and Y. Noguchi, "Design and Demonstration of Polarization-Insensitive Mach-Zehnder Switch Using a Lattice-Matched InGaAlAs/InAlAs MQW and Deep-Etched High-Mesa Waveguide Structure", Journal of Ligthwave Technology, Vol. 17, No. 9, 1999, pp. 1662-1669

[33] N. Yoshimoto, Y. Shibata, S. Oku, S. Kondo, Y. Noguchi, K Wakita and M. Nagamuna, "Fully Polarisation Independent Mach-Zehnder Optical Switch Using Lattice Matched InGaAlAs/InAlAs MQW and High-Mesa Waveguide Structure", Electronics Letters, Vol. 32, No. 15, 1996, pp.1368, 1369.

[34] Y. Silberberg, P. Perlmutter, and J.E. Baran, "Digital Optical Switch", Int. Conf. Optical Fiber Communication, 1998

[35] J.F. Vichant, M. Renaud, A. Goutelle, M. Erman, P. Svensson, and L. Thylen, "Low Driving Voltage or Current Digital Optical Switch on InP for Multiwavelength System Applications" Electronics Letters, Vol. 28, No. 12, 1992, pp. 1135-1136.

[36] J.A. Cavailles, M. Renaud, J.F. Vinchant, M. Erman, P. Svensson, L. Thylen, "First Digital Optical Switch Based on In/InGaAsP Double Heterostructure Waveguides", Electronics Letters, Vol. 29, No. 4, 1993, pp. 699-700

[37] J.F. Vinchant, M. Renaud, M. Erman, J.L. Peyre, P. Jarry, P. Pagnod-Rossiaux, "InP Digital Optical Switch: Key Element for Guidade-Wave Photonic Switching", IEE Procedings-J, Vol. 140, No. 5, 1995, pp. 301 307.

[38] M. Nisa Khan, "High-Speed InP-Based Digital Optical Switches", IEEE LEOS 1995, Vol. 1, 1995, pp.114-115.

[39] A. Sneh, J.E. Zucker, B.I. Miller, and L.W. Stulz, "Polarization-Insensitive InP-Based MQW Digital Optical Switch", Photonics Technology Letters, Vol. 9, No. 12, 1997, pp. 1589-1591.

[40] T.A. Ramadan, R. Scarmozzino, and R.M. Osgood, "A Novel 1x4 Coupler-Multiplexer Permutation Switch for WDM Applications", Journal of Ligthwave Technology, Vol. 18, No. 4, 2000, pp. 579-588.

[41] M. Gustavsson, B. Lagerstrom, L. Thylen, M. Janson, L. Lundgren, A.-C. Morner, M. Rask, and B. Stoltz, "Monolithically integrated 4x4 InGaAsP/InP Laser Amplifier Gate Switch Arrays", Electronics Letters, Vol. 28, No. 24, 1992, pp.2223-2225.

[42] R. van Roijen, J.M.M. van der Heijden, L.F. Tiemeijer, P.J.A. Thijs, T. van Dongen, J.J.M. Binsma, and B.H. Verbeek, "Over 15dB Gain from monolithically Integrated Optical Switch, with an Amplifier", IEEE Photonics Technology Letters, Vol.5, No.5, 1993, pp.529-531.

[43] K. Komatsu, "Hybrid Optical Matrix Gate Switches for Photonic Switching", ECOC 97, 22-25 September 1997, Vol. 2, 1997, pp.85.

[44] N. Yoshimoto, K. Magari, T.Ito, Y. Kawagichi, O. Mitomi, Y. Tohmori, "Polarisation-Insensitive Semiconductor Optical Amplifier Gate Switch with Butt-Jointed Spot-Size Convertors - Its Uniformity", IEE Proceedings – Optoelectronics, Vol. 146, No. 1, 1999, pp.71-76.

[45] S. Kitamura, H. Hatakeyama, K. Hamamoto, T. Sasaki, K. Komatsu, and M. Yamaguchi, "Spot-Size Converter Integrated Semiconductor Optical Amplifiers for Optical Gate Applications", IEEE Photonics Technology Letters, Vol. 35, No. 7, 1999, pp.1067-1074.

[46] A. Mircea, A. Ougazzaden, N. Bouadma, F. Devaux, J.-Y. Marzin, A. Ramdane, J. Barrau, A. Ponchet, "Strained multi-quantum well heterostructures for lasers, modulators and integrated optical devices at 1.3-1.55 um", Materials Science & Engineering B: Solid-State Materials for Advanced Technology, Vol. B28, No. 1-3, 1994, pp. 279-283.

[47] B.C. Qiu, Y.H. Qian, O.P. Kowalsky, A.C. Bryce, J.S. Aitchison, R.M. De La Rue, and J.H. Marsh, M.Owen, I.H. White and R.V.Penty, A. Franzen, D.K. Hunter and I. Andovonic, "Low Cost Fabrication of 2x2 Crosspoint Switches", ECOC 1999 September 26-30, 1999, Nice, France.

[48] Y.S. Kuzminov, "Lithium Niobate Crystals", Cambridge International Science Publishing

[49] H. Nishinoto, M. Iwasaki, S. Suzuki, and M. Kondo, "Polarization Independent $LiNbO_3$ 8x8 Matrix Switch", IEEE Photonics Technology Letters, Vol. 2, No. 9, 1990, pp.634-636

[50] P. Granestrand, B. Lagerstrom, P. Svensson, H. Olofsson, J.-E. Falk, and B. Stoltz, "Pigtailed Tree-Structured 8x8 $LiNbO_3$ Switch Matrix with 112 Digital Optical Switches", IEEE Photonics Technology Letters, Vol. 6, No. 1, 1994, pp.71-73

[51] E.J. Murphy, C.T. Kemmerer, D.T. Moser, M.R. Serbin, J.E. Watson, and P.L. Stoddard, "Uniform 8x8 Lithium Niobate Switch Arrays", Journal of Lightwave Technology, Vol. 13, No. 5, 1995, pp.967-970

[52] Y. Nakabayashi, M. Kitamura, and T. Sawano, "DC-Drift Free Polarization Independent Ti:$LiNbO_3$ 8x8 Optical Matrix Switch", ECOC 96, Oslo, 1996, ThD 2.4.

[53] E.J. Murphy, T.O. Murphy, R.W. Irvin, R. Grencavich, G.W. Davis, and G.W. Richards, "Enhanced Performance Switch Arrays for Optical Switching Networks", ECIO 97, Stockholm, 1997, EFD5.

[54] L.Y. Lin, E.L. Goldstein, R.W. Tkach, "Free-Space Micromachined Optical Switches with Submillisecond Switching Time for Large-Scale Optical Crossconnects", IEEE Photonics Technology Letters, Vol. 10, No. 4, 1998, pp.525-527.

[55] V. Aksyuk, B. Barber, C.R. Giles, R. Ruel, L. Stulz, and D. Bishops, "Low Insertion Loss Packaged and Fibre Connectorised MEMS Reflective Optical Switch", Electronics Letters, Vol. 34, No. 14, 1998, pp.1413-1414.

[56] R.T. Chen, H. Nguyen, M.C. Wu, "A High-Speed Low Voltage Stress-Induced Micromachined 2x2 Optical Switch" IEEE Photonics Technology Letters, Vol. 11, No. 11, 1999, pp.1396-1398.

[57] J.E. Ford, V.A. Aksyuk, D.J. Bishop, and J.A. Walker, "Wavelength Add-Drop Switching Using Tilting Micromirrors" Journal of Lightwave Technology, Vol. 17, No. 5, 1999, pp.904-911.

[58] E.L. Goldstein, L.Y. Lin, and R.W. Tkach, "Optical-MEMS-Based Tail-End Switching for restoration of Line-Rate Services" ECOC'99, 26-30 September 1999, Nice France, pp. I62-I63.

[59] D.W. Van Krevelen, "Properties of Polymers", Elsevier, Amsterdam, 1990

[60] N.Keil, H.H. Yao, and C. Zawadzki, "Polymer Waveguide Optical Switch with <-40dB Polarisation Indipendent Crosstalk", Electronics Letters, Vol. 32, No. 7, 1996, pp.655-657.

[61] N.Keil, H.H. Yao, and C. Zawadzki, "Digital Optical Switch Realised by Low Cost Polymer Waveguide Technology", Electronics Letters, Vol. 32, No. 16, 1996, pp.1470-1471.

[62] R. Moosburger, G. Fischbeck, C. Kostrzewa, and K. Peterman, "Digital Optical Switch Based on 'Oversized' Polymer RIB Waveguide", Electronics Letters, Vol. 32, No. 6, 1996, pp.544-545.

[63] R. Moosburger, and K. Peterman, "4x4 Digital Optical Matrix Switch Using Polymeric Oversized RIB Waveguide", IEEE Photonics Technology Letters, Vol. 10, No. 5, 1998, pp.684-686.

[64] Q. Lai, W. Hunziker, and H. Melchior, "Low-Power Compact 2x2 Thermooptic Silica-on-Silicon Waveguide Switch with Fast Response", IEEE Photonics Technology Letters, Vol. 10, No. 5, 1998, pp.681-683.

[65] M.-C. Oh, H.-J. Lee, M.-H Lee, J.-H. Ahn, and S.G. Han, "Asymmetric X-Junction Thermooptic Switches Base on Fluorinated Polymer Waveguides", IEEE Photonics Technology Letters, Vol. 10, No. 6, 1998, pp.813-815.

[66] T. Goh, M. Yasu, K. Hattori, A. Himeno, M. Okuno, and Y. Ohmori, "Low-Loss and High-Extinction-Ratio Silica-Based Strictly Nonblocking 16x16 Thermooptic Matrix Switch", IEEE Photonics Technology Letters, Vol. 10, No. 6, 1998, pp.810-812

[67] T. Goh, A. Himeno, M. Okuno, H. Takahashi and K. Hattori, "High-Extinction-Ratio and Low-Loss Silica-Based 8x8 Strictly Nonblocking Thermooptic Matrix Switch", Journal of Lightwave Technology, Vol. 17, No. 7, 1999, pp.1192-1198.

[68] N. Keil, C. Weinert, W. Wirges, H.H. Yao, S. Yilmaz, C. Zawadzki, J. Schneider, J. Bauer, M. Bauer, K. Losch, K. Satzke, W. Wischmann, and J.V. Wirth, "Thermo-Optic Vertical Coupler Switches Using Hybrid Polymer/Silica Integration Technology" Electronics Letters, Vol. 36, No. 5, 2000, pp.430-431.

[69] N. Keil, H.H. Yao, C. Zawadzki, K. Losch, K. Satzke, W. Wischmann, J.V. Wirth, J. Schneider, J. Bauer, and M. Bauer, "Hybrid Polymer/Silica Vertical Coupler Switches with <-32dB Polarisation-Independent Crosstalk" Electronics Letters, Vol. 37, No. 2, 2001, pp.89-90.

[70] L.R. Dalton, W.H. Steier, B.H. Robinson, C. Zhang, A. Ren, S. Garner, A. Chen, T. Londergan, L. Irwin, B. Carlson, L. Fifiled, G. Phelan, C. Kincaid, J. Amend, and A. Jen, "From Molecules to opto-chips: Organic Electro-Optic Materials", Journal of Materials Chemestry, No.9, 1999, pp. 1905-1920.

[71] R.M. de Ridder, A. Driessen, E. Rikkers, P.V. Lambeck, M.B.J. Diemmer, "Design and Fabrication of Electro-Optic Polymer Modulators and Switches", Optical Materials, Vol.12, 1999, pp. 205-214.

[72] W.-Y. Hwang. J.-J. Kim, and T. Zyung, "Postphotobleaching Method for the Control of Coupling Constant in an Electro-Optic Polymer Directional Coupler Switch", Applied Physics Letters, Vol. 67, No.6, 1995, 763-765.

[73] W.-Y. Hwang, M.-C. Oh, H.-M. Lee, H. Park, and J.-J. Kim, "Polymeric 2x2 Electrooptic Switch Consisting of a Asymmetric Y Junctions and Mach-Zehnder Interferometer", IEEE Photonics Technology Letters, Vol.9, No.6, 1997, pp.761-763.

[74] S.-S. Lee, and S.-Y. Shin, "Polarisation-Insensitive Digital Optical Switch Using an Electro-Optic Polymer RIB Waveguide", Electronics Letters, Vol.33, No.4, 1997, pp.314-316.

[75] S.-S. Lee, and S.-Y. Shin, "Polymeric Digital Optical Switch Incorporating Linear Branch with Modified Coupling Region", Electronics Letters, Vol.35, No.15, 1999, pp.1245-1246.

[76] http://www.nel-dwdm.com/product/switch/

[77] http://www.nel-dwdm.com/product/switch/swp8m.html

[78] http://www.agilent.com/cm/photonicswitch/white_papers/wp_prelim.shtml

[79] http://www.agilent.com/cm/photonicswitch/white_papers/wp_prelim_figures.shtml?02

[80] http://www.agilent.com/cm/photonicswitch/32x32_ovrvw.shtml

[81] http://www.lucent.com/press/0201/010226.mea.html

[82] http://www.bell-labs.com/org/physicalsciences/projects/mems/mems3.html

[83] M. Cada, R.C. Gauthier, B.E. Paton, and J. Chrostowski, "Nonlinear Guided Waves Coupled Nonlinearly in a Planar GaAs/GaAlAs Multiple Quantum Well Structure", Applied Physics Letters, Vol.49, No.13, 1986, pp. 755-777.

[84] J.P. Weber, "Optimization of the carrier-induced effective index change in InGaAsP waveguides – Applications to Tunable Bragg Filters", Journal of Quantum Electronics Vol.30, 1994, pp. 1801-1816.

[85] L.F. Tiemejier, P.J.A. Thijs, T. van Dongen, J.J.M. Binsma, E.J. Jansen, S. Walczyk, G.N. van Hoven, and E.C.M. Pennings, "High-Gain, High-Power 1550-nm Polarization Independent MQW optical amplifier", IEEE Photonics Technology Letters, Vol.8, No.9, 1996, pp.1142-1144.

[86] T. Ito, N. Yoshimoto, K. Magari, and H. Sugiura, "Wide-Band Polarization-Independent Tensile-Strained InGaAs MQW-SOA Gate", IEEE Photonics Technology Letters, Vol.10, No.5, 1998, pp.657-659.

[87] D.W. Langer, and Marek Chmielowski, "Quantum-Well Waveguide Coupler", Superlattices and Microstructures, Vol.6, No.1, 1989, pp.17-22

[88] L.C.So, and C.A. Lee, "A New Integrable Optical Modulator-Switch Optimised for Speed and Power Consumption", Journal of Applied Physics, Vol.66, No.5, 1989, pp.2200-2204.

[89] J.A. Cavailles, M. Erman, and K. Woodbridge, "Experimental Study of Switching in a p-i(MQW)-n Vertical Coupler", IEEE Photonics Technology Letters, Vol.1, No.11, 1989, pp.373-375.

[90] M. Kohtoku, S. Baba, S. Arai, and Y. Suematsu, "Switching Operation in a GaInAs-InP MQW Integrated-Twin-Guide (ITG) Optical Switch", IEEE Photonics Technology Letters, Vol.3, No.3, 1991, pp.225-226.

[91] T. Yamaguchi, K. Tada, and T. Ishikawa, "Vertical Multiple-Quantum-Well Directional-Coupler Switch with Low Switching Voltage", IEEE Photonics Technology Letters, Vol.4, No.7, 1992, pp.723-725.

[92] F. Dollinger, M. v. Börcke, G. Bohm, G. Tränkle, and G Weimann, "Ultrashort Low-Loss Optical Multiquantumwell GaAs/GaAlAs Verical Directional Coupler Switch", Electronics Letters, Vol.32, No.16, 1996, pp.1509-1510.

[93] S. Baba, K. Shimomura, and S. Arai, "A Novel Integrated-Twin-Guide (ITG) Optical Swith with a Built-in TIR Region", IEEE Photonics Technology Letters, Vol.4, No.5, 1992, pp.486-488.

[94] R. Maciejko, A. Champagne, B. Reid, and H. Mani, "Analysis of an InGaAsP/InP Twin-Overlayed-Waveguide Switch", IEEE Journal of Quantum Electronics, Vol. 30, No.9, 1994, pp.2106-2113.

[95] D.A.B. Miller, D.S. Chemla, T.C. Damen, A.C. Gossard, W. Wiegmann, T.H. Eood, and C.A. Burrus, "Electric Field Dependence of Optical Absorption near the Band Gap in Quantum Well Structures", Physical Review B, Vol.32, No.2, 1985, pp. 1043-1060.

[96] J.A. Cavaillès, M. Erman, and K. Woodbridge, "Experimental Study of Switching in a p-i(MQW)-n Vertical Coupler", IEEE Photonics Technology Letters, Vol.1, No.11, 1989, pp. 373-375.

[97] I.H. White, J.J.S. Watts, J.E. Carroll, C.J. Armistead, D.J. Moule, J.A. Champelovier, "InGaAsP 400x200um Active Crosspoint Switch Operating at 1.5um Using Novel Reflective Y-Branch Coupler Components", Electronics Letters, Vol.26, No.10, 1990, pp.617-618.

[98] G. Sherlock, J.D. Burton, P.J. Fiddyment, P.C. Sully, A.E. Kelly, M.J. Robertson, "Integrated 2x2 Optical Switch with Gain", Electronics Letters, Vol. 30, No.2, pp. 137-138.

[99] M. Owen, M. Asghari, I.H. White, K.R. Poguntke, M.J. Robertson, "Theoretical design of a novel N×N two-dimensional integrated optical crosspoint switch architecture", J. of Lightwave Technology, Vol. 16, No. 3, 1998, pp. 380-387.

Chapter 3

Design of a highly compact, lossless vertical coupler optical space switch

This chapter deals with the theoretic model used to design the vertical coupler switch presented in the previous chapter 2.

It first does a theoretical analysis of each single layer of the VC followed by the coupling model. It investigates also the characteristics for the Total Internal Reflection (TIR) mirror and the waveguide crossing loss and crosstalk. The simulation of the OXS as a whole closes the chapter.

Glossary of the abbreviations

(TIR) Total Internal Reflection

(AVC) Active Vertical Coupler

(LC) Lower Cladding

(SL) Spacing Layer

(PLW) Passive Lower Waveguide

(UC) Upper Cladding

(CL) Cap Layer

(VC) Vertical Coupler

3.1. Motivation

Future optical packet routing networks will require OXS with very short switching times, low crosstalk, low power consumption, scalability compactness and other similar characteristics that make it suitable for the purpose. The challenge is to design a device based on the vertical coupler presented in the previous chapter and the design is treated in the following sections of this chapter.

It is hoped that using an active VC structure most of these targets can be achieved, in particular high compactness, reconfiguration time in the order of nanoseconds, low crosstalk and high ON-OFF contrast.

3.2. Active Vertical Coupler (AVC)

This section gives a theoretical description of the wafer structure. In particular describes each single layer and the their functions inside the vertical coupler.

The AVC structure can be realised by MOVPE growth of 6 different main layers on a (100) InP substrate for effect carrier injection. Different doping level is adopted for each layer using Si as "*n*" and Zn as "*p*" dopant to make a p-i-n structure.

The first layer, grown on the n^+-InP substrate is "*n*" doped InP. It works as *Lower Cladding (LC)* permitting the device, together with the *Spacing Layer (SL),* to confine the light into the InGaAsP *Passive Lower Waveguide (PLW)* between them.

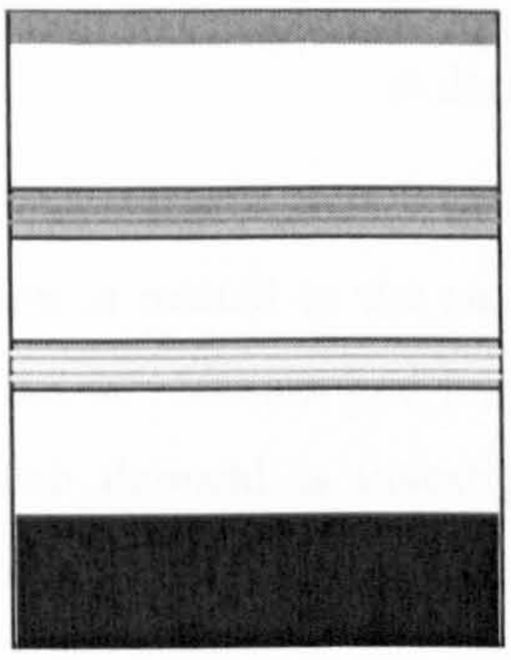

Figure3.1 Wafer layer structure

The PLW is lightly *n*-doped and is designed to be low absorption at λ=1500 nm and longer. It is made of MQW or bulk materials and is used to provide the input waveguide, the output waveguide and one arm of the coupler for the OXS.

On top of it the *SL* assumes different functions with the *OXS* state. In "OFF state"it is the upper cladding for the *PLW,* in "ON state" it becomes a spacer between the *PLW* and the *AUW*. Its thickness is very important to the coupling analysis because large thickness could reduce the coupling factor, resulting in too long coupling length. Small thickness instead could induce high loss for light propagating in the

PLW. In the investigation, the thickness adopted should give the best coupling factor – loss ratio for the layers adopted. Such a thickness value is fairly small compared with the distance between the waveguides achievable in horizontal couplers. In fact fabrication technology limitation often do not allow the two waveguides to be too close in horizontal structures.

The *AUW* follows the spacing layer on the stack composition. It is undoped InGaAsP layer active at 1550 nm made by a MQW or bulk material. The *AUW* layer forms a p-i-n structure with surrounding layers and is responsible for the switching function.

InP *Upper Cladding (UC)* and InGaAs *Cap Layer (CL)* stack on top of the *AUW* and use Zn as p and p^+ dopant.

3.2.1. Passive Lower Waveguide

As it has been shown the function of this layer is to carry the optical signal, which can be switched to the cross output or guided to the bar output, as shown in Figure3.2.

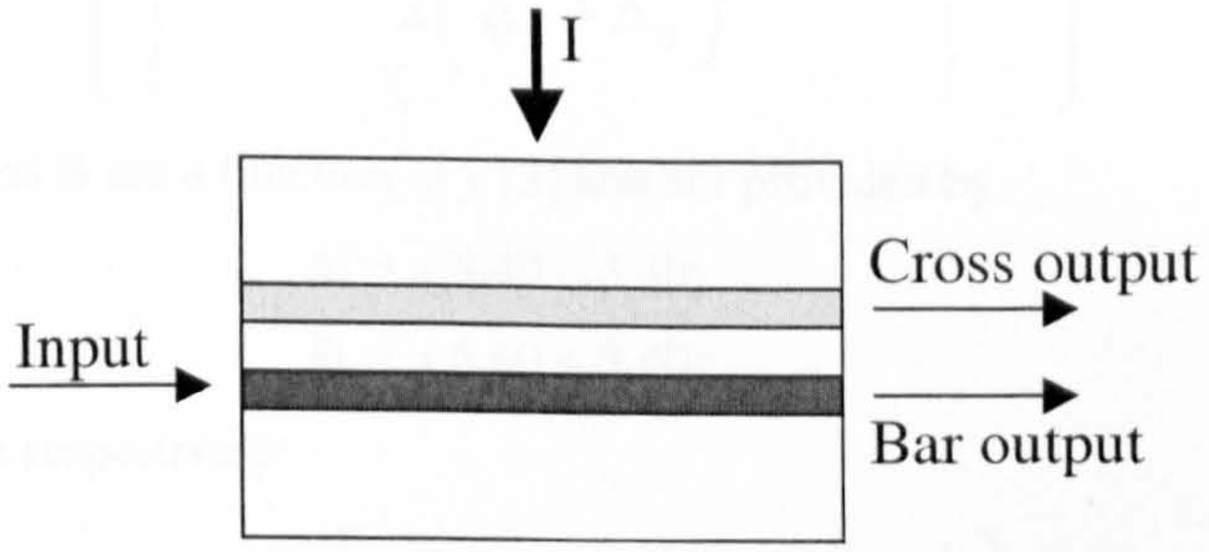

Figure3.2 Active Vertical Coupler: in light grey the Upper Active Waveguide
in dark grey the Bottom Passive Waveguide

Thus, it is very important that such a layer have a low absorption at the working wavelength. Naturally, the *PLW* absorption is related to the structure design and it is kept low by adopting a *PLW* layer that becomes transparent at 1500 nm and longer wavelength. The possibility to get a *PLW* alloy compound able to satisfy such demand is investigated below. An analysis of the refractive index and of the confinement factor of such waveguide is also studied.

3.2.1.1. The In1-xGaxAsyP1-y alloy compound

The *PLW* absorption on the signal path is related to the structure design and it is kept low by adopting a layer that becomes transparent at 1500 nm and longer. Thus it is inportant to find an $In_{1-x}Ga_xAs_yP_{1-y}$ alloy compound able to satisfy such demand.

The calculation of the x and y fractions starts setting the wavelength bandgap which permit to achieve the material energy gap from the relation

$$E_g(\lambda) = \frac{hc}{\lambda e} \tag{3.1}$$

E_g can be expressed by a quadratic function as a function of the y value [1]. In particular the Pearsall theoretical relation (3.2), shows an excellent agreement with the experimental data [2] and gives y

$$E_g(y) = 0.149y^2 - 0.775y + 1.35 \tag{3.2}$$

Furthermore, the $In_{1-x}Ga_xAs_yP_{1-y}$ to lattice matched InP requires the x value:

$$x = \frac{0.1896y}{0.4176 - 0.0125y} \quad (0 \le y \le 1.0) \tag{3.3}$$

3.2.1.2. Refractive Index of the material

Having obtained x and y values, it is useful to calculate the refractive index $n(\lambda)$ of the material, which can be related to the bandgap energy E_g and, in the transparency region below bandgap it can be expressed as [1]

$$n(\lambda) = \left\{ A\left[f(\chi_0) + \frac{1}{2}\left(\frac{E_g}{E_g + \Delta_0} \right)^{\frac{3}{2}} f(\chi_{so}) \right] + B \right\}^{\frac{1}{2}} \tag{3.4}$$

The numeric values A and B are a function of y [3] and are provided by

$$A(y) = 8.40 - 3.40y \tag{3.5}$$

$$B(y) = 6.60 + 3.40y \tag{3.6}$$

$f(\chi_0)$, $f(\chi_{so})$, χ_0, χ_{so} are respectively:

$$f(\chi_0) = \chi_0^{-2}\left[2 - (1+\chi_0)^{\frac{1}{2}} - (1+\chi_0)^{\frac{1}{2}} \right] \tag{3.7}$$

$$f(\chi_{so}) = \chi_{so}^{-2}\left[2 - (1+\chi_{so})^{\frac{1}{2}} - (1+\chi_{so})^{\frac{1}{2}} \right] \tag{3.8}$$

$$\chi_0 = \frac{\hbar\omega + i\Gamma}{E_g} \tag{3.9}$$

$$\chi_{so} = \frac{\hbar\omega + i\Gamma}{E_g + \Delta_0} \tag{3.10}$$

where Γ corresponds to the InP value: 0.36 eV [4] and $E_g + \Delta_0$ is defined [5] by the quadratic function:

$$E_g(y) + \Delta_0 = 0.092y^2 - 0.468y + 1.472 \tag{3.11}$$

The model presented can design the passive lower waveguide, which can be done with just one bulk layer or with MQWs.

3.2.1.3. Effective Refractive Index and Confinement Factor for the PLW structure

In order to find out the *PLW Effective Refractive Index* n_{eff} and the *Confinement Factor* Γ for the TE fundamental mode the vectorial waveguide solver "Fimmwave" is used. The solver permits to model 2 and 3 dimensional waveguide structures basing the calculation on the film mode matching method due to Subdo [6, 7].

3.2.2. the Active Upper Layer

The input optical signal, see Figure3.2, is switched to the cross output of the vertical coupler when current is injected into it. The *refractive index* of the active region is a function of the *carrier density N*, therefore of the *current density J*. As a result, by adjusting the current the refractive index can be matched to the respective value of the passive lower waveguide redirecting the signal to the cross output by the consequent strong optical coupling that happens.

Also in this case the calculation of the x and y fractions for the $In_{1-x}Ga_xAs_yP_{1-y}$ alloy compound of the *AUL* can be done following the (3.1), (3.2) and (3.3) with the condition that the layer becomes active at 1550 nm (i.e., with λg at ~1550nm).

Effective refractive index n_{eff} and confinement factor Γ for the TE fundamental mode in this case need to be calculated in both states: "OFF state" when the structure is not biased, N=0 and "ON state" structure is biased with N calculated as follow.

3.2.2.1. Carrier Density in an active region

The analysis starts from the rata equation for carrier density N

$$\frac{dN}{dt} = \frac{\eta_i I}{qV} - \frac{N}{\tau} - v_g g N_p \tag{3.12}$$

The spontaneous emission term $\frac{N}{\tau}$ can be described by the polynomial $AN + BN^2 + CN^3$. The term $v_g g N_p$ can be neglected assuming input signal below saturation level and finally applying stationary condition, $\frac{dN}{dt} = 0$, the carrier density can be calculated by solving the following equation

$$\frac{\eta_i J}{qh} - AN + BN^2 + CN^3 = 0 \tag{3.13}$$

where h is the layer thickness, q the electron charge, η_i the injection efficiency and A, B, C are constants defined as in [8]. (3.13) express the *carrier density* as a function of the *current density* and the maximum J value is assumed to be 10,000 A/cm^2. The parameter N found is consequently introduced into FIMMWAVE model that procures n_{eff} and Γ for the TE fundamental mode and for the particular structure given.

3.2.2.2. Gain and Differential Gain

The injection of carriers into an active region [9] increases the gain from an unpumped absorption level to the transparency point. where the gain is zero. With further carrier injection the gain continues to rise.

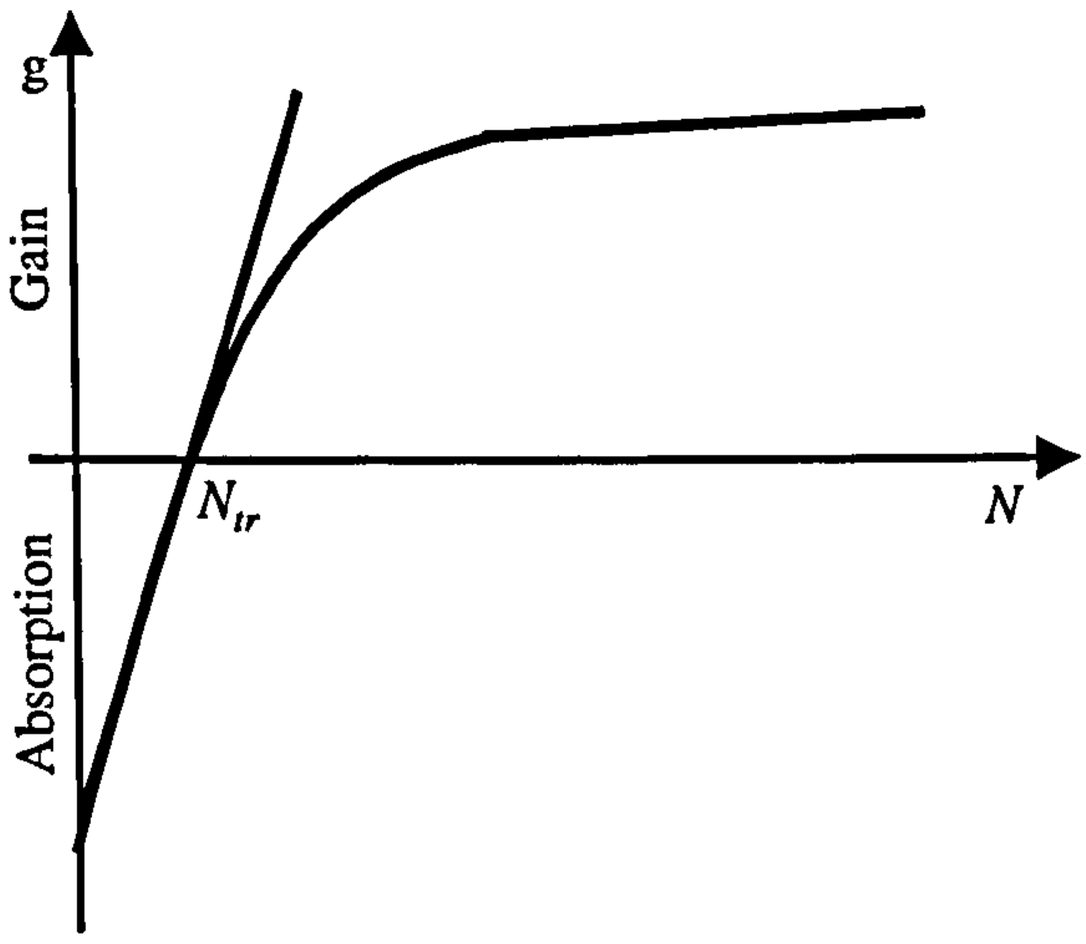

Figure 3.3 Gain vs. carrier density with (3.14) valid under limited range

The relationship described and shown in Figure3.3, can be approximated by the linear function

$$g \approx a(N - N_{tr}) \tag{3.14}$$

expressing the gain as a function of the injected carrier density near the N_{tr} values. N_{tr} is the *transparency carrier density*, a is the *differential gain dg/dN* which for quaternary InGaAsP materials, is in the range of $1.2 - 6\times10^{-16}$ cm^2, depending on the structure being bulk or MQW, and for N_{tr} within $0.9 - 1.5\times10^{18}$ cm^{-3} [9]. Fixing N_{tr} and with the *carrier density* values previously calculated, the *gain g* can be calculated as a function of the *differential gain dg/dN*. Finally fixing the *differential gain dg/dN* to an appropriate value the the *modal gain* $\langle g \rangle = \Gamma g$ is given, where Γ is the *confinement factor* of the structure.

3.2.3. 2D Coupling Analysis

Once the main parameters are calculated, characterising passive lower waveguide and the active upper waveguide of the Vertical Coupler (VC), the entire VC structure can be investigated.

The section is split into 2-dimentional and the 3-dimentional mode coupling analysis. The first finds the correct carrier density '*N*' value needed to match the refractive indices of the waveguides. The latter introduces the coupling length into the analysis extending the investigation to a 3D design. The correct VC length necessary to transfer the entire optical signal from the bottom to the top waveguide is decided as a result.

3.2.3.1. Coupling analysis between two single waveguides

A first approach to the directional coupler analysis can be based on the coupled equations for the modes of each single waveguide. A light wave launched in one of the waveguides can be coupled into the other when the waveguides modes have equal phase velocity or equal propagation constants β_1 and β_2.

The propagation constant can be expressed in terms of refractive index with the equation [8]:

$$\beta = [\mathrm{Re}(\beta) + i\,\mathrm{Im}(\beta)] = kn + i\frac{\alpha}{2} \tag{3.15}$$

The notation Re and Im stand for the real and imaginary parts, respectively while k is the free space propagation constant defined by:

$$k = \frac{\omega}{c} = \frac{2\pi}{\lambda} \tag{3.16}$$

n is the refractive index of the material and α represent the absorption coefficient.

With active material n can be expressed with the relation

$$n = n_u + \Delta n_p \tag{3.17}$$

where n_u is the refractive index of the unpumped material and Δn_p the amount which it changes in the presence of charge carriers.

The term α instead is tied to the characteristics of the active material and can be definite by the:

$$\alpha = -\Gamma g + \alpha_{\mathrm{int}} \tag{3.18}$$

with Γ *confinement factor* which is the part of the mode energy present in the active region and α_{int} representing the other internal losses.

Usually $\alpha << kn$ making $\mathrm{Im}(\beta)$ negligible reducing the (3.15) to

$$\beta = k(n_u + \Delta n_p) \tag{3.19}$$

Thus in order to have the best energy coupling between two waveguides, indicated as 1 and 2, it is necessary that:

$$\beta_1 = \beta_2 \rightarrow n_1 = n_2 \tag{3.20}$$

The (3.19) permits to use the effective refractive index, n_{eff}, for the two waveguides *PLW* and *AUW*, calculated in the previous section. Thanks to the active nature of the *AUW* that makes n_{eff_AUW} a function of the *carrier density N*, the (3.20) can be achieved. In fact, increasing N the n_{eff_AUW} is reduced and equalised to the n_{eff_PLW}.

It is clear that the bottom layer needs to be designed in order to have the n_{eff_PLW} in the range of the n_{eff_AUW} variation and in particular depending from the position of n_{eff_PLW}, the coupler assume different characteristics as shown below.

- $\mathbf{n}_{eff\_PLW} \leq \mathbf{n}_{eff\_AUW\_OFF\_state}$

  the two waveguides are almost matched when the coupler is in "OFF state", N=0, hence the *AUW* is highly absorptive making the device highly lossy. When in "ON state" the two waveguides are completely mismatched and no coupling can be achieved.

- $\mathbf{n}_{eff\_AUW\_OFF\_state} >> \mathbf{n}_{eff\_PLW} > \mathbf{n}_{eff\_AUW\_ON\_state}$

  the coupling occur when *N* is adjusted to a best coupling value, which is lower than maximum values achievable at the designed current density. The vertical coupler will lack gain and if *N* is further increased, the coupling will pass the optimised point.

  In this situation, in "OFF state" high quantity of light power can couple up into the AUW and be absorbed, increasing the loss.

- $\mathbf{n}_{eff\_PLW} \approx \mathbf{n}_{eff\_AUW\_ON\_state}$

  when in "ON state", $N=N_{max}$, the coupling is maximised and the highest level of gain is reached. The two waveguides are matched and all the light power is transferred from one waveguide to the other. On the other hand when the coupler is in "OFF state", *N=0*, the refractive indexes are different, the (3.20) is not verified anymore and no light power, or really little, is coupled from one waveguide to the other. Under this condition the best ON-OFF contrast and the best crosstalk is achieved.

Effective refractive index	OFF State		ON State	
	Coupling	Loss	Coupling	Loss
$n_{eff\ PLW} \leq n_{eff\ AUW\ OFF\ state}$	Yes	High	No	-
$n_{eff\ AUW\ OFF\ state} >> n_{eff\ PLW} > n_{eff\ AUW\ ON\ state}$	Partial	High	Yes	High
$n_{eff\ PLW} \approx n_{eff\ AUW\ ON\ state}$	No	Very Low	Yes	No

Table3.1 Switching and Loss as a function of the *neff* of the PLW

Table3.1 summarises the theoretical characteristics of the optical vertical coupler at different n_{eff} values of the *PLW*.

Therefore, it is very important to design a structure that

1. allows maximum Δ_{neff} in AUW at a given current
2. has PLW properly designed to fully exploit this Δ_{neff}

3.2.3.2. Coupling analysis of the entire structure

The previous section has given an approximate solution to the problem of the directional coupler which, has been expressed in terms of individual waveguides. However, from the theory of the directional coupler formulated by Marcuse [10], when two waveguides are inserted in a compound structure the resulting directional coupler cannot be treated as two different waveguides. It has to be expressed in terms of the modes of the compound structure which can be expressed in terms of even and odd super modes characterised by slightly different propagation constant β_o β_e, and shown in Figure3.4.

Let us suppose the modes are propagating in the z direction, which is the same direction of the coupler path and let us assume that both fields are in phase at $z = 0$, the resulting field $\overline{E_{in}}$ is given by the sum of

$\overline{E_e}$ and $\overline{E_o}$. Because of the different propagation constants the two modes will become out-of-phase after a length

$$z = L = \frac{\pi}{\beta_e - \beta_o} \tag{3.21}$$

the resulting field $\overline{E_{out}}$ after z = L is given by the difference of the modes which practically results in a transfer of the light power from the bottom to the top waveguide as shown in Fig. 3.4.

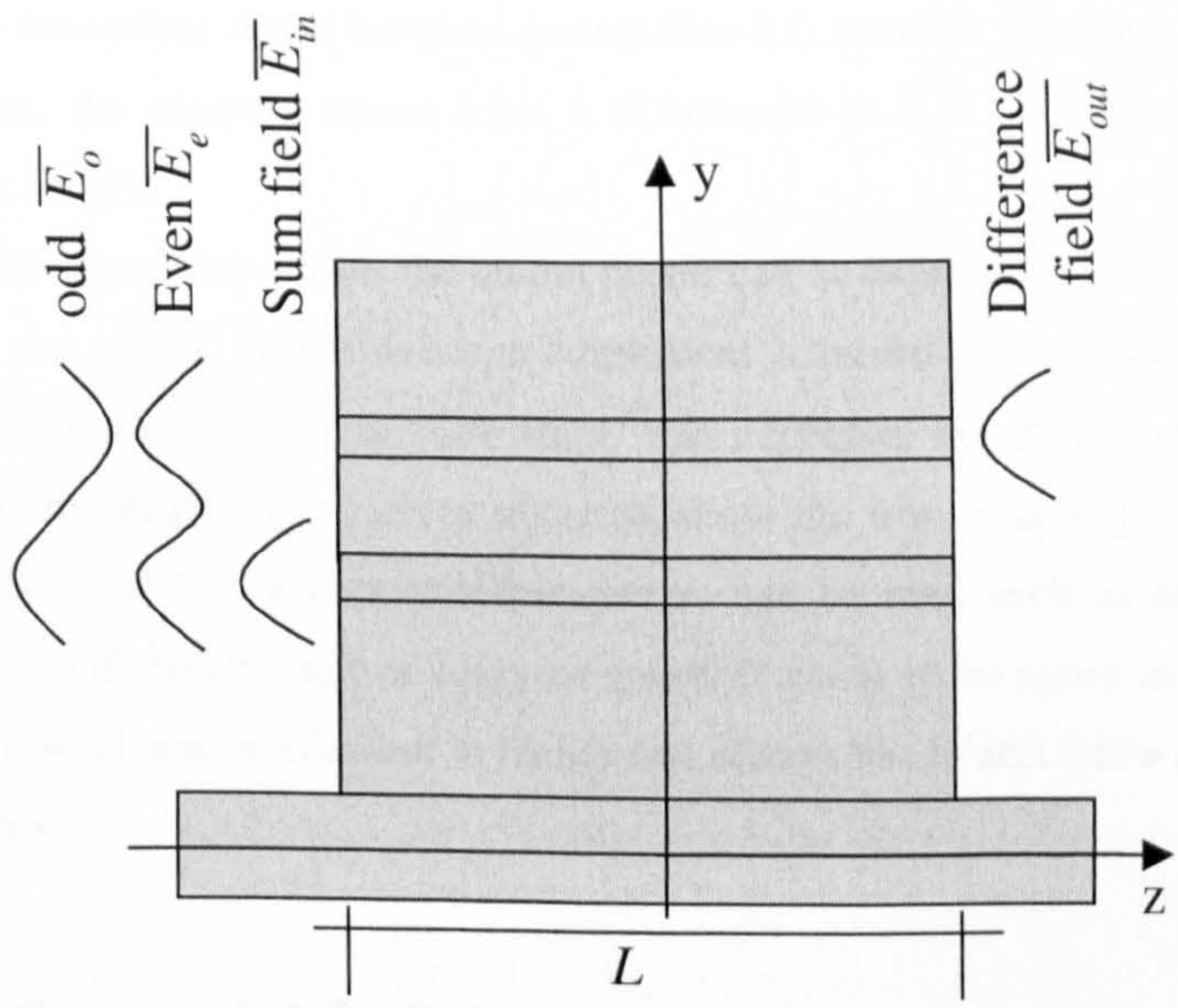

Figure3.4 The modes used for the coupling analysis

Nevertheless, in our particular situation the presence of an active layer makes the resulting field $|E_{out}|$ a function of the material gain. Hence, at z = 0 $|E_{in}|$ is expressed by the equations (3.22)

$$\begin{aligned} \left|E_{in\_top}\right| &= \left|E_e\right|_t - \left|E_o\right|_t \cong 0 \quad \text{- top waveguide} \\ \left|E_{in\_bot}\right| &= \left|E_e\right|_b + \left|E_o\right|_b \qquad \text{- bottom waveguide} \end{aligned} \tag{3.22}$$

while at z = L $|E_{out}|$ is given by the (3.23)

$$\begin{aligned} \left|E_{out\_top}\right| &= \left|E_e\right|_t \exp(\alpha_e L) + \left|E_o\right|_t \exp(\alpha_o L) \quad \text{- top waveguide} \\ \left|E_{out\_bot}\right| &= \left|E_e\right|_b \exp(\alpha_e L) - \left|E_o\right|_b \exp(\alpha_o L) \quad \text{- bottom waveguide} \end{aligned} \tag{3.23}$$

Maximum energy transfer from one waveguide to the other is achieved when the second of the (3.23) is equal to zero. Furthermore, from the first of (3.22) it can be assumed that $|E_e|_t = |E_o|_t = |E|_t$, therefore the equations (3.23) become:

$$\left|E_{out\_top}\right| = \left|E\right|_t \left[\exp(\alpha_e L) + \exp(\alpha_o L)\right] \quad \text{- top waveguide}$$

$$\left|E_{out\_bot}\right| = \left|E\right|_b \left[\exp(\alpha_e L) - \exp(\alpha_o L)\right] \text{ - bottom waveguide} \tag{3.24}$$

Hence $|E_{out\_bot}| = 0$ when $\alpha_e = \alpha_o$ or in terms of refractive index when:

$$\mathrm{Im}(n_e) = \mathrm{Im}(n_o) \rightarrow n_{i\_e} = n_{i\_o} \tag{3.25}$$

(3.25) indicates that when a structure is matched in the real index so that perfect coupling is achieved, the supermode should also have identical values.

3.2.4. 3D Coupling Analysis

In order to exchange the optical signal between waveguides it is necessary to introduce a new parameter: the propagation. Thus, the analysis moves from a 2D domain to a 3D domain by introducing in the calculation the device length.

In particular under "ON state" conditions the output power can be expressed as a function of the coupling length. Once again the solver Fimmwave can implement a model to find such results. The model simulates a ridge waveguide coupler in "ON state" and expresses the transferred optical power as a function of the coupling length. The curves obtained show the best coupling length for the structure analysed. Nevertheless, other very important parameters can be read such as the gain which is very important to understand if the structure is lossy or gainy. It needs to be taken in consideration that the model shows the on chip characteristics but in reality one always has to add a few more dB of loss due to the fibers coupling loss.

3.3. Optical Crosspoint Switch

In the 4x4 matrix configuration, as shown in Figure3.5, it is easy to understand that the loss is path dependent. The shortest path "In4 – Out1" is just subject to the *PLW* absorption loss and the TIR mirror loss. On the other hand, other paths, such us the longest one "In1 – Out4", are affected by two more different kinds of loss, which are:

- OXS absorption loss in "OFF state"
- Crossing loss

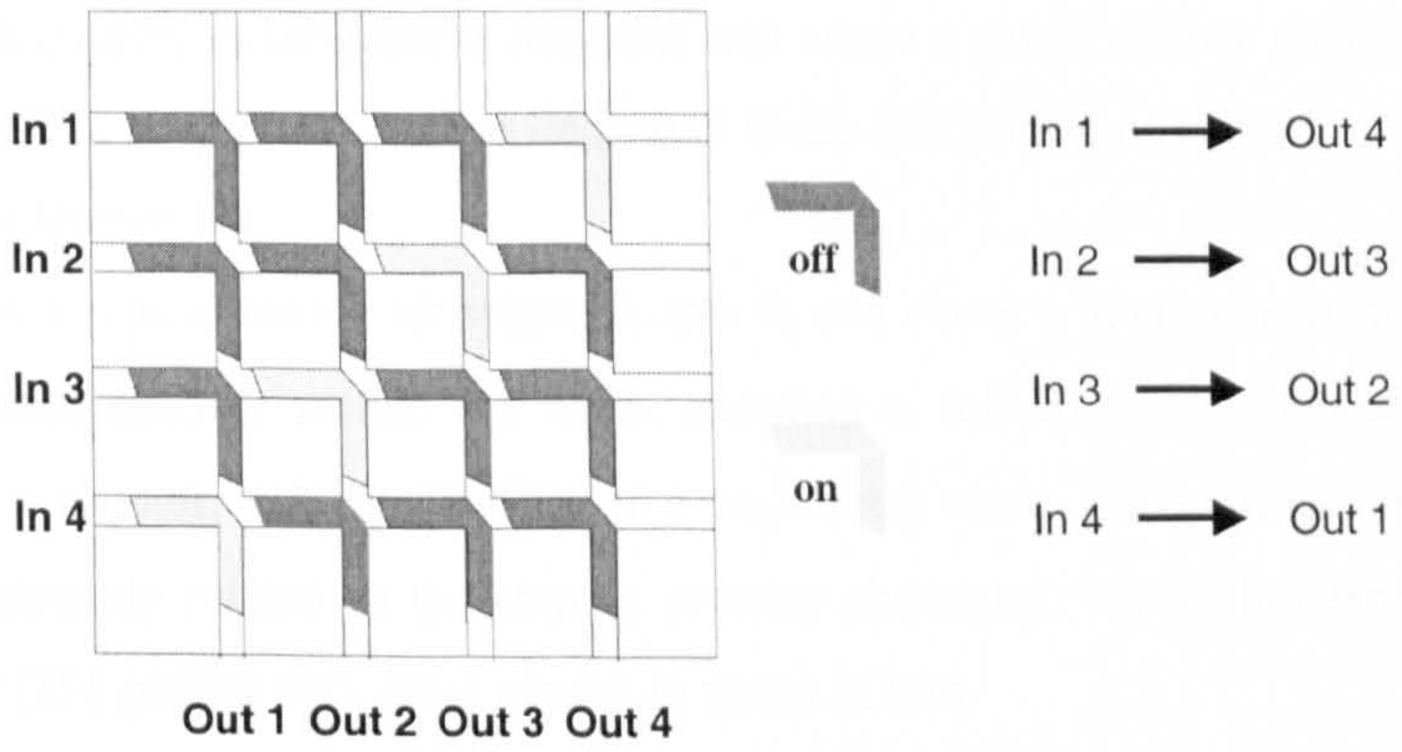

Figure3.5 The 4x4 space switch matrix

Next sections will give an overview of the losses involved in the model of the crosspoint switch.

3.3.1. Total Internal Reflecting Mirror

Redirecting an optical beam in a short distance is a key point of this device. Beam steering can be realised using a bent waveguide but unfortunately, the shorter is the curvature radius, the higher is the bent loss. A valid alternative is the Total Internal Reflecting mirror (TIR).

According to the Fresnel equations [11] total internal reflection is achieved when the incident angle is equal or above the critical incident angle given by equation 3.26.

$$\sin\theta_c = \frac{n_t}{n_i} = \frac{1}{n_{eff}} \tag{3.26}$$

and shown in Figure3.6

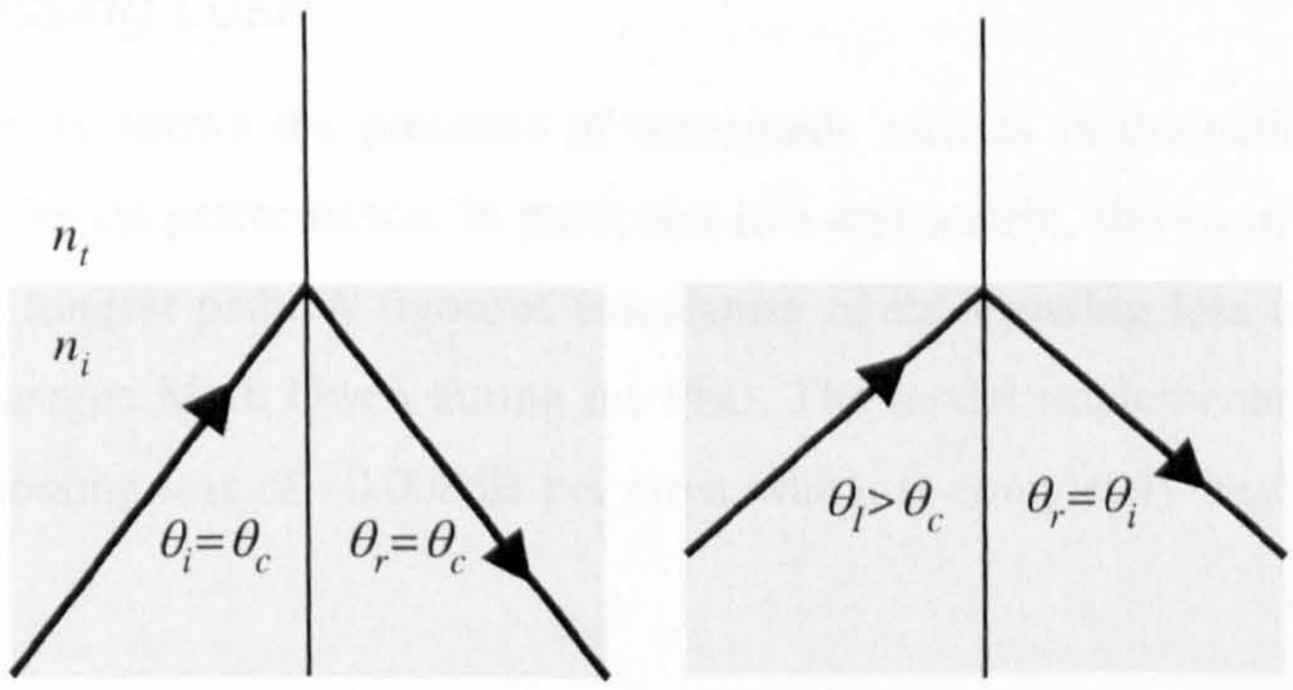

Figure3.6 Critical angle and total internal reflection

Theoretical studies upon semiconductor waveguide TIR mirrors can be found in literature and in particular it has been shown that for a 45° turning mirror almost all the incident power is above θ_c, hence the mirror can reflect the beam effectively [12]. It has also been shown that mirrors with loss <0.08 dB can be realised [13]. However TIR device suffer from fabrication limitations [14] such as:

1. *Loss Induced by Mirror Shift*

   Due to photolithography misalignment error that can cause a wrong corner mirror position [13]. It is discussed in detail in chapter 4, which is dedicated to the fabrication process.

2. *Loss Induced by Mirror Tilt*

   Figure3.7 shows a typical mirror tilt where θ_t and Φ_t can cause a deviation from the 45° angle. The double layer mask used to realise the OXS, adopting a self-alignment photolithography process explained in next chapter, reduces the tilt ϕ_t to a neglecting value. The vertical flip θ_t is also a source of loss and is strongly related to the etching process chemistry. Verticality with 1° off-set can be easily achieved [15] getting very good results in terms of loss.

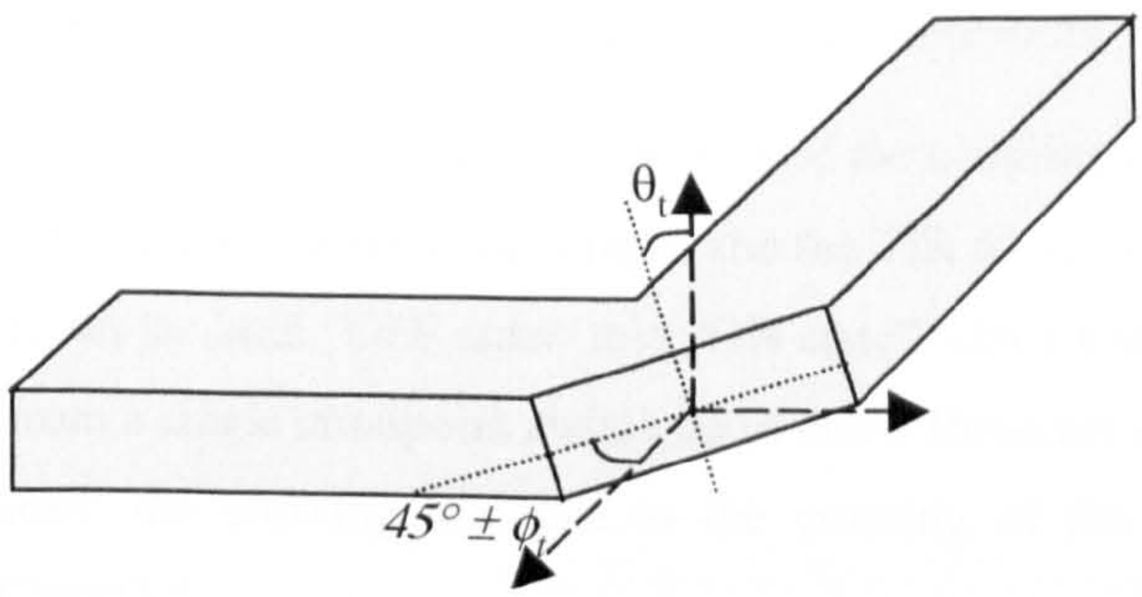

Figure3.7 ϕ_t and θ_t are the cause of tilt mirror losses

3. *Mirror Surface Roughness*

   Mirror Scattering is another important factor cause of loss. It is produced by using a poor quality mask during the dry etching process [16] or by a non-optimised etching gas mixture.

Under optimised conditions the total loss for a TIR mirror can be reduced to 1-1.5 dB [17].

3.3.2. Crossing Loss

As it has been previously shown the presence of waveguide crosses in the paths of the space switch matrix could limit the device performance. In particular in a 4x4 matrix, shown in Figure3.5, the crosses can be up to 6 in the longest path. A rigorous calculation of the crossing loss and crosstalk has been carried out by the colleague Mark Owen during his PhD. The model implemented and described in his thesis [18] shows a crossing loss of –0.008dB per cross which is completely negligible when compared with the other losses.

3.3.3. Analysis of the optical crosspoint switch

The model is realised with different blocks: two bottom waveguides to simulate the input and output, two VCs and a top waveguide that represent the TIR mirror. It is based on the results achieved in the previous section while the TIR mirror is assumed with a conservative loss of 1.5 dB.

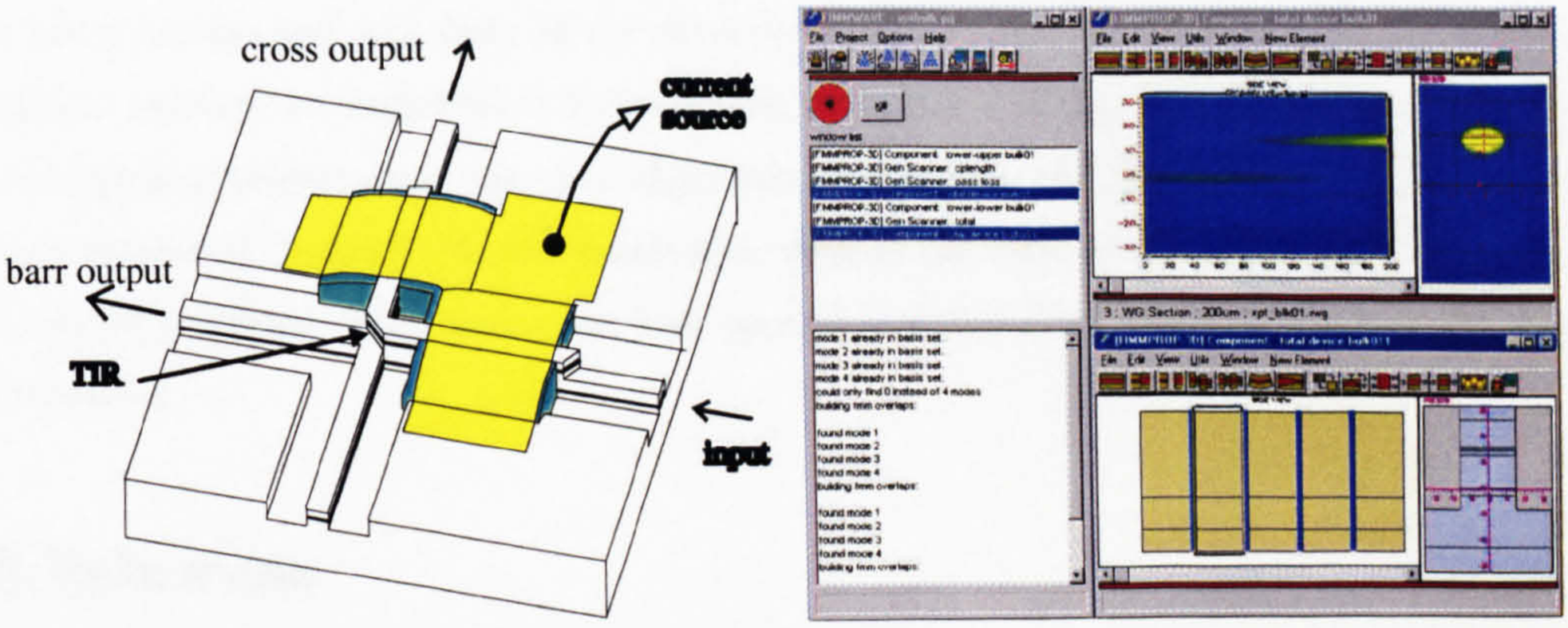

Figure3.8 Schematic representation of the OXS and a FIMWAVE simulation

Using FIMMWAVE it is calculated the coupling as a function of the coupling length at the main points of the optical crosspoint switch: the Bar output, Cross output and the TIR mirror as illustrated in Figure3.8. The investigation is carried on for both "OFF state" and "ON state". Once found the coupling values the analysis can be extended from a single crosspoint switch up to NxN. However in this case another form of loss needs to be introduced: the crossing loss due to the crossing of the input and output passive waveguides as shown in Figure3.5.

A first investigation to be carried on is the Optical Signal Transmission as a Function of the Path. It permits to have a better idea of the quality of the coupling permitting also to understand the maximum number of crosspoints, which can be introduced in a matrix switch without making any regeneration of the signal.

Another test is the calculation of the Multipath Interference. This permits to understand the interaction between different signals once they are coupled in and redirected by the matrix switch.

In next chapter it is shown that with the wafer structures used the maximum number of crosspoints is N=4, thus a 4x4 matrix switch will be also investigated.

3.4. Conclusions

In this chapter theoretical analysis of the optical crosspoint switch has been given. Starting from the active coupler, the theory behind the calculation of the compound refractive indexes has been studied.

The whole vertical coupler has been analysed. First a 2D followed by a 3D analysis has permitted the best coupling length to be achieved with the minimum current injection in the active region. The TIR mirror has been also briefly treated and the incurred loss has been shown.

With all the information's about each single part, the OXS has been studied and it has been shown that the wafer that gives the best performances in terms of absorption, crosstalk, and scalability is MR1392 made using bulk material layers.

In next chapter the fabrication of the 4x4-matrix switch will be discussed. The first section is dedicated to the fabrication process and will show all the clean room action taken in order to make the device. The following two sections are dedicated to the problems encountered during the manufacture. In particular one of the typical problems about the mask alignment is shown. In the second section RIE-Dry etching process is approached. A novel sidewall passivation method has been proposed in order to ensure from the RIE etching problems. The process has been applied to Fabry-Perot ridge waveguide lasers and the results are shown.

3.5. References

[1] S. Adachi, "Physical Properties of III-V Semiconductor Compounds", 1992, John Wiley & Soons.

[2] T.P. Pearsall, "GaInAsP Alloy Semiconductors", 1982, John Wiley & Soons

[3] S.Adachi, "Refractive indices of III–V compounds: Key properties of InGaAsP relevant to device design", Journal of Applied Physics, Vol.53, No.8, 1982, pp. 5863-5869

[4] A.B. Djurisic, A.D. Rakic, P.C.K. Kwok and Herbert Li, M.L. Majewski, "Modelling the optimal constants of GaP, InP, and InAs", Journal of Applied Physics, Vol.85, No.7, 1999, pp.3638-3642

[5] J.A. Lahtinen and T.Tuomi, "Energy-Band Structure Of In1-XGAXASYP1-Y Lattice Matched To Inp By Means Of The Line-Profile Analysis Of The Electroreflectance Spectra" Physics Status Solidi B, Vol. 130, No.2, 1985, pp. 637-641

[6] A.S. Subdo, "Film Mode Matching: a Versatile Numerical Method for Vector Mode Field Calculations in Dielectric Waveguides", Pure and Applied Optics, Vol.2, 1993, pp.211-233.

[7] A.S. Subdo, "Numerical Stable Formulation of the Transverse Resonance Method for Vector Mode Field Calculations in Dielectric Waveguides", IEEE Photonic Technology Letters, Vol.5, 1993, pp.342-345.

[8] G.P. Agrawal, N.K. Dutta, "Semiconductor Lasers - 2nd ed.", 1993, Van Nostrand Reinold N.Y.

[9] L.A. Coldren, S.W. Corzine, "Diode Lasers and Photonic Integrated Circuits", 1995, John Wiley & Soons.

[10] D. Marcuse, "Theory of Dielectric Optical Waveguides - 2nd ed", 1993, Academic Press Inc.

[11] E. Hecht, "Optics – 3rd ed.", 1998, Addison-Wesley.

[12] S.T. Lau, J.M. Ballantyne, "Two-Dimensional Analysis of a Dielectric Waveguide Mirror", Journal of Lightwave Technology, Vol. 15, No. 3, 1997, pp. 551-558.

[13] L. Faustini, C. Coriasso, A. Stano, C. Cacciatore, D. Campi, "Loss Analysis and Interference Effect in Semiconductor Integrated Waveguide Turning Mirrors", IEEE Photonics Technology Letters, Vol. 8, No. 10, 1996, pp. 1355-1357.

[14] R. Orobtchouk, S. Laval, D. Pascal, and A. Koster, "Analysis of Integrated Optical Waveguide Mirrors", Journal of Lightwave Technology, Vol. 15, No. 5, 1997, pp. 815-820.

[15] S.E. Hicks, C.D.W. Wilkinson, G.F. Doughty, et al, "Reactive Ion Etching of Low-Loss Mirrors in InP/InGaAsP/InP Heterostructures Using $CH_4/H_2/O_2$ Chemestry", Proc ECIO '93.

[16] U.K. Chakrabarti, S.J. Pearton, F. Ren, "Sidewall Roughness During Dry Etching of InP", Semiconductor Science Technology, No.6, 1991, pp. 408-410.

[17] E. Gini, G. Guekos, H. Melchior, "Low Loss Corner Mirrors with 45° Deflection Angle for Integrated Optics", Electronics Letters, Vol.28, No.5, 1992, pp.499-500.

[18] M. Owen, "Monolithic Integration of Optical Space Switches", 1998, PhD Thesis University of Bristol

Chapter 4

Theoretical Characterisation of Different Vertical Coupler Structures

This chapter analyses different wafer structures that have been designed prior to the developing of the model described in chapter 3. From all the structures investigated, 3 adopt different InP/InGaAsP bulk layers. The remaining 5 have an InGaAs/InGaAsP MQW structure for the *Active Upper Waveguide (AUW)* and the *Lower Passive Waveguide (LPW)*. In each case the *AUW* adopts either the same material for the bulk structures or the same number of QWs for the MQW structures. Different materials or QW number are used for the *PLW*.

Furthermore, only 4 structures have been grown as wafers, so throughout the chapter the characterisation will focus the analysis on only two wafer structures, one that uses bulk layers and another realised with MQW's.

The layout of these wafer structures is fully illustrated in Appendix 1 including composition thickness and doping level of each single layer.

Glossary of the abbreviations

(AUW) Active Upper Waveguide

(PLW) Passive Lower Waveguide

(XT) Crosstalk

(MI) Multipath Interference

(MPI) Multi-Path Interchannel

(SNR) Signal to Noise Ratio

4.1. Active Vertical Coupler Results

From the analysis of each single layer this section goes through the first part of the model, described in section 3.2, permitting to verify and find a wafer structure that shows good results in terms of vertical coupling.

4.1.1. Characterisation of the coupler waveguides

Table4.1 shows the main parameters characterising the compounds involved in the design of the structures. The first 4 rows indicate the compounds involved in the bulk structures with the first representing the *AUW* layer and the others used for the *PLW*.

Sample	Bandgap wavelength [nm]	Bandgap Energy [eV]	Composition	Refractive index
Bulk *AUW*	1550	0.8012	$In_{0.606}GaAs_{0.846}P$	3.5355
Vcwblk1	1500	0.8279	$In_{0.63}GaAs_{0.795}P$	3.4943
MR1392	1450	0.8564	$In_{0.655}GaAs_{0.743}P$	3.4599
MR1394	1200	1.0348	$In_{0.795}GaAs_{0.445}P$	3.3179
Barrier	1300	0.8329	$In_{0.736}GaAs_{0.572}P$	3.4878
Well	1490	0.75*	$In_{0.53}GaAs$	3.5770
InP	920	1.35**	InP	3.1662

*value measured [1], ** [2]

Table4.1 Passive lower waveguide layers of some Vertical Coupler structures

The composition of barrier and well define the MQW layers for the MQW structures. In particular their number and their thickness are responsible for the wanted bandgap and refractive index value.

Finally, last row shows the characteristics of the InP compound that is used for all the other layers.

Sample	Thickness [Å]	Composition	n_{eff}	Γ
Vcwblk1	2000	$In_{0.63}GaAs_{0.8}P$	3.2513	0.3845
MR1392	2400	$In_{0.655}GaAs_{0.743}P$	3.2628	0.4600
MR1394	7000	$In_{0.795}GaAs_{0.445}P$	3.2580	0.7738
Vcwmqw2	11 x 60 barrier 12 x 37 QW	$In_{0.736}GaAs_{0.572}P$ $In_{0.53}GaAs$	3.2446	0.0869
Vcwmqw3	13 x 60 barrier 14 x 37 QW	$In_{0.736}GaAs_{0.572}P$ $In_{0.53}GaAs$	3.2459	0.1021
MR1468	11 x 53 barrier 12 x 37 QW	$In_{0.736}GaAs_{0.572}P$ $In_{0.53}GaAs$	3.2491	0.0878
MR1453	11 x 37 barrier 12 x 37 QW	$In_{0.736}GaAs_{0.572}P$ $In_{0.53}GaAs$	3.2445	0.0878
Vcwmqw6	13 x 26 barrier 14 x 37 QW	$In_{0.736}GaAs_{0.572}P$ $In_{0.53}GaAs$	3.2460	0.1044

Table4.2 n_{eff} and Γ of the passive lower waveguide

Inputting these values into Fimmwave model the *Confinement Factor*, Γ and *Effective Indexes*, n_{eff} for the *PLW* and *AUW* are calculated at carrier density N=0. All the results are expressed for the TE fundamental mode at waveguide width of 3 μm and shown in Table4.2.

As it has been shown, the carrier density N plays an important role in the definition of the *AUW effective index* and in the *confinement factor*. Thus, following equation (3.13) the carrier density can be expressed as a function of the current density, as plotted in Figure4.1.

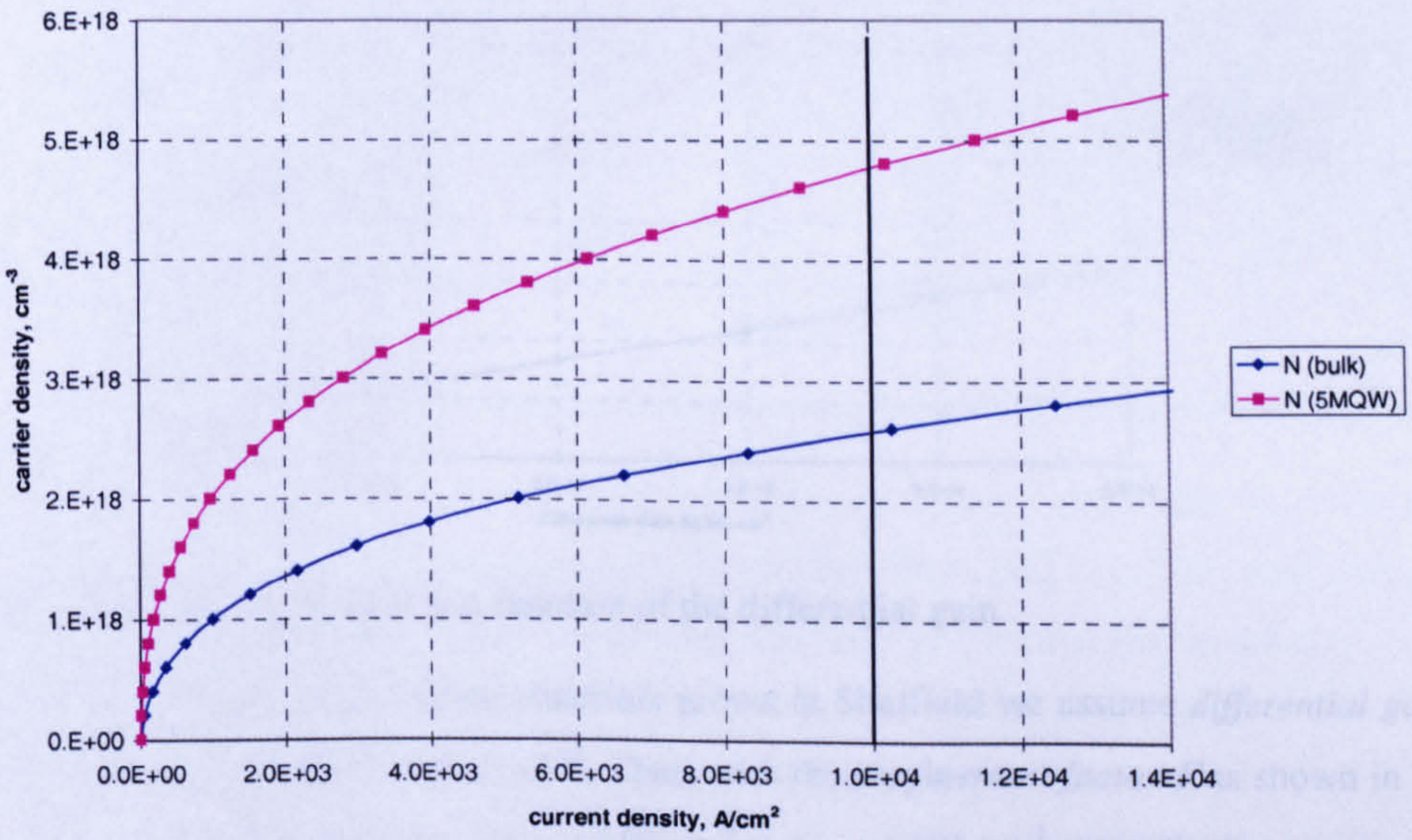

Figure 4.1 Carrier density as a function of current density

Fixing the maximum current density up to 10,000 A/cm^2 it yields the values $N_{bulk} = 2.6\text{x}10^{18}$ cm^{-3} for the bulk waveguide and $N_{MQW} = 5\text{x}10^{18}$ cm^{-3} for 5 MQWs waveguide. The calculated n_{eff} and Γ, when N=N_{max}, are summarised, together with values at N=0 results are shown in Table4.3.

	Sample	Thickness *[Å]*	Composition*	*N* *[cm^{-3}]*	n_{eff}	Γ
BULK	Vcwblk1 MR1392 MR1394	2000	$In_{0.606}GaAs_{0.8457}P$	0 $2.6\text{x}10^{18}$	3.2737 3.2501	0.4225 0.3845
MQW	Vcwmqw2 Vcwmqw3 MR1468 MR1453 Vcwmqw6	4 x 120Å barrier 5 x 75 Å QW	$In_{0.736}GaAs_{0.572}P$ $In_{0.53}GaAs$	0 $5\text{x}10^{18}$	3.2485 3.2409	0.0717 0.0682

* All the samples have the same active bulk or MQW compound structure

Table4.3 n_{eff} and Γ of the active layer region with different Carrier Densities

Comparing Table 4.2 and 4.3, it can be seen that, as expected, most of the *AUW* designed have an effective refractive index higher than that of the bottom waveguide. Thus, when bias current is applied to the device, n_{eff_AUW} reduces to match n_{eff_PLW} enabling the coupling.

Information about the gain of the active material can also be achieved. Fixing N_{tr} at the conservative value of $1.5x10^{18}$ cm^{-3} and N to the values indicated in Table4.3 with the help of equation (3.14), the *gain* g, as shown in Figure4.2, can be represented as a function of the *differential gain dg/dN*.

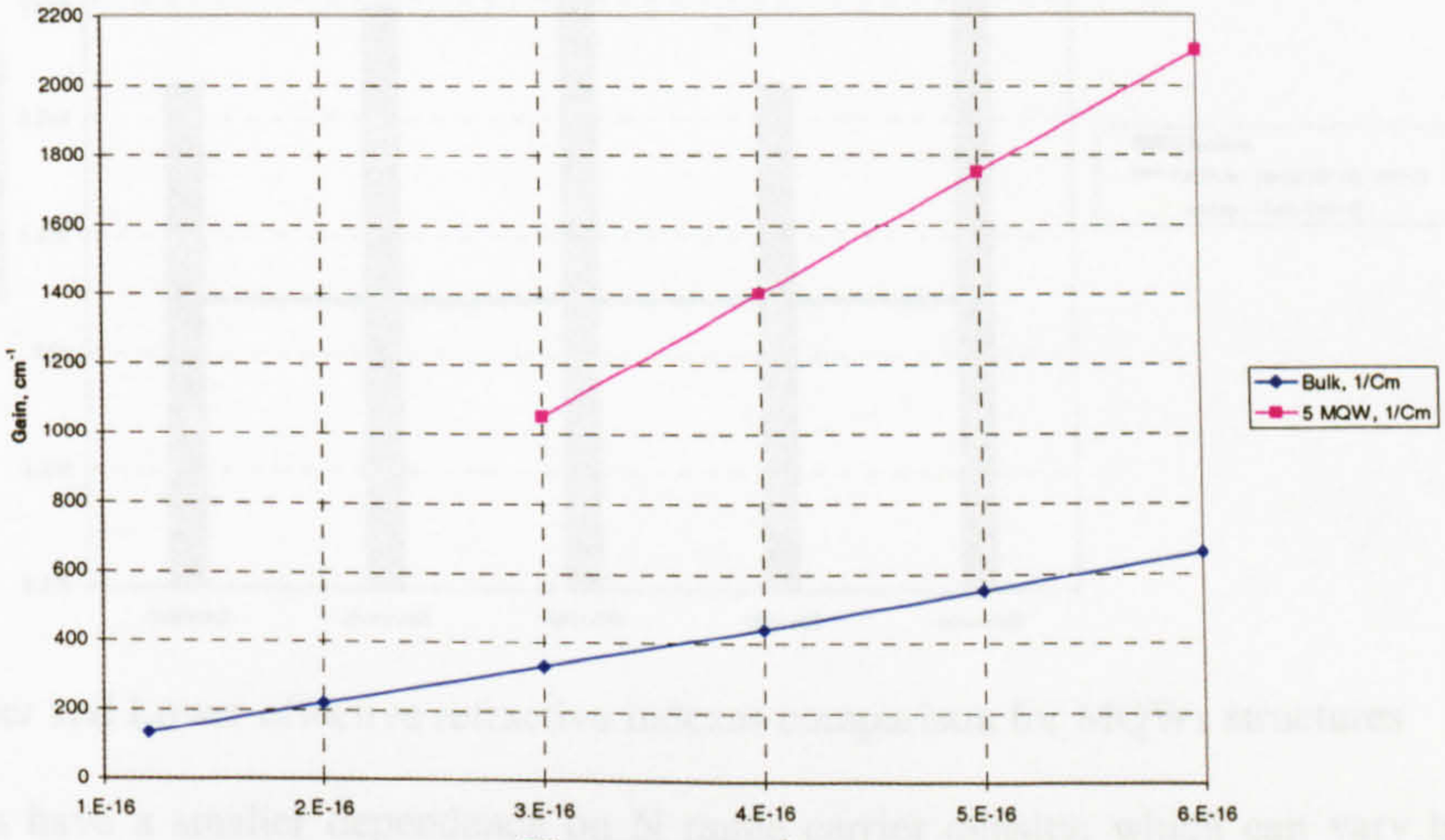

Figure4.2 Calculated material gain as a function of the differential gain

From the experience done with 1.55μm materials grown at Sheffield we assume *differential gain dg/dN* for bulk and MQW to be $3x10^{-16}$ and $4x10^{-16}$. Thus, with the *confinement factor* Γ as shown in Table4.3, the *modal gain* $\langle g \rangle = \Gamma g$ is given by $\langle g \rangle_{bulk}=150$ cm^{-1} $\langle g \rangle_{MQW}=101$ cm^{-1} respectively.

4.1.2. 2D Coupling characterisation

From the refractive index data shown in Table 4.2 and 4.3 the different structures can be compared. In particular the analysis of the effective refractive index between upper and lower waveguide can give a lot of information about the quality of the coupling. The two charts shown in Figure4.3 and Figure4.4 help in this analysis.

They compare the n_{eff} of the two waveguides, upper and lower, at the two levels of carrier density.

Figure4.3, representing the MQWs structures, show that for MR1468 $n_{eff\_PLW} > n_{eff\_AUW\_N0}$ hence a device made with this structure cannot work at all. Perhaps it was designed as a coupler, which couples when not biased and decouples when biased. However, it cannot work because of the high absorption nature of the active layer when not biased.

Following the suggestions of Table3.1, wafer MR1453 is the only grown wafer which could work, achieving n_{eff} equalisation at $N = 2.445x10^{18}$ cm^{-3}. However, such a value is at half way of N range, therefore a device made with this material is expected with high coupling loss when in "OFF state" and high crosstalk when in "ON state".

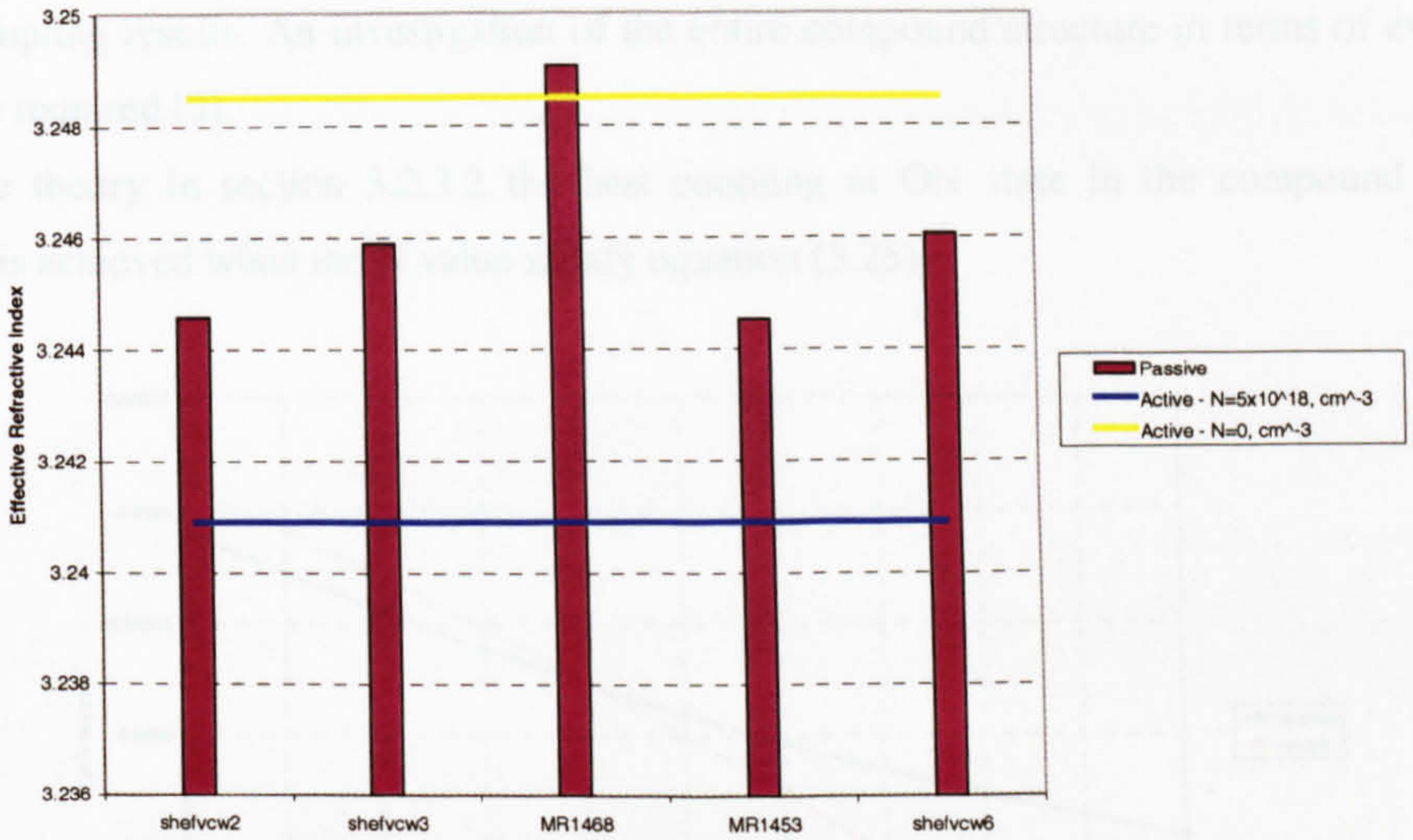

Figure4.3 Upper and Lower effective refractive indexes comparison for MQWs structures

Bulk materials have a smaller dependence on N range carrier density, which can vary between 0 and $2.6\text{x}10^{18}$ cm^{-3}. Only wafer MR1392 has n_{eff_PLW} near the lowest limit of n_{eff_AUW}. The two indexes match at N=$2.3\text{x}10^{18}$ cm^{-3} suggesting a good coupling with high ON-OFF contrast and low cross talk.

The position between the two refractive indexes is very important from a coupling point of view. In next sections it will be shown that a structure as MR1453 is already not suitable for good couplings. Thus in the future the two wafer structures MR1453 and MR1392 will be used as example of bad and good devices respectively.

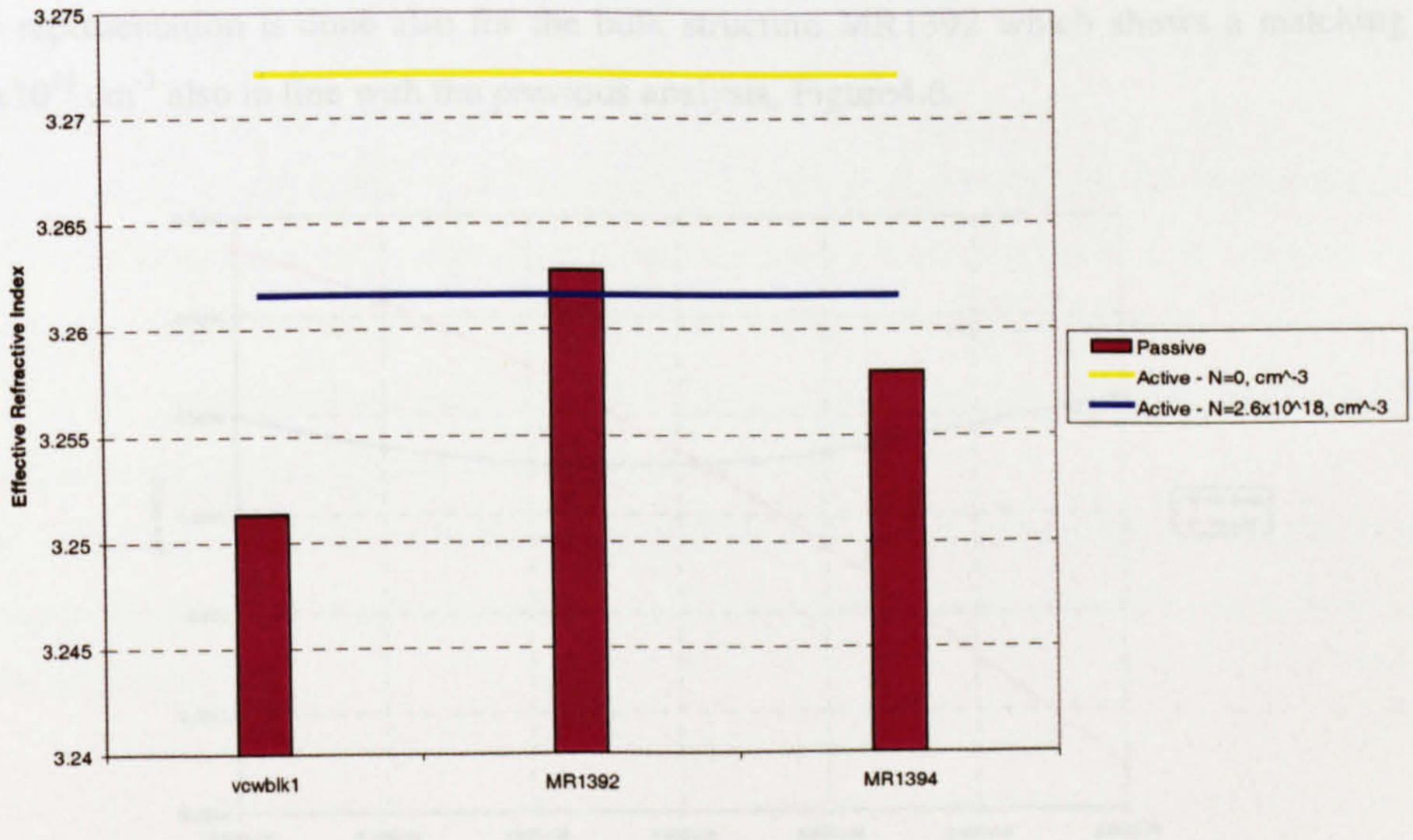

Figure4.4 Upper and Lower effective refractive indexes comparison for Bulk structures

However, the analysis done so far, for the reasons seen in the previous section 3.2.3.2, gives only qualitative coupling results. An investigation of the entire compound structure in terms of even and odd modes will be required [3].

Following the theory in section 3.2.3.2 the best coupling at ON state in the compound structure is calculated. It is achieved when the N value satisfy equation (3.25).

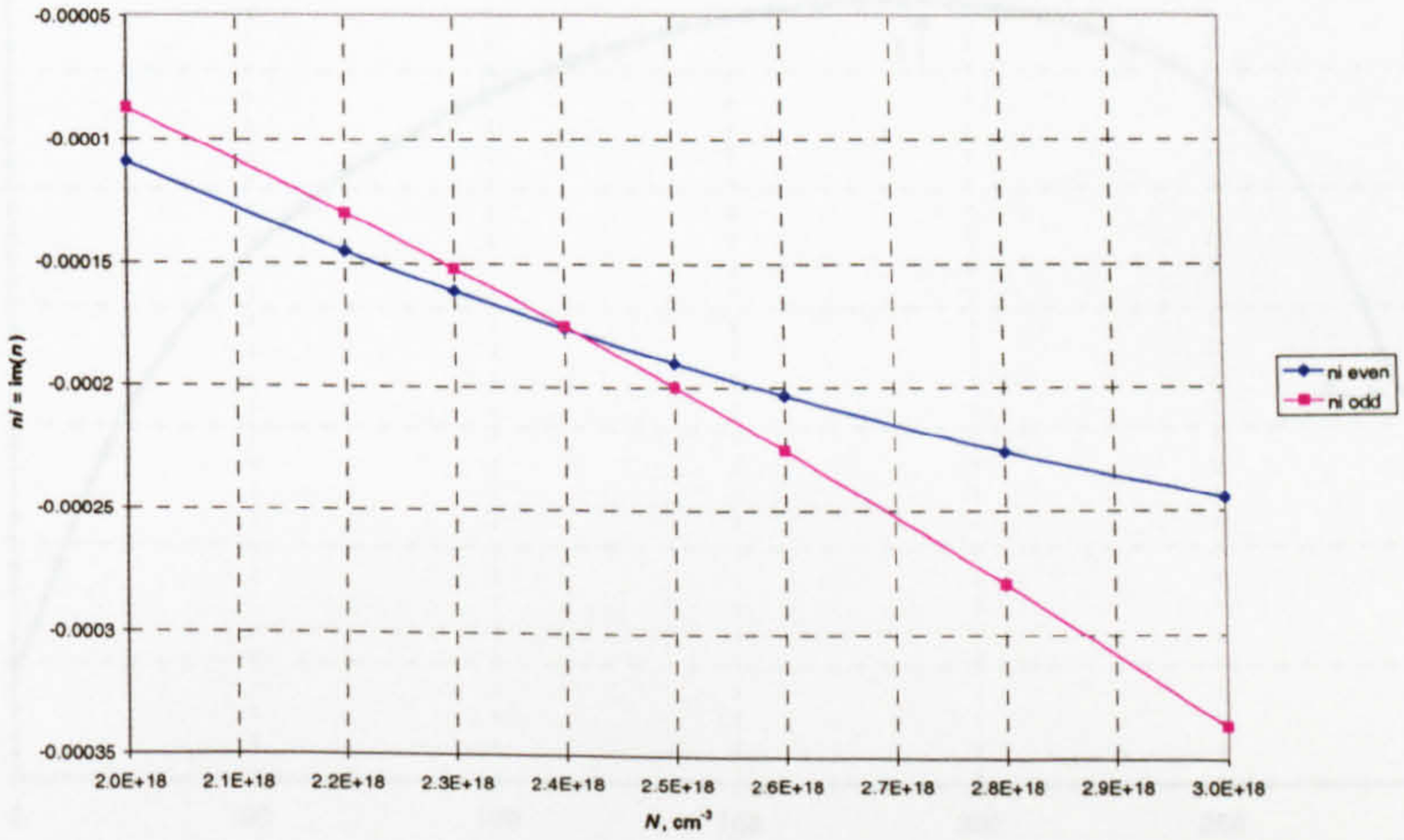

Figure4.5 Supermode *Im(n)* as a function of the carrier density *N* for MR1453 MQW material

Hence, expressing *Im(n)* for both even and odd modes as a function of *N*, the condition im(n_e)=im(n_o) is plotted and N_{on} is found.

The chart of Figure4.5 shows the plot of the *Im(n)* for wafer MR1453. Condition (3.25) is satisfied at $N_{on}=2.42x10^{18}\ cm^{-3}$ in perfect agreement with the analysis of the previous section.

The same representation is done also for the bulk structure MR1392 which shows a matching value at $N_{on}=2.32x10^{18}\ cm^{-3}$ also in line with the previous analysis, Figure4.6.

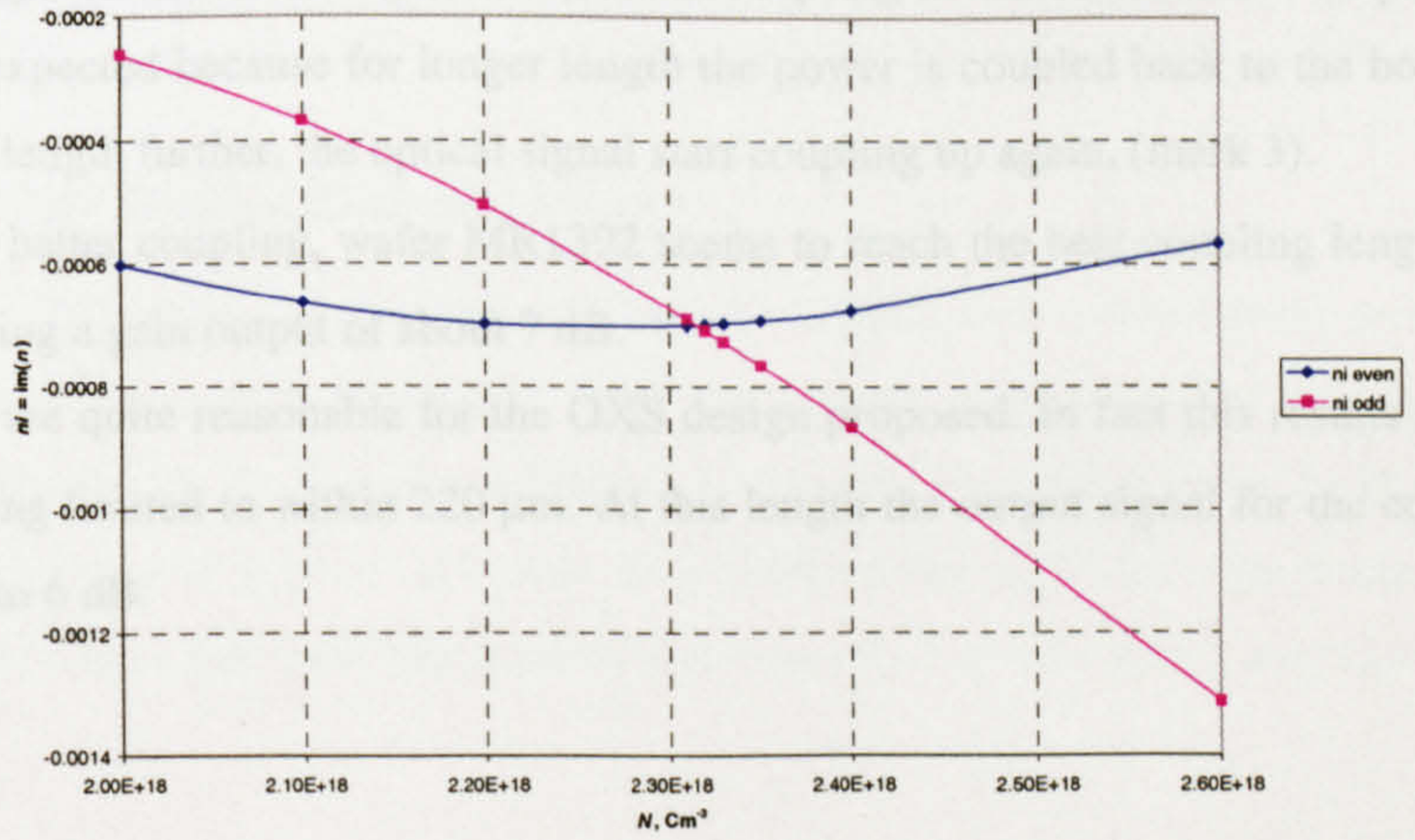

Figure4.6 Supermode *Im(n)* as a function of the carrier density *N* for MR1392 bulk material

4.1.3. 3D Coupling Characteristics

So far, from the analysis two main structures have been identified: MR1453 and MR1392. The first one seems to have worse characteristics than the second one. The carrier density values necessary to switch the power from one waveguide to the other have also been found.

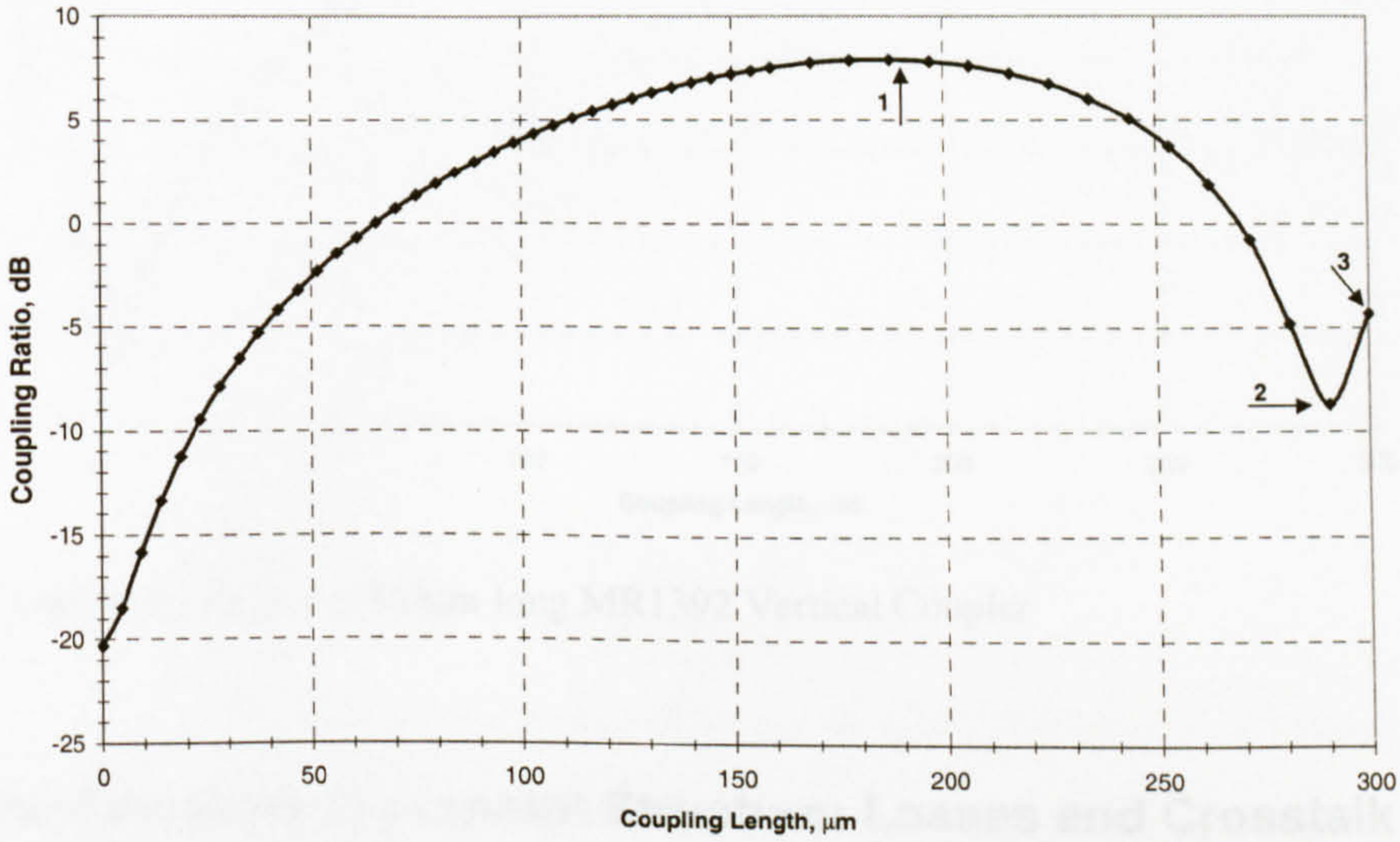

Figure4.7 Coupling process in a 300μm long MR1453 Vertical Coupler, which shows the transfer of power from PLW to AUW

Fix the carrier density at the values found and assume maximum length of 300μm, the coupled power is calculated as a function of the coupling length. The model simulates a 3μm wide ridge waveguide whose length increase from 0 up to 300μm. The structure used is MR1453 and MR1392 and the state is ON.

At the correct *N* the MQW structure MR1453, see Figure4.7, shows the best coupling approximately at 190μm reporting a gain of 8dB (mark 1).

Increasing the length of the device up to 290μm the coupling is reduced and the output drops to –9dB (mark 2). This is expected because for longer length the power is coupled back to the bottom waveguide, but increasing the length further, the optical signal start coupling up again, (mark 3).

As confirm of the better coupling, wafer MR1392 seems to reach the best coupling length at 300μm, see Figure 4.8, achieving a gain output of about 7 dB.

The values found are quite reasonable for the OXS design proposed. In fact this results allows the single coupler length being limited to within 220 μm. At this length the output signal for the coupler made with MR1453 reduces to 6 dB.

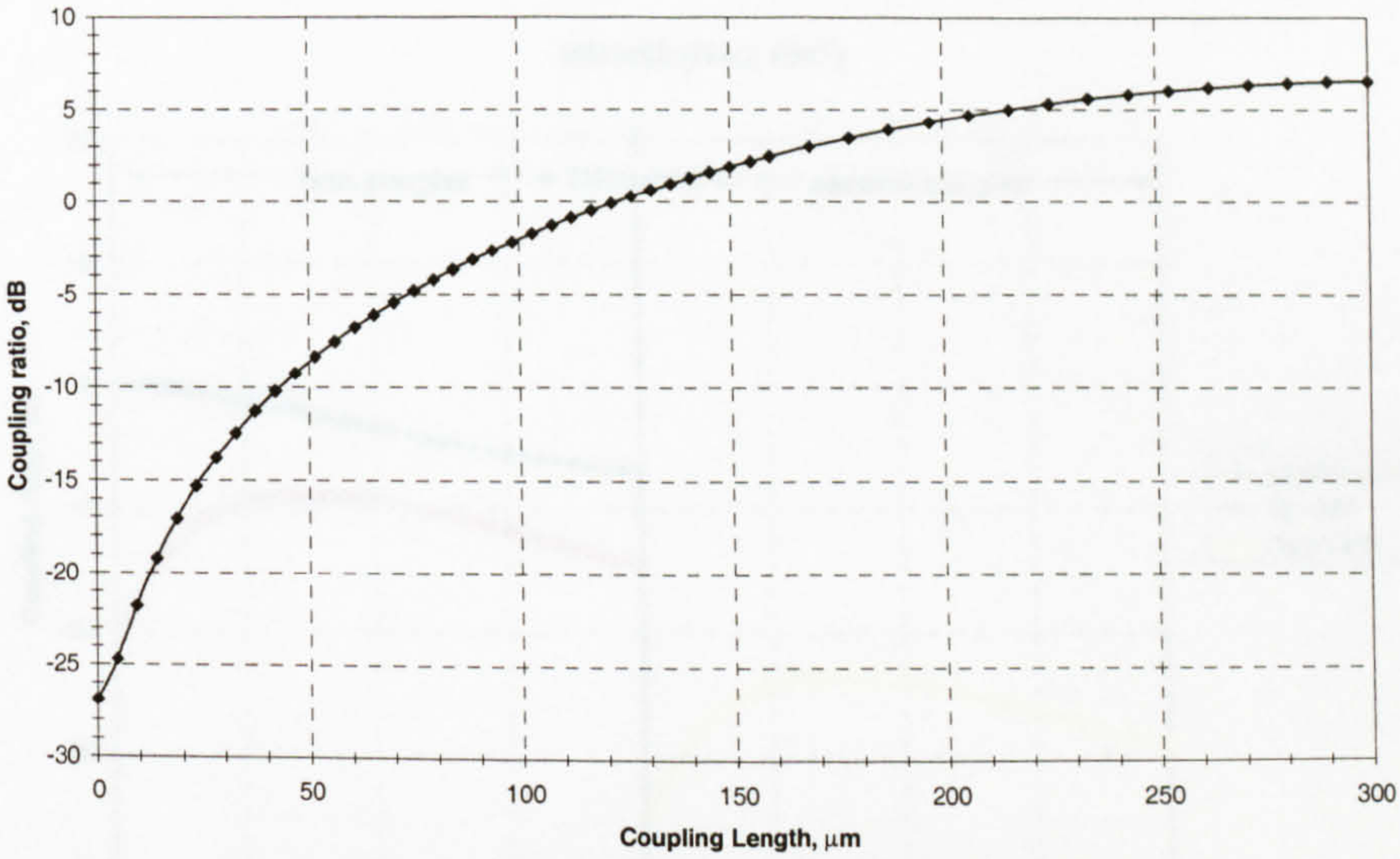

Figure4.8 Coupling process in a 300μm long MR1392 Vertical Coupler

4.2. The Complete Crosspoint Structure: Losses and Crosstalk

This section shows the calculated results of an entire OXS made with the two structures MR1453 and MR1392. It is assumed that each vertical coupler is 200 μm long and when in "ON state", the carrier density is $N = 2.42\text{x}10^{18}$ and $N = 2.32\text{x}10^{18}$ cm^{-3} for MR1453 and MR1392 respectively.

The transmission is calculated at the Bar output, Cross output and the TIR mirror as shown in Figure 4.9. The investigation is carried out for both "OFF state" and "ON state" and plotted in two different charts, which are divided in two main areas horizontally. The first half area expresses the optical signal along the two waveguides of the first VC, arriving at the bar output and on the TIR mirror in the centre of the chart. The second half, instead, represents the optical signal in the PLW of the second VC, or else on the cross output.

4.2.1. MQW structure MR1453

With the OXS in "OFF state" the device shows high absorption even when signals propagate along the PLW layer (curve: *passive OFF* Figure4.9). This has already been predicted as caused by the high refractive index value of the PLW (refer to Figure4.3) allowing the optical signal to be coupled into and absorbed (VC OFF) by *AUW* even in OFF state. This causes a loss in the bar-output transmission of 7dB. Naturally, the cross output also feels this residual coupling effect at OFF states showing a *Crosstalk* (*XT*) of almost -30 dB.

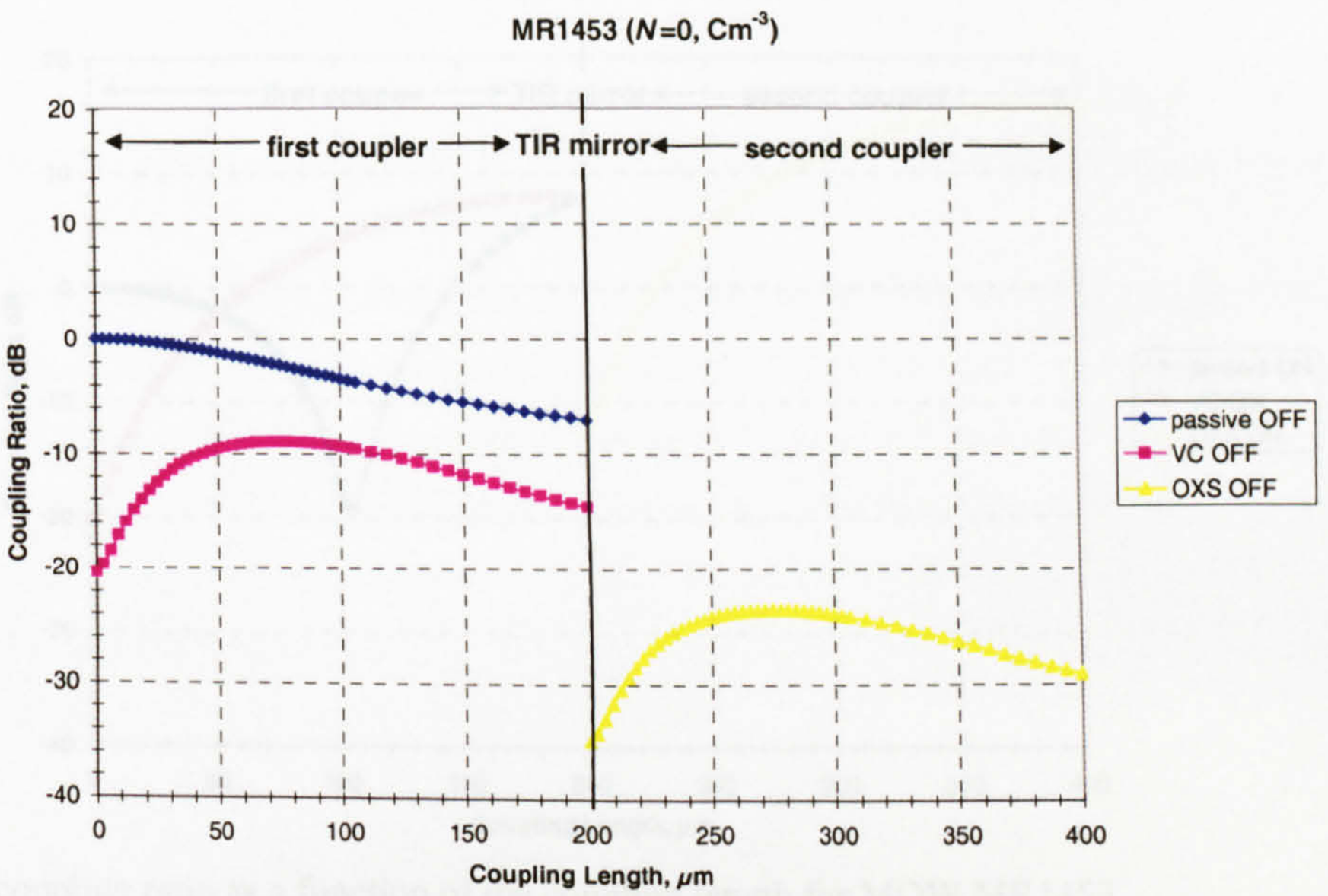

Figure4.9 Coupling process along the OXS coupler length for MQW MR1453 at OFF state

- Passive OFF: Transmission at the bar-output when in OFF state
- VC OFF: Transmission at the end of the first VC when in OFF state
- OXS OFF: Transmission at the cross-output when in OFF state

With the OXS in "ON state" the signal is clearly transferred into the *AUW*, reflected by the TIR mirror and coupled down to the cross output. Figure4.10 represent the ON state results, showing a gain of roughly 16dB at the cross-output and therefore, an ON-OFF contrast of 45dB. The optical signal at the bar-output drops in the first half of the first VC and rises up on the second part of it. This is thought because the input optical signal is coupled up during the first half of the coupler and coupled down, even amplified, during the second half. Thus at the bar end the optical signal transmission is slightly below than 8dB. In principle this high value is not very important because the others OXS down on the same line are all in OFF-state. However, this not true in terms of *Multipath Interference (MI)*. A later section is completely dedicated to the problem.

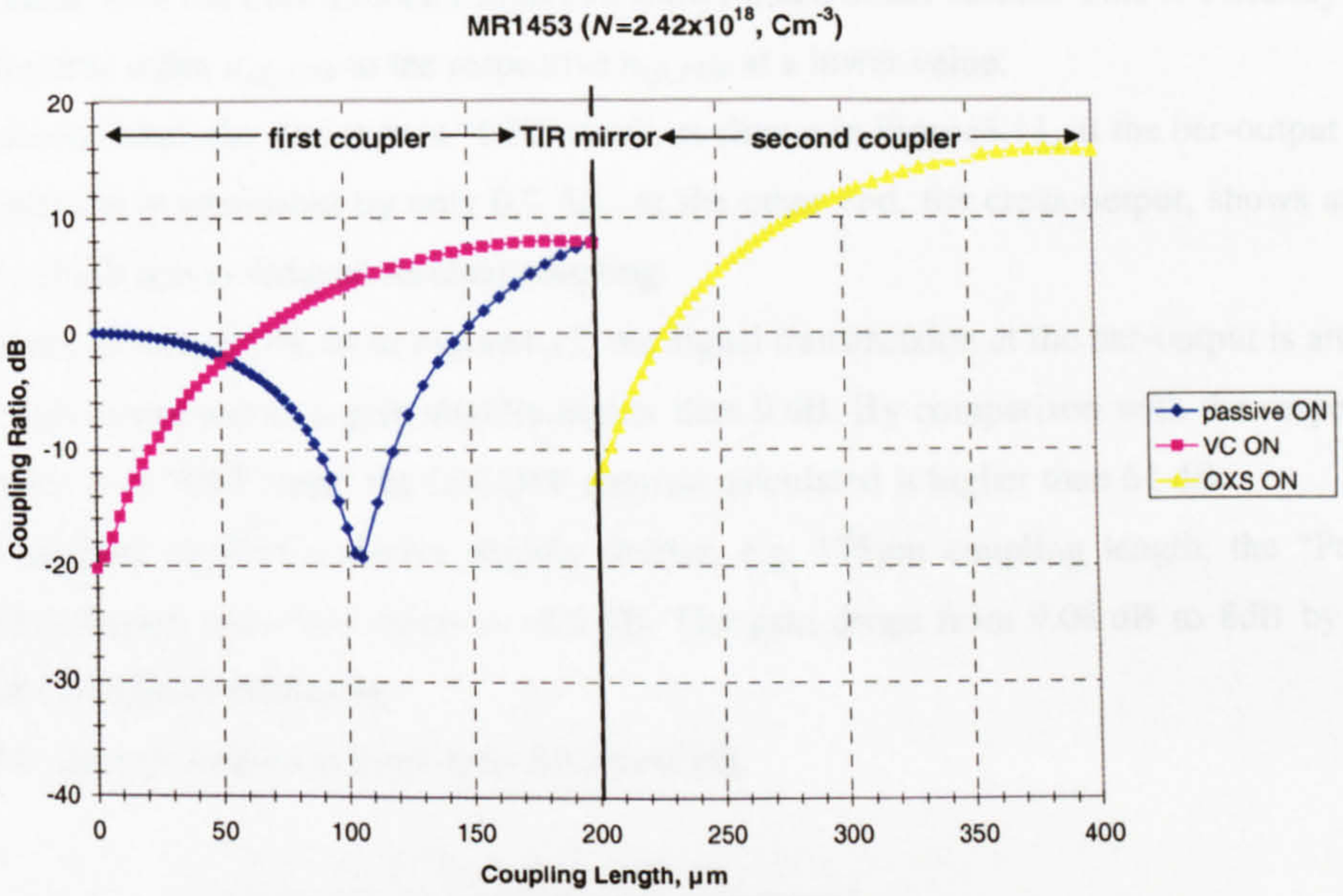

Figure4.10 coupling ratio as a function of the coupling length for MQW MR1453

- Passive ON: Transmission at the bar-output when in ON state
- VC ON: Transmission at the end of the first VC when in ON state
- OXS ON: Transmission at the cross-output when in ON state

4.2.2. Bulk structure MR1392

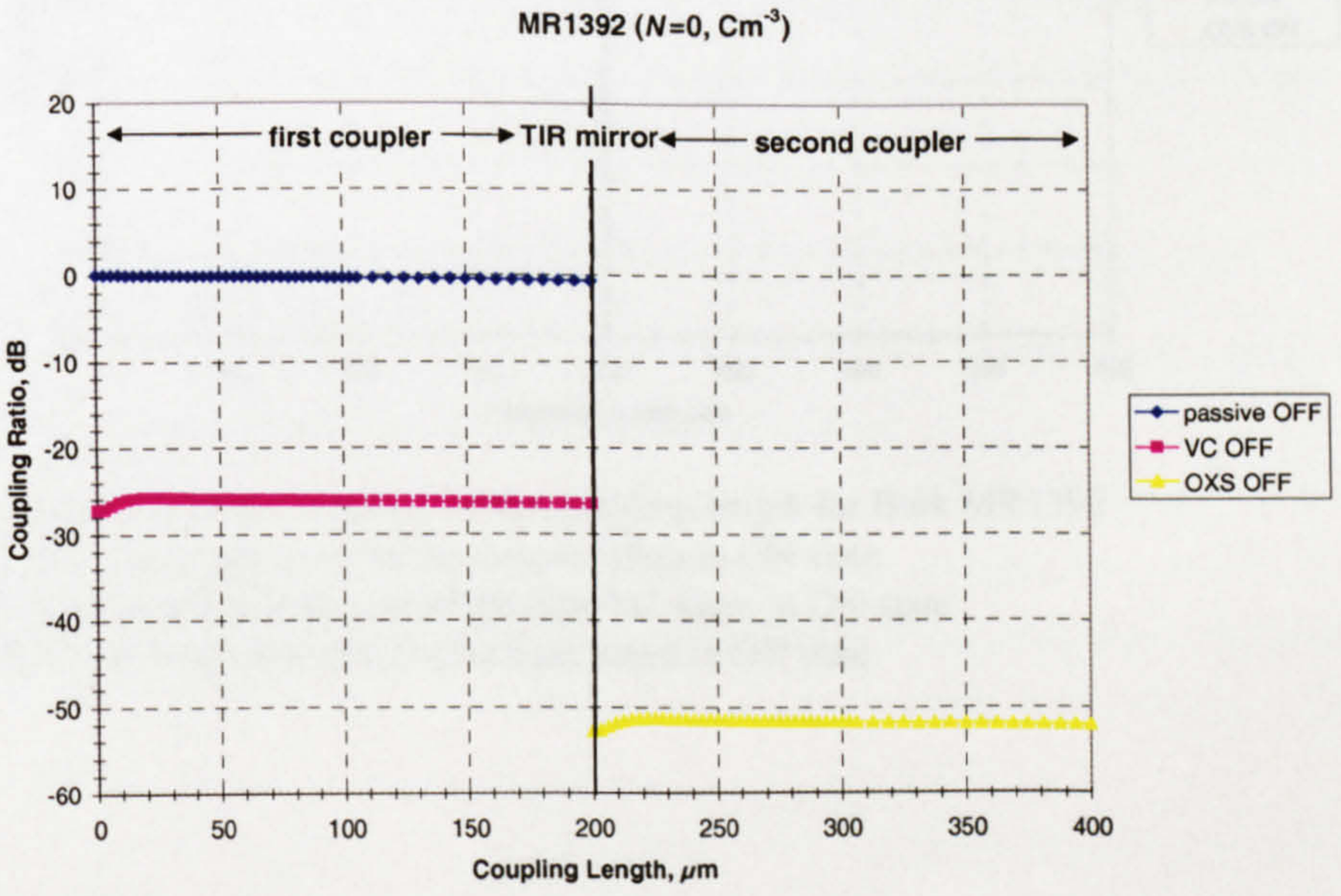

Figure4.11 Coupling process along the OXS coupler length for Bulk MR1392 at OFF state

- Passive OFF: Transmission at the bar-output when in OFF state
- VC OFF: Transmission at the end of the first VC when in OFF state
- OXS OFF: Transmission at the cross-output when in OFF state

The device made with the bulk structure MR1392 shows much better results. This is certainly due to the match of refractive index n_{eff_AUW} to the respective n_{eff_PLW} at a lower value.

With this material when the device is in "OFF state", as shown in Figure4.11, at the bar-output the optical signal transmission is attenuated by only 0.7 dB. At the other end, the cross-output, shows an excellent crosstalk of –52 dB due to reduced residual coupling.

When the device is turned ON, as in Figure4.12, the signal transmission at the bar-output is attenuated by 6 dB. The cross-output shows a gain slightly higher than 9 dB. By comparison with the respective value when the device is in "OFF state" the ON-OFF contrast calculated is higher than 61 dB.

Let us now suppose to have a device slightly shorter, e.g. 175μm coupling length, the "Passive ON" curve, shows a further reduction down to –8.5 dB. The gain drops from 9.08 dB to 8dB by only 1 dB, which can be considered negligible.

The ON-OFF contrast instead reduces from 61.2 to 60dB.

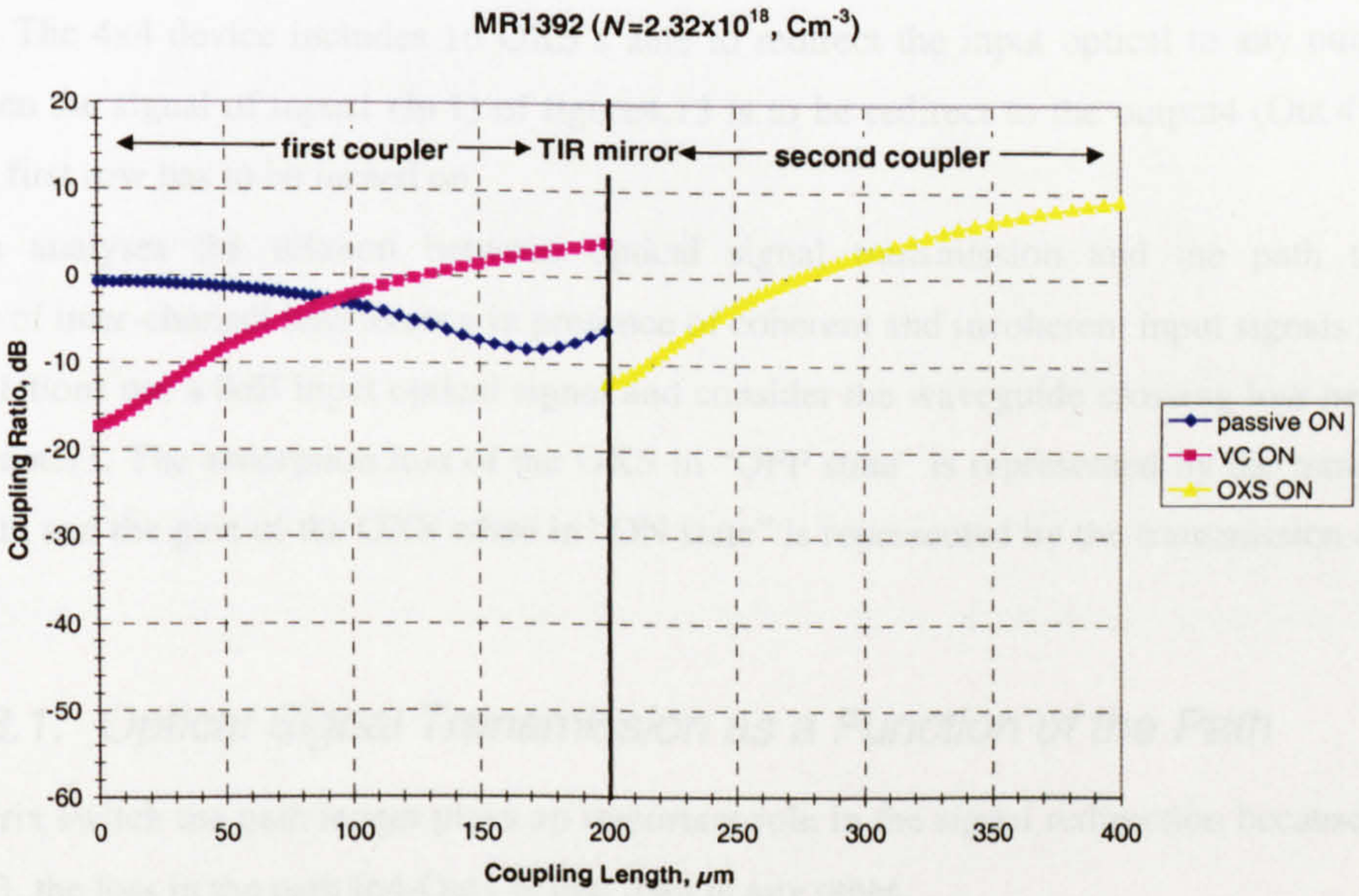

Figure4.12 coupling ratio as a function of the coupling length for Bulk MR1392

- Passive ON: Transmission at the bar-output when in ON state
- VC ON: Transmission at the end of the first VC when in ON state
- OXS ON: Transmission at the cross-output when in ON state

4.3. The 4x4 Matrix Switch

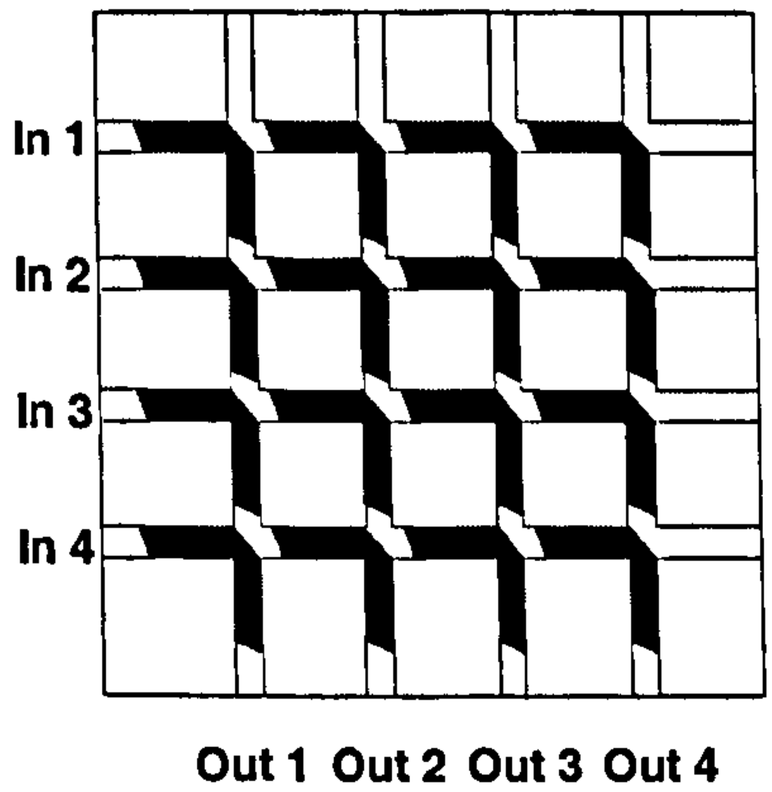

Figure4.13 The 4x4 switch matrix

Using the results achieved in the previous section an accurate analysis of the 4x4 matrix switch device can be done. The 4x4 device includes 16 OXS's able to redirect the input optical to any output. As an example, when the signal of input1 (In 1) of figure4.13 is to be redirect to the output4 (Out 4), the forth switch in the first row has to be turned on.

This section analyses the relation between optical signal transmission and the path taken. The investigation of inter-channel interference in presence of coherent and incoherent input signals follows.

All the calculations use a 0dB input optical signal and consider the waveguide crossing loss negligible, as shown in Chapter3. The absorption loss of the OXS in "OFF state" is represented by the transmission at the bar-output, and the gain of the OXS when in "ON state" is represented by the transmission at the cross output.

4.3.1. Optical Signal Transmission as a Function of the Path

In a 4x4 matrix switch the path length plays an important role in the signal redirection because, as shown in Figure4.13, the loss in the path In4-Out1 is less than in any other.

Table4.4 and Table4.5 estimate the transmitted signal as a function of the path. The first column on the left and the last row at the bottom represent respectively the input and the output channels for the matrix switch as shown in Figure4.13. The other numbers, at the matrix intersection, represent the optical signal transmission at the output. For example the signal transmitted through path In4-Out1 of the MR1453 device is of 15.56 dB.

In 1	-5.46	-12.47	-19.47	-26.48
In 2	1.55	-5.46	-12.47	-19.47
In 3	8.55	1.55	-5.46	-12.47
In 4	15.56	8.55	1.55	-5.46
	Out 1	Out 2	Out 3	Out 4

Table4.4 Optical signal transmission at the cross-output for a MR1453 4x4matrix switch (data in dB)

It can be seen that the structure MR1453 has high loss in most of the paths The difference between the shortest and the longest path is very high not making MR1453 wafer really suitable for applications.
The results of device MR1392, shown in Table4.5 instead, confirm the high quality of the design. It does show an output signal in the range of 5 and 9dB gain respectively on the longest and shortest path.

In 1	7.03	6.34	5.66	4.97
In 2	7.71	7.03	6.34	5.66
In 3	8.40	7.71	7.03	6.34
In 4	9.08	8.40	7.71	7.03
	Out 1	Out 2	Out 3	Out 4

Table4.5 Optical signal transmission at the cross-output for a MR1392 4x4matrix switch (data in dB)

4.3.2. Multipath Interference in the 4x4 Matrix Switch Device

It is also interesting to investigate the channel interference in terms of crosstalk. It can due to different reasons:

- Crosstalk at the switching cell
- Crosstalk at the cross between waveguides
- Crosstalk coupled between waveguides

The first one is the most important because it is strictly related to the wafer structure. As it has been shown for wafer MR1453, a device made with an approximate vertical coupler structure gives problems in terms of unwanted transmitted signal or high absorption loss. In particular the presence of a signal transmitted to the bar-output when the switch is in "ON state" highlight the problem that is going to be treated in this section.
Before starting any analysis let us assume no power coupling between two parallel waveguides. This is due to the big separation gap of 250 μm. Thus, the analysis is limited to the crosstalk due to the presence of the switch cells in the path and it is done with optically coherent and optically incoherent input signals.

The total number of switching path combinations in a 4x4 matrix is 36 but in terms of multipath interference only two extreme cases need be treated. Following the layout of figure4.13, the matrix configurations are:

CASE A: switches In1-Out1, In2-Out2, In3-Out3, In4-Out4, in "ON state"

CASE B: switches In1-Out4, In2-Out3, In3-Out2, In4-Out1, in "ON state".

λ 1	-5.46	-27.09	-34.10	-41.10
λ 2	-43.08	-5.46	-27.09	-34.10
λ 3	-36.07	-43.08	-5.46	-27.09
λ 4	-29.07	-36.07	-43.08	-5.46
	Out 1	Out 2	Out 3	Out 4

CASE A

λ 1	-35.09	-42.09	-49.10	-26.48
λ 2	-28.08	-35.09	-12.47	-49.10
λ 3	-21.07	1.55	-35.09	-42.09
λ 4	15.56	-21.07	-28.08	-35.09
	Out 1	Out 2	Out 3	Out 4

CASE B

Table 4.6 Multipath Interference for 4x4 matrix MR1453 (data in dB)

Matrix switch made with wafer MR1453 shows poor results due to the high crosstalk. In particular all the outputs show an interchanel crosstalk as high as –21.63dB, which become –8.61dB in the worst case between wavelength λ1 and λ4 on the output 4 as shown in Table4.6.

Improved results are achieved with the wafer structure MR1392. In fact looking at Table 4.7 it can be seen that the situation is much improved. The worst case is with the matrix in configuration with switches In1-Out1, In2-Out2, In3-Out3, In4-Out4, in "ON state".

λ 1	7.03	-65.73	-66.42	-67.10
λ 2	-53.53	7.03	-65.73	-66.42
λ 3	-52.85	-53.53	7.03	-65.73
λ 4	-52.16	-52.85	-53.53	7.03
	Out 1	Out 2	Out 3	Out 4

CASE A

λ 1	-59.63	-60.32	-61.00	4.97
λ 2	-58.95	-59.63	6.34	-61.00
λ 3	-58.26	7.71	-59.63	-60.32
λ 4	9.08	-58.26	-58.95	-59.63
	Out 1	**Out 2**	**Out 3**	**Out 4**

CASE B

Table 4.7 Multipath Interference for 4x4 matrix MR1392 (data in dB)

However, the results show in both situations that the multipath interference is almost negligible. In fact in the worst situation the interference crosstalk always lower than -52dB. Value this that becomes almost -60dB in the best configuration.

4.3.2.1. Optically Incoherent Input Signals

Four optical signals, λ_1, λ_2, λ_3, λ_4, are called incoherent when they differ in phase and in wavelength. The total *Multi-Path Interchannel (MPI)* is the sum of all incoherent crosstalk, and expressed by the formula:

$$P_{MPI} = \sum P_i \tag{4.1}$$

where I_i is the absolute power of each channel.

As result of it, it can be calculated the *Signal to Noise Ratio (SNR)* expressed by the:

$$SNR(dB) = 10\log\left(\frac{P_{signal}}{P_{MPI}}\right) \tag{4.2}$$

The results for incoherent signals and MR1453 structure expressed in next Table4.8, represent both cases of Table4.6 a) and b).

P_{signal}	-5.46	-5.46	-5.46	-5.46
P_{MPI}	-28.14	-26.48	-26.21	-26.16
SNR	22.68	21.02	20.75	20.70
	Out 1	**Out 2**	**Out 3**	**Out 4**

CASE A

P_{signal}	15.56	1.55	-12.47	-26.48
P_{MPI}	-20.14	-20.87	-27.26	-34.15
SNR	35.70	22.42	14.79	7.67
	Out 1	**Out 2**	**Out 3**	**Out 4**

CASE B

Table4.8. Multi Path Interference and Signal Noise Ratio for 4x4 matrix MR1453, (all the data are expressed in dB)

The same can be done also for MR1392, which results are shown in next Table4.9.

P_{signal}	7.03	7.03	7.03	7.03
P_{MPI}	-48.04	-50.05	-53.07	-61.61
SNR	55.07	57.07	60.10	68.64
	Out 1	Out 2	Out 3	Out 4

CASE A

P_{signal}	9.08	7.71	6.34	4.97
P_{MPI}	-54.14	-54.55	-55.01	-55.51
SNR	63.22	62.26	61.35	60.48
	Out 1	Out 2	Out 3	Out 4

CASE B

Table4.9. Multi Path Interference and Signal Noise Ratio for 4x4 matrix MR1392 (data expressed in dB)

4.3.2.2. Optically Coherent Input Signals

The analysis become even worse for MR1453 with coherent input signals. In this case the signals have the same wavelength and the switched signal overlap with the others that generate interference strong enough to alter the real output. With well-designed material like MR1392 instead the interference signals are very low power that the contribution to the switched signal is almost imperceptible.

$$P_{MPI} = \left(\sqrt{P_1} + \sqrt{P_2} \ldots\right)^2 \tag{4.3}$$

With MPI for coherent signals given by the (4.3) the SNR can be calculated for MR1453

P_{signal}	-5.46	-5.46	-5.46	-5.46
P_{MPI}	-24.74	-23.49	-22.98	-22.76
SNR	19.28	7.83	17.52	17.30
	Out 1	Out 2	Out 3	Out 4

CASE A

P_{signal}	15.56	1.55	-12.47	-26.48
P_{MPI}	-16.75	-18.87	-24.35	-30.76
SNR	32.31	20.42	11.89	4.28
	Out 1	Out 2	Out 3	Out 4

CASE B

Table4.10. Multi Path Interference and Signal Noise Ratio for 4x4 matrix MR1453 (data expressed in dB)

And for structure MR1392

P_{signal}	7.03	7.03	7.03	7.03
P_{MPI}	-43.29	-46.19	-50.17	-56.86
SNR	50.31	53.22	57.20	63.89
	Out 1	Out 2	Out 3	Out 4

CASE A

P_{signal}	9.08	7.71	6.34	4.97
P_{MPI}	-49.39	-49.82	-50.28	-50.76
SNR	58.47	57.53	56.62	55.73
	Out 1	Out 2	Out 3	Out 4

CASE B

Table4.11. Multi Path Interference and Signal Noise Ratio for 4x4 matrix MR1392 (data in dB)

4.4. Conclusions

Following the theoretical model of the previous chapter a characterisation of two vertical coupler structures already grown in earlier times has been given. From the first part of the investigation it has been possible to categorise material MR1453 as a bad example of design and MR1392 instead as a well designed structure.

The first part of the 2D analysis is used to verify the position of the passive waveguide refractive index in between the range of the active waveguide refractive index, which reduce its value when carrier density is injected into the device. In particular MR1392 shows a n_{eff_PLW} exactely half way of the n_{eff_AUW} range while for MR1392 the refractive index equalisation is achieved at $N=N_{max}$. The right value of carrier density necessary to get the best coupling between the two waveguides is calculated with the second part of the 2D model. The 3D model shows that both materials transfer all the power from one waveguide to the other within 200μm.

At this point all the device is modelled and MR1453 device show a low ON-OFF contrast and an high crosstalk which make the device unsuitable in 4x4 matrix configuration. It is also affected by high multipath interference.

MR1353 show a ON-OFF contrast as high as roughly 61dB and an excellent crosstalk of 52dB. This results permit to get a device with a very low multipath interference.

In next chapter the fabrication of the 4x4 matrix switch will be discussed.

4.5. References

[1] Y. Takeda, A. Sasaki, Y. Imamura, and T. Takagi, "Electron Mobility and Energy Gap of $In_{0.53}Ga_{0.47}As$ on InP", Journal of Applied Physics, Vol. 47, No.12, 1976, pp.5405-5408.

[2] S.M.Sze, "Physics of Semiconductor Devices - 2nd ed.", 1981, John Wiley & Soons

[3] D. Marcuse, "Theory of Dielectric Optical Waveguides - 2nd ed.", 1991, Academic Press Inc.

[4] M. Owen, "Monolithic Integration of Optical Space Switches", 1998, PhD Thesis University of Bristol

Chapter 5

4X4 Crosspoint Fabrication

After the theoretical analysis covered in the previous chapters, this part of the thesis describes working procedures and typical problems that are related to the fabrication of the optical crosspoint switch.
Starting from the grown wafer, the first section of the chapter details all the fabrication phases involved. Then, it is analysed how the loss introduced by the fabrication can be attributed to the photolithography alignment and to the quality of the etch process adopted.
Finally the descriptions of a novel process to passivate the sidewall of the ridge present in the switch cell close the chapter. The tests over a sample of ridge waveguide lasers confirm that this method can be introduced into the fabrication process of future OXS's.

Glossary of the abbreviations

(DI) De-Ionised

(RIE) Reactive Ion Etching

(SEM) Scanning Electron Microscope

(COD) Catastrophic Optical Damages

(RW) Ridge Waveguide

(OXS) Optical Crosspoint Switch

5.1. Fabrication Procedure

5.1.1. Basic Information

From the theoretic simulation in the previous chapter, two wafers have been chosen for the realisation of the OXS. Wafer MR1453, based upon a MQW structure and wafer MR1392, which is realised with bulk material.

The wafers are MOVPE grown upon a (100) InP substrate and based on an InGaAsP/InGaAs/InP multilayer structure. They have been made at the EPSRC III-V Central Facilities at the University of Sheffield. The OXS fabrication, instead, is completely executed at the Clean Room Facilities of the Optics Group of the University of Bristol. Appendix A shows the layer structure for both wafers MR1453 and MR1392.

The device is based on two different etching steps. The first one defines two perpendicular groups of ridge waveguides, 3 μm wide with a 250 μm separation that form the input and the output of the OXS. The second etch, instead, realises the TIR mirror and defines the coupling regions.

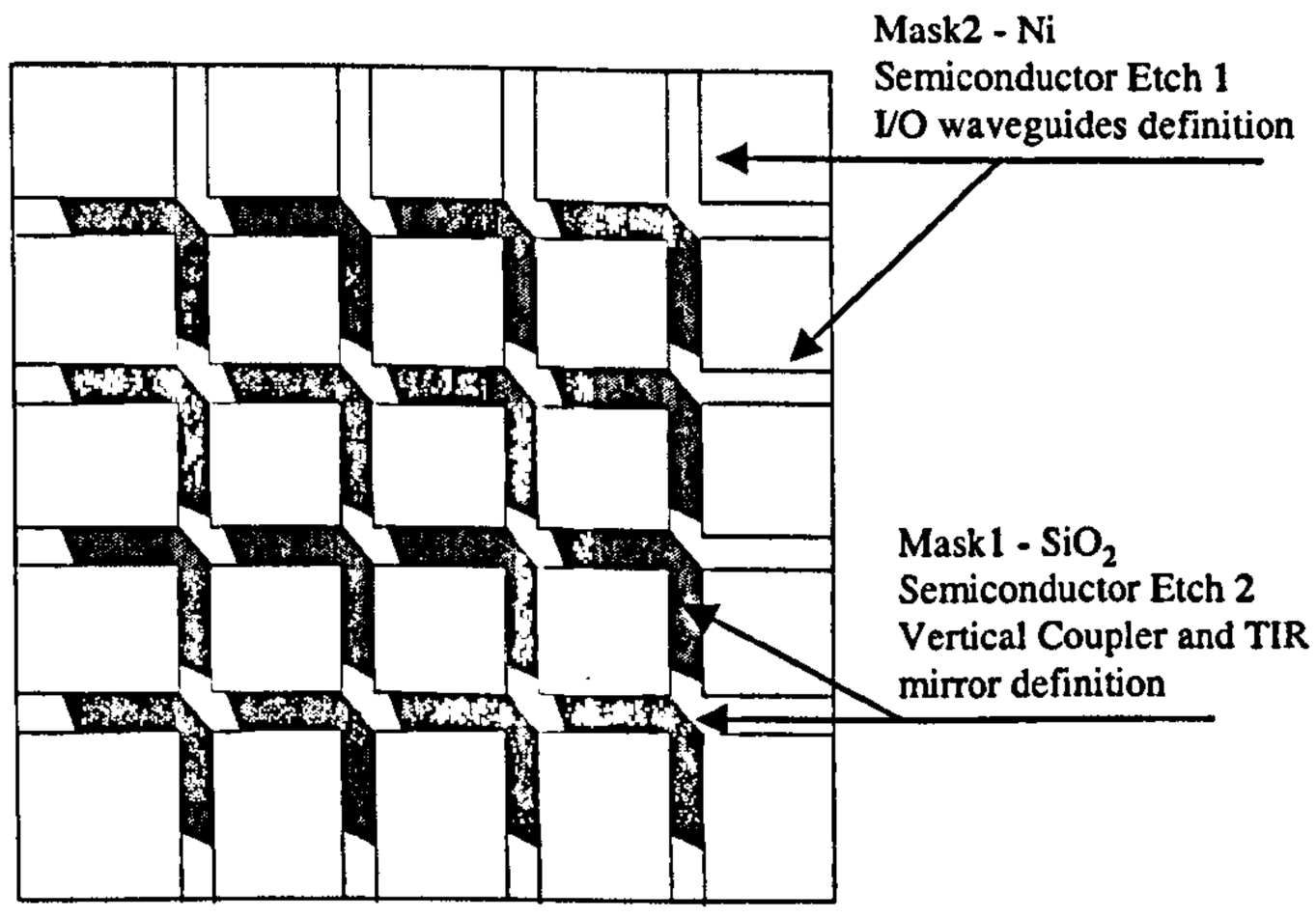

Figure5.1 Masks and etch steps defines the shape of the crosspoint

SiO_2 is used in order to passivate the device and contact windows are opened on it to permit the electrical connection. The p-contact and n-contact are obtained adopting Au based multilayers described in details in the next section.

5.1.2. Fabrication Steps

After a brief introduction to the process this part describes in details each single phase of the process. Different photolithography masks are used in particular to prepare the samples for the semiconductor etching steps and to open the p-contact window on top of the ridge of the crosspoint.

The process is divided into 3 main phases:

- Preparation of the etching mask
- Semiconductor dry etching
- Finally contacts realisation.

5.1.2.1. Define TIR mirror and ridge waveguides (self aligned masks)

Step	Description
1	Surface clean: realised using methanol/acetone/isopropanol ultrasound bath for 5min each, followed by rinse in De-Ionised (DI) water and blown dry with Nitrogen (N_2).

Following the cleaning, Mask 1 is made on top of the semiconductor cap layer. The semiconductor etch with this mask defines the TIR mirror and the coupler length, see Figure5.1.

2	Etch-Mask1: Sputter of 500nm of Silicon Dioxide (SiO_2)
3	Etch-Mask1: Spin on photoresist S1805, prebake 30 minutes and photolithography exposure for 35seconds using photolith mask1. Photoresist develop for 45 seconds by dipping the sample in MF319 positive developer.

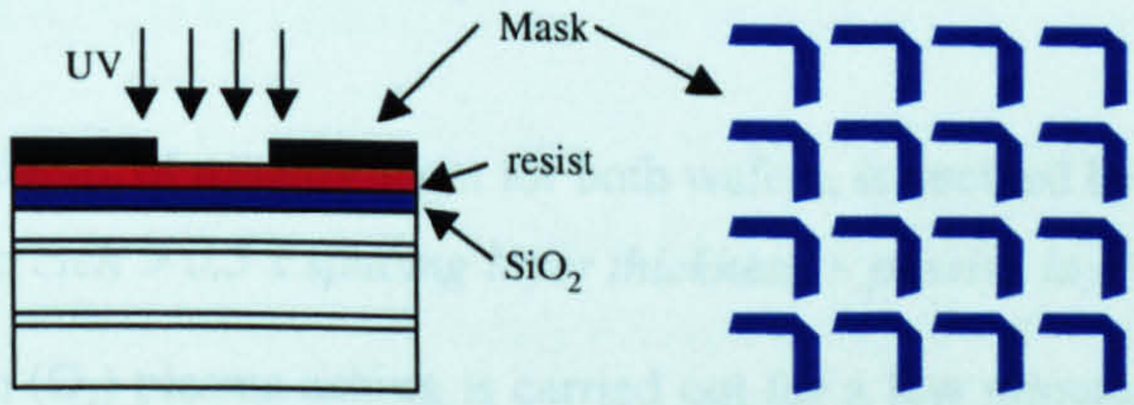

4	Etch-Mask1: Thermal evaporation of 50 nm of Nickel (Ni) followed by photoresist, then lift off in acetone.

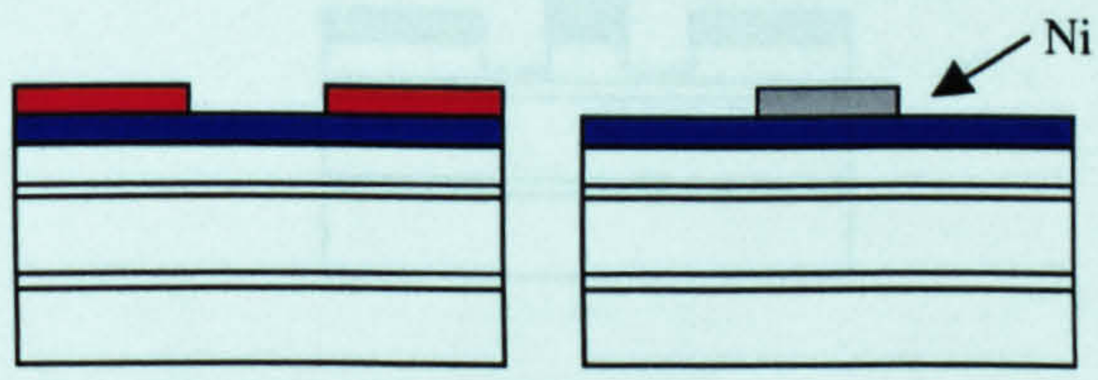

5	Etch-Mask 1: SiO_2 dry etching inside Reactive Ion Etching (RIE) chamber with Hexafluoroethane (C_2F_6) ambient. Afterwards the Ni is removed by soaking the sample into a solution of Sulphuric Acid (H_2SO_4), then rinse in RO water and dry up with N_2.

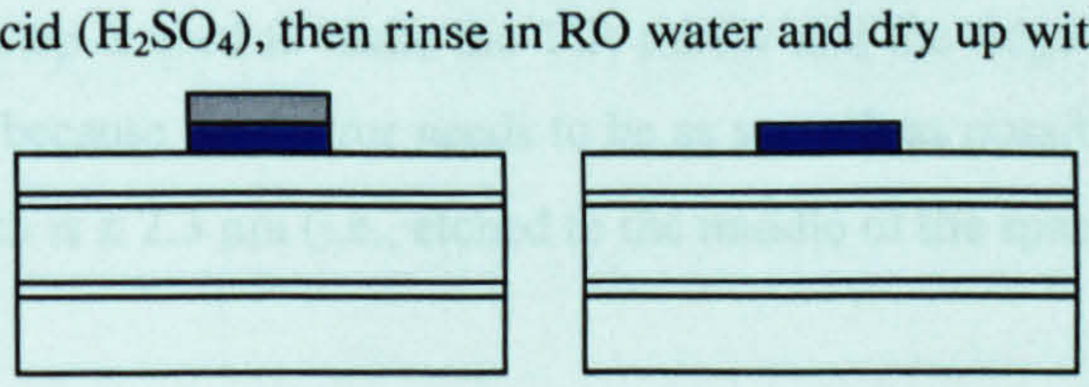

Following Mask 2 is made on top of Mask 1. It defines the waveguides that, properly aligned to the TIR mirrors, form the coupler and the passive waveguides that connect the switches, see Figure5.1.

6 Etch-Mask 2: The process starts with the spins of a layer of S1805 photoresist and photolithography patterning as described in previous step 3. Thermal evaporation of 50nm of Ni follows and finally the lift off of the photoresist gives the right shape to the mask. The sample is then SiO_2 etched as in the previous step and then ready to be semiconductor etched.

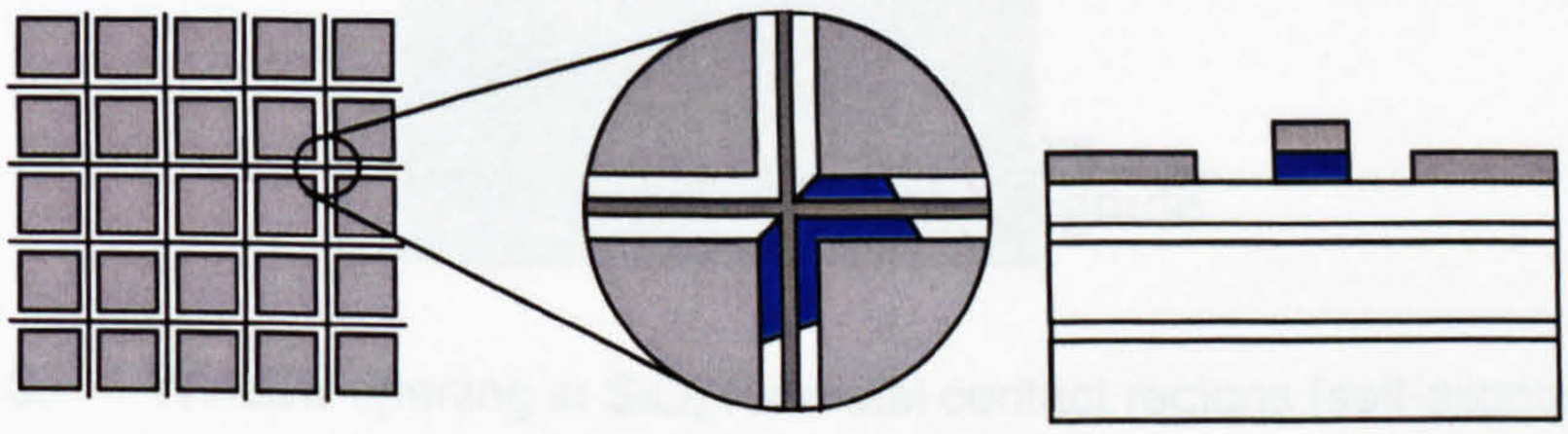

5.1.2.2. Definition of the couplers by RIE dry etching

The etching of the semiconductor layers is done in a reactive ion-etching chamber pre-vacuumed to a base pressure of $5x10^{-5}$ mTorr and then filled up with a Hydrogen/Methane (H_2/CH_4) gas mixture in flow rate of 10/13 sccm. Under such conditions the expected etch-rate is of ≈50nm/min for InP and ≈30nm/min for InGaAsP at a power of 300W and DC bias voltage of 400V.

Step	Description
7	Etch 1: The etching depth, of roughly 1 μm for both wafers, is decided by *Depth 1st etch > 0.5 x spacing layer thickness + passive layer thickness*
8	Etch 1: First Oxygen (O_2) plasma ashing is carried out for a few minutes in order to get rid of any unwanted layer created during the previous SiO_2 etch. The InP RIE etching follows, making two trenches that go into the material according to the above requirement.

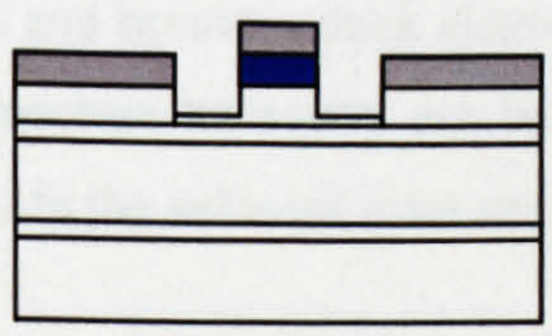

Before starting the second etch, Etch-Mask2 in Ni has to be removed as shown in previous step 5. It reveals Etch-Mask1 in SiO_2.

9 Etch 2: This etching step is used to make the TIR mirror and the ridge of the vertical coupler. This is a critical step because the mirror needs to be as smooth as possible with a vertical angle 90°±2°. The etch-depth is ≅ 2.3 μm (i.e., etched to the middle of the space layer)

10 Mask1 removal: the immersion of the sample for few seconds into aqueous solution of Hydrogen Fluoride (HF) etches off the SiO_2 of Mask1. At this point of the process the sample looks like the figure shown below. The picture is a real sample seen under the Scanning Electron Microscope (SEM).

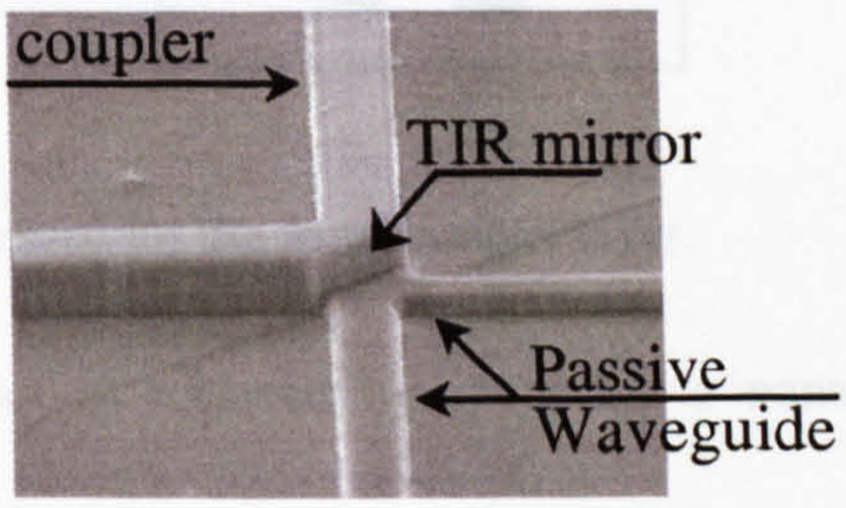

5.1.2.3. Window opening in SiO_2 for metal contact regions (self-aligned process)

The top and back surface of the samples need to be metal coated in order to make the contacts. For the top p-contact layer, the samples are passivated with an isolation layer that is removed only from the top of the vertical couplers. The backside of the sample is first lapped removing a few hundred μm of InP substrate and then coated with a n-contact.

Step	Description
11	p-Side passivation: It is made by coating the top side of the samples with 160nm of SiO_2.
12	Contact Window mask: Spin on photoresist S1813 and prebake 30 min. Use of a reduced dose of UV exposure, 35 sec. with the window mask, then develop the photoresist for 45 sec. by immersing the sample in a beaker containing positive developer MF319. Rinse in DI water, blow dry with N2 and finally postbake for 30 sec. The reason to under-expose to the UV light it is because after photoresist spinning the sample has a layer that is thin on the ridges and becomes thick elsewhere. Thus, because our target is to remove only such thin layer the exposure necessary can be reduced. This will permit to clear only the top of the ridge and keep safe the sidewall from any unwanted SiO_2 etch.

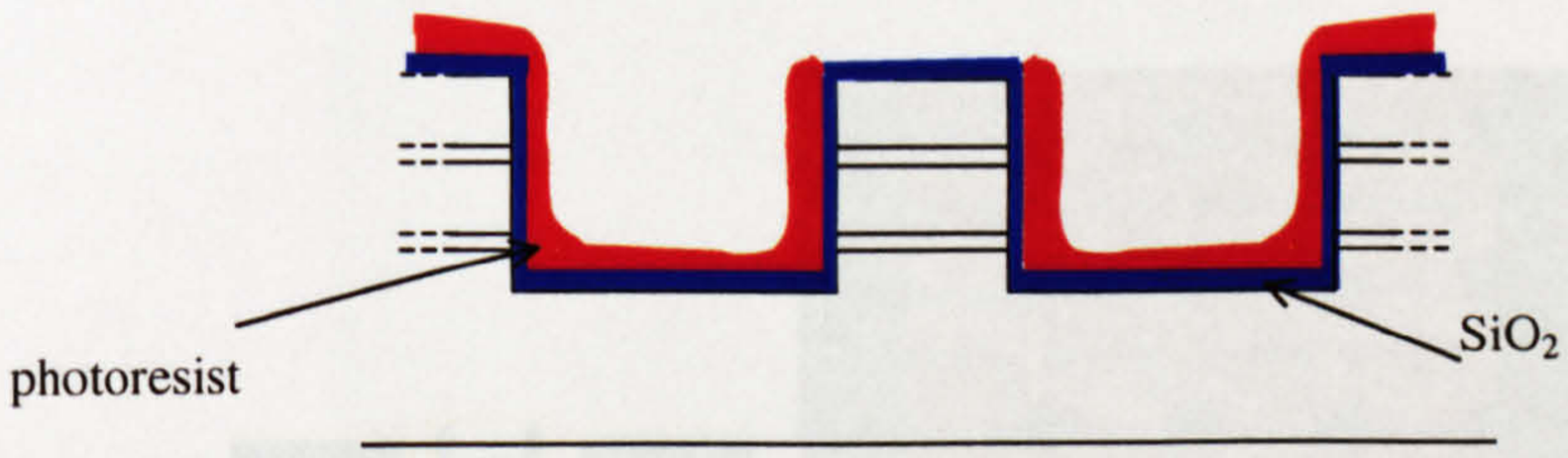

13 Contact Window opening: SiO2 dry etching inside RIE chamber with C2F6 ambient.. The figure below shows that window open into the SiO2 layer just on top of the coupler ridges

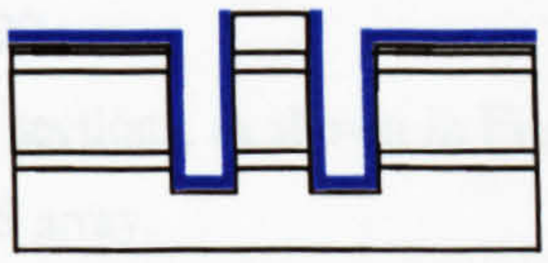

Then, the top layer is ready to be processed for the metal contact layer.

14 p-contact: the metal contact is achieved by sputtering a nonalloy Titanium/Gold (Ti/Au 100/400 nm) multilayer.

15 Separation contact: the window mask is patterned as shown in point 12 but using exposure time of 120 secs, because the gold layer reflect the UV light, causing interference fringes in the resist.

16 Separation contact: Gold wet etching with aqueous solution of Iodine–Potassium Iodide (ratio 3/42). It is an etchant with etch rate as fast as 2500Å/sec. The Ti is dry etched in RIE chamber with SiCl4 ambient

Now the thickness of the samples needs to be reduced by lapping and polishing the backside.

17 Wafer thinning: The samples are fixed to the thinning chuck with wax and mechanically thinned down to the thickness of 100/120 μm using alumina powder.

18 n-contact: After being removed from the chuck the samples are mounted up side down on a glass slide and coated with a multilayer made of Au/Ge/Au/Ni/Au

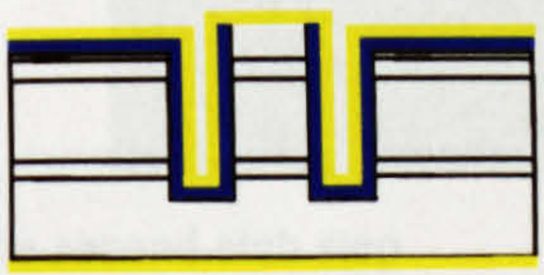

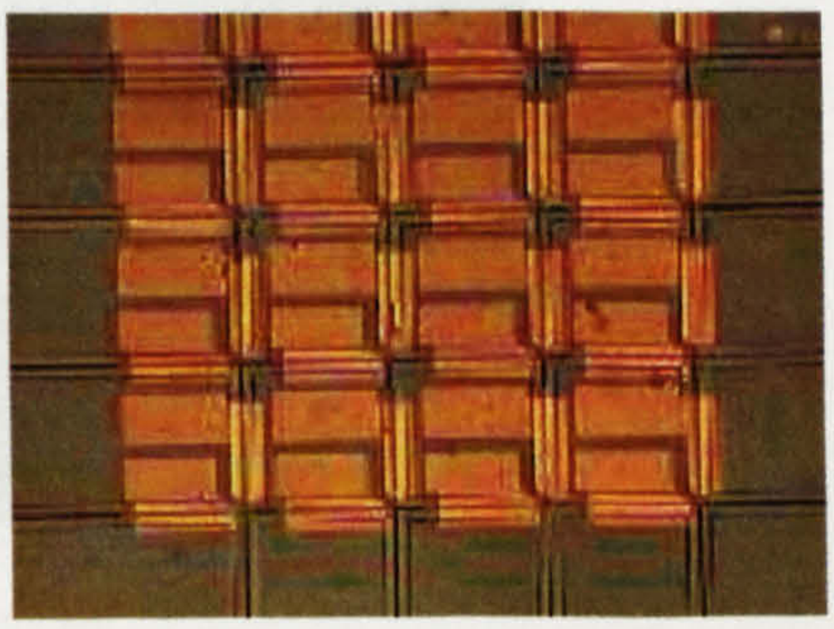

The samples are ready to be cleaved in 4x4 or 1x4 arrays and tested.

5.1.3. Wafer Layout

The samples, which are 8x8 mm, are divided into four rows, with each one including OXS's with a coupling length ranging 100, 150, 200, and 220 μm.

Each row is made up by four 4x4 OXS array sections, as shown in Figure5.2 a), the sample layout and in Figure5.2 b), a partial picture of one 4x4 OXS array.

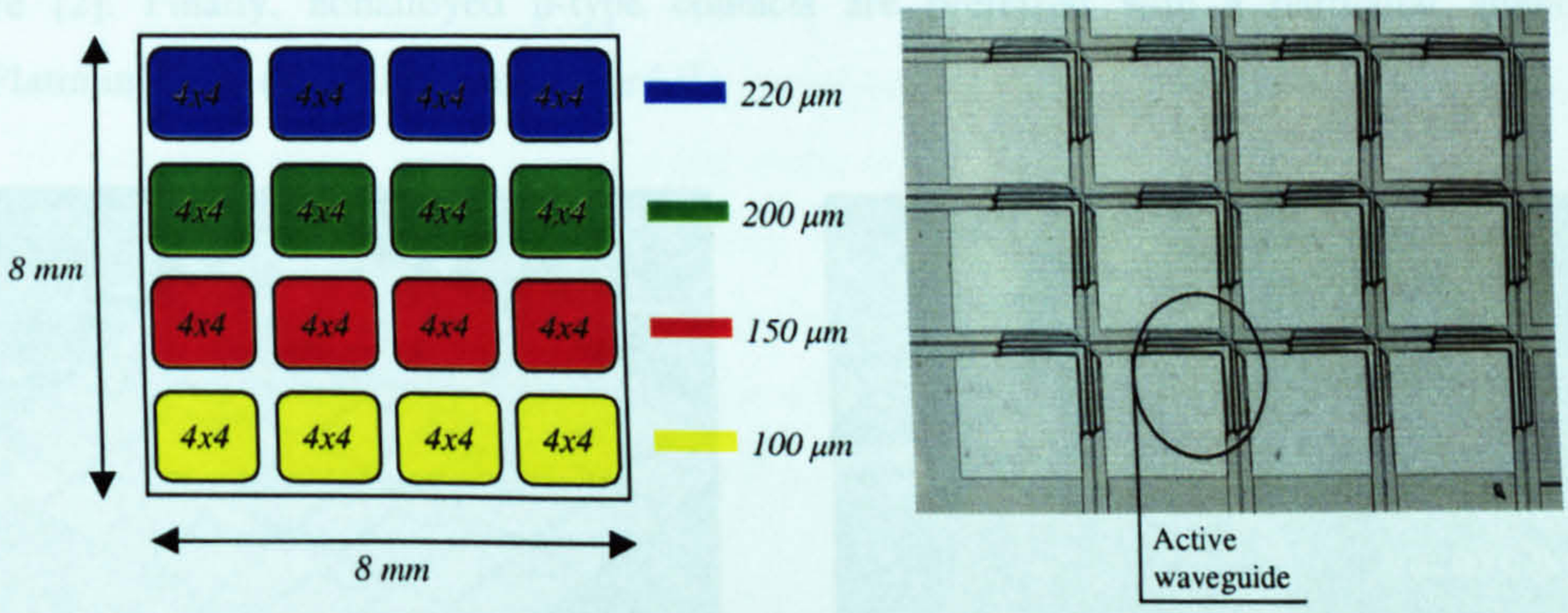

Figure5.2 OXS, wafer layout (left) and part of a 4x4 device prior to metalisation (right)

Sixteen 4x4 array chips are cleaved from each sample, which measure approximately 1-1.5 mm^2 each. However, the devices can be further cleaved into single and 1x2 switching cells, bonded up and tested.

5.1.4. Etching Quality and final Test Device

The previous section has shown that the OXS is fabricated with two etching steps.

- *Shallow etch,* which defines the two perpendicular groups of ridge passive waveguides.
- *Deep etch,* which defines the TIR mirror and the ridge of the vertical coupler.

Both processes require high anisotropy and smoothness in order to reduce the waveguides scattering loss and to improve the reflectivity of the TIR mirror.

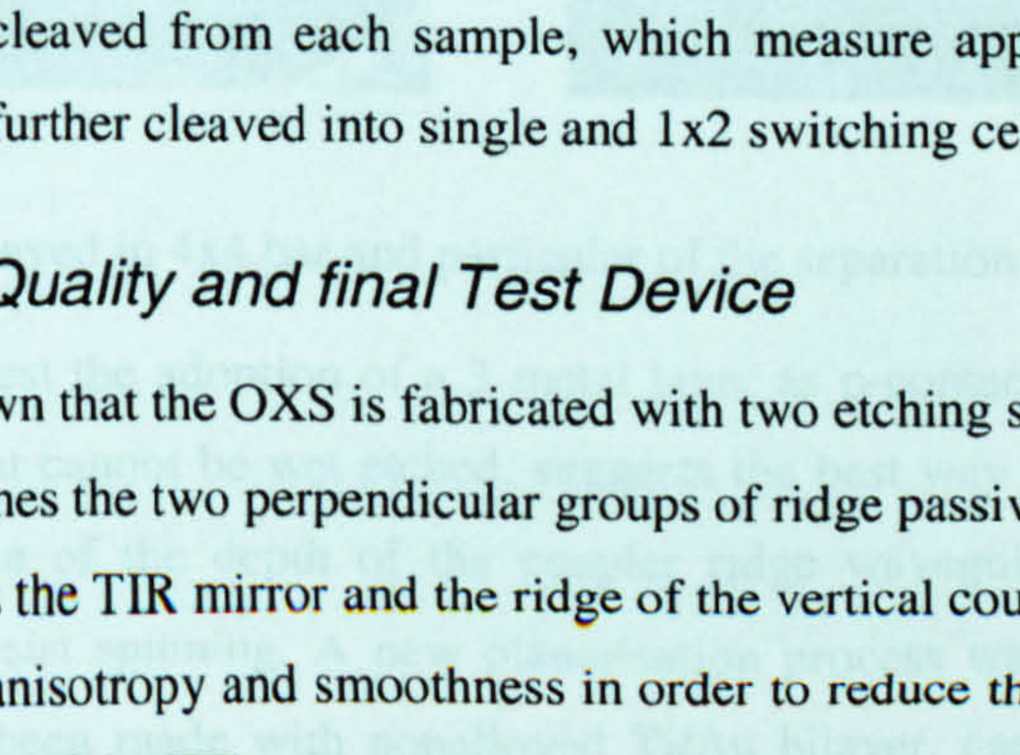

Figure5.3 OXS, end of the second etch step

Etching quality is strongly related to the quality of the Ni/SiO_2 mask. Thus, the following section is dedicated to this relation and presents the problems incurred during the mask patterning and semiconductor etching stages.

As for the metal contacts, it is well known that a good metalisation improves the electrical characteristics of the device and that the lower is the parasitic resistance the higher would be the operation frequency [1]. It is also demonstrated that deposition by sputter evaporation does not introduce extra damages to the III-V structure [2]. Finally, nonalloyed p-type contacts are preferred with a particular attention for Titanium/Platinum/Gold (Ti/Pt/Au) multilayer [3].

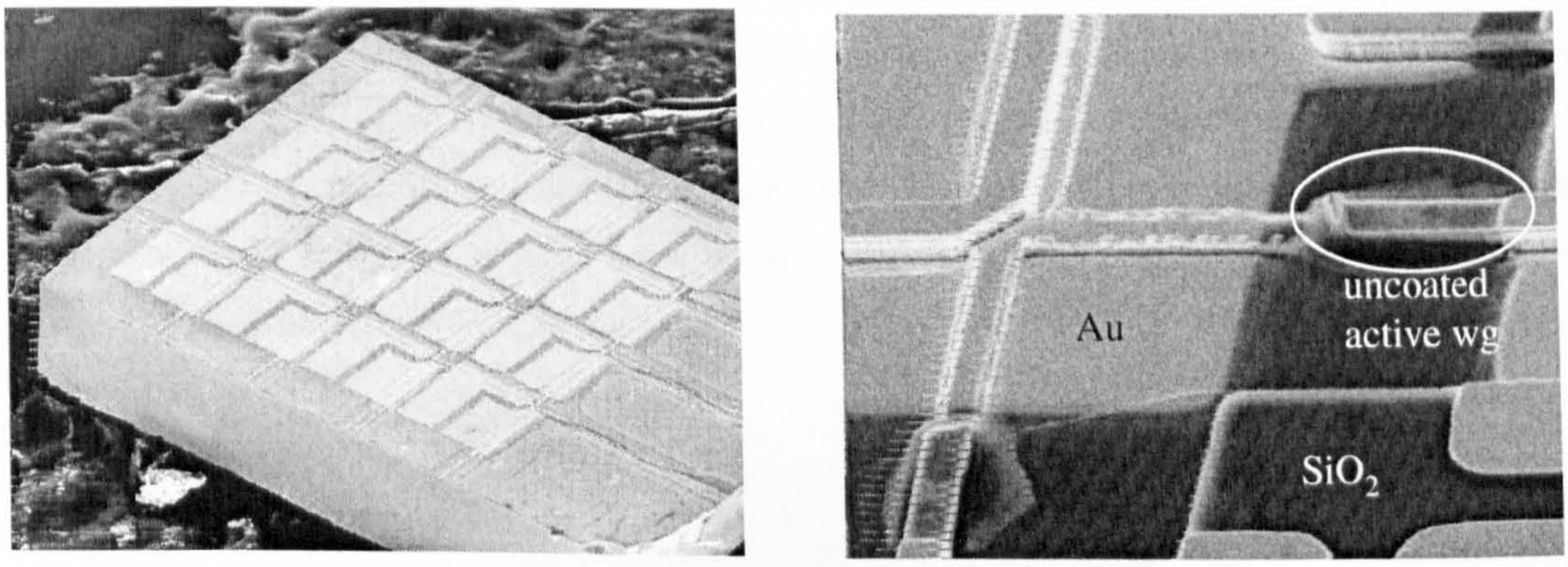

a) b)

Figure5.4 OXS, ended and cleaved in 4x4 bar and particular of the separation contact

All these considerations suggest the adoption of a 3 metal layer as p-contact. However, the presence of the Pt, which is a material that cannot be wet etched, suggests the best way of separating the contacts is by a lift-off process. Because of the depth of the coupler ridge waveguide the samples need to be planarised before the photoresist spinning. A new planarisation process was still under test and in the meantime the p-contact has been made with nonalloyed Ti/Au bilayer, capable of being separated by etching instead of lift off. In this case Au is etched using a wet gold etchant diluted in water (1/5 ratio) while Ti can easily be removed in a RIE chamber with silicon-tetrachloride $SiCl_4$ ambient.

Figure5.4 a) shows a cleaved 4x4OXS sample, with a zoom-in view of the metalisation contact, Figure5.4 b). The brighter region is gold that ends just few microns before the end of the coupler. This do not affect the coupling characteristic of the device but allows a higher contact separation mask alignment tolerance and reduces eventual parasites capacitance between couplers.

5.2. Mask Alignment Problems

It has already been stated that the device needs two etching steps. Thus, it is necessary to make two etch mask layers (Ni/SiO_2) with two photolithography steps. It is clear that the mask shape assume a very

important role for good etching results. The success of the switch is also related to the accurate alignment of the masks, as a twist or a shift between them can seriously deteriorate device performance.

5.2.1. The Etch Mask

The realisation of a well-made double mask is very important. A smooth pattern minimises the mask-induced roughness during the semiconductor etching. A rough sidewall on the ridge increases the scattering losses.

It has been shown before that the bilayer etch mask is realised with a Ni layer stacked on top of a layer of SiO_2. The Ni layer is lifted off from the unwanted areas, while the pattern of the SiO2 layer is made by dry etch, as described in steps 3 to 5 of the previous section. Because the etching of the TIR mirror is achieved using the SiO_2 mask, it is very important that this mask has a very smooth edge and a very vertical profile. This is because a rough mask shape could be transferred into the semiconductor etching profile, and a sloped etch mask profile would result in non-vertical etch profile in III-V semiconductor, both reducing the quality of the TIR mirror.

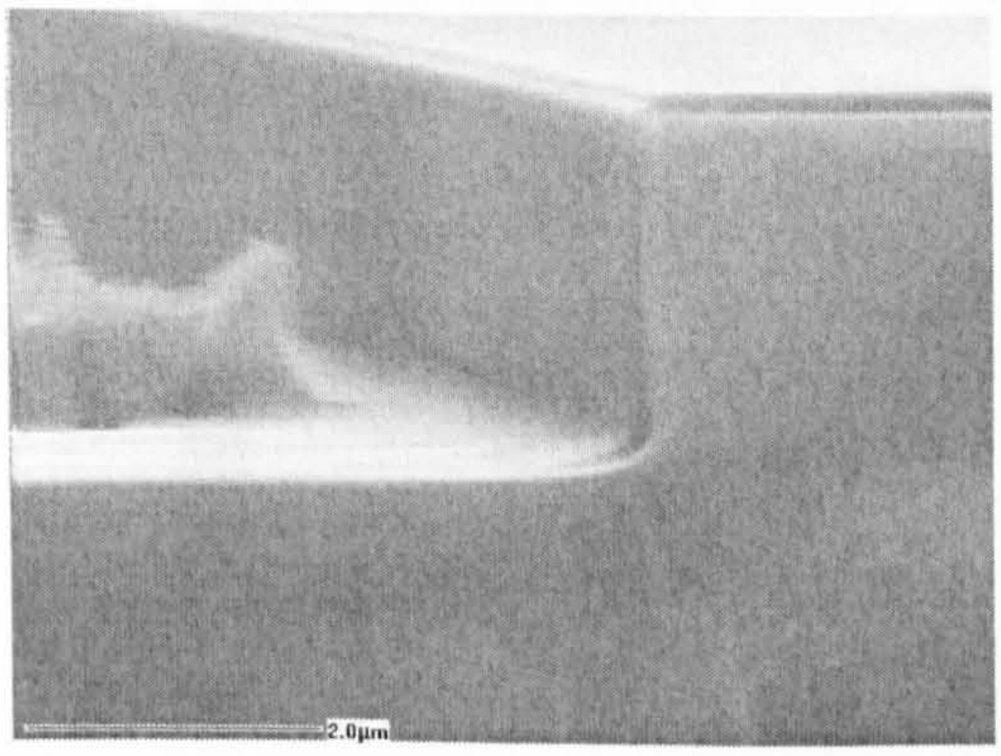

Figure5.5 dry etched SiO_2 sample

The gas mixture adopted for the etching of the mask plays a very important role in terms of smoothness and verticality. Figure5.5 shows a 2 µm deep etch in a SiO_2 sample with excellent verticality and smoothness worked out by a study on silica samples and carried out by a colleague, Chris Morgan, who works in silica and silicon passive devices.

5.2.2. The TIR Mirror – Alignment Error

Ni/SiO2 mask definition reflects all its quality to the etched device below affecting smoothness and verticality of the sidewall. However, it is not the only problem incurred. The alignment between the SiO_2 and Ni layers is also very important, because it defines the position of the TIR mirror relative to the waveguide cross. Figure5.6 and Figure5.7 below show pre and post etching results for different mask alignments. The first figure (a) shows the mask composition where the striped pattern is the SiO_2 layer

laying below the Ni mask which defines the cross waveguides. The second figure (b) shows the sample at the end of the semiconductor etching.

Figure5.6 shows a perfect alignment on the left hand side. In this case the SiO_2 masks edge exactly crosses corner to corner under the Ni mask. Hence, once etched the TIR mirror will be in the right position and at 45° with the passive waveguides direction.

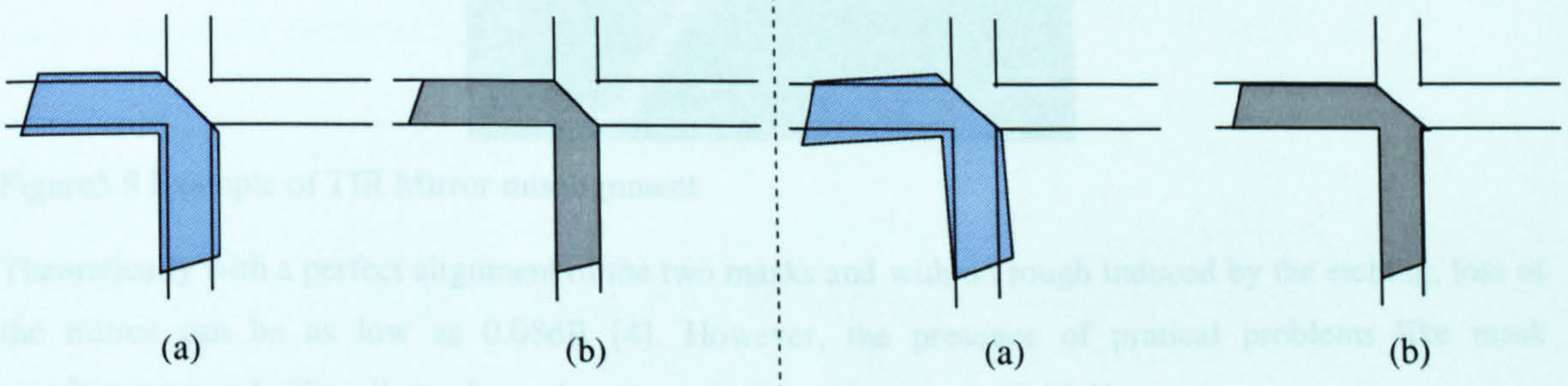

Figure5.6 LHS: Perfect Alignment; RHS: tilted

(a) mask composition, (b) resulting etched sample

The right hand side of Figure5.6, shows the two masks slightly twisted. In this case after the semiconductor etch the TIR mirror is not at a 45° angle, which may increase the losses.

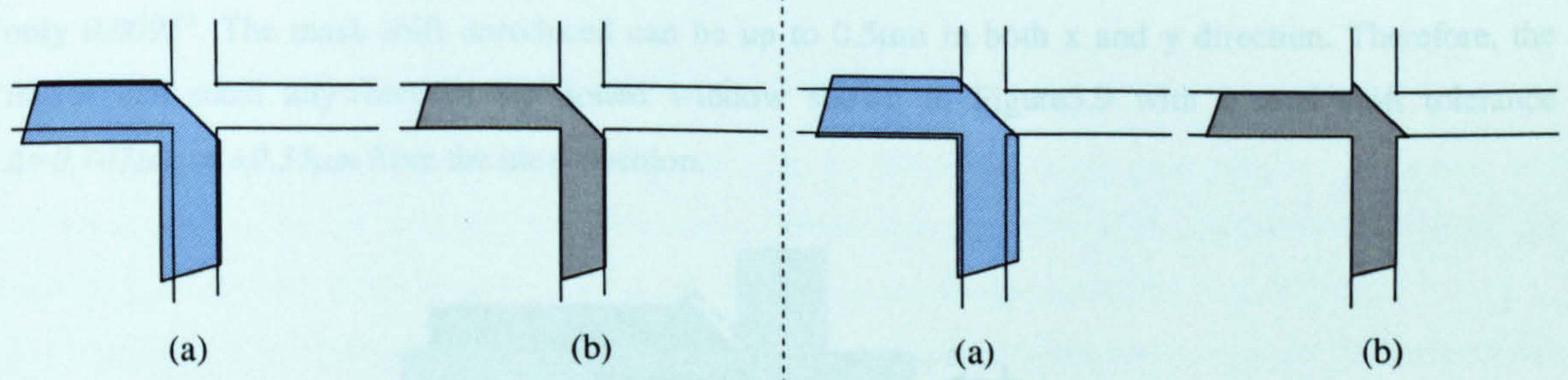

Figure5.7 mask misalignment due to shift error

(a) mask composition, (b) resulting etched sample

Figure5.7 shows how a shift can occur between the two masks. Once etched the mirror can be on either sides of the diagonal of the passive waveguides cross, thus high loss is expected. The test sample of Figure5.8 has a large mask misalignment placing the TIR mirror very far from the expected position represented in the picture by the dark line.

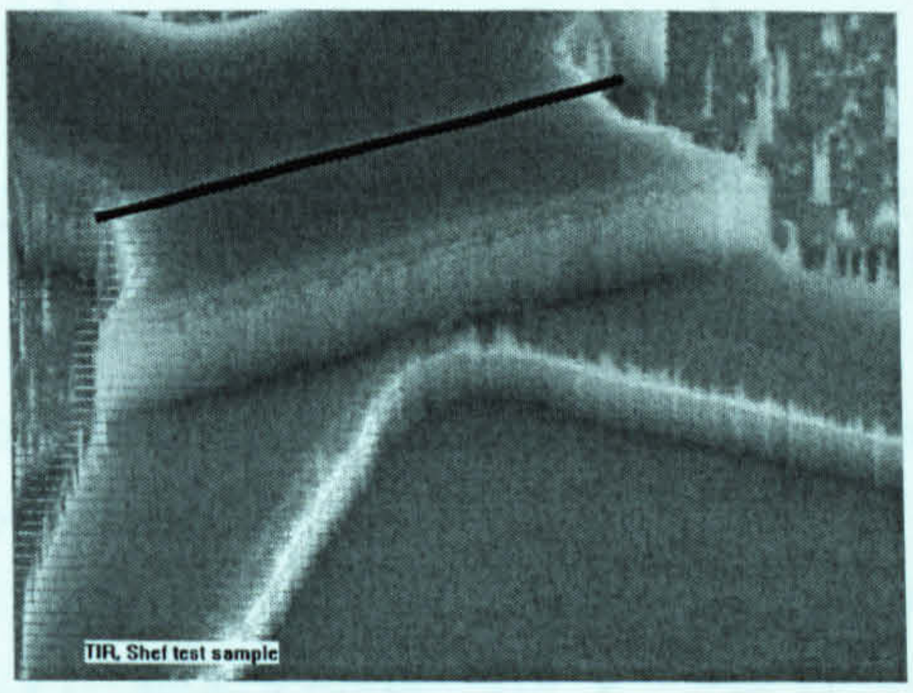

Figure5.8 Example of TIR Mirror misalignment

Theoretically with a perfect alignment of the two masks and with no rough induced by the etching, loss of the mirror can be as low as 0.08dB [4]. However, the presence of pratical problems like mask misalignment and sidewall roughness increases the losses by 1 or 2 dB [5,6].

Mask tilt or mask shift are caused by limited photolithographic mask alignment accuracy which is in the order of ±0.5μm with our mask aligner.

In our fabrication process, the mask tilt can almost be completely neglected because the alignment is done over a 6mm base line, thus if the mis-alignment at the two extreme points is 1μm, the tilt angle is θ_t is only *0.0095°*. The mask shift introduced can be up to 0.5μm in both x and y direction. Therefore, the mirror can stand anywhere in the dotted window shown in Figure5.9 with a total shift tolerance $\Delta = 0.707\mu m$ or $\pm 0.35\mu m$ from the ideal position.

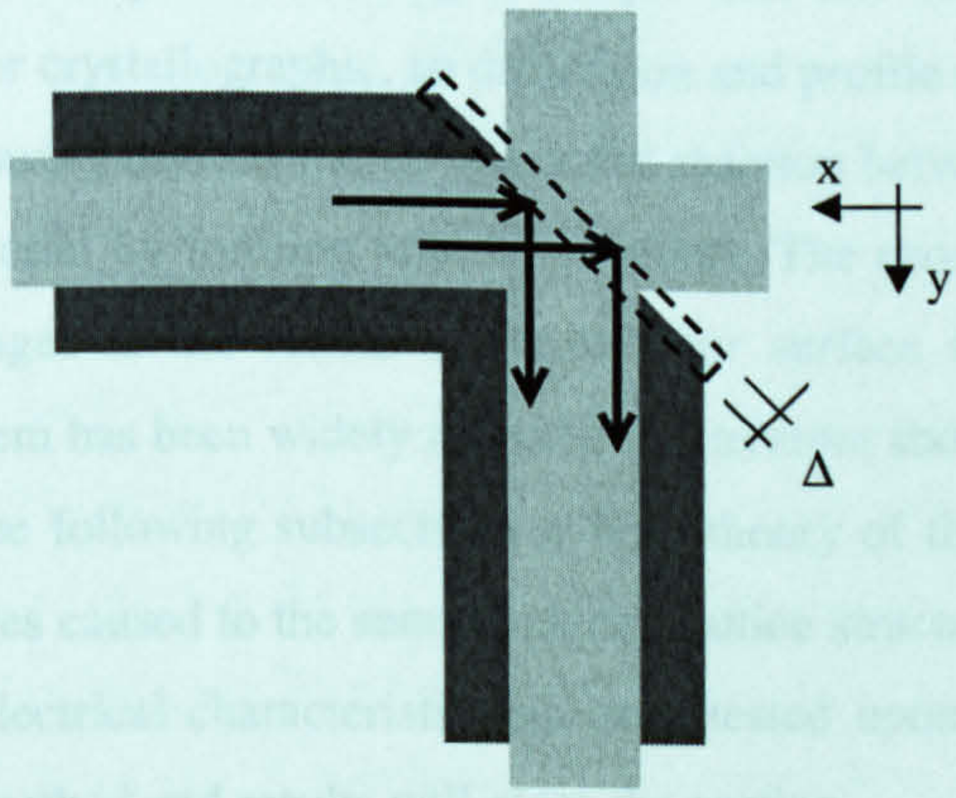

Figure5.9 Possible offset of the Mirror

The displacement of the mirror can induce a reduction of the launch efficiency η between input and output waveguides. Such value is given by the overlap integral of the modes in the mirror plane $S=(x,y)$ and can be calculated as shown in [7] (ψ_1, ψ_2 complex mode amplitude).

$$\eta = \frac{\left| \int_s \psi_1(x, \tilde{y}) \psi_2^*(x, \tilde{y}) dx d\tilde{y} \right|^2}{\int_s \psi_1(x, \tilde{y}) \psi_1^*(x, \tilde{y}) dx d\tilde{y} \int_s \psi_2(x, \tilde{y}) \psi_2^*(x, \tilde{y}) dx d\tilde{y}} \tag{5.1}$$

For quasi-TE modes with a strong dominance of E_y and H_x, the field distribution of the input and output mode in the mirror plane can be expressed by:

$$\begin{aligned} E_1(x, \tilde{y}) &= E(x, y) \exp\left[-i\beta \left(y - \frac{\Delta}{\sqrt{2}} \right) \right] \\ E_2(x, \tilde{y}) &= E\left(x, y - \sqrt{2}\Delta\right) \exp\left[-i\beta \left(y - \frac{\Delta}{\sqrt{2}} \right) \right] \end{aligned} \tag{5.2}$$

where Δ is the shift tolerance. Applying equations 5.2 to 5.1 it has been found that for a 3μm waveguide and a Δ within 0.707μm the loss is less than 0.8dB. Furthermore, 5.2 do not take into consideration the tilt between the two waveguides, θ_t, because it can be neglected together with the verticality of the mirror wall when his angle is of 90°±2° [8].

5.3. Reactive Ion Etching (RIE) Problems

The ridge waveguides in optoelectronics devices can be fabricated using two different processes: wet chemical etching or dry etching. Wet etching is simple and can offer high selectivity. However, the etching is often isotropic or crystallographic, so dimension and profile control is very difficult.

Dry etching is a low-pressure gaseous process where the reaction between an ionised gas mixture and the material removes the material by forming volatile products. The process can be highly anisotropic, but can introduce deep damages to the etched semiconductor surface and sidewall due to energetic ion bombardment. This problem has been widely reported in literature showing that it can lead to optical and electric degradation. In the following subsections a brief theory of the RIE is presented with particular interest paid to the damages caused to the semiconductor lattice structure. Furthermore, a novel treatment able to enhance device electrical characteristic has been tested upon different ridge waveguide Fabry-Perot lasers. Fabrication method and results will close the section.

5.3.1. The RIE Process

By definition RIE is the etching by ions which react with and remove substrate material [9]. When a surface is hit by an ion flux it is chemically attacked and gasificated. RIE is an anisotropic process and higher etch effect can be seen long the ion direction, see Figure5.10. In the other directions the etching is limited and it can be reduced or even eliminated by tuning the typical etching variables like gas mixture, pressure, power, table temperature etc.

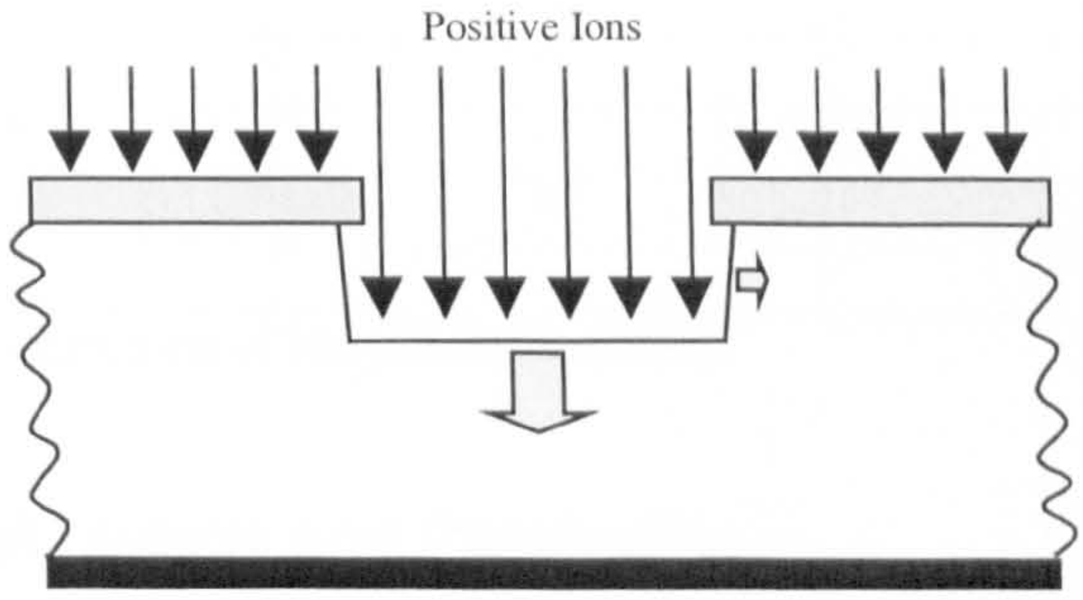

Figure5.10 Reactive Ion Etching, anisotropic process

Figure5.11 shows the schematic representation of the RIE chamber. The sample lies on top of a plate which functions as cathode and the chamber acts as anode. The chamber is first pumped down to $<5x10^{-5}$ mTorr. When the gas mixture is introduced into the chamber the pressure rise roughly up to 5-100 mTorr. With the RF generator turned ON, a plasma strikes and the reaction between samples and positive ions is facilitated.

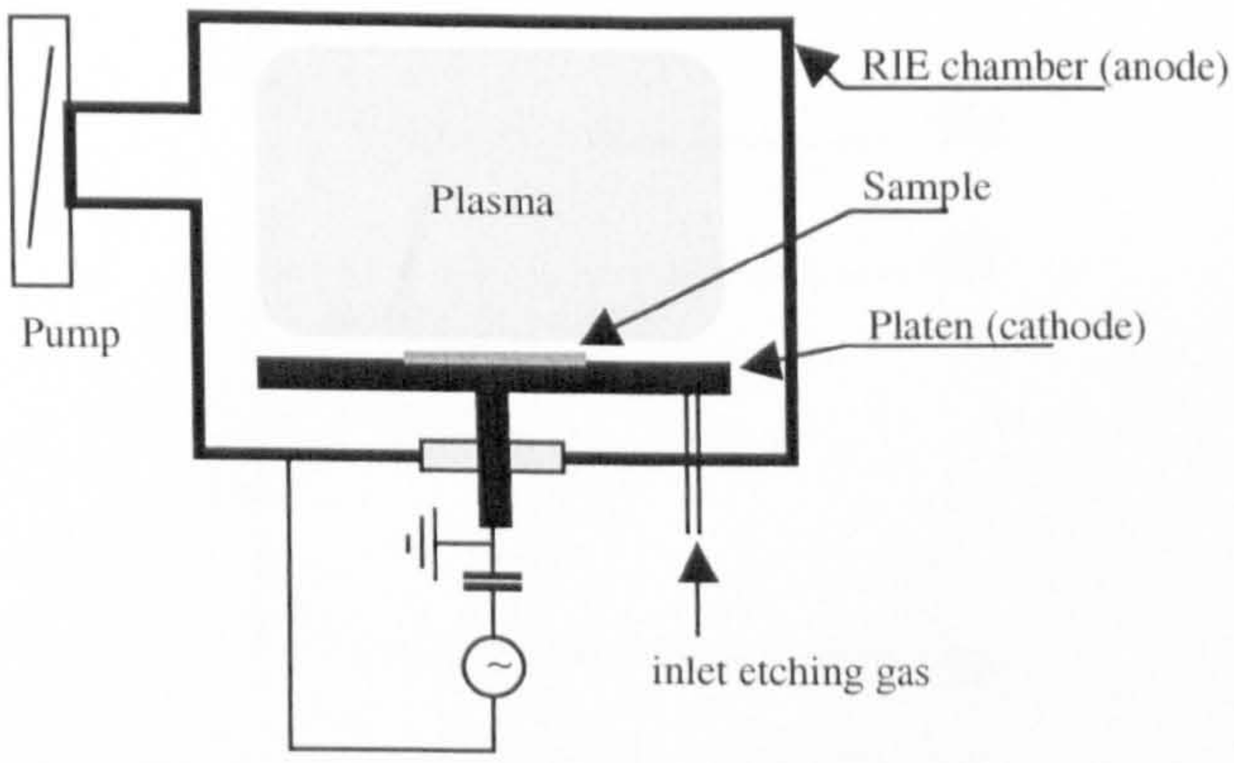

Figure5.11 Schematic RIE chamber

For III/V semiconductors applications of different gas mixtures have been evaluated, which containing Chlorine (Cl_2) and Boron (Br) compounds [10]. However, the use of Methane and Hydrogen (CH_4/H_2) for InP etching gives the best surface morphology and anisotropy results [11]. In this case different possible chemical reactions can occur between the gases and the semiconductor components, Indium (In), Gallium (Ga), Arsenic (As) and Phosphor (P). A possible one deploying GaAs [12] is

$$GaAs + 3H^+ + 3CH_3^+ \rightarrow AsH_3 + Ga(CH_3)_3 \tag{5.3}$$

The same interaction for InP producing $In(CH_3)_3$ and PH_3 volatile compounds [13]

$$InP + 3H^+ + 3CH_3^+ \rightarrow PH_3 + In(CH_3)_3 \tag{5.4}$$

Time and ion flux/power used defines the etching depth the etching characteristics change with the variation of the main process parameters as Table5.1 shows.

	CH4/H2 ratio	**Pressure**	**DC Bias** (RF power)
Etch rate	-	-	↑↑
Selectivity	-	↑	↓↓
Undercut	↑↑	-	↓
+ve slope	↓↓	↑?	↓
Facetting	-	-	↑↑

Table5.1 Etching results as a function of the process variables

5.3.2. Sidewall Defects and Passivation

Even if RIE based on CH_4/H_2 is the technique mostly used in In-containing III-V semiconductors, these processes are not safe from inducing problems. Three main impairments are present on the sidewall surface of an etched ridge:

- surface states
- mechanical damages
- hydrogen diffusion

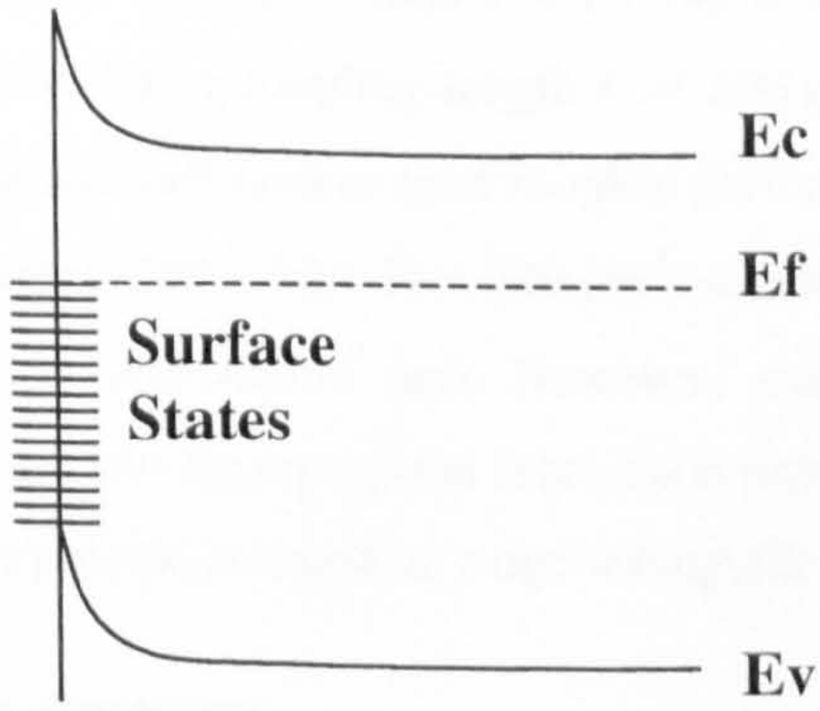

Figure5.12 Energy band diagram of semiconductor at the termination

In all the theoretical crystal models it is always supposed that the crystal lattice is perfectly periodic. This is not true on the surface, which means a termination of the periodic potential of the crystal lattice, as a result, localised states at the surface that reduce the potential on the surface is generated. The density of the surface states is greatly increased by other factors. Chemical species that are absorbed on the surface can forms bonds with crystal elements, resulting in further modification of the surface. Mechanical damages generate on the surface of the crystal lattice increase also the localised states on the surface Furthermore, on the surface, hydrogen and other species, made free during the RIE process, recombines with the doped semiconductor molecules creating fault-containing zones that work as traps for the injected carriers. As a consequence of all these effects, the injected carriers, rather than passing through the p-i-n junction would by-pass it via recombination at these surface states and trap on the sidewall. This degrades the optoelectronics performances, even lead to the loss of the device [14].

It has also been proved that species such as H, deactivates the Zn acceptors in the InGaAs cap layers and in the InP layers [15] increasing the contact resistance [16].

Improvements in InP-based devices [17] have been achieved using a double step treatment before the PECVD passivation. It is based on dry UV-Ozone, which produce a stochiometric surface, followed by HF wet etching, that removes the surface oxides. It has also been shown that annealing recovers the hydrogen passivation damages [18] and restores the Zn acceptors [15,16] to the near pre-etched ionisation levels. Polyamide is another material used to passivate InGaAs, InGaAsP, InP and InGaAsP/InP p-n junction structures, showing low and stable leakage current maintained for prolonged bias [19]. However, particular polyamides (e.g., Pyralin 2555) could have high optical absorption depending on the curing conditions [20] or could need specific curing steps that increase the difficulty and the length of the process.

GaAs, InP, and quaternary compound surfaces also react promptly with sulphur-contain agents. This process reduces the oxygen concentration on the etched sidewall, eliminating oxide species and creating a sulphide coating-layer. This layer has been shown to reduce the surface recombination current considerably [21]. Earlier studies have been carried out on GaAs surfaces [22] have shown that under Na_2S treatment the oxides Ga_2O_3 and As_2O_3 are dissolved. Quaternary compounds like AlGaInP have also been tested showing Catastrophic Optical Damage (COD) improvement up to 80% [23].

The crosspoint switch studied so far has a coupling length L of 200 μm a ridge width w of 3 μm and a thickness d of 0.2 μm. The *etched sidewall surface* is of roughly $(200 \times 0.2) \times 4 = 160\ \mu m^2$, where 4 is the number of sidewalls. The *volume* $(200 \times 0.2 \times 3) = 120\ \mu m^3$ which take to a *surface/volume ratio* $= 4/3\ \mu m^{-1}$ necessitating a sidewall passivation step. However, some tests need to be done before introducing any passivation process into the crosspoint fabrication process. Thus, in the following section a novel sulphur based passivation process is tested on ridge waveguide lasers.

5.3.3. Passivation Process

Depth etched Ridge Waveguide (RW) Fabry-Perot lasers have been made using the same Optical Crosspoint Switch (OXS) wafer MR1392. The choice to test the process on normal Fabry-Perot lasers is due to the simplicity of making them. In this case just one etch step is needed reducing time and difficulty. However, the process involves identical fabrication steps with respect to the thickness and the same mask processes of Ni lift off and SiO_2 dry etching.

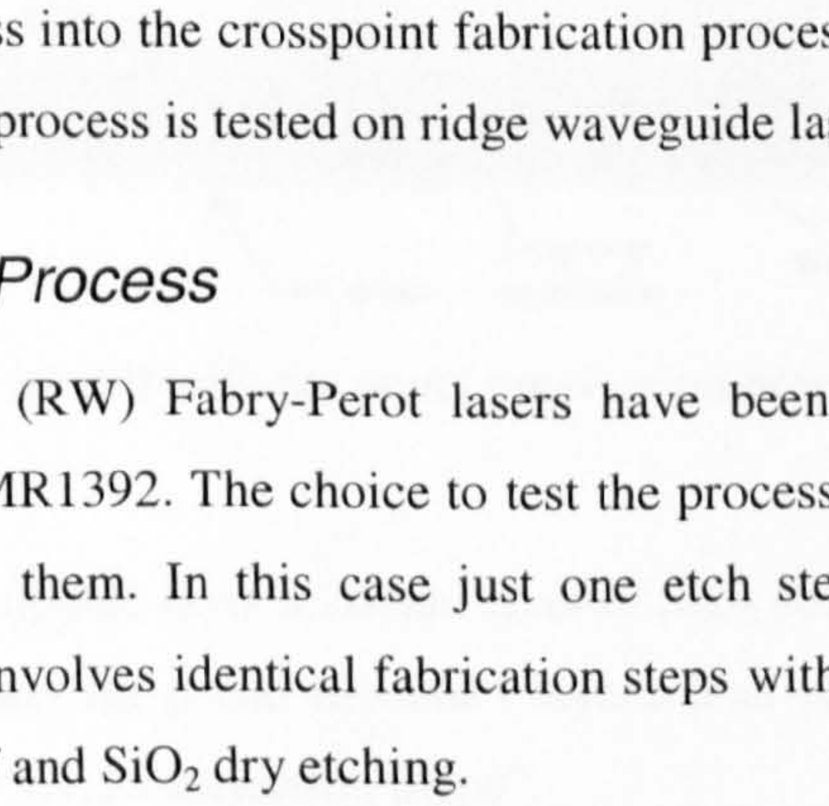

Figure5.13 Example of the chip treated with the novel passivation process

Four samples are etched using CH_4/H_2 RIE process resulting in, on top of each one, ridge waveguides between 5 and 50μm wide and depth of 2.3 - 2.5μm deep. After the mask is removed, half of the samples undergo surface passivation.

The surface passivation process includes three stages.

- Wet etching

This unselective fast wet etching [24] eliminates any surface layer that could have been mechanically damaged during the etching process.

- Sulphur Treatment

This is realised by spinning an aqueous solution of Sodium Sulphide (Na_2S) on the samples followed by baking. It generates a sidewall coating-layer that is stable during the device lifetime, able to reduce the recombination centres and to prevent the interaction with other elements.

When the samples are removed from the oven, they are covered under a Na_2S crust that needs to be removed by soaking in DI water and drying with N_2.

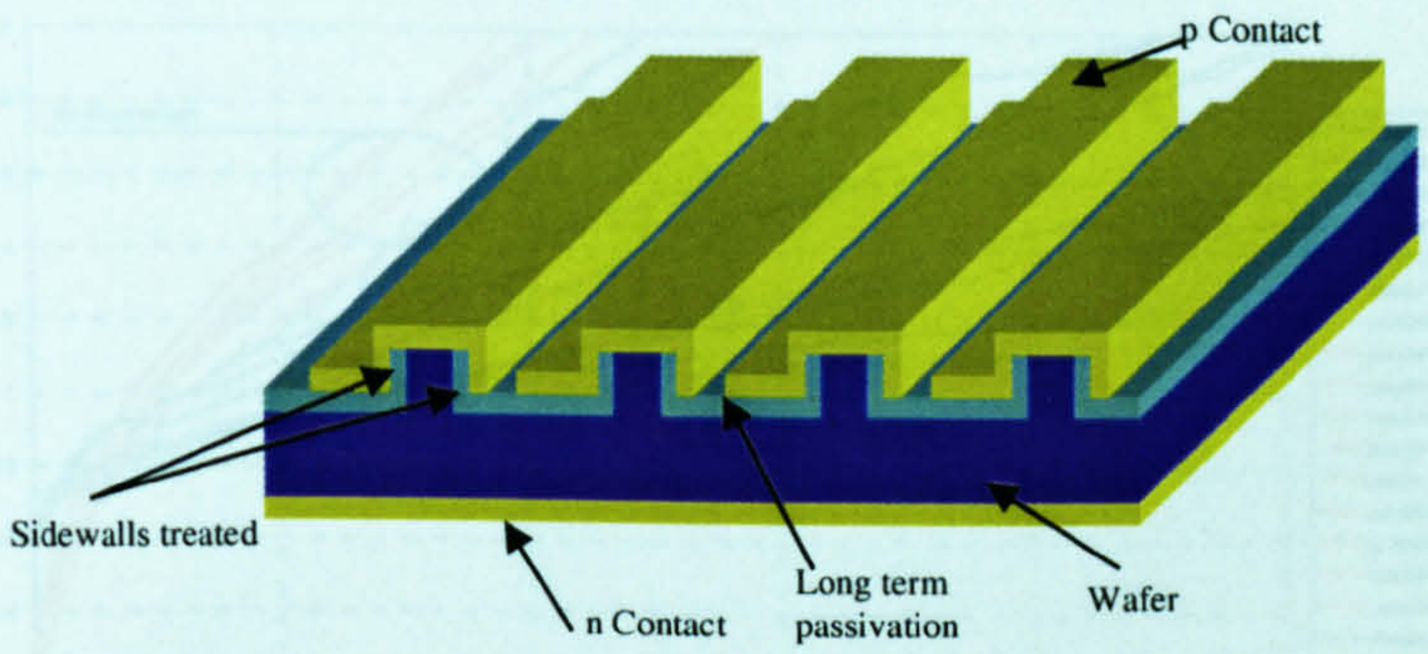

Figure5.14 Example of the device treated with the novel passivation process

- Permanent Passivation

In order to secure the sub-mono sulphide layer a 200nm layer of SiO_2 coating is sputtered.

Finally the samples are made ready for p and n-contact layers. The process follows the same steps as described in the previous section "5.1.2 Fabrication Steps".

The finished samples are low temperature annealed in order to reduce the device resistance, to recover ulterior damages and to restore Zn acceptors.

5.3.4. Passivated Test Device

All the samples, whether passivated or not, have been cleaved into 400μm bars, corresponding to the length of an OXS. The only lasers lasing were those with waveguide width of 5,10 and 20μm. The samples with waveguides width of 30, 40 and 50μm do not lase, this is probably due to the large size of the ridge.

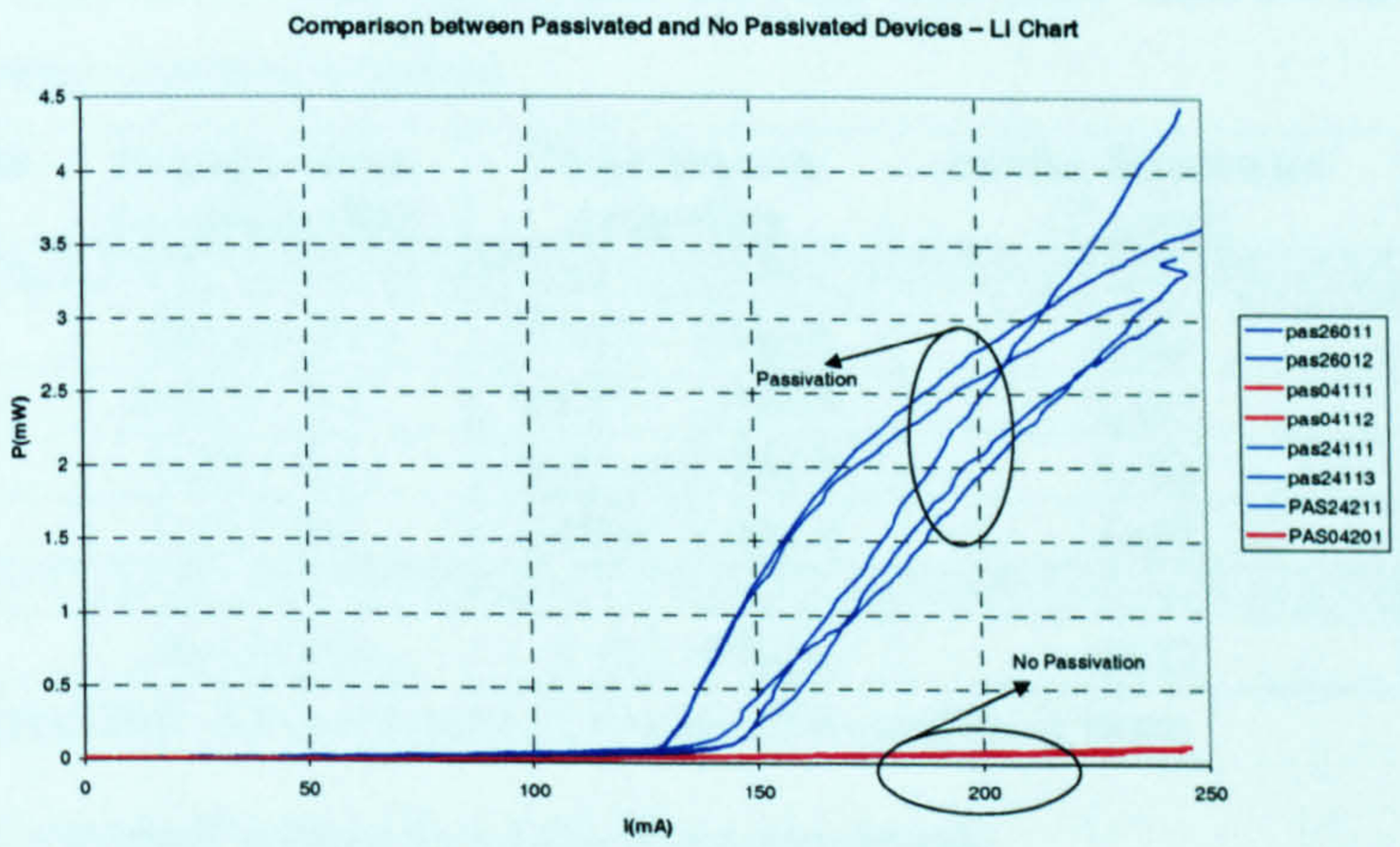

Figure5.15 LI chart for passivated and unpassivated devices

Figure 5.15 shows that the unpassivated samples do not work at all and, in particular, 5μm wide lasers tend to fail as soon they are forward biased.

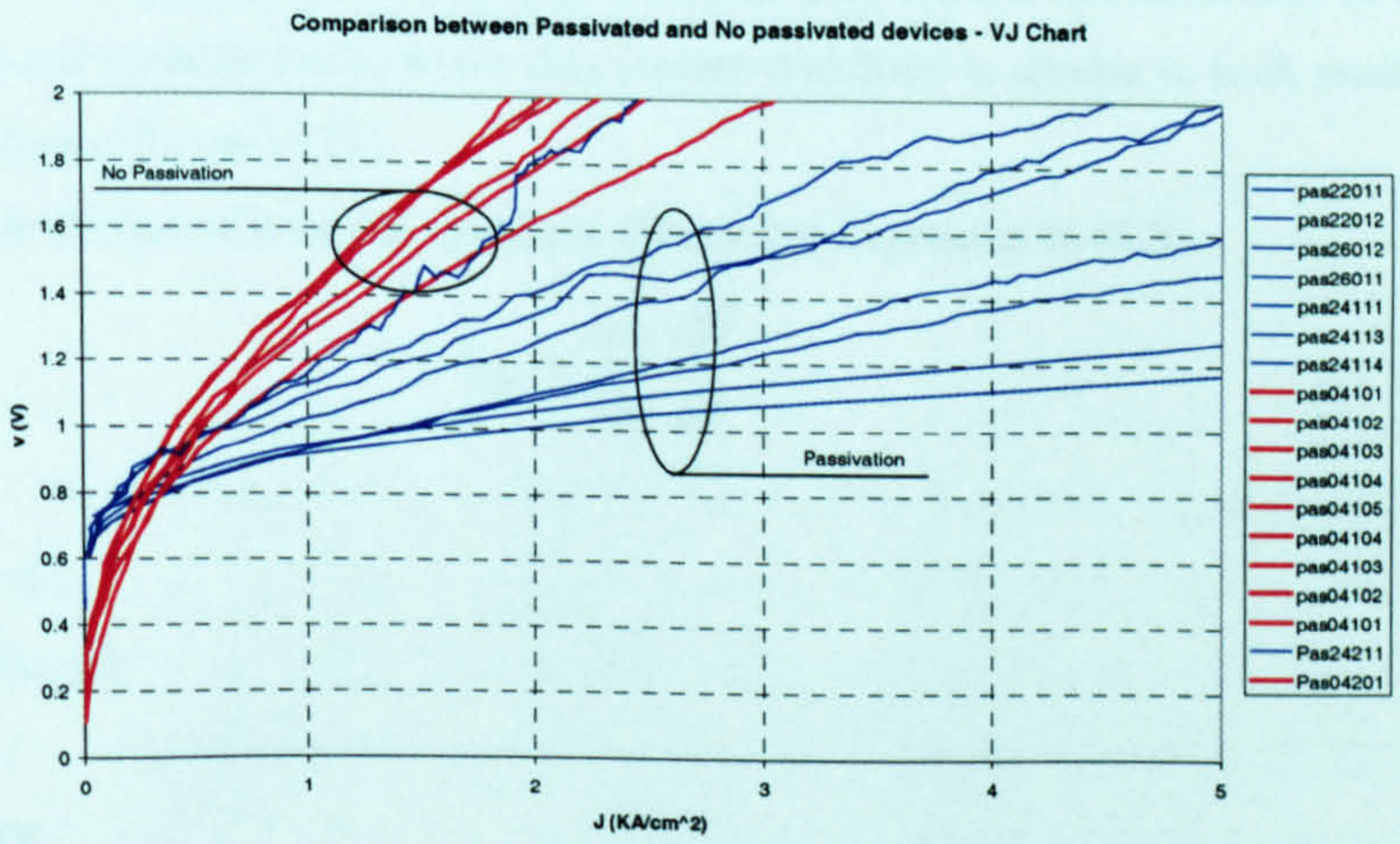

Figure5.16 VJ curve for passivated and unpassivated samples

Passivated and annealed samples instead lase with a current threshold between 130 and 140mA. The different width of the ridge waveguides used suggests that the threshold should double with the doubling of the waveguide width. Unfortunately this does not happen and it is thought to be due to the high scattering loss present on the sidewall because of its rough surface.

The V-J charts of Figure5.16 show two main changes between unpassivated and passivated and low temperature annealed devices. The first change is the rise in voltage threshold from around 0.3V up to 0.7 – 0.75V close to the typical value of 0.8V at 1550nm. The change in the slope of the curves is also very important because it confirms an improvement of the device resistance, which shows a reduction down to 4Ω.

Table5.2 shows a comparison between unpassivated and passivated lasers. Each test has been carried out with an average number of at least 4 devices.

Laser Ridge Width x Cavity Length	No passivation No annnealing	Passivation & Annealing	Device Resistance (Typical)
Bulk			
5x400 μm	Device Dies	0.70V / 120mA	4.8Ω
10x400 μm	0.35V / N.L.	0.65V / 1.35mA	4.6Ω
20x400 μm	0.2V / N.L.	0.65V / 1.45mA	4.0Ω
30x400 μm	0.3V / N.L.	0.60V / 1.60mA	4.0Ω
MQW			
3x300μm	Device Dies	1.0V / 90mA	5.2Ω

All laser etched 2.5μm deep. All data typical or average of 4 samples or more.
N.L.: *Not Lasing*.
Data shown are: *I-V threshold voltage(V)/L-I threshold current(mA)*

Table5.2 Sidewall Passivation Results

The bottom row of the table summarises the results achieved with the MQW wafer MR903, which is not a crosspoint structure but is a useful study. In fact with a ridge waveguide width of 3μm the voltage threshold is near 1V and the current threshold is of 90mA. This current threshold may be high for a MQW structure but previously studies have shown that current threshold is similar in both studies such material has very low quantum efficiency [25].

From the general definition of External Quantum Efficiency expressed in (5.5)

$$\eta_{ex} = \frac{e\lambda}{hc}\frac{dP}{dI} \tag{5.5}$$

where

e = *Electron Charge,*

λ = *Optical Wavelength,*

c = *light speed,*

h = *Plank Constant,*

dP/dI can be calculated from the LI curve,

The external efficiency can be calculated, which is η_{ex} = 10.0 % for wet etched devices and η_{ex} of 7.5 % for RIE etched, passivated and annealed devices.

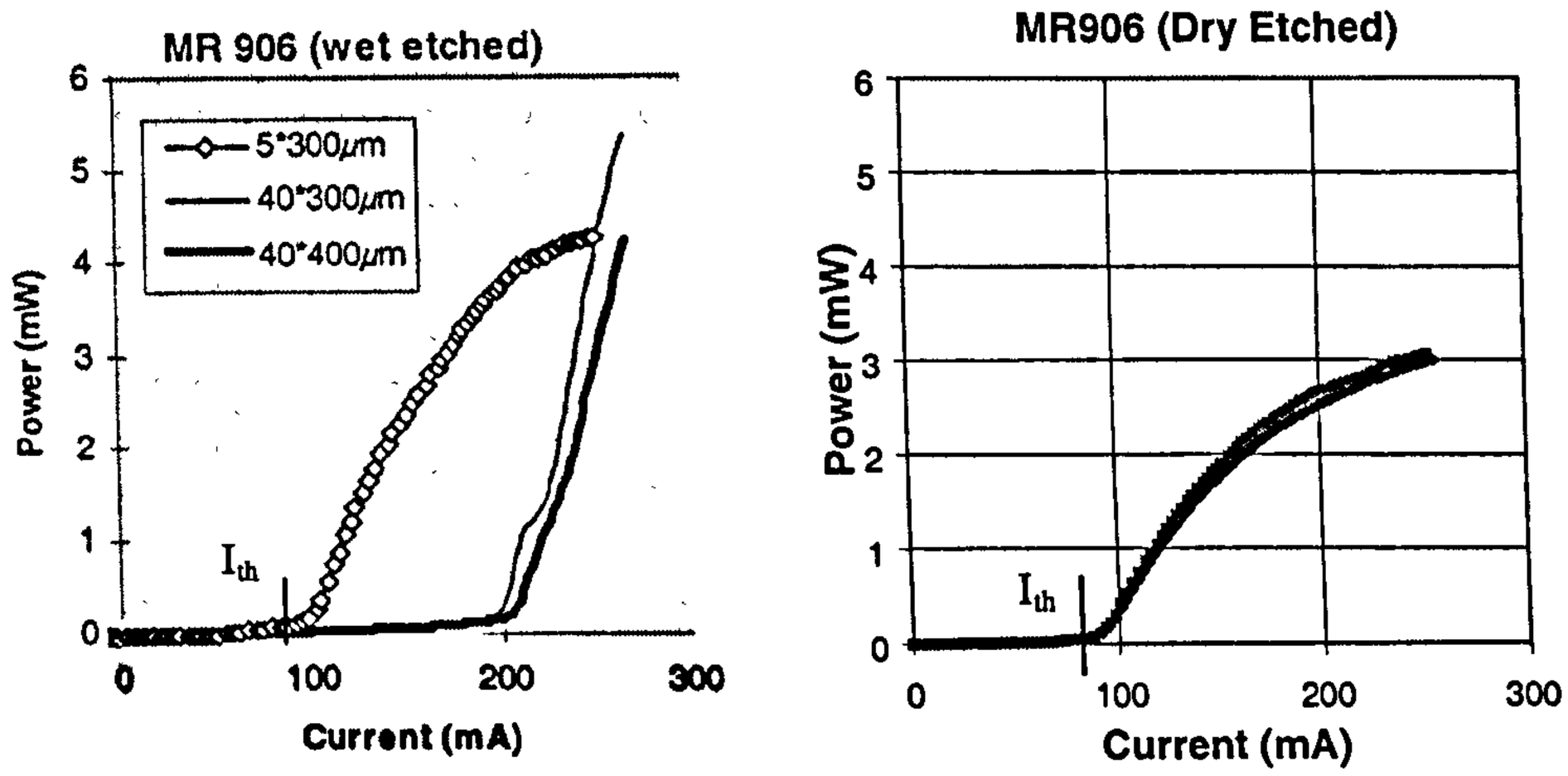

Figure5.17 LI curves for wet etched [25] and dry etched and passivated device

Wet etching is considered to give the best laser efficiency because it does not introduce etch damage related carrier leakage problems. Thus, from the comparison of the two values achieved it can be said that all the RIE induced degradation is largely recovered by the passivation. The external efficiency difference can be due to the sidewall scattering loss generated by the higher sidewall roughness in the deep dry-etched structures, as the previous wet-etched devices are shallow ridge waveguide devices.

5.4. Conclusion

In this chapter the fabrication phases involved in the crosspoint have been discussed. The importance of the etching steps has been highlighted because a good semiconductor etching with flat and smooth sidewalls plus high mirror verticality would reduce the device losses. The results are directly dependent on the mask resolution and on the RIE etching process. Mask quality plays a very important role for the etching process because a good pattern mask and a good TIR mirror mask alignment will influence the sidewall flatness and its verticality.

On the other hand, RIE process induces device degradation due to ion bombardment damages and carrier traps on the sidewall. This causes the bias current to leak through the sidewall recombination path rather than the PIN junction. A novel passivation process able to drastically reduce such a problem has been tested. It involves wet etching, sulphur passivation, SiO_2 passivation and annealing, all of which counteracting particular effects generated by the dry etch.

In the next chapter the test results of the novel optical crosspoint switch will be shown. Starting with the characterisation of each single layer the chapter moves to the dynamic characteristics of the device. Finally the device is used as all-optical switch showing the flexibility in being used without any bias current injected.

5.5. References

[1] T.C. Shen, G.B. Gao, and H. Morkoç, "Recent Developments in Ohmic Contacts for III-V Compound Semiconductors", Journal of Vacuum Science Technologies B, Vol.10, No.5, 1992, pp.2113-2132

[2] C-H Chen, and E.L. Hu, W.V. Schoenfeld, and P.M. Petroff, "Metallization-induces demage in III-V Semiconductor", Journal of Vacuum Science Technologies B, Vol.16, No.6, 1998, pp.3354-3358

[3] D. Caffin, A.M. Duchenois, F. Heliot, C. Besombes, J-L Benchimol, and P. Launay, "Base-Collector Leakage Currents in InP/InGaAs Double Heterojunction Bipolar Transistors", IEEE Transactions on Electron Devices, Vol.44, No.6, 1997, pp.930-936

[4] M. Owen, "Monolithic Integration of Optical Space Switches", 1998, PhD Thesis University of Bristol

[5]L. Faustini, C. Coriasso, A. Stano, C. Cacciatore, and D. Campi, "Loss Analysis and Interference Effect in Semiconductor Integrated Waveguide Turning Mirrors", IEEE Photonics Technology Letters, Vol.8, No.10, 1996, pp.1355-1357

[6] U.K Chakrabarti, S.J. Pearton, F. Ren, "Sidewall Roughness During Dry Etching of InP", Semiconductor Science and Technology, No.6, 1991, pp.408-410

[7] P. Buchmann, and H. Kaufmann "GaAs Single-Mode Rib Waveguides with Reactive Ion-Etched Totally Reflecting Mirrors", Journal of Lightwave Technology, Vol. 3, No. 4, 1985, pp. 785-788.

[8] E. Gini, G. Guekos, and H. Melchior, "Low Loss Corner Mirrors with 45° Deflection Angle for Integrated Optics", Electronics Letters, Vol. 28, No. 5, 1992, pp. 499-501

[9] P.F. Williams, "Plasma Processing of Semiconductors", 1997, Kluwer Academic Publishers

[10] K. Takimoto, K. Ohnaka, J. Shibata, "Reactive Ion Etching of InP with Br2-Containing Gases to Produce Smooth, Vertical Walls-Fabrication of Etched Faceted Lasers", Applied Physics Letters, Vol.54, No.5, 1989, pp.1947-1949

[11] J.W. McNabb and H.G. Craighead, H. Temkin and R.A. Logan, "Anisotropic Reactive Ion Etching of InP in Methane/Hidrogen based plasmas" Journal of Vacuum Science Technologies B, Vol.9, No.6, 1991, pp.3535-3537

[12] A. Semu and P. Silverberg, "Methane-Hydrogen III-V Metal-Organic Reactive Ion Etching", Semiconductor Science Technology, Vol.6, 1991, pp.287-289

[13] G Franz, "Hydrogen in Dry Etching Processes", Physics of Status Solid (a), Vol.159, 1997, pp137-144

[14] A.S. Grove, "Physics and Technology of Semiconductor Devices", 1967, Wiley

[15] T.R. Hayes, W.C. Dautremont-Smith, H.S. Luftman, and J.W. Lee, "Passivation of Acceptors in InP Resulting from CH_4/H_2 Reactive Ion Etching", Applied Physics Letters, Vol.55, No.1, 1989, pp.56-58

[16] M. Moehrle, "Hydrogen Passivation of Zn Acceptors in InGaAs during Reactive Ion Etching", Applied Physics Letters, Vol.56, No.2, 1990, pp.542-544

[17] R. Driad, Z.-H. Lu, S. Laframboise, D. Scansen, W.R. McKinnon, and S. P. McAlister, "Reduction of Surface Recombination in InGaAsP/InP Heterostructures using UV-Irradiation and Ozone", Japanese Journal of Applied Physics, Vol.38, N. 2B, 1999, pp.1124-1127

[18] B.C. Qiu, B.S. Ooi, A.C. Bryce, S.E. Hicks, C.D.W.Wilkinson, R.M. De La Rue, and J.H. Marsh, "Reduced Demage Reactive Ion Etching Process for Fabrication of InGaAsP/InGaAs Multiple Quantum Well Ridge Waveguide Lasers", Journal of Vacuum Science Technologies B, Vol.16, No.4, 1998, pp.1818-1822

[19] R.Yeats, and K. Von Dessoneck, "Polyimide Passivation of In0.53Ga0.47As, InP and InGaAsP/InP *p-n* Junction Structures", Applied Physics Letters, Vol.44, No.1, 1984, pp.145-147

[20] U. Koren, T.R. Chen, C. Harder, A. Hasson, K.L. Yu, L.C. Chiu, S. Margalit, and A. Yariv, "InGaAsP/InP Undercut Mesa Laser With Planar Polyimide Passivation", Applied Physics Letters, Vol.42, No.5, 1983, pp.403-405

[21] K. Rajesh, L.J. Huang and W.M. Lau, R. Bruce and S. Ingrey, D. Landheer, "Oxidation and Sulphur Passivation of GaInAsP(100)", Journal of Applied Physics, Vol.81, No.7, 1997, pp.3304-3310

[22] C.J. Sandroff, M.S. Hegde, and C.C. Chang, "Structure and Stability of Passivating Arsenic Sulfide Phases on GaAs Surfaces", Journal of Vacuum Science Technologies B, Vol.7, No.4, 1989, pp.841-844

[23] S. Kamiyama, Y. Mori, Y. Takahashi, and K. Ohnaka, "Improvement of Catastrophic Optical Damage level of AlGaInP Visible Laser Diodes by Sulfur Treatment", Applied Physics Letters, Vol.58, No.23, 1991, pp.2595-2597

[24] S.D. McDougall, "Monolithic Colliding Pulse Mode-Locking of AlGaAs/GaAs and InGaAs/InGaAsP Quantum Well Lasers", PhD Thesis, University of Glasgow, 1997, pp.127-135

[25] B. Cakmak, "Fabrication and Characterisation of InP and GaAs Based Optoelectronic components", PhD Thesis, University of Bristol, 2000

Chapter 6

Characterisation of Crosspoint Switches

Chapter 6 is dedicated to the characterisation of the novel Optical Crosspoint Switch (OXS) designed, modelled and fabricated as described in the previous chapters of this thesis. It is divided into 4 main sections.

The first one is dedicated to the characterisation of the Vertical Coupler (VC) structure base of the device. It pays particular attention to the parameters of transparency wavelength and losses of the bottom passive layer of such a VC. The top layer of the VC is an active layer, hence when it is cleaved in such a way to obtain a Fabry-Perot (FP) laser, it can be characterised in terms of current and voltage threshold, resistance and operating wavelength.

Section 2 describes the switching characteristics for single cell and arrayed cells of the complete OXS. The analysis of these characteristics determine ON-OFF contrast, interchannel crosstalk and device loss in ON state.

Section 3 is dedicated to the dynamic characteristics of the device. Results showing successful device operation as a 622Mb/s optical modulator are presented. The open eye diagram and correctly recovered data output confirm that the switching time of the device is sufficiently fast to permit optical packet routing. This successful result is used to introduce the next chapter, which is dedicated to optical packet routing applications.

The final section follows with the description of an attempt to use the device as a non-linear all-optical switch. Switching characteristics are investigated using a powerful optical signal used as carrier pump. The results of two main test experiments are considered: one based on Continuos Wave (CW) self-switching signal and the second using a short pulsed pump signal.

Glossary of the abbreviations

(OXS)	Optical Crosspoint Switch
(VC)	Vertical Coupler
(FP)	Fabry-Perot
(CW)	Continuos Wave
(PLW)	Passive Lower Waveguide
(AUW)	Active Upper Waveguide
(TIR)	Total Internal Reflection
(OBPF)	Optical BandPass Filter
(OSA)	Optical Spectrum Analyser
(PRBS)	Pseudo Random Bit Sequence
(TOAD)	Terahertz Optical Asymmetric Demultiplexer
(CPMZ)	Colliding-Pulse Mach-Zender
(SMZ)	Symmetric Mach-Zender
(EDFA)	Erbium Doped Fiber Amplifier
(DCF)	Dispersion Compensation Fiber (DCF)
(VOA)	Variable Optical Attenuator
(PC)	Polarisation Controller
(TL)	Tuneable Laser
(PM)	Power Meter

6.1. Layers Test

This section describes the characteristics of each single waveguide layer, in the device under test. Initially the bottom waveguide is analysed and the transparency wavelength is found from the measured transmission characteristics. Then, following a theoretical introduction, the losses in the device are calculated using the experimental results obtained by ripple effect in a passive FP cavity [1].

A second subsection will introduce devices cleaved as lasers for the analysis of the active top waveguide. This permits L-I, V-I and spectra curves to be obtained, which allow the current and voltage threshold, resistance and operating wavelength to be specified.

6.1.1. Loss Measurement on the Passive Layer

Two samples, cleaved from the same wafer MR1392, have been used for characterising the Passive Lower Waveguide (PLW) loss. Sample one is a PLW sample 400 μm long, obtained from the region between two 4x4 matrix switches. Sample 2 is 800 μm long and includes two actual switch units on it.

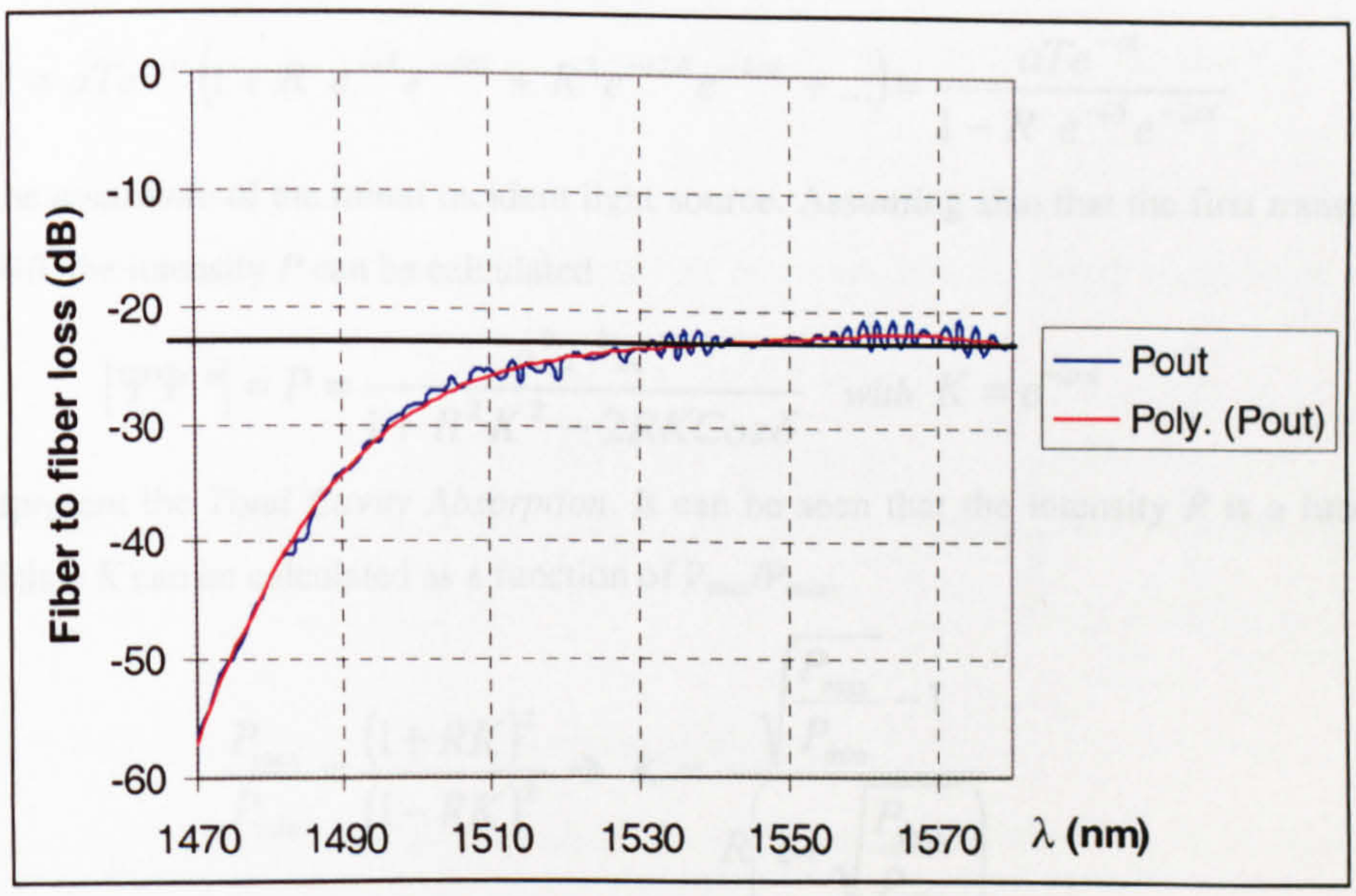

Figure6.1 Transmission characteristics vs wavelength

Injecting light at different wavelengths into the first sample and reading the output from the other end allows the observation of the transmission curve as a function of the wavelength, shown in Figure6.1. As shown in the previous chapters, the waveguide structure is designed to become transparent at wavelength above 1500 nm. This is confirmed from the experimental curve that shows first a rise of the fiber to fiber transmission from –55dB up to –22dB. For wavelength of 1530nm and above the transmission become flat, indicating an end to the band edge absorption tail at ~ 1530nm, therefore low loss for ~ 1550nm.

However, because a total fibre coupling loss of approximately 13dB is known to exist for the two facets, the cavity losses in the waveguide cannot be determined by simple methods.

A better method for measuring the waveguide loss uses the resonant effect in a FP cavity [1]. Let's consider such cavity and call Transmitted and Reflected power signal at the mirror planes T and R respectively.

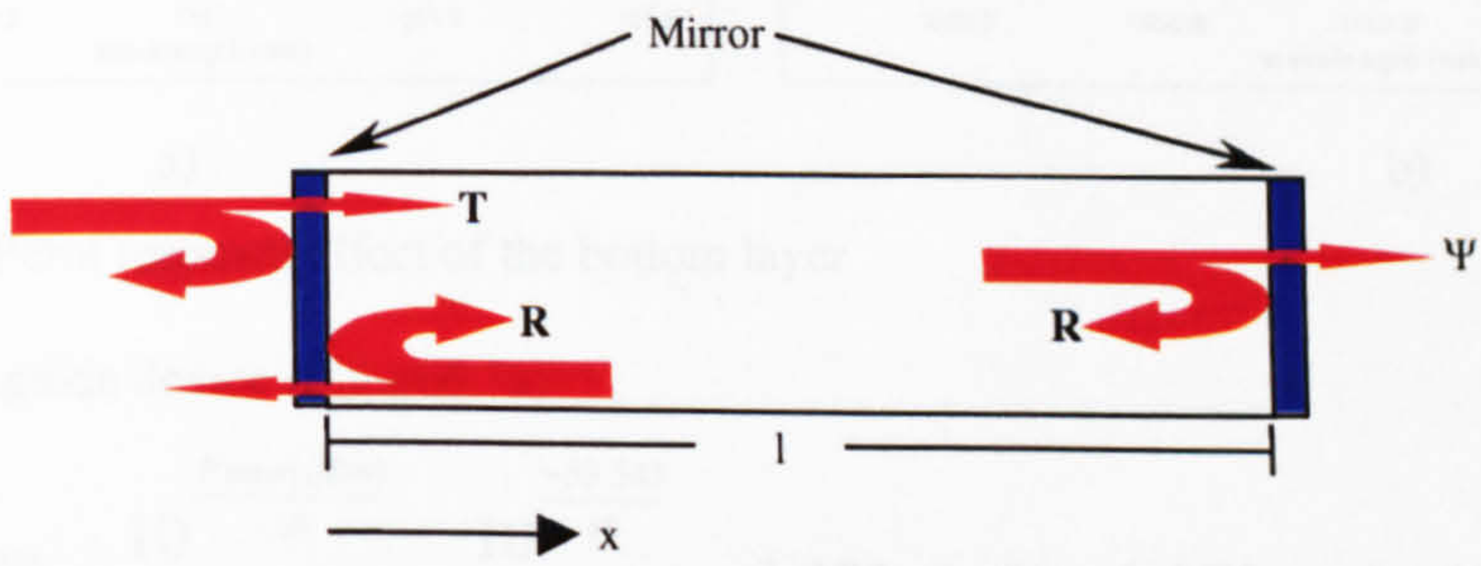

Figure6.2 Schematic Fabry-Perot cavity

The total outgoing wave **Ψ** resultant at one mirror output of the cavity can be expressed, with the geometrical progression (6.1)

$$\Psi = aTe^{-\alpha x}\left(1 + R\ e^{-i\delta}e^{-2\alpha l} + R^2 e^{-i2\delta}e^{-4\alpha l} + \ldots\right) = \frac{aTe^{-\alpha l}}{1 - R\ e^{-i\delta}e^{-2\alpha l}} \tag{6.1}$$

where *a* is the *amplitude* of the initial incident light source. Assuming also that the first transmitted beam has phase $\delta=0$, the intensity *P* can be calculated

$$\left|\Psi\Psi^*\right| = P = \frac{a^2T^2K}{1 + R^2K^2 - 2RKCos\delta} \quad with\ K = e^{-2\alpha l} \tag{6.2}$$

Where *K* represent the *Total Cavity Absorption*. It can be seen that the intensity *P* is a function of the phase δ and thus *K* can be calculated as a function of P_{max}/P_{min}.

$$\frac{P_{\max}}{P_{\min}} = \frac{(1+RK)^2}{(1-RK)^2} \rightarrow K = \frac{\sqrt{\frac{P_{\max}}{P_{\min}}} - 1}{R\left(1 + \sqrt{\frac{P_{\max}}{P_{\min}}}\right)} \tag{6.3}$$

Figure6.3 plots the experimental data showing the transmission as a function of the wavelength due to the FP resonance. They are measured at a working wavelength range of 1550-1552 nm. Hence, injecting a light signal into the cavity and scanning the cavity as a function of the wavelength P_{max}/P_{min} can be calculated. From Fresnel equations [2], the mirror reflectivity factor *R* can be fixed at 30% when the material is InGaAsP.

Thus, Following the results achieved respectively for the simple waveguide device (Figure6.3a) and for the double crosspoint included device (Figure6.3b), *K* can be calculated.

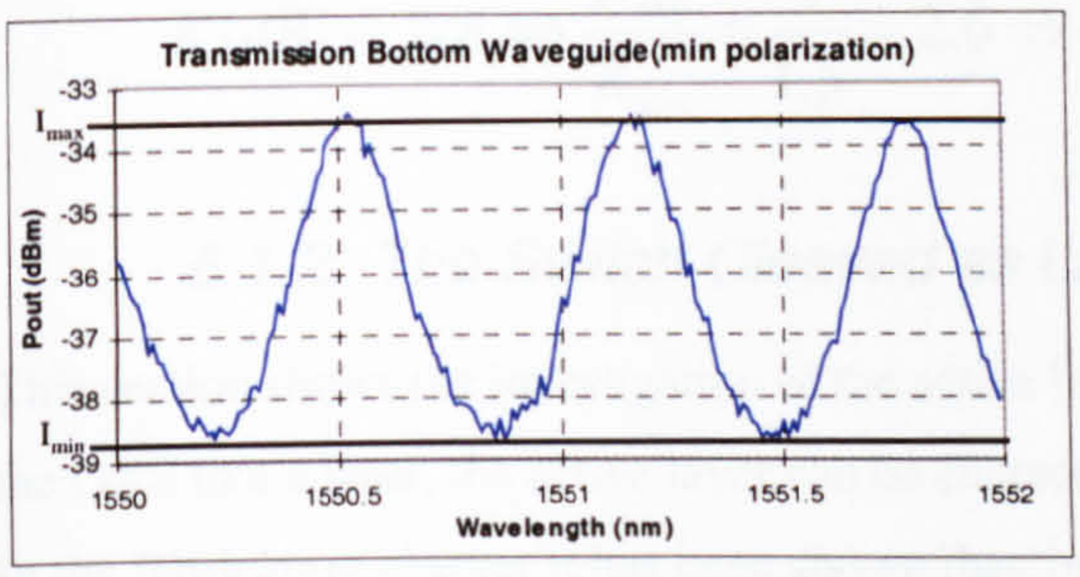

a)

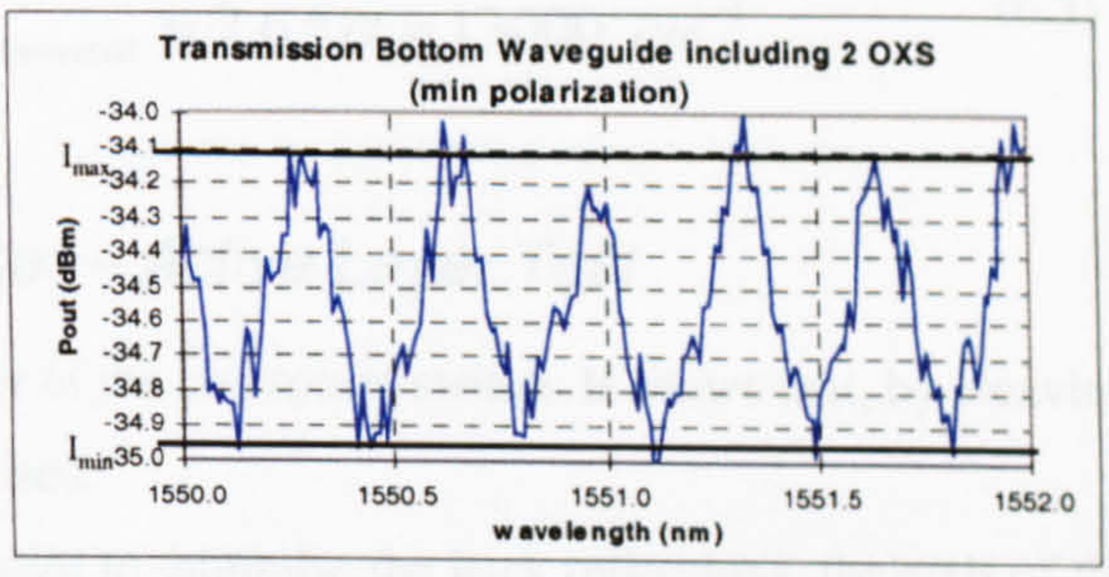

b)

Figure6.3 Fabry-Perot resonant effect of the bottom layer

- Simple waveguide device (Figure6.3a)

$$\frac{P_{max}}{P_{min}} = \frac{10^{\frac{P\max(dBm)}{10}}}{10^{\frac{P\min(dBm)}{10}}} = \frac{10^{\frac{-33.543}{10}}}{10^{\frac{-38.666}{10}}} = 3.253 \rightarrow K = 0.955 = -0.198\ dB$$

- double crosspoint included device (Figure6.3b)

$$\frac{P_{max}}{P_{min}} = \frac{10^{\frac{P\max(dBm)}{10}}}{10^{\frac{P\min(dBm)}{10}}} = \frac{10^{\frac{-34.190}{10}}}{10^{\frac{-34.927}{10}}} = 1.185 \rightarrow K = 0.141 = -8.498\ dB$$

Let us make a complete loss analysis for both samples and summarise it in Figure6.4.

It is known that the total fibre coupling loss for the two facets are approximately 13dB while 3 dB are lost at the facets for light reflection.

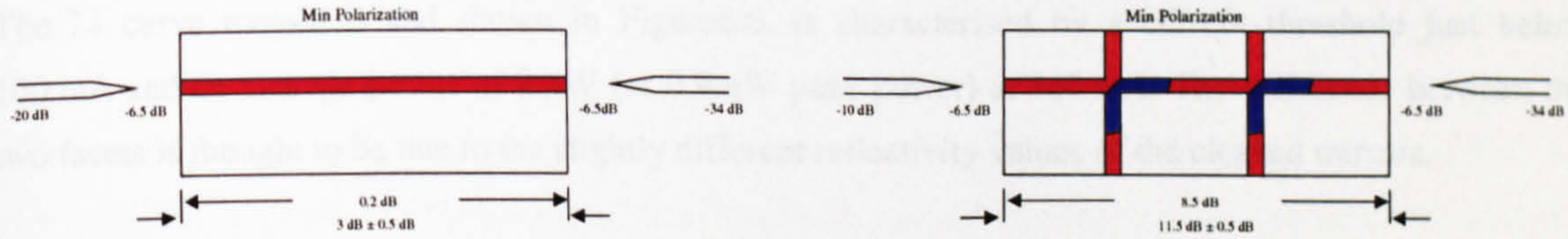

Figure6.4 Simple waveguide and double crosspoint samples loss

From the first sample results, using the formula (6.4), absorption α of 0.58cm^{-1} for the PLW is calculated.

$$K[dB] = 10\log(e^{-2\alpha l}) \Rightarrow \alpha = -\frac{K_{db}}{2*4.3*l} \text{ with } 10log(e) = 4.3 \qquad (6.4)$$

value this that at working wavelength is quite low and can be neglected.

From the second sample it can be deduced that the vertical coupler absorbs ~4dB over 200μm length showing an absorption α for the PLW of 23.26cm^{-1}. By comparison with the theoretical results of chapter 3 such value is more than double the calculated value, 1.5 dB. A reason of it could be due to a low active material absorption α assumed, in the simulation, of 5000cm^{-1}. Therefore, from the proportion with the loss, it has to increase of a factor 2.6, which means α = 13000 cm^{-1}.

$$K[dB] \propto 2\alpha d \Rightarrow \frac{K_{\exp}}{K_{sim}} = \frac{4}{1.5} = 2.6 \Rightarrow \alpha_{corrected} = 2.6 * \alpha = 13000 \ cm^{-1} \tag{6.5}$$

6.1.2. The Switch Cleaved as Laser – Active Layer Test

This section shows the investigation of the active layer of the crosspoint switch. It shows that, by cleaving the OXS like a laser, the active layer can be characterised.

In the fabrication chapter it has been shown that, in order to minimise the back reflections, the ends of the coupler are terminated with Brewster angle etched facets. Cleaving the crosspoint switch on the dotted lines shown in figure6.5 allows us to get rid of the angled terminal and replace it with two facet mirrors, realising a Fabry-Perot cavity laser, containing both active sections and the TIR mirror as shown in Figure6.5.

The bias of the device with 1% duty cycle current pulses generates light inside the active cavity that is picked up by a lensed fiber aligned to the mirror facet and measured with a power meter (PM).

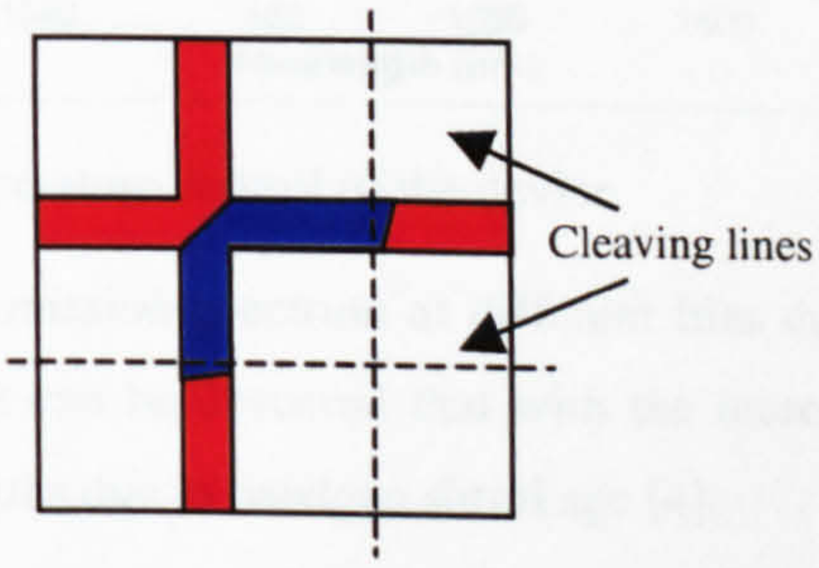

Figure6.5 Cleaving lines where the crosspoint switch is cleaved

The LI curve measured and shown in Figure6.6. is characterised by a current threshold just below 100 mA and an average power of 9 μW (or 0.9mW peak power) at 160 mA. The difference between the two facets is thought to be due to the slightly different reflectivity values of the cleaved mirrors.

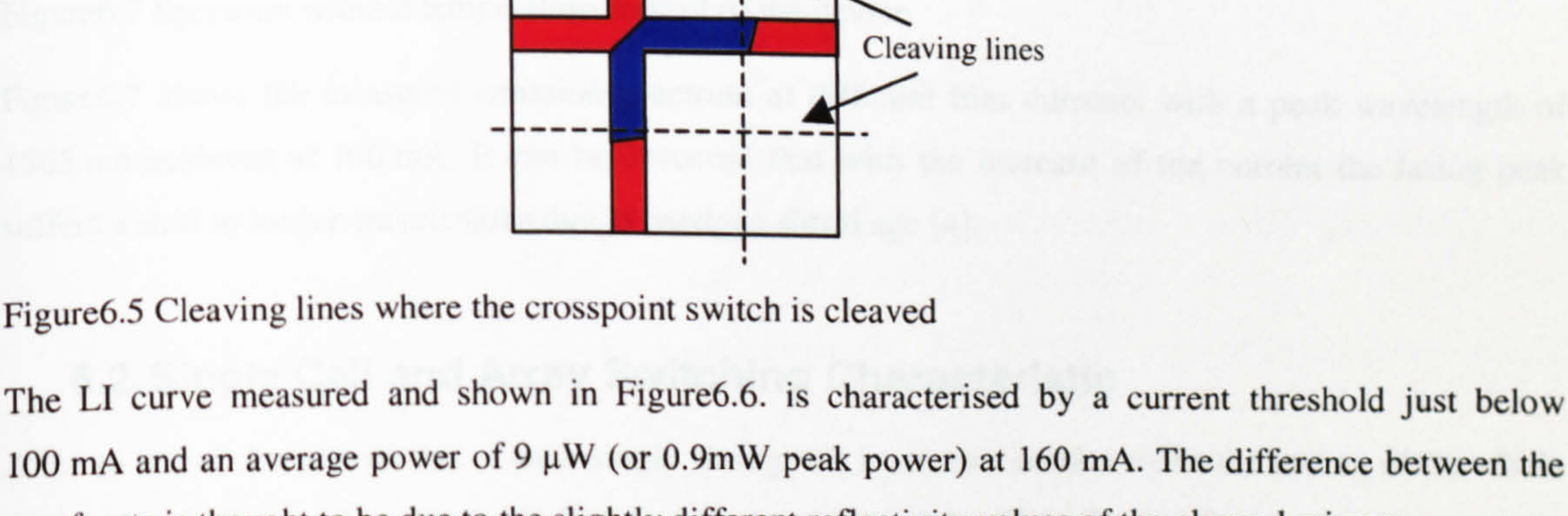

Figure6.6 LI and VI curves for the OXS as laser

Figure6.6 also shows the VI curve that is characterised by a voltage threshold of 0.65 V. Such a low value shows that the device is affected by current leakage along the sidewall. The measured resistance is higher than 9 Ω, this is probably due to the low N-doping levels characterising the wafer structure [9].

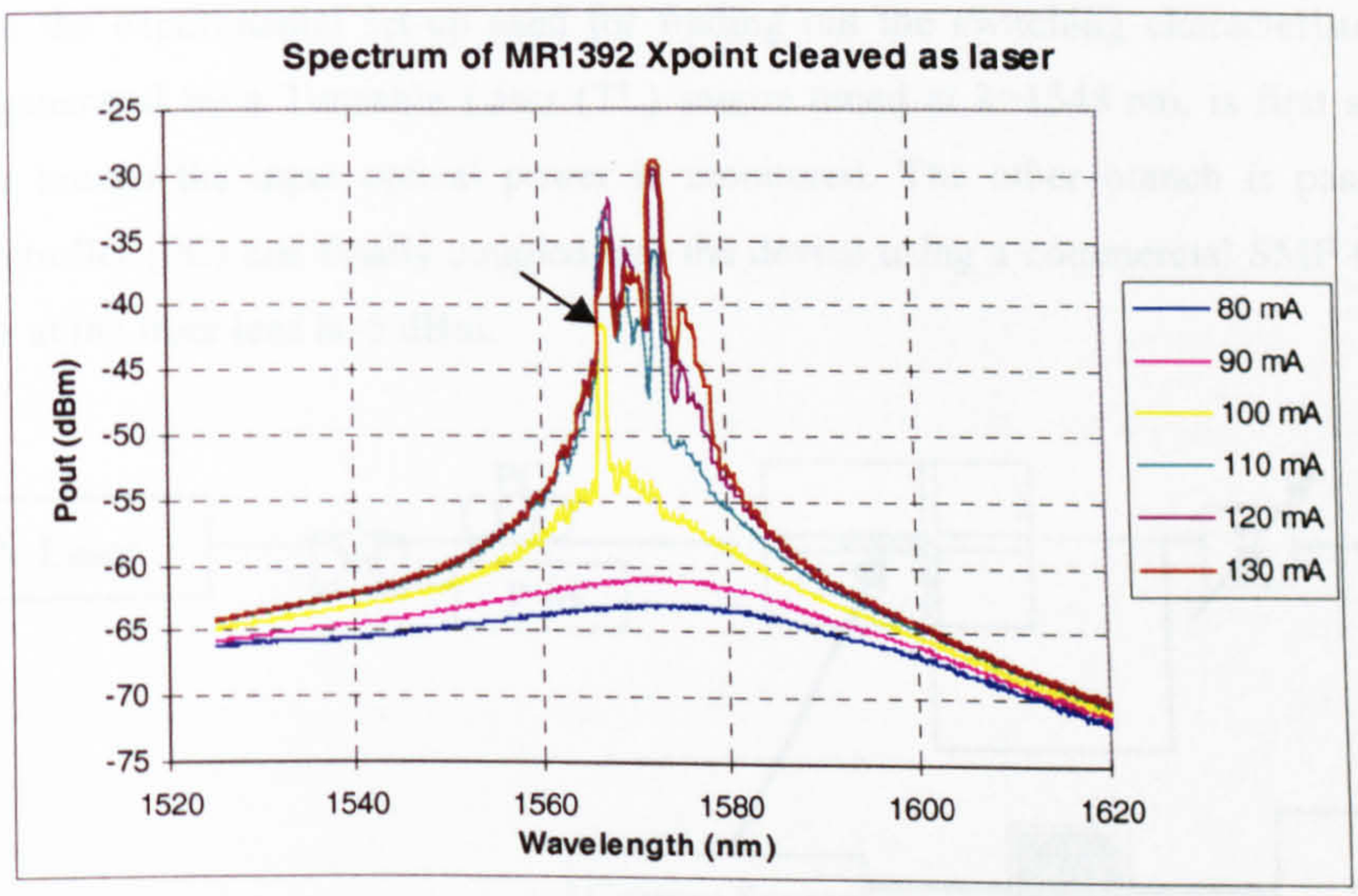

Figure6.7 Spectrum without temperature control of the device

Figure6.7 shows the measured emission spectrum at different bias currents with a peak wavelength of 1565 nm achieved at 100 mA. It can be observed that with the increase of the current the lasing peak suffers a shift to longer wavelengths due to bandgap shrinkage [4].

6.2. Single Cell and Array Switching Characteristic

After an initial characterisation of each single waveguide layer, this section treats the testing of the whole device. Using the sample containing 2 optical crosspoint switches described in the previous section, the transmission characteristic curves are determined with a focus on ON-OFF contrast values and Crosstalk. However, before the experiment description, it is useful to repeat of some definitions given in the past chapters.

- The switch is in "ON" state: when bias current is injected onto the device. This produces an increase of carriers, which is able to reduce the refractive index of the active upper layer down to the same value of the lower waveguide. This allows the light signal to couple from one waveguide to the other. Hence, the input optical signal couples strongly from the PLW to the Active Upper Waveguide (AUW), reflected by the Total Internal Reflection (TIR) mirror, then coupled down to the PLW and cross-output.
- The switch is in "OFF" state: when no carrier is injected. Thus, an ultra-low crosstalk level is expected by the combination of a much weakened signal coupling into the active upper waveguide

and the drastic attenuation of any residual coupled signal by the highly absorptive nature of the active layer.

6.2.1. Crosspoint: The Single Switch

Figure6.8 shows the experimental set-up used for finding out the switching characteristics. The input optical signal, generated by a Tuneable Laser (TL) source tuned at λ=1548 nm, is first split by a 3dB coupler. At one branch the input optical power is monitored. The other branch is passed through a Polarisation Controller (PC) and finally coupled into the device using a commercial SMF fiber lens. The measured power at the fiber lens is–5 dBm.

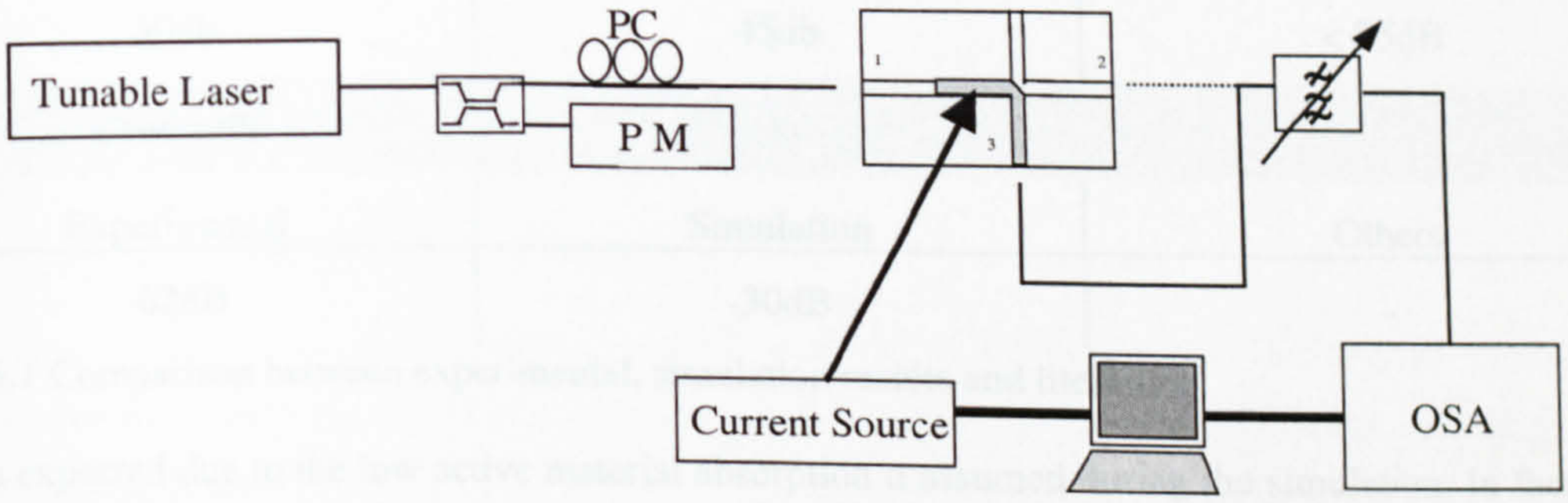

Figure6.8 Schematic experimental Set-up used for the switching characteristic

Each switch cell has two VCs of 150 μm length. At its output the switched signal is coupled into a lensed fiber, filtered by an Optical BandPass Filter (OBPF) to reduce the spontaneous emission generated by the device, and then measured by an Optical Spectrum Analyser (OSA) set as PM.

Forward biasing the VCs activates the switch. A computer through GPIB interface drives the current source and reads the OSA input power values.

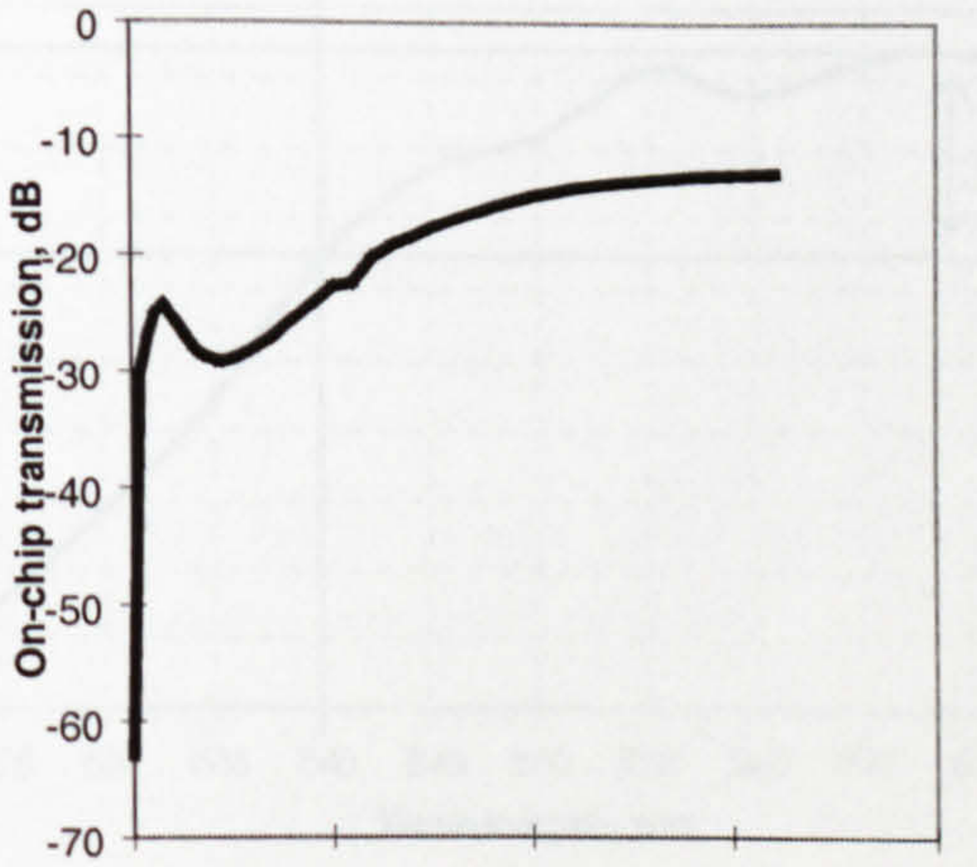

Figure6.9 Switching characteristics of the crosspoint switch unit cell

Figure6.9 shows the switching characteristic of a switching cell and in particular, in "OFF" state (injected current =0) it shows an on chip crosstalk as low as –62 dB. In "ON" state, instead, with current at 70 mA, the ON-OFF contrast is, 45 dB, and further increases to higher than 50 dB as the current value increases up to 160 mA.

Comparing the experimental result and the simulation values, shown in Table6.1, the real device shows better performances than the simulated one.

ON-OFF Contrast		
Experimental	Simulation	Others
50db	45db	< 25dB
Crosstalk		
Experimental	Simulation	Others
-62dB	-30dB	-

Table6.1 Comparison between experimental, simulation results and literature

This is expected due to the low active material absorption α assumed during the simulation. In fact, from the (6.5), an increase of α up to 13000 cm^{-1} will lower the Crosstalk down to –30 x 2.6 = -78 dB and as a consequence of it will increase the ON-OFF contrast.

The column on the right of Table6.1 confirms the better performances of the OXS realised with the novel active coupler concept (High ON-OFF contrast and low Crosstalk) compared with the device characteristics made with the passive coupler concept (low ON-OFF contrast and high Crosstalk) and seen in previous chapter 2.

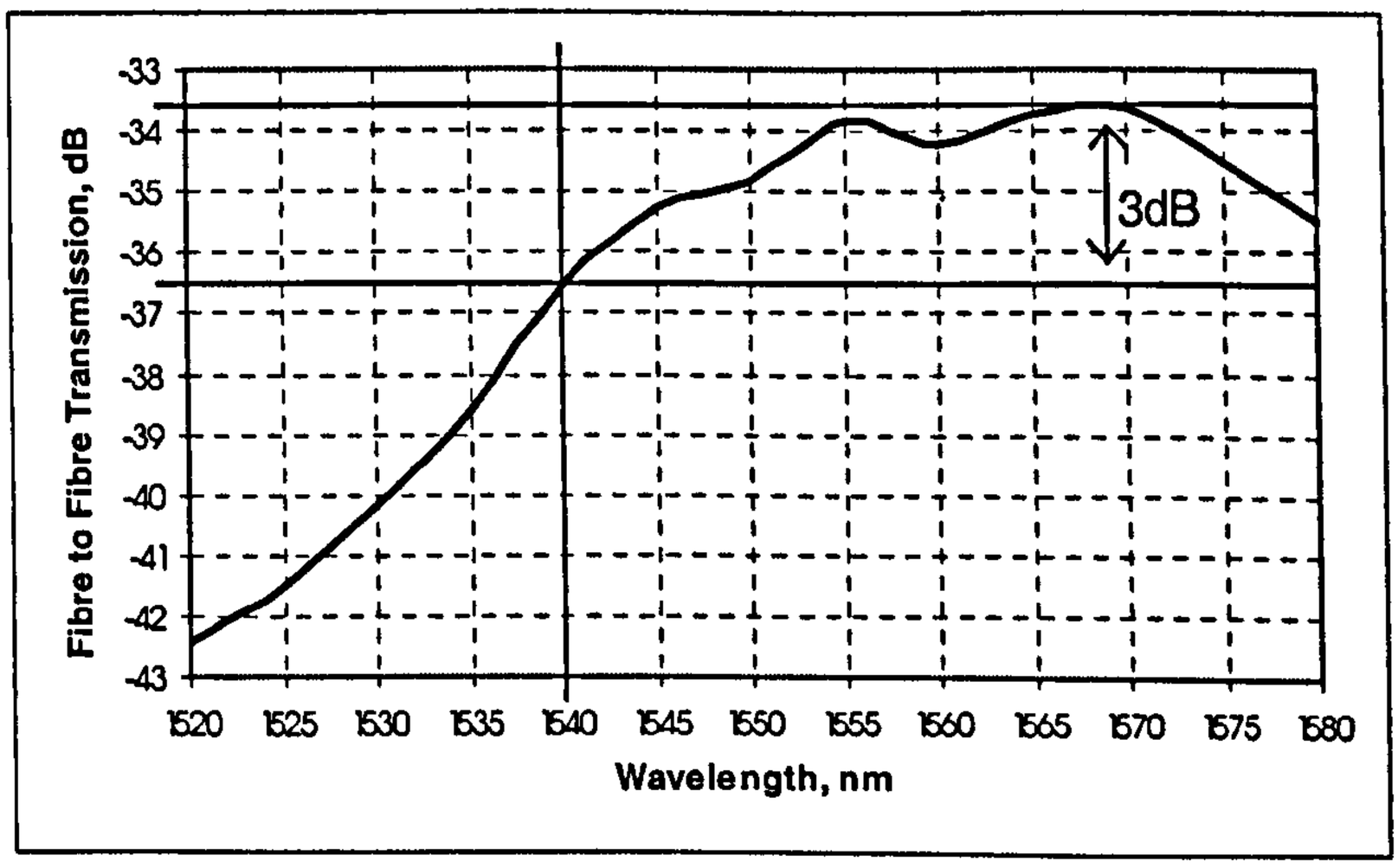

Figure6.10 3dB-bandwidth for the crosspoint switch unit cell

With the same set-up of Figure6.8 but with the Tuneable Laser computer assisted and no filter on the output it has been possible to express the cross-output transmission as a function of the wavelength. In this case the computer automatically changed the wavelength of the input signal. On the cross-output the signal is coupled into the fiber, read by the OSA and the data stored in the computer. During the experiment the device has been forward biased at the fixed value of 100mA. This is enough to keep the switch in ON state. The wavelength range of 1520-1580nm is related to the tuneable laser range.
The curve achieved and shown in Figure6.10, has permitted to measure the 3dB bandwidth of the device. It has been found greater than 40nm making the device suitable for any application in the EDFA bandwidth range. The curve is bandwidth limited on the left from the absorption of the passive waveguide at short wavelength and from the SOA characteristics of the device. On the right side of the 3dB bandwidth the limitation is due to the tuneable laser limit.

6.2.2. Crosspoint: 1x2 Array

In order to investigate the effectiveness of optical coupling in the switch cell, this section measures the interplay between two adjacent switches. A second current source, driving the second switching cell, is introduced into the set-up.

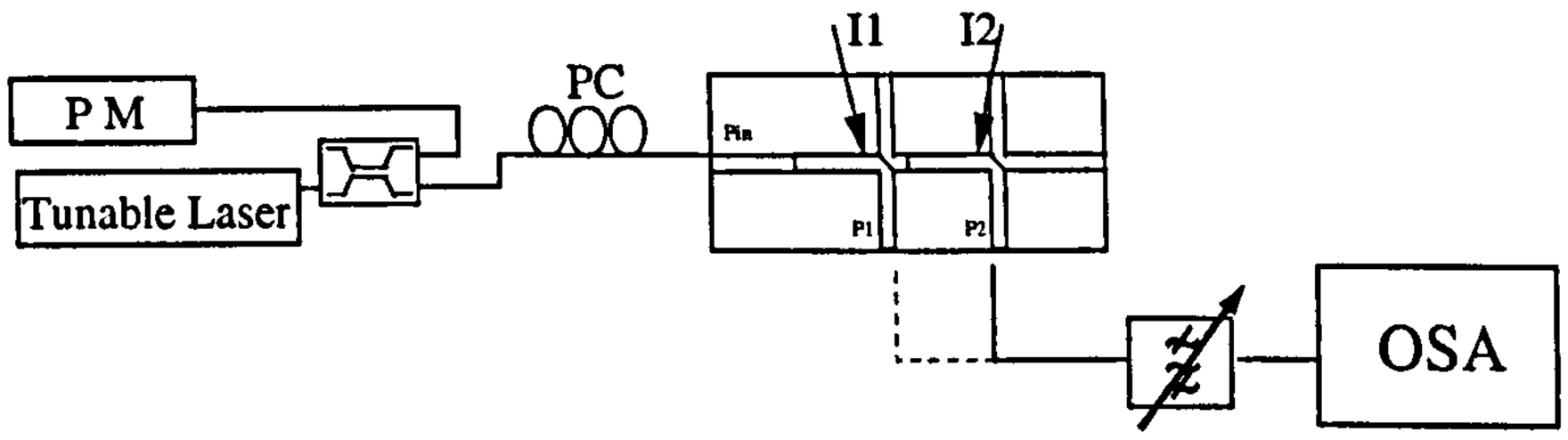

Figure6.11 Switching characteristics of the crosspoint switch unit cell

Similar transmission is observed at two neighbouring outputs, shown as the two thick curves in Figure 6.12. The same figure shows also the switching interplay between adjacent switches. When switch 1 is "ON" and switch 2 is biased no change is noticed at the first cell output. On the other hand, when switch 1 is gradually switched ON with switch 2 already ON, a drop of roughly 12 dB can be observed at output 2.
These 2 experiments clearly demonstrate that, for an array of optical switches:

- The switch's operation is not affected by any switch after it.
- A switch in ON state is able to couple more than 90% of the signal power into the upper waveguide, which shows that the vertical coupler is operating as expected. The drop at the output of subsequent switches is directly resulted from the fact that most optical power is picked up by the ON switch before it.

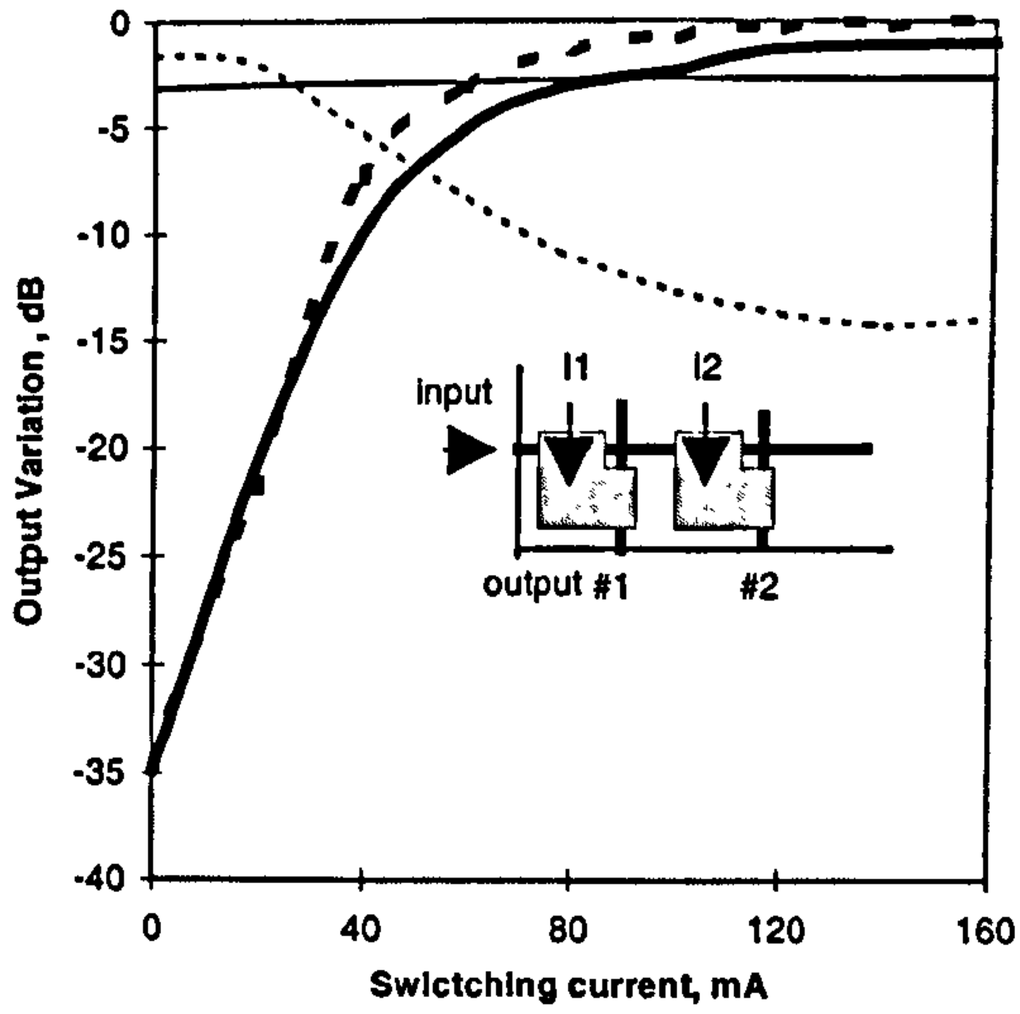

Figure6.12 Switching characteristics of 1x2 crosspoint switch

——— Signal at the output #1 as a function of I1 with I2=0

– – – Signal at the output #2 as a function of I2 with I1=0

——— Signal at the output #1 as a function of I2 with I1=78mA

····· Signal at the output #2 as a function of I1 with I2=80mA

6.3. Dynamic Performance

It is known that speed performance, for III-V semiconductor devices, is related with the carrier lifetime of the device that is of few nanoseconds [4]. For this reason a good dynamic performance with switching times in the nanoseconds order is expected from this device making it suitable for Optical packet switching network.

This section investigates the dynamic responses of the optical crosspoint switch by transmitting a bit sequence using the switch cell as optical modulator.

6.3.1. Optical Components Test Set-Up

In the experimental set-up of Figure 6.13, the switch is mounted on a RF submount with temperature control. It is wire bonded in series with a 47Ω impedance-matching resistor. The temperature of the sample was fixed at 18.7 °C. The CW optical signal is generated using an optical tuneable laser set at λ=1550nm. After being amplified, filtered and polarisation controlled the signal is coupled into the space switch by a lensed fibre.

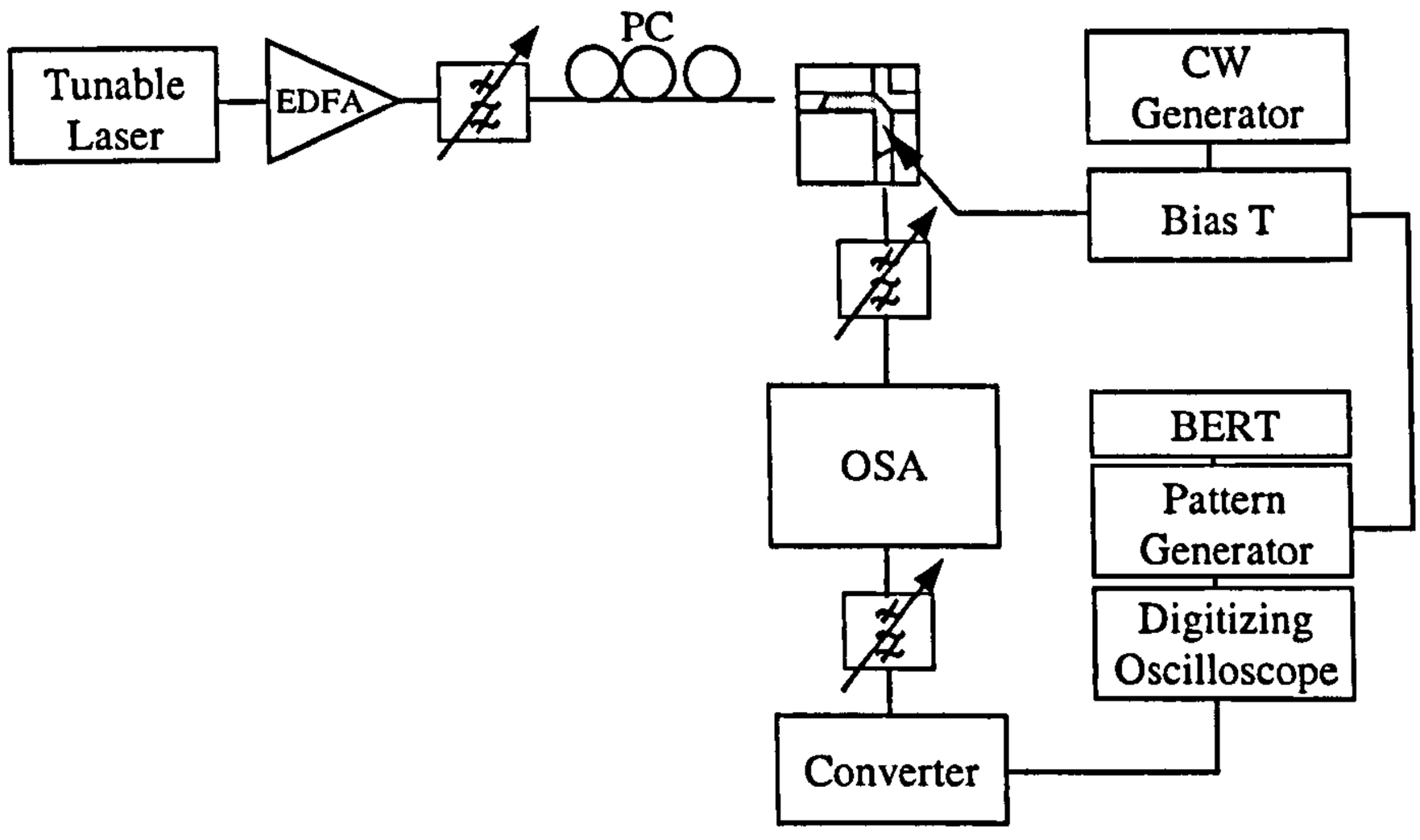

Figure6.13 Experimental Set-up used for dynamical performances test

The driving electrical signal is obtained using a pattern generator to provide a Pseudo Random Bit Sequence (PRBS) with length of $2^7 - 1$ with 2V p-p amplitude. This is applied to the switch to generate current modulation amplitude of 47mA p-p.

The transmitted signal is coupled into a lensed fiber, passed through an optical band pass filter that suppresses the spontaneous emission noise, detected by a lightwave converter and displayed on an oscilloscope.

6.3.2. Data Pattern and Switching Time

Using the set-up shown in Figure6.13 open eye diagram representing a successfully transmitted data pattern has been achieved. Figure 6.14 shows an open eye with a rise time of 1.4ns and a slightly shorter fall time of 1.1 ns.

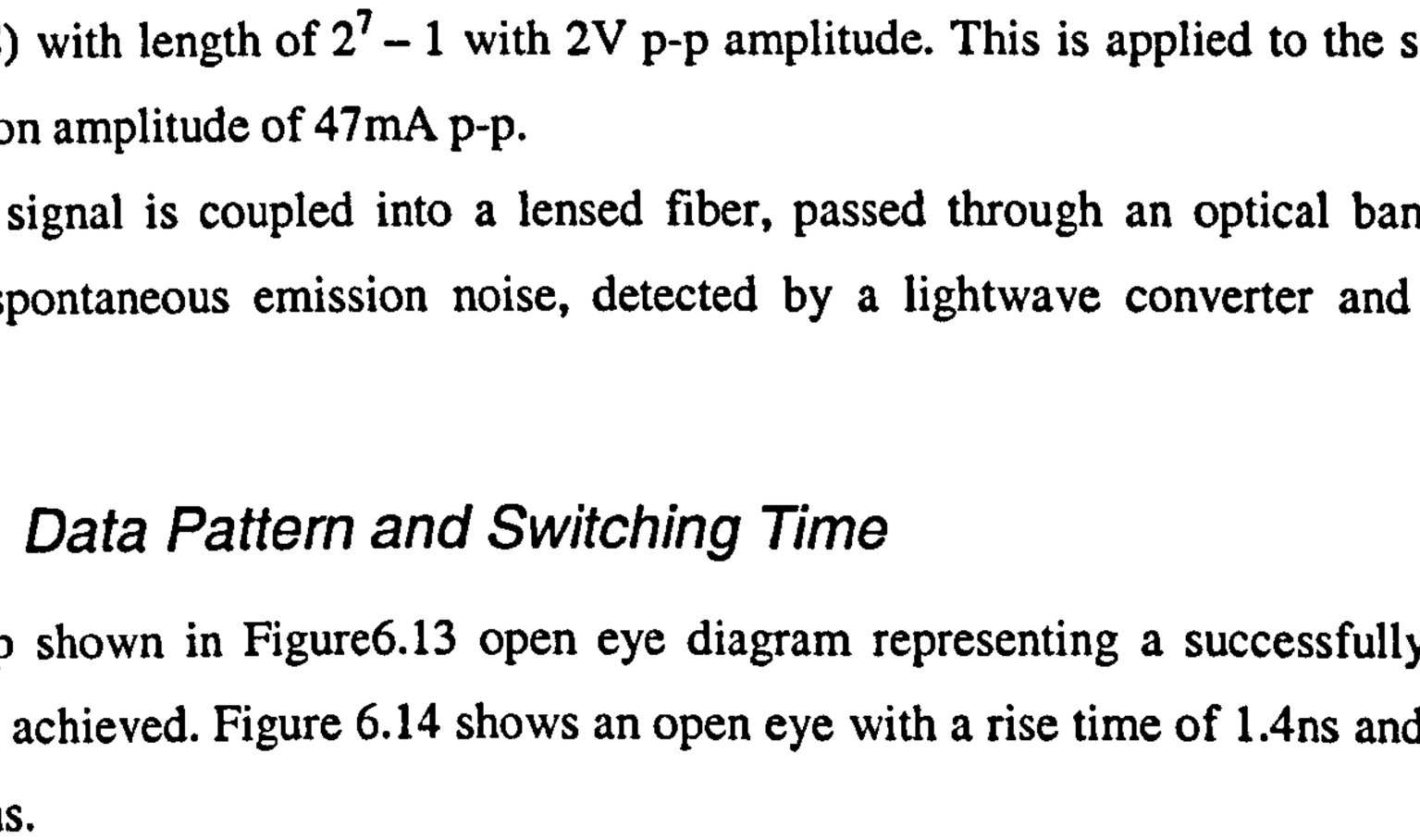

Figure6.14 Eye diagram obtained with direct light injection.

The 622Mbps data sequence at the cross output, as shown in Figure6.15, demonstrates clear switching from 0 to 1 with only the single one bit and the single zero bit showing a small deficit, which is in amplitude different due by the difference between switching ON and switching OFF time.

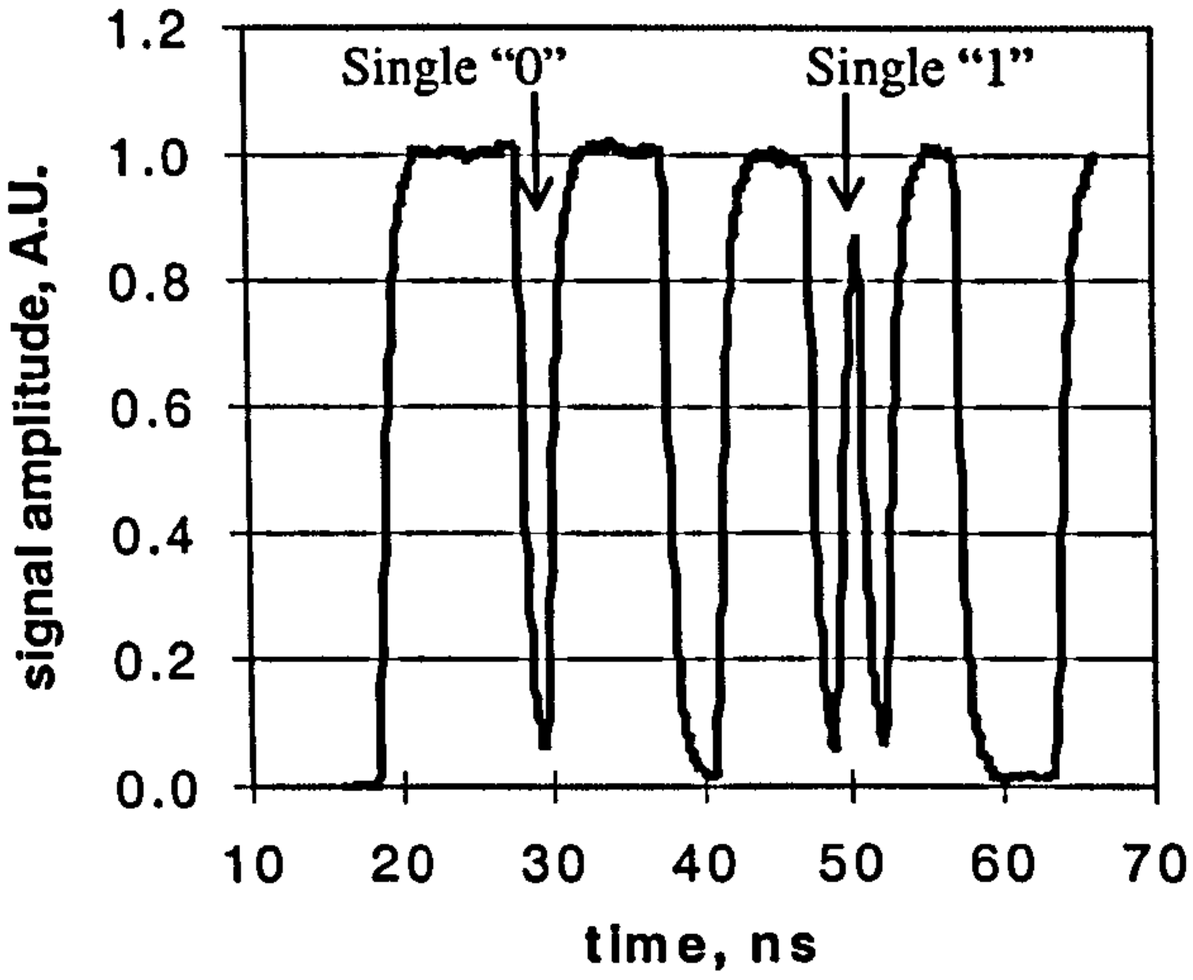

Figure6.15 Optical output data sequence at 622 Mb/s

This dynamic switching measurement is a simple test to show that the device is fast enough to be used in packet switching networks where switching times in the order of 1.5 ns are fast enough for interpacket guard time. The next chapter is completely dedicated to packet switching applications including an experimental deployment in the real packet switching network WASPNET.

6.4. All Optical Switching

Non-linear optical switches are considered a key device in order to realise all-optical signal processing and so far several kinds of all-optical switch based on different principles or geometries have been developed in the past years. A comparison between different optical switches using a variety of interferometers has been shown in [5]. They are based on Sagnac and Mach-Zender interferometers and are more commonly known as a Terahertz Optical Asymmetric Demultiplexer (TOAD), Colliding-Pulse Mach-Zender (CPMZ) and Symmetric Mach-Zender (SMZ). Additionally the literature proposes other novel designs based on interferometers [6,7] and non-linear distributed feedback structures [8] have been used too.

In this section the attempt to use the crosspoint switch in a non-linear all-optical configuration is described. It is shown that encouraging results are achieved using a self pump switching configuration and varying the signal used or the coupler (usually ON, usually OFF).

6.4.1. The Vertical Coupler Crosspoint as All-Optical Switch

It has been shown theoretically that a device, based on vertical coupler structure, using non-linear effects can make an effective non-linear optical switch [10].

A non-linear medium illuminated by intense optical field changes its refractive index value. Mathematically the refractive index consist of a linear part together with an optical constant that is directly proportional to the optical intensity of the incident field [9]:

$$n = n_0 + 2\overline{n_2}\left|E(\omega)\right|^2 \tag{6.6}$$

Where the linear and nonlinear coefficients are related to the first and third order susceptibility coefficients by

$$n_0 = \left(1 + 4\pi\chi^{(1)}\right)^{1/2} \quad \text{and} \quad \overline{n_2} = \frac{3\pi\chi^{(3)}}{n_0} \tag{6.7}$$

When the incident field increases, the second part of the formula becomes very important in the determination of the refractive index. This ability to change the refractive index through interaction of the light with matter can be used to achieve all-optical switching. The method is often realised in III-V semiconductor at the band edge, mainly due to its large carrier-induced non-linearity index and quite fast time constant in the 10 ps range, depending on the carrier sweep-out time [11].

The section shows two approaches used to demonstrate such a switch. Both adopt a strong optical signal, one CW and the other short pulsed, which supplies photo-carriers that induce a change of the refractive index of the waveguide. Switching occurs when the change is enough to match the vertical coupler.

6.4.2. All-Optical Switch Employing CW Self-Switching

A self-switching experiment is the first experiment carried out. An optical CW signal coupled into the switch can work as a pump signal and by increasing its power, it is able to change the characteristics of the active layer, switching the input signal itself to the output.

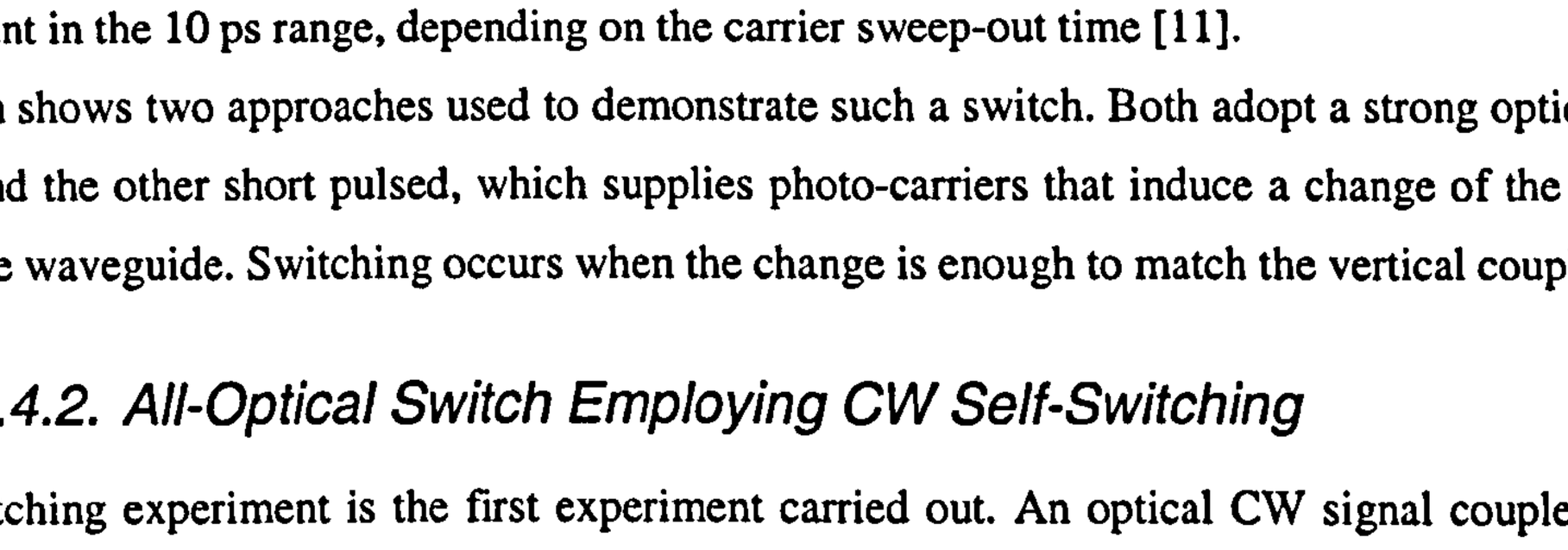

Figure6.16 All-Optical Switching Experimental Setup

The experimental set-up employed, shown in Figure6.16, consist of two main parts before and after the OXS. A Tuneable Laser provides the optical signal at λ=1548 nm. An Erbium Doped Fiber Amplifier (EDFA) is used to provide the power required. A Variable Optical Attenuator (VOA) is introduced to

control the optical power, a 3 dB coupler splits the signal to let a PM read the input power and a PC to minimise the polarization sensitivity. At the cross output of the switch the signal is coupled into a fiber lens, filtered at the input signal wavelength and read by an OSA in PM configuration.

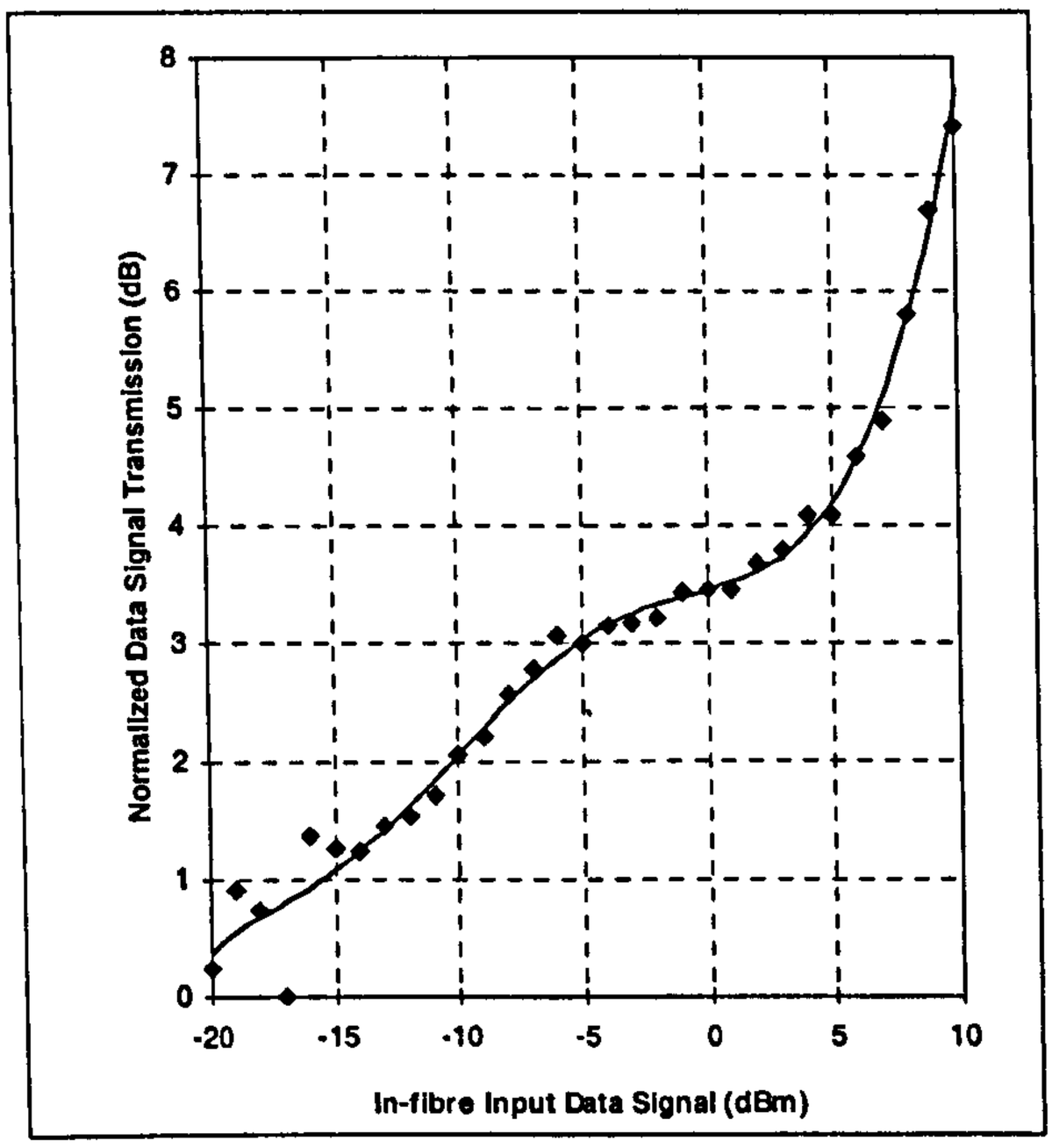

Figure6.17 Normalized transmission at the cross end employing a CW self switching signal

Figure6.17 shows the normalised transmission as a function of the input signal. An increase in transmission of 8 dB is achieved with an in-fibre input signal increase from –20 dBm to 10 dBm. In the graph can be seen a flex point that changes the gradient. This is believed to be due to the photo-carrier density being sufficiently high to start to saturate the absorption of the active layer. Thus, from that point forward more input signal is switched to the cross end.

6.4.3. All-Optical Switching Employing Pulsed Self-Switching

A much sharper switch can be achieved using a short-pulse. In this case the shorter is the pulse width, the higher is the peak power and hence the higher is the refractive index change. Thus the second all-optical experiment employs a pulsed self-switching optical signal.

Short-pulse generation can be achieved through mode-locking, Q-switching and gain-switching [12]. In this experiment the light source used is a gain-switching DFB laser that Dr. Igor Y. Khrushchev has realised by driving the current of a DFB laser with a pulsed signal produced with a RF generator, see Figure6.18. The gain-switched pulse is chirp compensated using Dispersion Compensation Fiber (DCF). A pulsed optical signal with a pulsewidth of 5 ps and repetition rate of 250 MHz at wavelength of 1548 nm is obtained. An EDFA amplifies the pulse stream up to 15dBm average power, which may be reduced if necessary, by a Variable Optical Attenuator (VOA). A fiber polarisation controller following

the variable attenuator ensures correct polarisation launch. The output signal level is filtered at the DFB laser wavelength and measured by an optical PM.

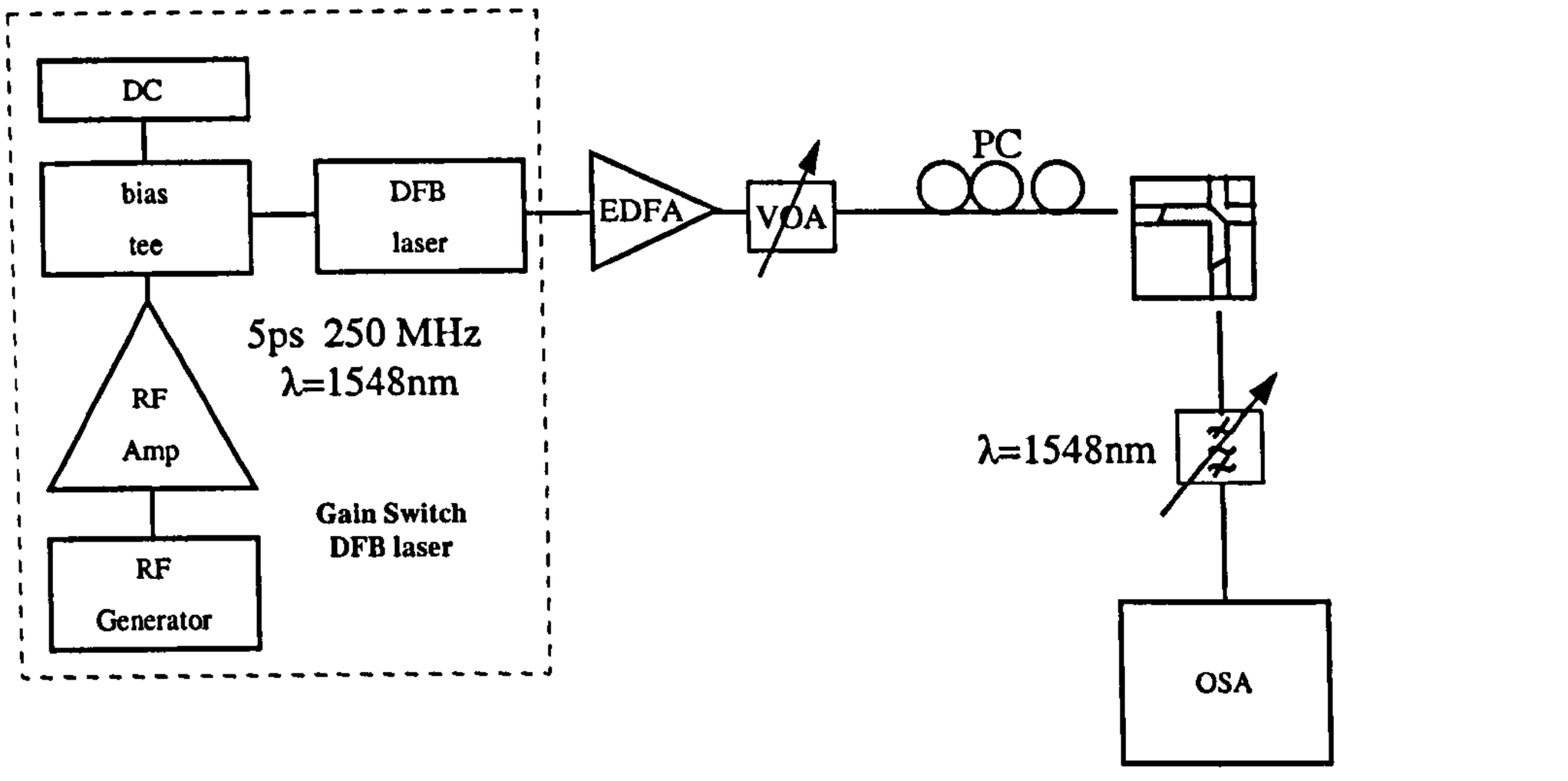

Figure6.18 All-Optical Switching Employing Photocarrier-Induced Non-Linearity

By choosing the coupler lengths at either side of the coupler two kinds of device ('initially on' and 'initially off') are made.

Figure6.19 shows the pulsed optical self-switching characteristics of the switches. With the 'initially off' device, a switching contrast of about 12dB is achieved while the contrast is as high as 23dB for the 'initially on' device.

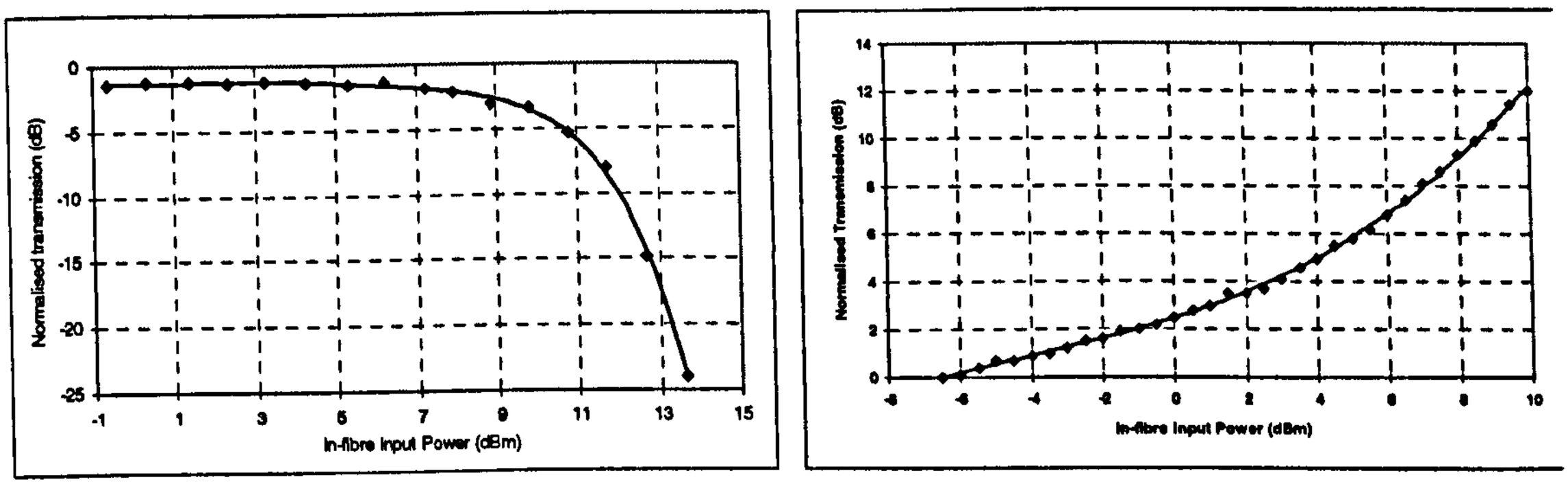

(a) (b)

Figure6.19 Normalised transmission of (a) 'initially on' and (b) 'initially off' devices

The 'initially off' device shows a gradual increase in transmission while the 'initially on' device shows much sharper switching characteristics, with a switching contrast of 20dB observed in the input power range of 10dBm to 14dBm.

Such charts cannot be explained by saturation effect because under saturation conditions the *Absorption Coefficient* α in the active layer, expressed by the [13]:

$$\alpha = \frac{\alpha_0}{1 + \frac{P}{P_{sat}}} \tag{6.8}$$

reduces as P increases and the *Transmission coefficient T*

$$T = 1 - e^{\alpha L} \tag{6.9}$$

should increase. Thus, for example the transmission of the 'Initially ON' device should further increase rather then falling. It is therefore believed that index-induce coupling played a major role in this process.

6.5. Conclusions

After an initial analysis of the bottom and top layer of the device, static and dynamic characteristics of this novel device have been studied in this chapter. Operating at 1550 nm an ON-OFF contrast higher than 50 dB is observed. An ultralow crosstalk of roughly 50dB and a 3dB bandwidth of more than 40nm have been observed. Switch-ON and switch-OFF times are 1.4 ns and 1.1 ns respectively, suitable values for interpacket guard time in packet switching networks.

Non-linear tests have also been carried out and show some encouraging results that suggest further investigation like dynamic tests able to work out the switching speed of the device. Further loss reduction and switching power are two very important points to be investigated.

Chapter 7 is dedicated to the main applications of this novel device: Optical Packet Switching.

6.6. References

[1] R.S. Longhurst, "Geometrical and Physical Optics - 3rd ed.", 1973, Longmans

[2] E. Hecht, "Optics - 3rd ed", 1998, Addison-Wesley

[3] S.M. Sze, "Physics of Semiconductor Devices - 2nd ed.", 1981, John Wiley & Sons, Inc

[4] L.A. Coldren, S.W. Corzine, "Diode Laser and Photonic Integrated Circuits", 1995, John Wiley & Sons, Inc

[5] P. Tolivier, R.J. Runsen, I. Glesk, P.R. Prucnal: 'Comparison of three nonlinear interferometric optical switch geometries', Optics Communication, 2000, 175, (1-3), pp. 365-373

[6] J.H. Lee: 'Nonlinear switching behaviors in a compact all-semiconductor optical amplifier Sagnac interferometer device', IEEE J. of quantum electronics, 1999, 35, (10), pp. 1469-1477

[7] K. Tajima, et al.: 'Hybrid integrated symmetric Mach-Zehnder all-optical switch with ultrafast, high extinction switching', Electronics Letters, 1999, 35, (23), pp. 2030-2031

[8] K. Nakatsuhara, 'GaInAsP-InP distributed feedback waveguides for all-optical switching', IEEE J. of selected topics in quantum electronics, 2000, **6**, (1), pp. 143-149

[9] R.W. Boyd, 'Nonlinear Optics' 1992, Academic Press Inc.

[10] R.M. Geatches, S.V. Dewar, R.V. Penty, 'Reduced-power semiconductor all-optical switch design' IEE Proceedings-Optoelectronics, 1997, **144**, (1), pp. 2-7

[11] I.E. Day et al.: 'Low power all-optical polarisation gate switching a passive InGaAsP MQW waveguide at 1.53-MU-M', Electronics Letters, 1994, 30, (13), pp. 1050-1051

[12] P. Vassilev, 'Ultrafast Diode Lasers – Fundamentals and Applications' Artech House Publishers, Boston-London, 1995

[13] S. Schmitt-Rink, D.S. Chemla, and D.A.B. Miller, "Linear and Non-Linear Optical Properties of Semiconductor Quantum Wells", Advances in Physics, 1989, 12, (2), pp. 89-188.

Chapter 7

Packet Switching Performances

This chapter describes the experiments that demonstrate the novel crosspoint switch working in packet switching applications. The first part of the chapter demonstrates in-house experiments using the crosspoint device for packet switching at 10Gb/s payload data rate. The second section uses the device for an experiment of simultaneous packet switching and wavelength conversion. Finally the device is employed in a real optical packet switching network WASPNET.

Glossary of the abbreviations

(OXS)	Optical Crosspoint Switch
(NRZ)	Non Return to Zero
(PRBS)	Pseudo Random Bit Sequence
(OBPF)	Optical Band-Pass Filter
(OXC)	Optical Cross-Connect
(XGM)	Cross-Gain Modulation
(XIM)	Cross-Index Modulation
(AUW)	Active Upper Waveguide
(EDFA)	Erbium Doped Fibre Amplifier
(WASPNET)	Wavelength Switched Packet Network
(SCWP)	Scattered Wavelength Path

7.1.10 Gb/s Packet Routing Demonstration

Table7.1 shows a summary of the characteristics of the crosspoint produced as a result of the work set-out in previous chapters.

Matrix	4x4 space switch array
Material	InGaAsP/InP
Size	250x250μm/switch
Wavelength	1550nm
Crosstalk	<-50dB
On-Off Contrast	50dB
Optical Bandwidth	>40nm
Switch-ON Time	1.4ns
Switch-OFF Time	1.1ns

Table7.1 Optical characteristics of the novel crosspoint switch

This section investigates the Optical Crosspoint Switch (OXS) during a high-speed packet routing test with data rates up to 10Gb/s.

7.1.1. High Speed Routing Experimental Set-Up

Figure7.1 depicts the high-speed routing experimental set-up. The space switch array is bonded on top of a RF submount with one of its units wire bonded in series with a 47Ω impedance-matching resistor. The submount is fixed on the stage, which is without any temperature control or cooling system.

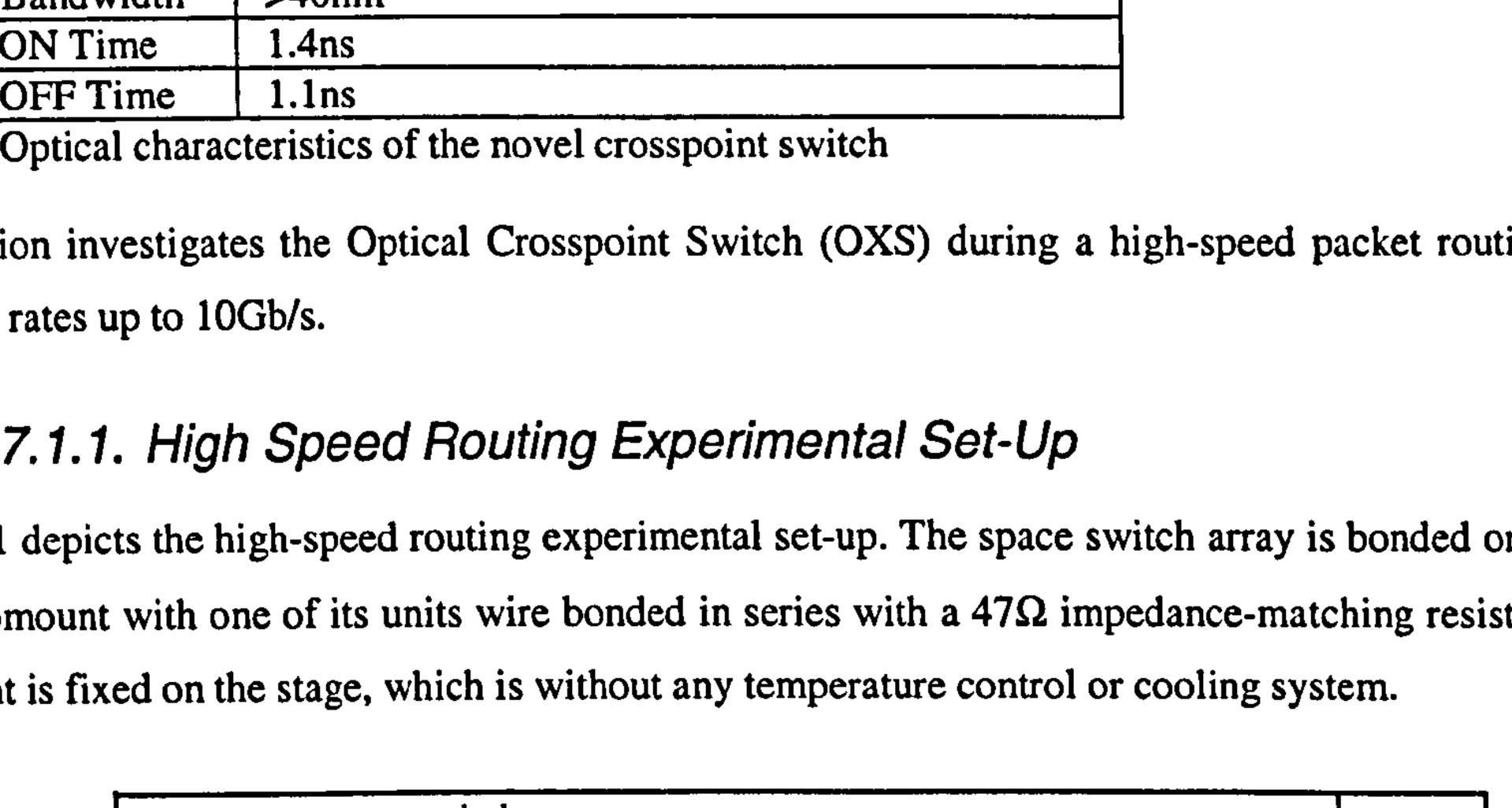

Figure7.1 The experimental set-up for high-speed packet routing

On the input side of the crosspoint, a pattern generator modulate a DFB laser at λ=1554nm. In order to emulate the packet streams, the laser is modulated with a Non Return to Zero (NRZ) Pseudo Random Bit Sequence (PRBS) of 2^7-1 length and data rate of 10Gb/s. The initial bits of the sequence are substituted by zeros, the number of which is varied between 10-63 to form inter-packet guard-band of 1.0-6.3ns.

After passing through a polarisation controller, a lensed fibre couples the generated optical packets into the space switch. This switch is driven by a pulse generator, synchronised to every other packet and able to produce a pulse of 5V amplitude, with 1.0ns leading and trailing edges, which corresponds to injection current amplitude of 80mA into the switch. No precise current control is needed for the device thanks to its levelling-off switching characteristics as shown in previous section 5.2.1.

The output signal from the perpendicular output port of the space switch is coupled into a lensed fibre. The signal passes through an Optical Band-Pass Filter (OBPF), to suppress spontaneous emission noise, and is detected by a HP11982A lightwave converter and displayed on the digital oscilloscope.

7.1.2. Optical Packet Routing Results

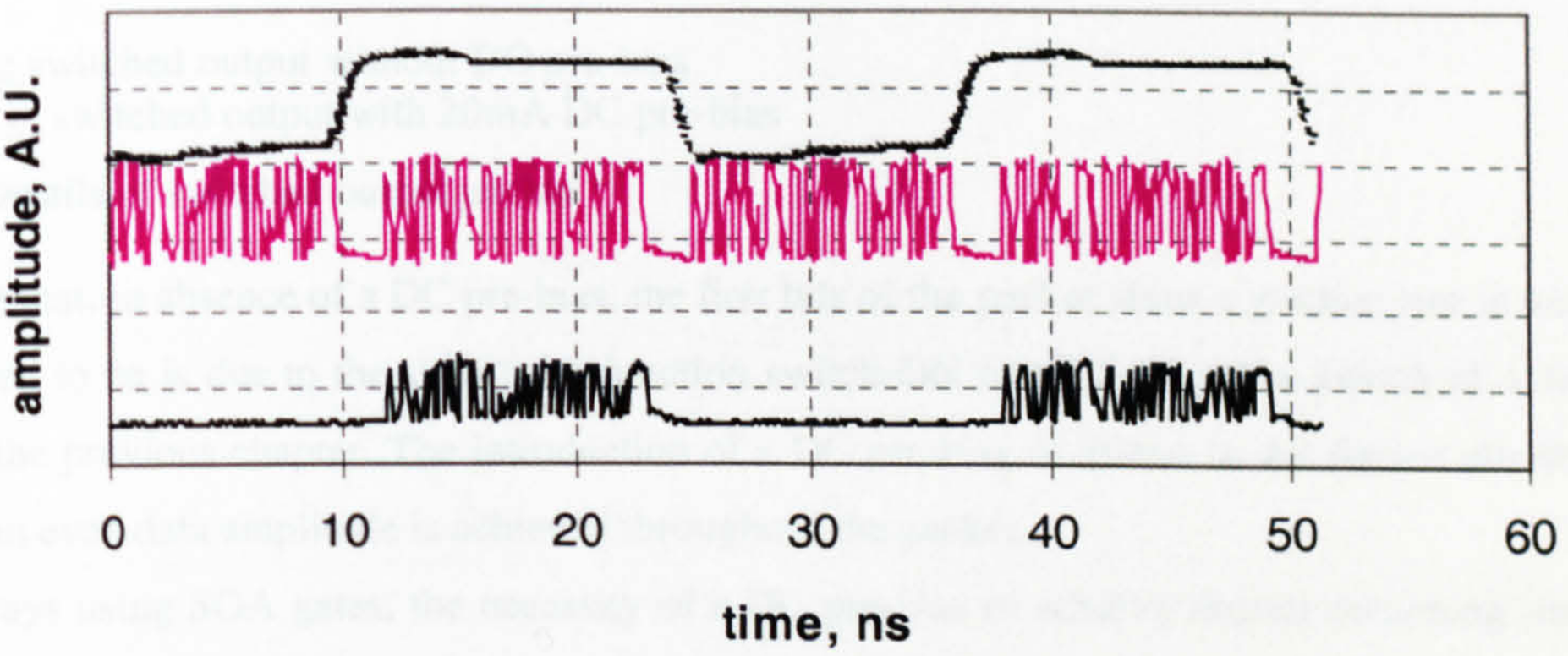

Upper trace: Control current to switch
Middle trace: Input packet train
Lower trace: Routed packet train

Figure7.2 Routing of packets with 2ns guard-band

Figure7.2 shows the routing results with the *upper trace* representing the driving switching current, the middle trace the packet stream, with a 2ns guard-band and the lower trace *the switched output of the* cross output.

Observing the lower trace it is clear that when the switch is in ON state, $I \neq 0$, the data packets are steered to the cross output. On the other hand, when the switch is in OFF state, $I = 0$, it suppress the packets by ~-50dB, which travel, instead, through the switch unit to the next switch unit.

Several routing tests have been carried out at different input optical power levels, from –5dBm up to 5dBm, without adverse effects observed.

Carrying on two different experiments, it has also found that the device needs to be DC pre-biased in order to give better results. Figure7.3 shows the details of 63 bit packets routed to the output.

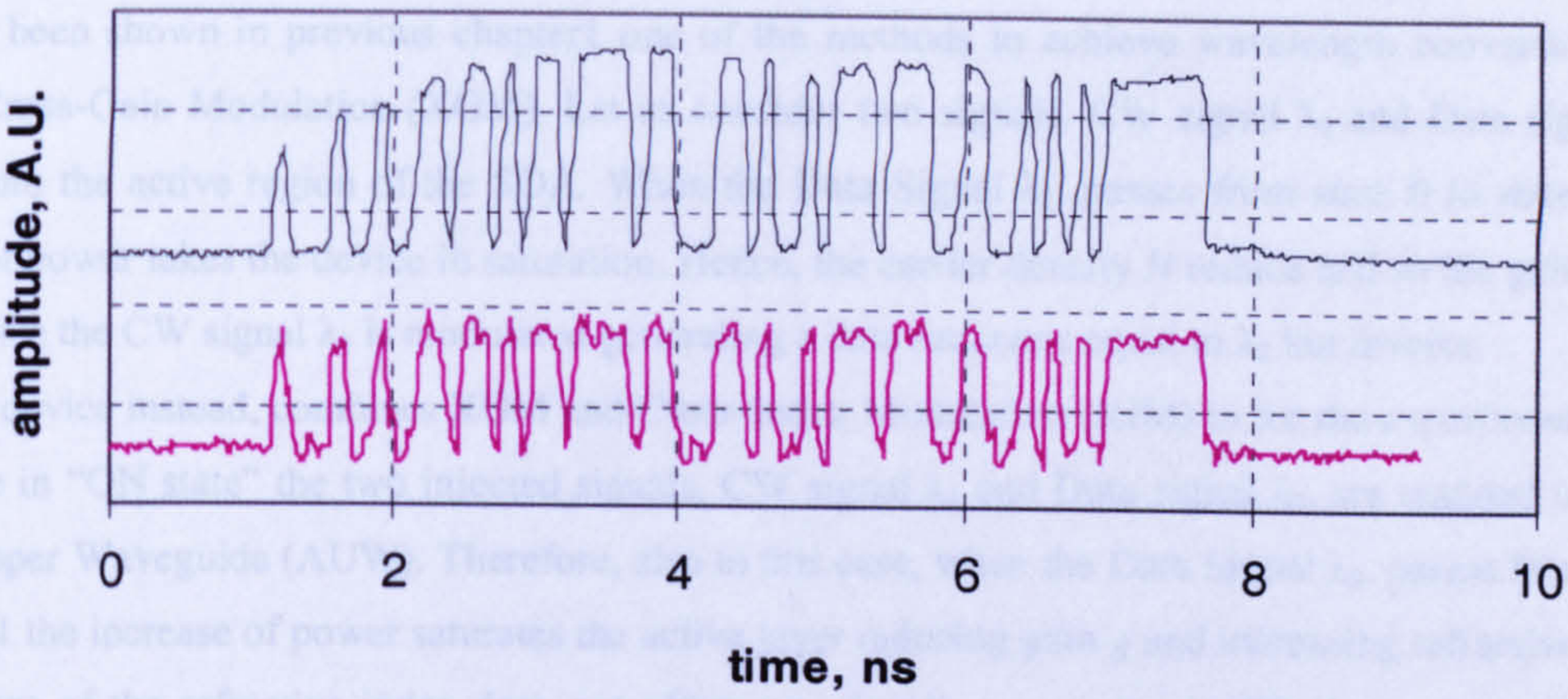

Upper trace: switched output without DC pre-bias
Lower trace: switched output with 20mA DC pre-bias

Figure7.3 Details of switched output packet

It is evident that, in absence of a DC pre-bias, *the first bits of the packet show a gradual rise in amplitude.* This believed to be is due to the slow p-i-n junction switch-ON time of the space switch of 1.4ns as we showed in the previous chapter. The introduction of a DC pre-bias of 20mA to the device eliminates the effect and an even data amplitude is achieved throughout the packet.

Like all arrays using SOA gates, the necessity of a DC pre-bias to achieve shorter switching time could deteriorate the crosstalk performance. In fact under such conditions the adjacent packet suppression reduces to ~-25dB as is predictable from the DC switching characteristics of figure6.9.

7.2.10 Gb/s Simultaneous Packet Routing and Wavelength Conversion

Both wavelength conversion and space switching are fundamental enabling technologies in future high speed optical networks. All-Optical wavelength conversion is very *useful in packet based networks* because it can resolve packet contention and reduce optical buffering requirements [1]. However, these technologies are usually performed by separate wavelength converters and space switch arrays, resulting in large number of components in the Optical Cross-Connect (OXC) nodes.

In the past it has proven that both functionalities can be performed simultaneously in a space switch array with data rates up to 2.5Gb/s[2]. Thus, this section investigates the possibility to use the novel OXS for wavelength conversion applications at routing speed up to 10Gbps. In this section the principle of this particular implementation is set out. Then an experiment on the OXS device, which realises the switching of the packets simultaneously with wavelength conversion, is described.

7.2.1. Theoretical Analysis of Wavelength Conversion in the OXS

As it has been shown in previous chapter1 one of the methods to achieve wavelength conversion in a SOA is Cross-Gain Modulation (XGM). Let us consider two signals, CW signal λ_1 and Data signal λ_2, coupled into the active region of the SOA. When the Data Signal λ_2, passes from state 0 to state 1, the increase of power takes the device in saturation. Hence, the carrier density N reduce and so the gain g. As consequence the CW signal λ_1 is modulated generating a data sequence equal to λ_2 but inverse.

The OXS device instead, combines XGM and Cross-Index Modulation (XIM) in for the experiment. With the device in "ON state" the two injected signals, CW signal λ_1 and Data signal λ_2, are coupled into the Active Upper Waveguide (AUW). Therefore, also in this case, when the Data Signal λ_2, passes from state 0 to state 1 the increase of power saturates the active layer reducing gain g and increasing refractive index n. A change of the refractive index does not effect wavelength conversion in SOA's but it does in the OXS device. A reduction in gain produces an increase in refractive index damaging the optimum coupling. Thereby the combination of both effects results in inverse data modulation on CW λ_1 wavelength. Figure7.4 present causes and effect generated by XGM.

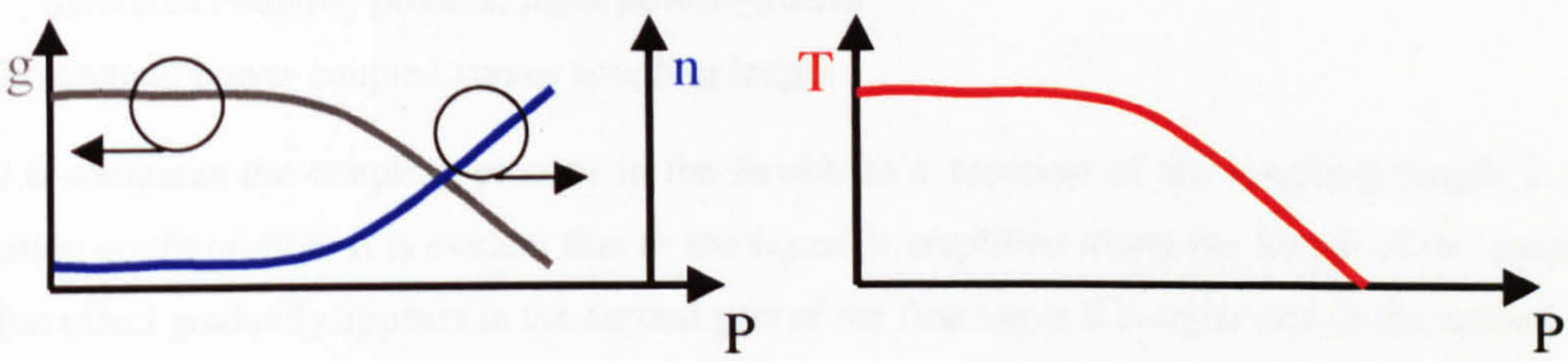

Figure7.4 Causes and effect of optical XGM

A simplified theoretical model has been used in order to calculate the transmission change of the device due to carrier density reduction under high input conditions.

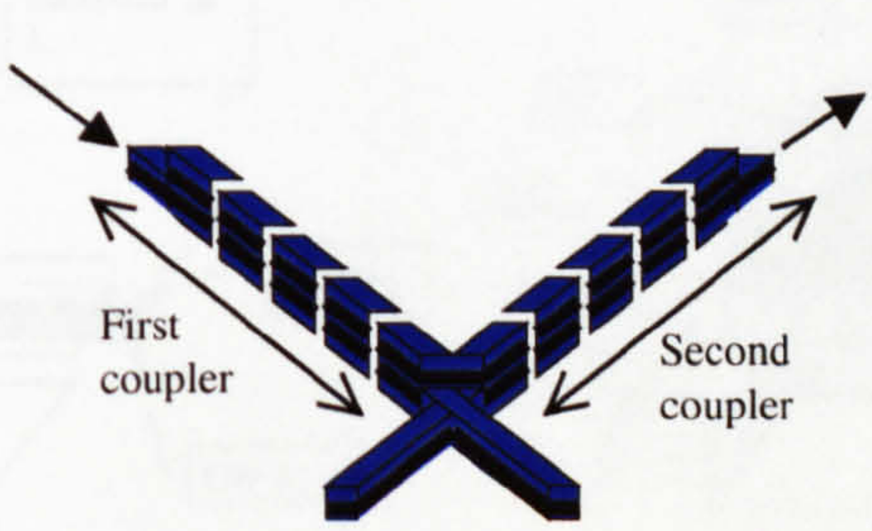

Figure7.5 Schematic diagram of the wavelength converter OXS structure

It is similar to the coupling model developed for the device described in chapter 3 but the coupling sections have been divided into a number of sections in order to take into consideration the carrier density distribution along the coupler length, as shown in Figure7.5.

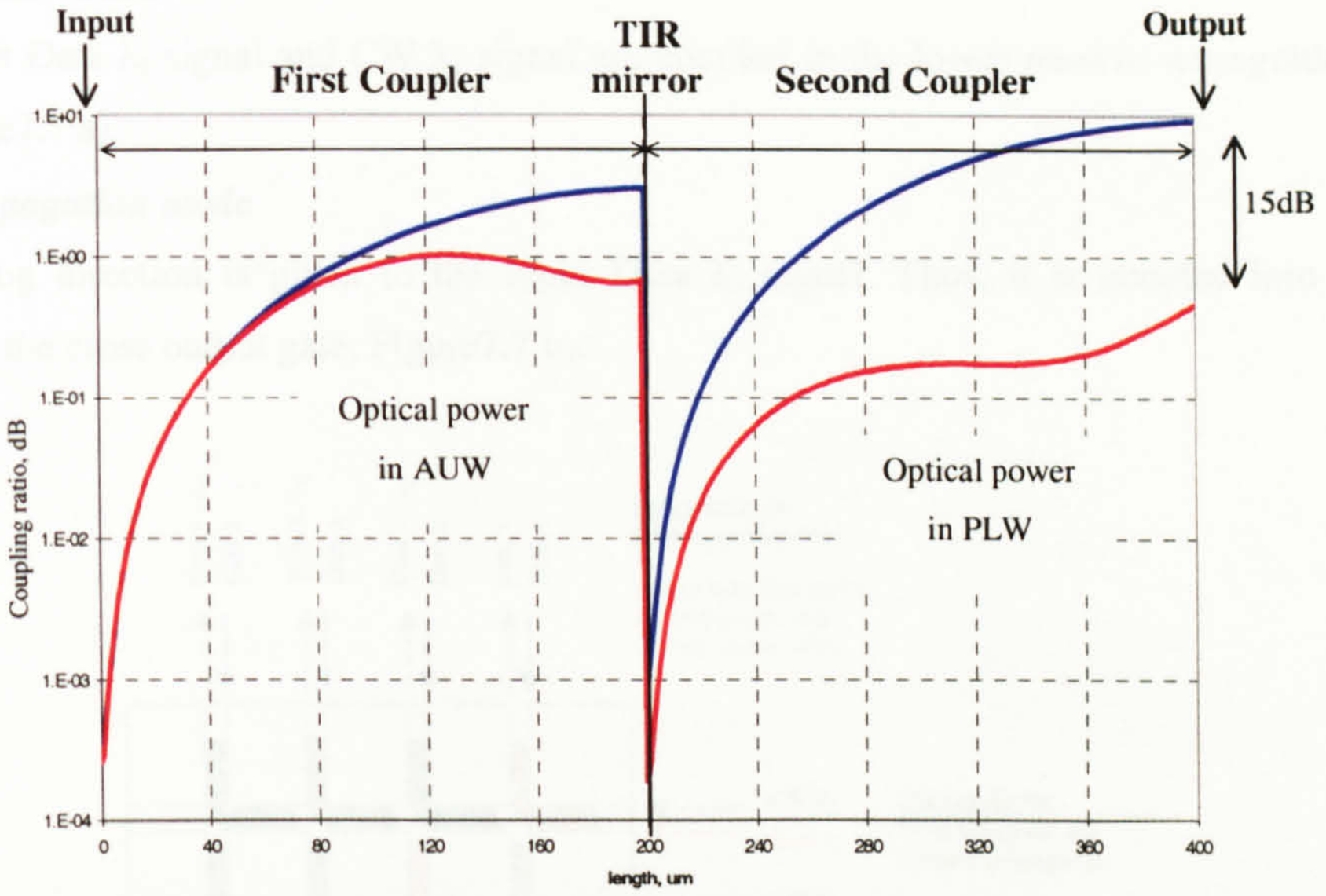

Un-saturated coupling process

Saturated coupling process, Input power ~5dBm

Figure7.6 Optical power coupled versus coupling length.

Figure7.6 compares the coupling process in the device as a function of the coupling length in the co-propagation configuration. It is evident that as the signal is amplified along the length of the couplers the saturation effect gradually appears in the second part of the first vertical coupler and in the second vertical coupler. Thus, as consequence of this effect 15 dB reduction of the transmission at the device output is achieved when compared with the Un-saturated coupling process.

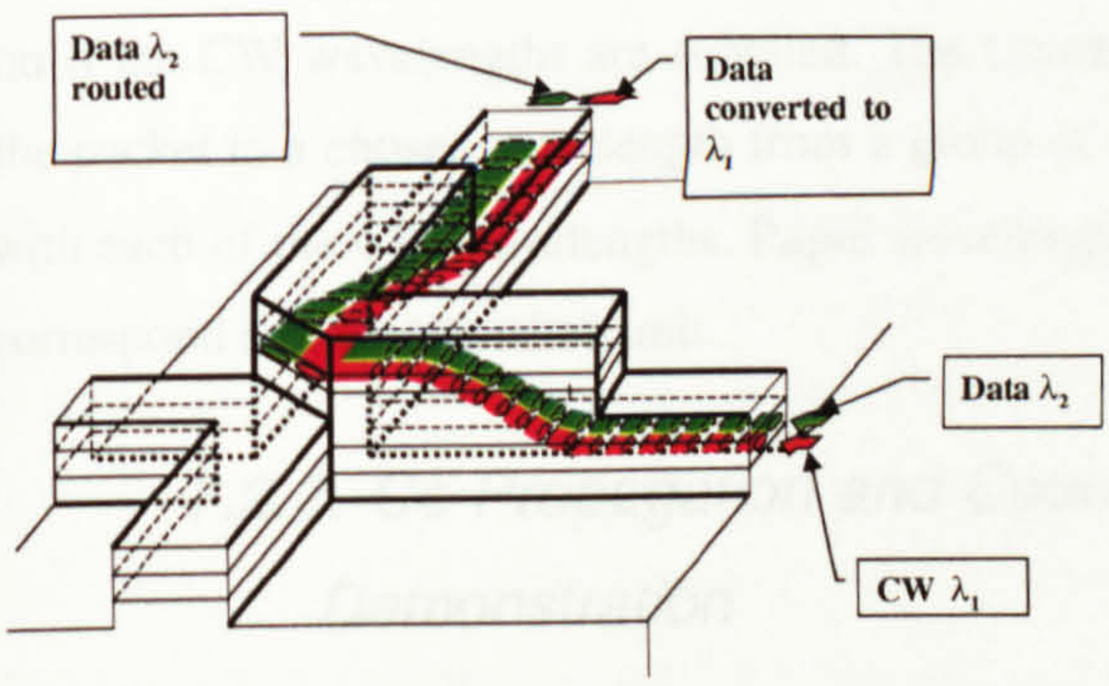

a)

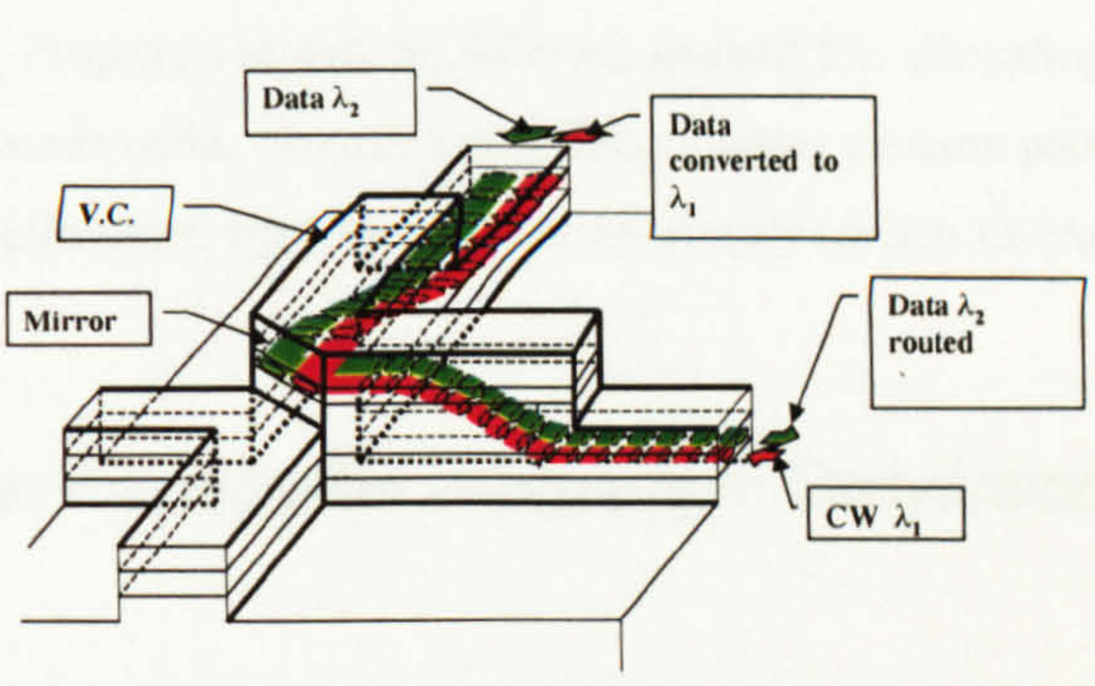

b)

a) Co-Propagation

b) Counter-Propagation

Figure7.7 Possible λ-conversion Modes

The single device can be used in two different wavelength conversion modes:

- ***co-propagation mode***

In this case Input Data λ_2 signal and CW λ_1 signal are coupled in the lower passive waveguide from the input gate, Figure7.7 a).

- ***counter-propagation mode***

Opposite coupling direction is given to the Input Data λ_2 signal. Thus, it is coupled into the lower waveguide from the cross output gate, Figure7.7 b).

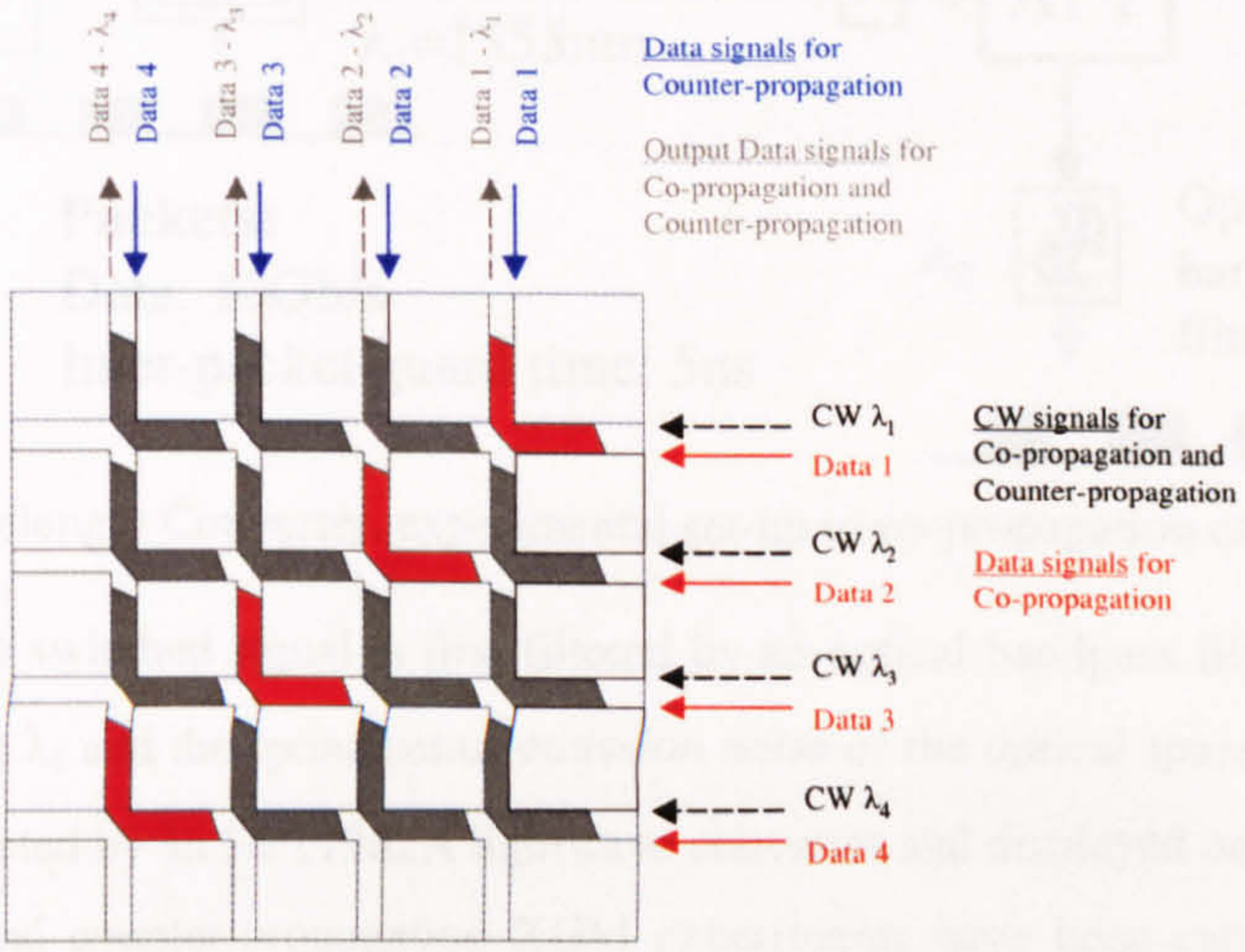

Figure7.8 Possible λ-conversion modes in the integrated matrix

Finally in an OXS matrix, as shown in Figure7.8, λ-Conversion Modes can be extended and again both Co- and Counter-Propagation can be realised. The co-propagation configuration can be used in order to achieve a simplified network node, which is able to switch, λ-convert or both at the same time depending on if the CW wavelengths are supplied. The Counter-Propagation can be adopted instead for allocating the packet to a chosen wavelength from a group of wavelengths, as each input data channel crosses path with each of the CW wavelengths. Rapid wavelength allocation may be realised by simply switch on the correspond crosspoint switch unit.

7.2.2. Co-Propagation and Counter Propagation Wavelength Conversion Demonstration

The experimental set-up is realised using a DFB laser as CW source with a emitting wavelength of λ_2=1548nm and optical power set at -10dBm measured at the input fibre lens. A 10Gb/s pattern generator generates the data packets which are applied to a $LiNbO_3$ Mach Zehnder modulator to modulate the light λ_1 from a 1470-1580nm tuneable optical source. The modulated signal is amplified in an Erbium Doped Fibre Amplifier (EDFA) which increases the power level up to about 10dBm at the input fibre lens.

The optical space switch used is made with the MR1392 material which contains InGaAsP bulk waveguides. At 160mA the device is able to give an internal optical gain of about 10dB, or fibre-fibre

transmission of about 0dB, at a gain peak wavelength at 1555nm. A variable amplitude pulse source synchronised through the pattern generator to the data packets, drives the space switch.

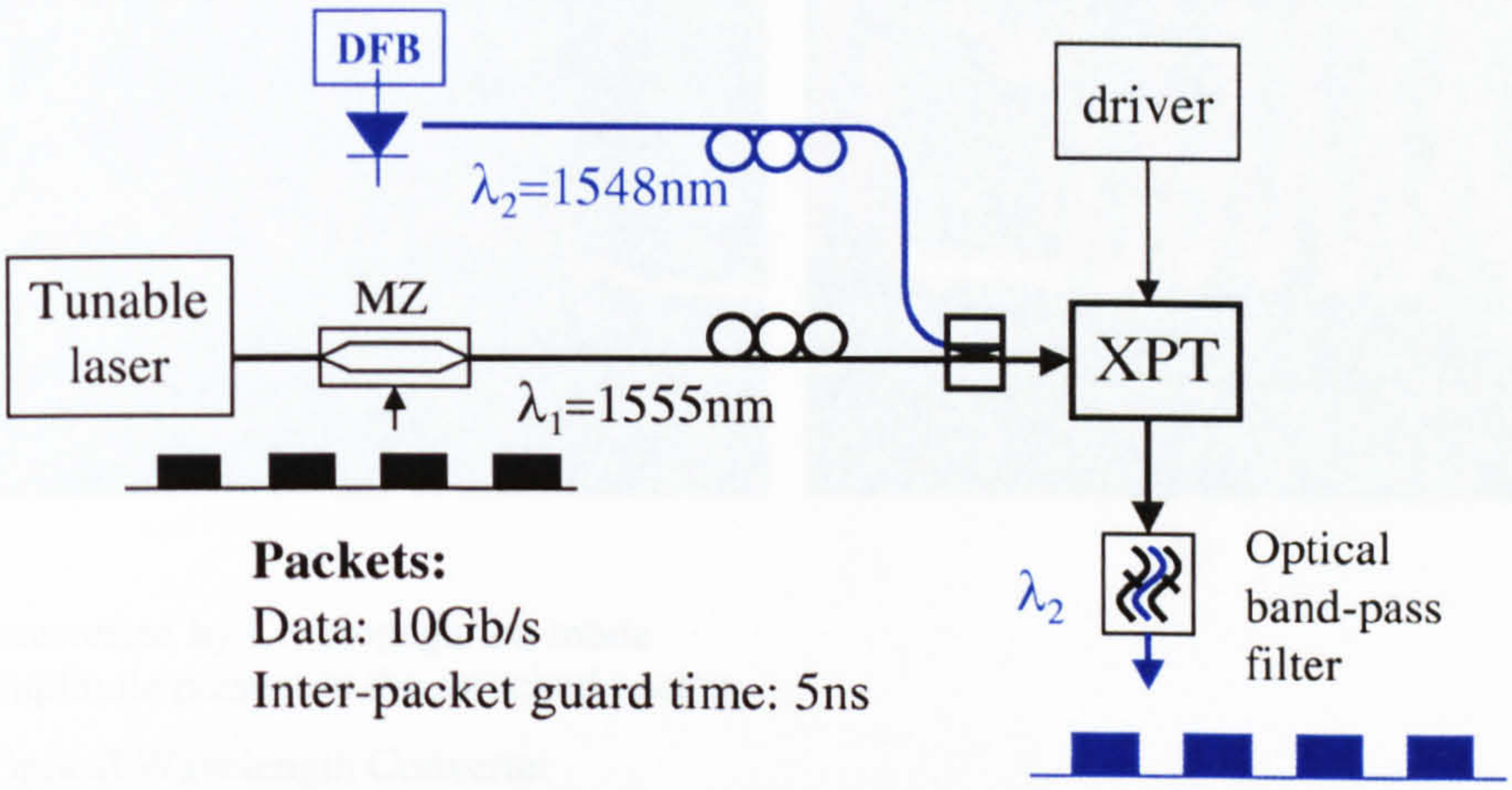

Figure7.9 Optical Wavelength Converter, experimental set-up in co-propagation configuration

On the cross output the switched signal is first filtered by an optical bandpass filter set at λ_2 to suppress both the original data at λ_1 and the spontaneous emission noise of the optical space switch. The converted signal at λ_1 is then detected by an HP11982A lightwave converter and displayed on an oscilloscope.

Both co-propagation and counter-propagation XGM experiments have been carried out, with the data wavelength set at λ_1=1555nm. in the co-propagation arrangement, shown in Figure7.9, the CW light and the data are combined with a 3dB coupler and coupled into the space switch from the same port using a fibre lens. In the counter-propagation arrangement, instead, the CW light is coupled into the space switch from the input port, while the data is coupled into the space switch from the cross output port.

7.2.3. Optical Wavelength Converted Packet Routed Results

Both co-propagation and counter-propagation experiments have successfully shown wavelength conversion while the data packet is routed at a data rate of 10Gb/s. The guard time is 5ns.

Figure 7.10 shows the results for the co-propagation mode and in particular Figure 7.10 *a)* shows a packet converted to λ_2 with an extinction ratio of about 9dB. Uneven amplitude has been observed which can be attributed to the um-matched contact probe used in this experiment, generating pulse fluctuations of the injection current. Carrier dynamics related structure shown in Figure 7.10 *b)* is also observed. While the data is largely clean, the slower recovery ($\tau \approx 300$ps) after the longer saturation, indicated by the arrow, is typical for the slow carrier transport across a bulk active layer. This may be rectified by improved AR coating, thus allowing higher injection current before the onset of too much gain ripples. Optimised QW structure could also reduce this recovery time.

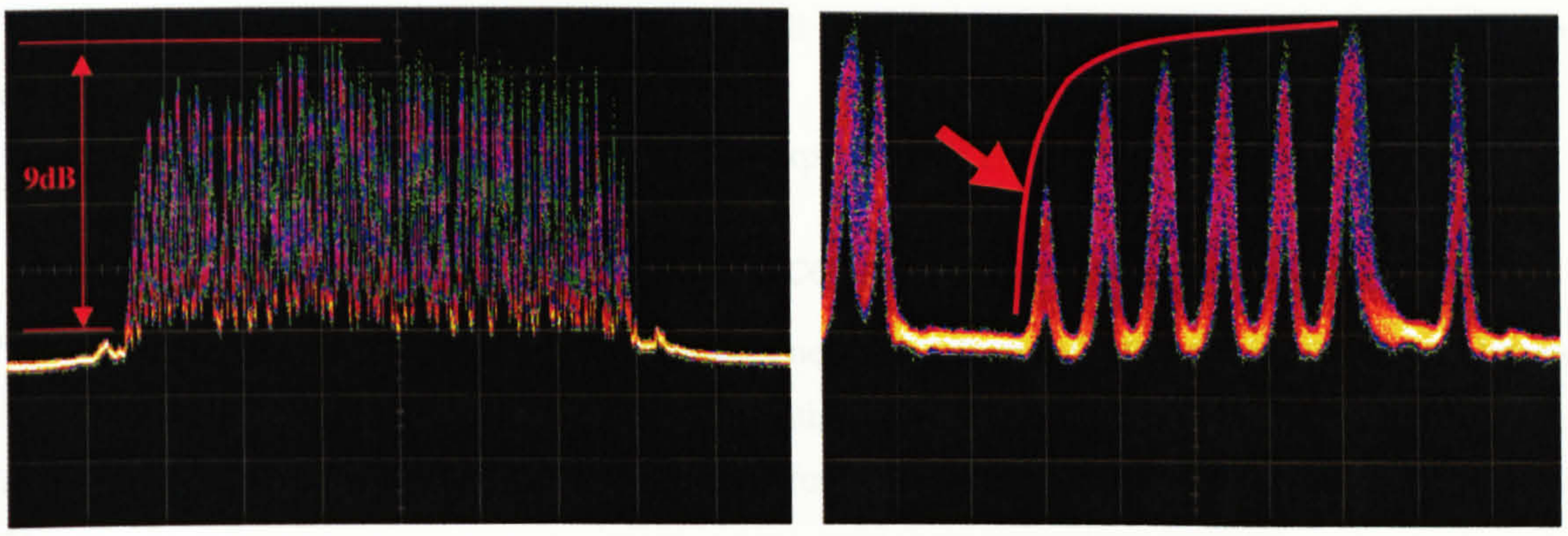

a) *b)*

a) Packet λ-converted by Co-propagation mode
b) Uneven amplitude present in the switched packet

Figure7.10 Optical Wavelength Converter

Figure7.11 shows similar results from the counter-propagation experiment. The best extinction ratio achieved is about 7.5dB, which is less than that in the co-propagation experiment.

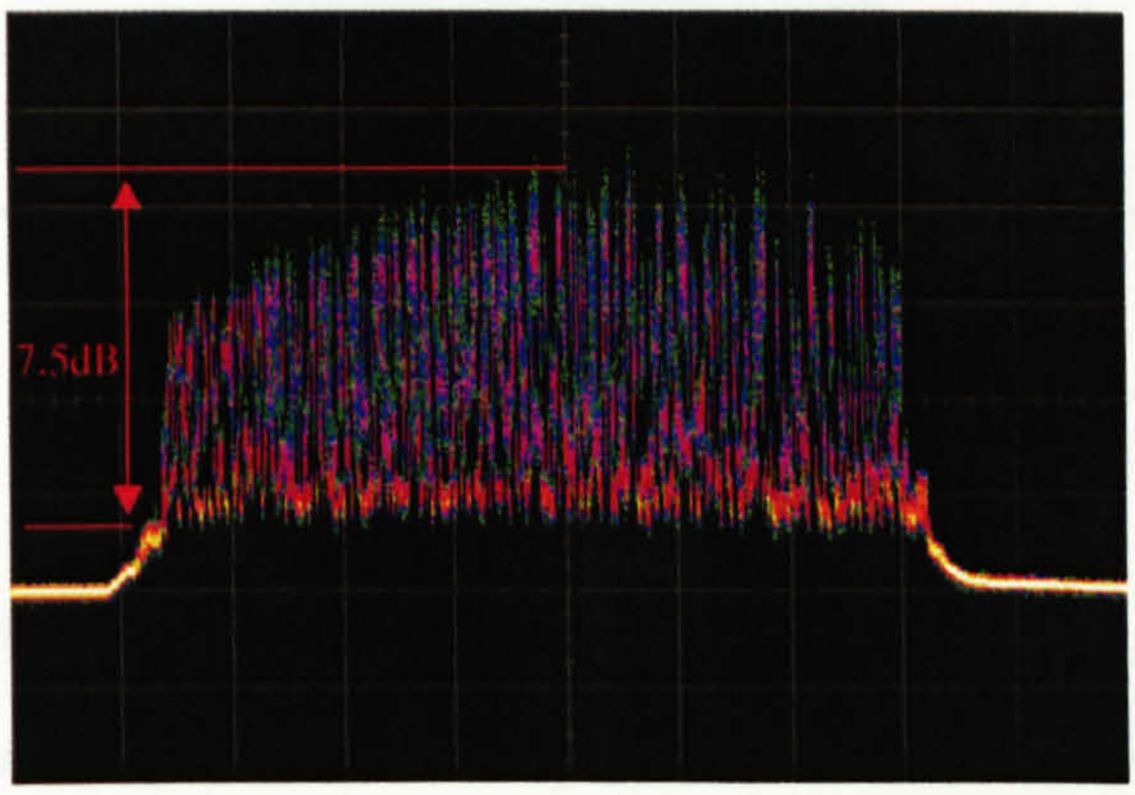

Figure7.11 Packet λ-converted by Counter-propagation mode

7.3. Demonstration in the Wavelength Switched Packet Network – WaSPNet project

7.3.1. What WaSPNet is

WASPNET (Wavelength Switched Packet Network) is a WDM transport network that uses optical packet switching to support IP, ATM or SDH traffic. The project is a collaboration between three UK universities, Essex, Bristol and Strathclyde and is supported by a number of industrial institutions.
The function of University of Bristol and in particular my author position inside the project is to make test a supply an optical crosspoint switch fast enough to be used in the node network

This section focuses on the results of a testbed experiment that evaluates the performance of a cascade of 14 optical packet routers, which supports the full functionality of header processing, contention resolution, packet switching and routing.

The crosspoint switch used for the realisation of the experiment is the same described in the past chapters.

7.3.2. WDM Transport Network Scenario

The WASPNET node is used in a WDM transport network, where to utilise the available wavelength channels efficiently each optical packet may be multiplexed onto any available wavelength within the fibres along its designated route. This technique is referred to as the Scattered Wavelength Path (SCWP) [3].

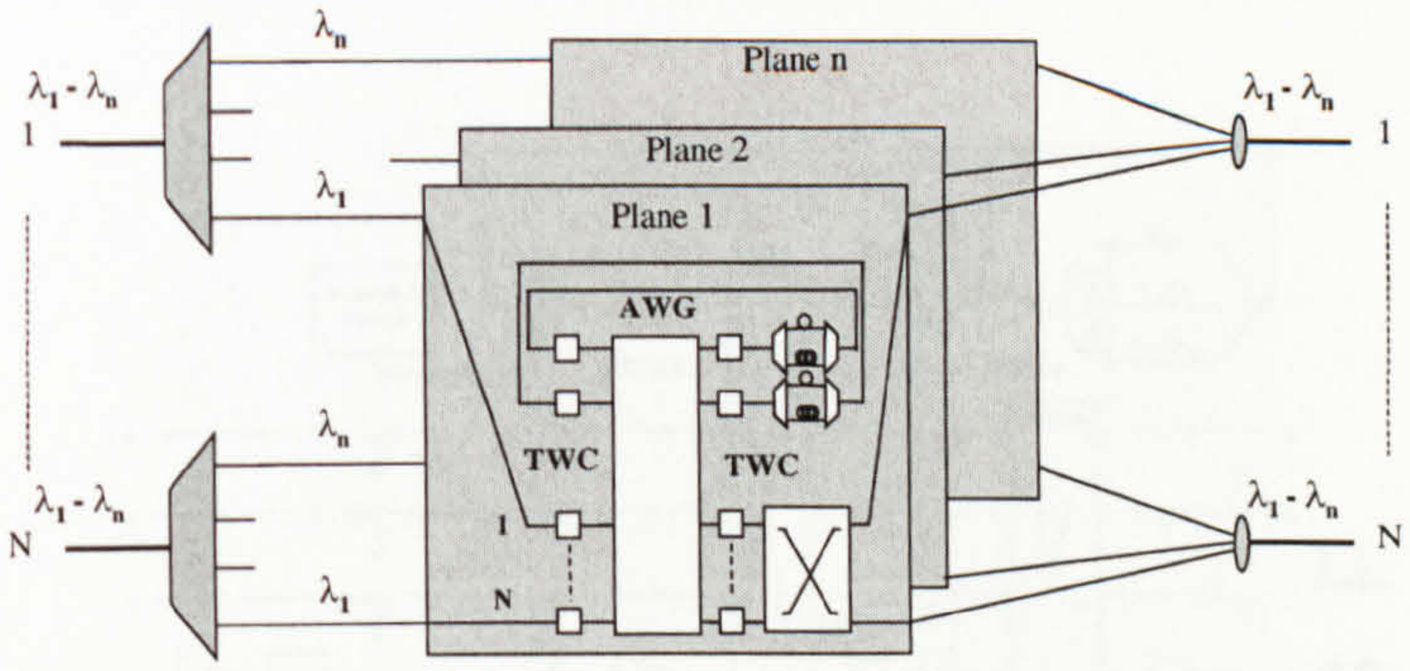

Figure7.12 Multi-plane architecture

There are a number of advantages to this, an important one being that SCWP can resolve packet contention by multiplexing contending packets onto different wavelength channels, this reduces the physical buffering depth requirement.

Figure7.12 shows the N fibre multi-plane architecture used to support the SCWP strategy, each plane being responsible for routing and buffering packets which arrive on a particular wavelength. Packets arriving at each plane undergo header decoding and this information is used to control the payload switching, through a combination of wavelength routing and space switching. Buffering and wavelength selection are used to overcome contention within the wavelength plane, the optical space switch overcomes contention between the planes.

7.3.3. Results for 2.5 Gb/s Cascading and Routing 14 Optical Packet Switches

Figure7.13 shows the hardware comprising one of the n switch planes. In this experiment 4 inputs/outputs fibre ports are supported. The wavelength plane is positioned within a recirculating loop, *not shown in the* diagram, which comprises three fibre amplifiers and a total distance of 135km.

The following section describes the switch operation. The payload generator inserts a stream of payloads into the add port of the 16x16 AWG, in number sufficient to fill the loop at a bit rate of 2.5 Gb/s. At this point, by a suitable wavelength choice the payloads are routed to SOA2 where appropriate headers are, by modulation, inserted using a subcarrier multiplex technique. SOA2 is also used as a tuneable XGM wavelength converter to condition the packet to the appropriate network wavelength, as determined by the node/network control algorithm. The out-of-band header is an 8bit sequence comprising a stop and start bit plus 6 data bits. The subcarrier frequency is 2.8 GHz.

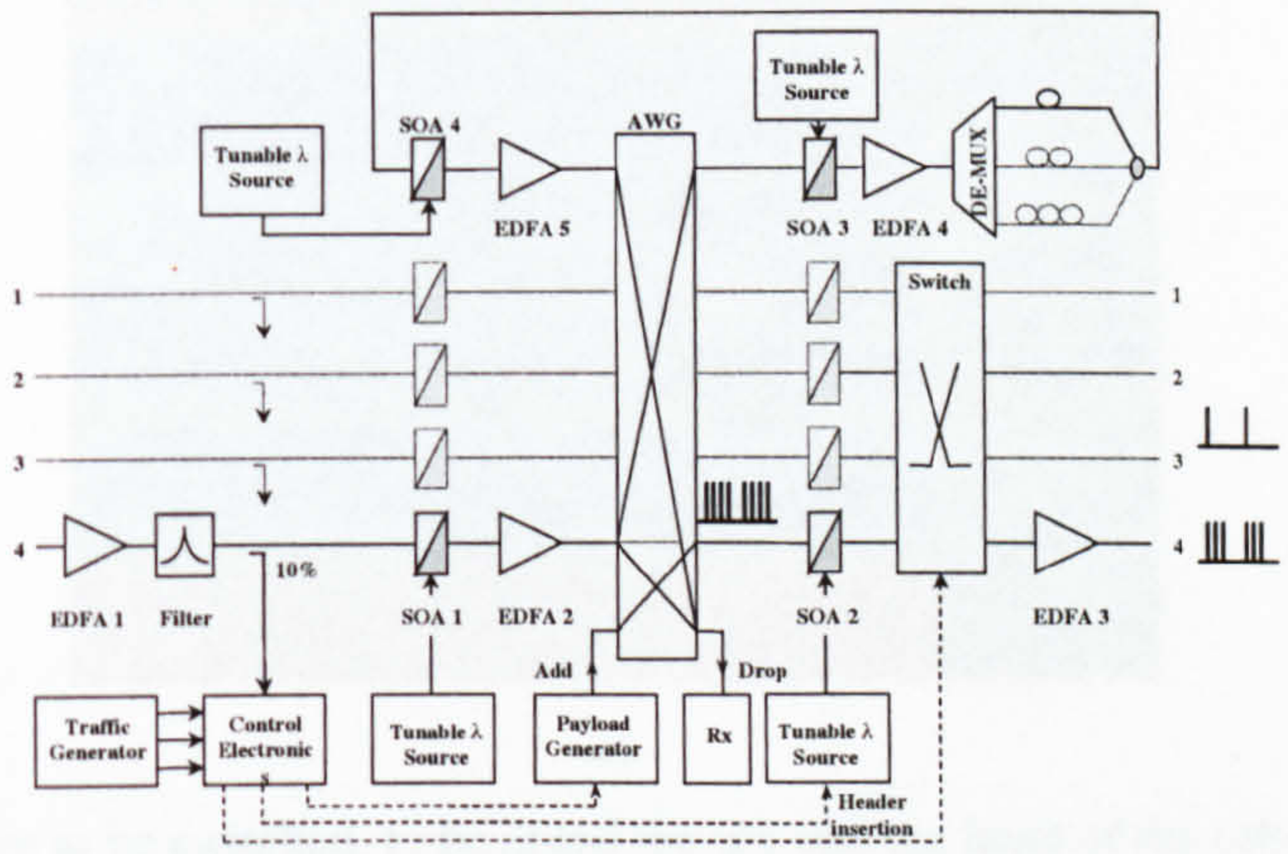

Figure7.13 Switch plane

Figure7.14 *a)* shows the packet format comprising the 52ns header a guard band of 8ns between header and payload and a conservative guardband of 60ns between packets. Total duration of the packet is 412ns and the payload duration is approximately 300ns.

Packets from the AWG enter the fast cross-point space switch, the same optical crosspoint switch investigated in this thesis, which provides switching between wavelength planes (controlled by the management algorithm) and controls access to the output fibres. Figure7.14 *b)* shows one by four switched packets. It can be seen that the head and the tail of the packets just before and after are removed from the packet train which is shown in Figure7.14 *c)*.

In this experiment output fibre 4 is selected and the output packets traverse the loop and re-enter the switch at the input of the same fibre.

The header is detected and evaluated in a look up table, which determines the payload wavelength necessary to route the packet through the AWG to the appropriate output port, and this information is used to control the SOA1 XGM converter. This converter also performs the function of header removal (through gating).

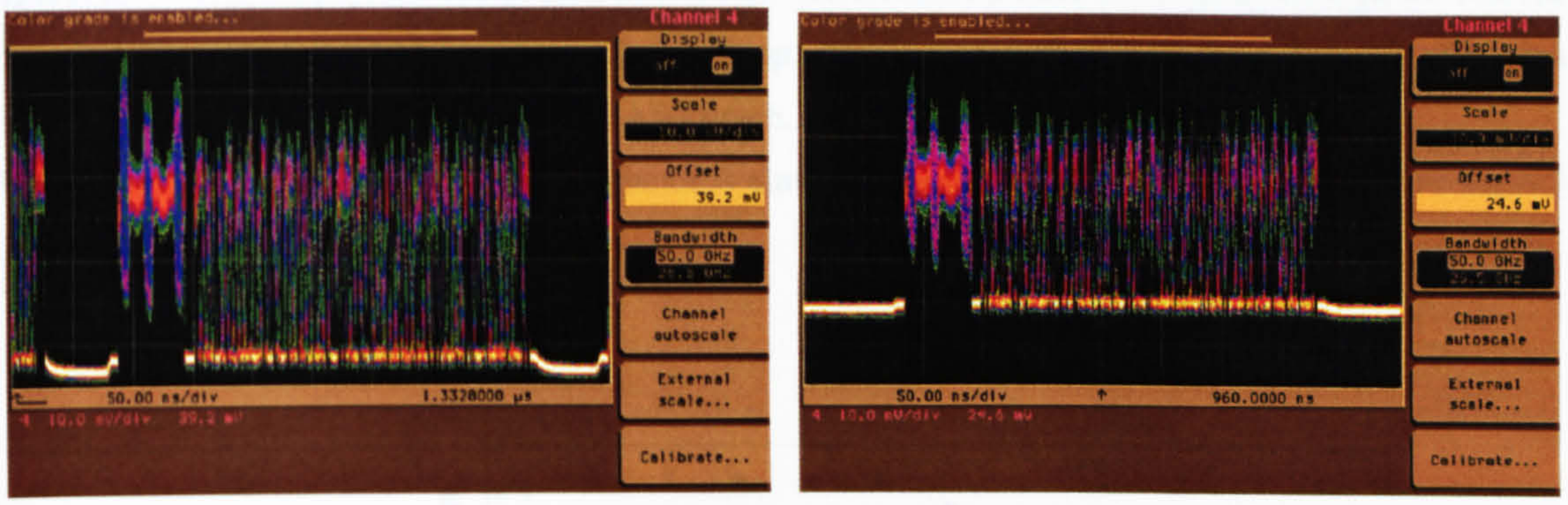

a) *b)* *c)*

a) The packet train before to be switched, to be noted the tail and the head of the other packets
b) The switched single packet
c) The switched packet train (1 packet switched each 4 packets)

Figure7.14 WASPNET Project: The packets before and after the OXS.

In the experiment contention resolution is demonstrated as follows [4]. The control electronics can be set to simulate the condition that any or all of fibre input ports 1-3 require accessing the same output port as input fibre 4. When the contention condition is detected packets from input port 4 are assigned a wavelength which routes them to the feedback buffer path.

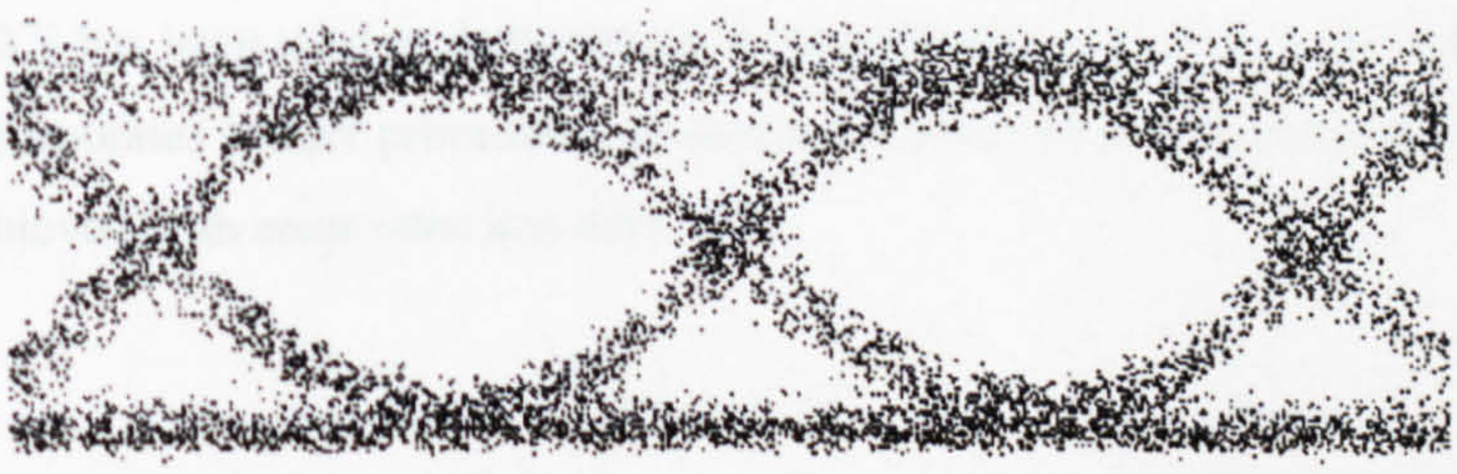

Figure7.15 Eye diagram after 10 circulations (1350km)

The switched delay lines are realised using a tuneable wavelength converter together with a demultiplexer. Studies show that use of the wavelength dimension considerably diminishes the number of physical buffers needed.

Figure7.15 shows the payload eye pattern after 10 circulations, for a total of 1350km, through the cascade of switches presented using the recirculating loop. The transmission path thus includes, for each circulation, 2 wavelength conversions, the AWG path, and the optical space switch.

From figure7.16 it can be seen that the Q-factor is almost constant within 10 circulations. It loses about 3 dB between 10 and 14 circulations.

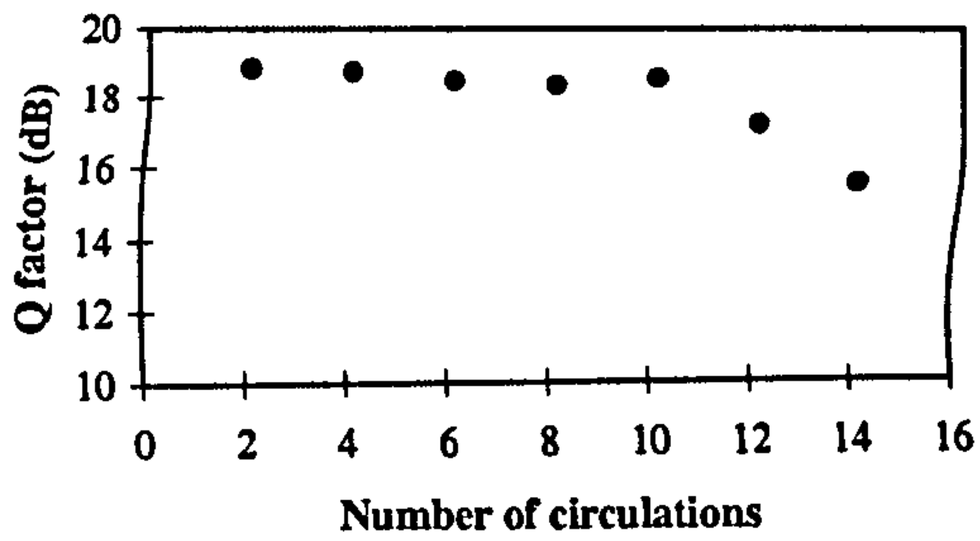

Figure7.16 Q-factor as a function of the numbers of circulations

7.4. Conclusions

Packet based networking is of particular interest for future highly dynamic optical networks. Thus this chapter has focused on some of the applications which could involve the novel vertical coupler space switch investigated in the previous chapters. It has been shown that such device can route optical data packets at data rates up to 10Gb/s with inter-packet guard-band time as short as 2ns.

Simultaneous wavelength conversion and routing of 10Gb/s optical packets has been successfully demonstrated. Both co-propagation and counter-propagation arrangements have been investigated. It is thought that the combination of packet routing and wavelength conversion in the same device can significantly simplify the wavelength/packet switched OXC design as well as providing additional flexibility in such OXC nodes.

Finally the same OXS has been used to demonstrate an optical packet routing node within a recirculating loop. The router incorporates header processing, contention resolution and signal conditioning. A cascade of 14 nodes was achieved with error rates less than 10^{-9}.

7.5. References

[1] S.L. Danielsen, P.B. Hansen, and K.E. Stubkjaer, "Wavelength Conversion in Optical Packet Switching", J. of Lightwave Technology, Vol. 16, No. 12, 1998, pp. 2095-2108.

[2] M. Owen, J.D. Baindridge, M.F.C. Stephens, R.V Penty, I.H. White, K. Poguntke, K. Young-Smith, and M.J. Robertson, "1x4 Space Switching and Simultaneous All-Optical Wavelength Conversion at 2.488Gbit/s Using a Single Monolithically Integrated Multiwavelength Laser", Electronics Letters, Vol. 34, No. 20, 1998, pp.1942–1943.

[3] D.K. Hunter, M.H.M. Nizam, M.C. Chia, I. Andonovic, K.M. Guild, A. Tzanakaki, M.J. O'Mahony, J.D. Baindridge, M. Stephens, R.V. Penty, and I.H. White, "WASPNET: a Wavelength Switched Packet Network", IEEE Communications Magazine, 1999, Vol. 37, No. 3, pp. 2095-2107.

[4] K.M Guild, M.J. O'Mahony, "Routing and buffering architecture in all-optical switching node", Electronics Letters, Vol. 35, No. 2, 1999, pp.161–162.

Chapter 8

Conclusions and Future Work

Glossary of the abbreviations

(OXS) Optical Crosspoint Switch
(TIR) Total Internal Reflection
(RIE) Reactive Ion Etching
(VC) Vertical Coupler
(ICP) Inductive Coupled Plasma

8.1. Conclusions

Optical Crosspoint Switches (OXSs) will play a very important role inside future optical networks. This is because they can be used to improve flexibility and routing management of such networks by resolving important problems such as packet contention with reduced optical buffering requirements.

Different kinds of architectures have been applied to different kinds of materials, III-V semiconductors, Lithium Niobate ($LiNbO_3$) and polymer materials, in order to produce OXSs. However, due to various shortcomings, in either the materials or the structures, a survey of a number of commercially available OXS has confirmed that at the moment there is not a technology meeting all the characteristics required by a future optical packet switching network. Therefore, for the first time, a description has been given of a novel OXS concept that was investigated in this PhD work. It is based on an InGaAsP/InGaAs/InP active vertical coupler structure and has been shown to be able to route data packets within few nanoseconds. The device concept is based on an active vertical coupler technology, which has all the potential characteristics to succeed in the future optical networks based on packet switching routing.

An analysis of the optical crosspoint switch has been carried out. A theory involving the complex compound refractive indices has been introduced.

A complete device model has also been developed. The vertical coupler has been investigated first in a 2D calculation of its modal distribution followed by a 3D-propagation calculation to determine coupling characteristics. The first 2D analyses the coupler as two single waveguides near each other. The second part instead has studied the whole compound structure, which gives the right value for the *carrier density N* that maximises the coupling. The introduction of the propagation model is then used to find the device coupling length achieved with the optimal injection current.

The Total Internal Reflection (TIR) mirror, as an important part of the device, has also been analysed with a particular focus on the loss that can be generated as a result of mirror imperfection inside the crosspoint switch. The model of the OXS device with the added TIR mirror loss allows the investigation of the whole device.

Using this theoretical investigation some wafer structures have been verified in Chapter 4. They have been designed and some of those also grown prior to the characterisation of the theoretical model. Two main structures have been investigated, one named MR1453, which adopts MQW structure, and a second, MR1392, based on bulk material. Both structures are based on InGaAs/InGaAsP/InP semiconductors. It has been found that the wafer giving the best performances in terms of absorption, crosstalk, and scalability should be MR1392, which gives high ON-OFF contrast and very low extinction ratio in the order of –60dB. Such characteristics make the device suitable to be employed in a 4x4matrix switch. Less efficient would be the MQW structure MR1453 with high loss and figures in the order of 45dB for the ON-OFF contrast while –30dB for the crosstalk.

The fabrication considerations of the crosspoint switch have been analysed. All the manufacturing phases involved have been discussed with a highlight of the highly critical etching steps, which are based on a Methane/Hydrogen (CH_4/H_2) process performed in a Reactive Ion Etching (RIE) chamber. It has been shown that good semiconductor etching with flat and smooth sidewalls supported by high mirror verticality would considerably reduce the device losses.

Device performance is directly dependent on the mask resolution and on the RIE etching process. In particular mask resolution plays a very important role for the etching process followed by the consideration that pattern mask and TIR mirror mask alignment have a great influence in the sidewall smoothness and its verticality during the semiconductor etching step.

The RIE process induced device degradation, due to ion damages, carrier traps, and surface states on the sidewall that cause a bias current leakage, has been analysed. A novel passivation process able to drastically reduce current leakage problem has been investigated.

The modelled, designed and fabricated OXS has been characterised. The Vertical Coupler (VC) structure, which is the key element of the device, was characterised first. Particular attention has been paid to the parameters of transparency wavelength and waveguide and coupler loss. These have been found as 0.2dB on-chip for a 400μm long passive waveguide sample, and 8.5dB for an 800μm, which includes two

crosspoint cells. The top layer of the VC has also been investigated but because of its active nature, it has been done cleaving the device in such a way to obtain a Fabry-Perot laser. This allows the characterisation of the active layer in terms of current and voltage threshold, which are respectively 100mA and less that 0.7V. Electrical resistance has been measured at roughly 9Ω and operating wavelength of 1565 nm.

The whole OXS has then been tested in terms of switching characteristics for a single cell and for arrayed cells. It has been shown that the device has an ON-OFF contrast higher than 50 dB, an interchannel crosstalk of roughly –60dB and 3dB-bandwidth higher than 40nm.

The dynamic performance of the device has been tested and results have shown successful device operation as a 622Mb/s optical modulator. The open eye diagram and correctly recovered data output confirm that the device switching time of <1.5ns is sufficiently fast for optical packet routing.

The use of the device as a non-linear all-optical crosspoint has also been studied. Encouraging switching characteristics for two different experiments have been considered. The first was based on CW self-switching signal while the second adopted a short pulsed pump signal. The ON-OFF contrast achieved was of 8dB and 23dB respectively.

Following these device characterisation measurements, some experiments have been carried out in order to demonstrate the packet switching performance of such a device. The device has demonstrated the ability to route optical data packets at payload speeds of up to 10Gb/s with inter-packet guard-band time as short as 2ns. It can also performs simultaneous wavelength conversion and routing of 10Gb/s optical packets with a guard-band time as short as 5ns. In this last test both co-propagation and counter-propagation arrangements have been investigated showing an extinction ratio of about 9dB and 7.5dB respectively.

Finally the same optical crosspoint switch has been used to demonstrate an optical packet switch within a recirculating loop. The switch incorporates header processing, contention resolution and signal conditioning. A cascade of 14 nodes was achieved with error rates less than 10^{-9}.

8.2. Future Works

Even though if the novel crosspoint switch has shown good performance, a lot can be done in order to improve it. In the future some features needs to be improved without penalising the others. The investigation of the 4x4 switch matrix sample has also to be carried out in order to better understand the relation between optical signal transmission and the input-output path. Finally the use of the vertical coupler used as a platform for other kinds of devices could be investigated.

One of the main problems of devices using MQWs is the polarisation sensitivity. In fact it is known that such materials are more likely to operate in TE mode rather than TM. It is also known that bulk material, even if polarisation insensitive, when used in a directional coupler will have different coupling length for the two polarisations TE and TM.

There could be two ways to address the polarisation sensitivity problem. Multi quantum wells can be polarisation insensitive when lattice strains are introduced. This lead to a new model of the vertical coupler structure, which could adopt one layer made with strained MQWs. The presence of the strain should be able to suppress the difference between the two modes. A second approach could be based on a vertical coupler made with bulk material but modelled in order to get a point where the two modes gives the same transmission and the same coupling length.

The improvement of the device gain would permit to extend the matrix number from 4x4 to 8x8 or even 16x16. Thus it is very important to investigate new high gain VC structures.

Already now some new devices can be thought and it would be very interesting being able to apply the vertical coupler platform in order to realise new optoelectronics devices. There are a number of devices, which are already under theoretical investigation and some others to come.

RIE etching is a process characterised by a slow etch rate. However, the etching process can be speeded up by the adoption of Inductive Coupled Plasma (ICP) etching together with RIE process. In this case the etch-rate is 10 times faster with excellent results including the surface/sidewall morphology. Unfortunately the presence of the double Ni/SiO_2 mask reduces the process application to just after the removal of the first nickel mask. This due to the ICP plasma that sputters Ni mask. Thus, the ICP process can be used only for the TIR mirror etching. However, the adoption of ICP etching could introduce different etch-damage effects that should be investigated and eventually removed with the introduction of an adequate passivation procedure.

In further investigation three main points can be focused.

The first one is the introduction of the optical crosspoint switch in high-speed data rate networks and its investigation in different configurations. This could permit better understanding of the limits of the device and what needs to be done to improve. In particular would be of great help knowing more about noise and dynamic range of the device.

It has been shown that the device gives good results in simultaneous packet switching and wavelength conversion, thus, further tests would be decisive for the improvement of the device. In this case both co and counter propagation tests could be carried out using a 4x4 matrix confirming the flexibility of the device in simultaneous switching and conversion or wavelength allocation.

The final further investigation point comes from the previous non-linear tests shown in chapter 5. It has been shown that the device gives results also using non-linear effects. This suggests that more time could be spent in testing the device under such non-linear conditions. Switching test can be repeated and hence followed by switching speed test and possibly data packet routing.

Appendix A: Designed and Grown Vertical Coupler Structures

As a consequence of the theoretical model developed during the PhD and described in chapter 3, it has been a good exercise to investigates some material structures which have been realised in earlier times. All the coupling analysis has been shown in chapter 4 while the description of the structures is given in this appendix.

University of Bristol Electrical & Electronic Dept.

Optoelectronics Clean Room

Epitaxial Growth Wafers Inventory

Inventory N.	015

Date	25/10/2001

Prefix	MR

Layer	1456

Description	MQW VCWS structure

Grant	GR/M37639

Layer Sequence

Repeats	Thickness (Å)	Material	Dopant	Type	Conc. (cm-3)
1	2000	GaAs contact	Zn	p	5.0e+18
1	500	Q1.1	Zn	p	2.0e+18
1	12000	InP	Zn	p	5.0e+17
1	1070	Q1.3		i	
4	120	Q1.3		i	
5	75	InGaAs QW		i	
1	1070	Q1.3		i	
1	11500	InP	Si	n	3.0e+17
1	1070	Q1.3	Si	n	3.0e+17
11	53	Q1.3	Si	n	3.0e+17
12	37	InGaAs	Si	n	3.0e+17
1	1070	Q1.3	Si	n	3.0e+17
1	20000	InP Buffer	Si	n	2.0e+18

	52162	**Total thickness (Å)**	**41 layers**	

University of Bristol Electrical & Electronic Dept.

Optoelectronics Clean Room

Epitaxial Growth Wafers Inventory

Inventory N.	014

Date	25/10/2001

Prefix	MR

Layer	1468

Description	MQW VCWS structure

Grant	GR/M37639

Layer Sequence

Repeats	Thickness (Å)	Material	Dopant	Type	Conc. (cm-3)
1	2000	GaAs contact	Zn	p	5.0e+18
1	500	Q1.1	Zn	p	2.0e+18
1	12000	InP	Zn	p	5.0e+17
1	1070	Q1.3		i	
4	120	Q1.3		i	
5	75	InGaAs QW		i	
1	1070	Q1.3		i	
1	11500	InP	Si	n	3.0e+17
1	1070	Q1.3	Si	n	3.0e+17
11	37	Q1.3	Si	n	3.0e+17
12	37	InGaAs	Si	n	3.0e+17
1	1070	Q1.3	Si	n	3.0e+17
1	20000	InP Buffer	Si	n	2.0e+18

	51986	Total thickness (Å)	41 layers	

University of Bristol Electrical & Electronic Dept.

Optoelectronics Clean Room

Epitaxial Growth Wafers Inventory

Inventory N.	XXX

Date	XX/XX/XX

Prefix	XX

Layer	XXXX

Description	SHEFVCW2 – NOT REALISED

Grant	XXXX

Layer Sequence

Repeats	Thickness (Å)	Material	Dopant	Type	Conc. (cm-3)
1	2000	$In_{0.53}GaAs$ contact	Zn	p	1.0e+19
1	500	Q1.1	Zn	p	2.0e+18
1	12000	InP	Zn	p	5.0e+17
1	1070	Q1.3 Barrier		i	
4	120	Q1.3 Barrier		i	
5	75	$In_{0.53}GaAs$ QW		i	
1	1070	Q1.3 Barrier		i	
1	11500	InP	Si	n	3.0e+17
1	946	Q1.3 Barrier	Si	n	3.0e+17
11	60	Q1.3 Barrier	Si	n	3.0e+17
12	37	$In_{0.53}GaAs$ QW	Si	n	3.0e+17
1	946	Q1.3 Barrier	Si	n	3.0e+17
1	20000	InP buffer	Si	n	2.0e+18

	51991	Total thickness (Å)	41 layers	

University of Bristol Electrical & Electronic Dept.

Optoelectronics Clean Room

Epitaxial Growth Wafers Inventory

Inventory N.	XXX

Date	XX/XX/XX

Prefix	XX

Layer	XXXXX

Description	SHEFVCW3 – NOT REALISED

Grant	XXXX

Layer Sequence

Repeats	Thickness (Å)	Material	Dopant	Type	Conc. (cm-3)
1	2000	$In_{0.53}GaAs$ contact	Zn	p	1.0e+19
1	500	Q1.1	Zn	p	2.0e+18
1	12000	InP	Zn	p	5.0e+17
1	1070	Q1.3 Barrier		i	
4	120	Q1.3 Barrier		i	
5	75	$In_{0.53}GaAs$ QW		i	
1	1070	Q1.3 Barrier		i	
1	11500	InP	Si	n	3.0e+17
1	849	Q1.3 Barrier	Si	n	3.0e+17
13	60	Q1.3 Barrier	Si	n	3.0e+17
14	37	$In_{0.53}GaAs$ QW	Si	n	3.0e+17
1	849	Q1.3 Barrier	Si	n	3.0e+17
1	20000	InP buffer	Si	n	2.0e+18

	57224	Total thickness (Å)	45 layers	

University of Bristol Electrical & Electronic Dept.

Optoelectronics Clean Room

Epitaxial Growth Wafers Inventory

Inventory N.	XXX

Date	XX/XX/XX

Prefix	XX

Layer	XXXXX

Description	SHEFVCW6 – NOT REALISED

Grant	XXXX

Layer Sequence

Repeats	Thickness (Å)	Material	Dopant	Type	Conc. (cm-3)
1	2000	$In_{0.53}GaAs$ contact	Zn	p	1.0e+19
1	500	Q1.1	Zn	p	2.0e+18
1	12000	InP	Zn	p	5.0e+17
1	1070	Q1.3 Barrier		i	
4	120	Q1.3 Barrier		i	
5	75	$In_{0.53}GaAs$ QW		i	
1	1070	Q1.3 Barrier		i	
1	11500	InP	Si	n	3.0e+17
1	1070	Q1.3 Barrier	Si	n	3.0e+17
13	26	Q1.3 Barrier	Si	n	3.0e+17
14	37	$In_{0.53}GaAs$ QW	Si	n	3.0e+17
1	1070	Q1.3 Barrier	Si	n	3.0e+17
1	20000	InP buffer	Si	n	2.0e+18

	51991	Total thickness (Å)	45 layers	

University of Bristol Electrical & Electronic Dept.

Optoelectronics Clean Room

Epitaxial Growth Wafers Inventory

Inventory N.	001

Date	25/10/2001

Prefix	MR

Layer	1392

Description	Q1.45/Q1.55 p-i-n structure

Grant	GR/M37639

Layer Sequence

Repeats	Thickness (Å)	Material	Dopant	Type	Conc. (cm-3)
1	2000	InGaAs contact	Zn	p	5.0e+18
1	500	Q1.1	Zn	p	2.0e+18
1	10000	InP	Zn	p	5.0e+17
1	2000	InP (p-spacer)		i	
1	2000	Q1.55		i	
1	13000	InP	Si	n	3.0e+17
1	2400	Q1.45	Si	n	2.0e+17
1	20000	InP	Si	n	3.0e+17
1	10000	InP buffer	Si	n	2.0e+18

	61900	Total thickness (Å)	9 layers	

University of Bristol Electrical & Electronic Dept.

Optoelectronics Clean Room

Epitaxial Growth Wafers Inventory

Inventory N.	003

Date	25/10/2001

Prefix	MR

Layer	1394

Description	Q1.2/Q1.55 p-i-n structure

Grant	GR/M37639

Layer Sequence

Repeats	Thickness (Å)	Material	Dopant	Type	Conc. (cm-3)
1	2000	InGaAs contact	Zn	p	5.0e+18
1	500	Q1.1	Zn	p	2.0e+18
1	10000	InP	Zn	p	5.0e+17
1	2000	InP (p-spacer)		i	
1	2000	Q1.55		i	
1	11000	InP	Si	n	2.0e+17
1	7000	Q1.2	Si	n	1.5e+17
1	20000	InP	Si	n	2.0e+17
1	10000	InP buffer	Si	n	2.0e+18

	64500	**Total thickness (Å)**	**9 layers**	

University of Bristol Electrical & Electronic Dept.

Optoelectronics Clean Room

Epitaxial Growth Wafers Inventory

Inventory N.	XXX	Date	XX/XX/XX
Prefix	XX	Layer	XXXX
Description	VCWBLK1 – NOT REALISED		
Grant	XXXXX		

Layer Sequence

Repeats	Thickness (Å)	Material	Dopant	Type	Conc. (cm-3)
1	2000	InGaAs contact	Zn	p	1.0e+19
1	500	Q1.1	Zn	p	2.0e+18
1	12000	InP	Zn	p	5.0e+17
1	2000	Q1.55 active		i	
1	14000	InP spacer	Si	n	3.0e+17
1	2000	Q1.50 passive	Si	n	2.0e+17
1	20000	InP cladding	Si	n	3.0e+17
1	10000	InP buffer	Si	n	2.0e+18

	62500	**Total thickness (Å)**	**8 layers**	